Xylylene Bridged Perylene Bisimide Cyclophanes and Macrocycles

Dissertation zur Erlangung des

naturwissenschaftlichen Doktorgrades

der Julius-Maximilians-Universität Würzburg

vorgelegt von

Peter Spenst

aus Saran (Kasachstan)

Würzburg 2016

Eingereicht bei der Fakultät für Chemie und Pharmazie am:

29.07.2016

Gutachter der schriftlichen Arbeit:

1. Gutachter: Prof. Dr. Frank Würthner
2. Gutachter: Prof. Dr. Tobias Brixner

Prüfer des öffentlichen Promotionskolloquiums:

1. Prüfer: Prof. Dr. Frank Würthner
2. Prüfer: Prof. Dr. Tobias Brixner
3. Prüfer: Prof. Dr. Matthias Lehmann

Datum des öffentlichen Promotionskolloquiums:

30.09.2016

Doktorurkunde ausgehändigt am:

_____

für Jessica

und

meine Familie

Danksagung

Vor allem möchte ich mich bei Herrn Prof. Dr. Frank Würthner für das Überlassen des sehr interessanten und vielfältigen Forschungsthemas, sowie die Möglichkeit zu einem vierwöchigen Aufenthalt in Evanston bedanken. Darüber hinaus bedanke ich mich für seine zahlreichen Hilfestellungen jeglicher Art, seine vielen Ratschläge an mich und für die exzellenten Arbeitsbedingungen in seinem Arbeitskreis.

Herrn Prof. Dr. Michael R. Wasielewski von der Northwestern University, Evanston, Ilionois, USA, möchte ich meinen Dank für die Ermöglichung eines Besuchs seiner Arbeitsgruppe aussprechen. Herrn Dr. Ryan Young und Brian Phelon möchte ich sehr für die herzliche Aufnahme in die Gruppe sowie die notwendige Hilfe bei Messungen für unser gemeinsames Projekt danken.

Für die finanzielle Unterstützung von Konferenz- und Workshop-Teilnahmen und die Reise nach Evanston bin ich der Forschergruppe FOR 1809 „Lichtinduzierte Dynamik in molekularen Aggregaten“ zu Dank verpflichtet.

Herrn Dr. Chantu R. Saha-Möller und Dr. David Schmidt danke ich für die hervorragende und zuverlässige Korrekturhilfe bei drei Manuskripten.

Für das Korrekturlesen dieser Arbeit bzw. Teile derer danke ich sehr herzlich Dr. David Schmidt, Dr. Matthias Stolte, David Bialas, Stefanie Herbst, Eva Kirchner, Annike Weißenstein, Dr. Vladimir Stepanenko und Meike Sapotta.

Herrn Dr. Vladimir Stepanenko danke ich für die AFM-Aufnahmen, seine stete Hilfsbereitschaft und viele hilfreiche Diskussionen.

Meinem Bachelor-Studenten Andreas Sieblist, sowie den Studenten Tim Görlich, Arthur Turkin und Lisa Lechner danke ich für die Unterstützung bei synthetischen Arbeiten.

Herrn Dr. Matthias Grüne sowie Frau Elfriede Ruckdeschel gebührt mein Dank für die Aufnahme von NMR-Spektren am 600 MHz-NMR-Gerät, sowie die immer freundliche und hilfreiche Unterstützung bei Fragen. Die zuverlässige Aufnahme von MS-Spektren durch Herrn Dr. Michael Büchner, Herrn Fritz Dadrich, Frau Antje Heckmann, sowie Frau Juliane Adelmann möchte ich voller Dank hier aufführen.

Danke allen Personen, die am Gelingen dieser Arbeit geholfen haben bzw. sich am Erfolg dieser beteiligt haben, die mir kleine und große Sachverhalte erklärt haben oder die mich an Geräten oder Programmen eingewiesen haben.

Frau Christiana Toussaint danke ich für ihre stete Hilfsbereitschaft bei allen Formalitäten.

Herzlichen Dank besonders den Arbeitskreismitgliedern der Labore 04.010 und 04.027 für die lustige Zeit und Hilfsbereitschaft.
Allen aktuellen sowie ehemaligen Arbeitskreismitgliedern danke ich für die schöne Zeit, die gute Zusammenarbeit und das freundschaftliche Arbeitsklima.
Meiner gesamten Familie bin ich für ihre Unterstützung und ihr Verständnis zu größtem Dank verpflichtet.
Besonderer Dank gilt vor allem meiner Frau Jessica, die mich bei meiner Arbeit stets unterstützt und motiviert hat.

List of Abbreviations

AFM	atomic force microscopy
ATP	adenosine triphosphate
(B)Chl	(bacterio)chlorophyll
Bz	Benzyl
CD	circular dichroism
CR	charge recombination
CS	charge separation
CT	charge transfer
CV	cyclic voltammetry
DCM	dichloromethane
DCTB	2-[(2*E*)-3-(4-*tert*-butylphenyl)-2-methylprop-2-enylidene]malononitrile
DNA	deoxyribonucleic acid
dpp	1,3-bis(diphenylphosphino)propane
EEH	excitation energy hopping
EET	excitation energy transfer
ENDOR	electron nuclear double resonance
EnT	energy transfer
EPR	electron paramagnetic resonance
eq.	equivalence
ESA	excited state absorption
ESI	electrospray ionization
ET	electron transfer
FD	ferredoxin
FE-SEM	field emission scanning electron microscopy
FNR	ferredoxin-NADP-reductase
FRET	Förster resonance energy transfer
FSRS	femtosecond stimulated Raman spectroscopy
GPC	gel permeation chromatography
GS	ground state
GSB	ground state bleach
HOMO	highest occupied molecular orbital
HOPG	highly ordered pyrolytic graphite

HPLC	high-performance liquid chromatography
HRMS	high resolution mass spectrometry
*i*Pr	*iso*-propyl
IV-CT	intervalence charge transfer
LH	light-harvesting
LUMO	lowest unoccupied molecular orbital
MALDI	matrix-assisted laser desorption/ionization
MB	methylene blue
Mp.	melting point
NADPH	nicotinamide adenine dinucleotide phosphate
NBI	naphthalene bisimide
NIR	near-infrared
NMR	nuclear magnetic resonance
OEC	oxygen-evolving complex
OTf	trifluoromethanesulfonate
PBA	perylene bisanhydride
PBI	perylene bisimide
PC	plastocyanine
Ph	phenyl
pos.	positive
PPI	pyrophosphate
PS	photosystem
PyBI	pyromellitic bisimide
Q	quinone
RC	reaction center
ROESY	rotating-frame nuclear Overhauser effect spectroscopy
RP	radical ion pair
RP-ISC	radical pair intersystem crossing
RT	room temperature
SB-CS	symmetry-breaking charge separation
SCOF	surface covalent organic framework
SE	stimulated emission
SF	singlet fission
SHBC	second harmonic bandwidth compressor

SOCT-ISC	spin-orbit charge transfer intersystem crossing
SO-ISC	spin-orbit coupling induced intersystem crossing
SOMO	single occupied molecular orbital
TA	transient absorption
TBAHFP	tetrabutylammonium hexafluorophosphate
*t*Bu	*tert*-butyl
TDDFT	time-dependent density functional theory
TIPS	tri-*iso*-propylsilyl
TOF	time-of-flight
Tol	toluene
Tyr	tyrosine
UV	ultraviolet
vis	visible

Table of Contents

Chapter 1

—

Introduction and Aim of the Thesis

Nature is often a good example for how chemical systems can work and how efficient they can be. Especially supramolecular architectures of self-assembled components play a unique role in biological systems, like the formation of the DNA double helix, the folding of proteins and enzymes or their selective recognition of substrates. One very prominent example of dye containing structures is the light-harvesting system (LH) of bacteria, where carotenoids and bacteriochlorophyll chromophores are arranged in a cyclic manner. Embedded into a matrix of proteins these chromophores are just tuned in the right way to absorb light in the LH2, to undergo energy transfer (EnT) to the next macrocycle LH1 and to bring this energy to a reaction center located in the cavity of these arrays. Herein, the light energy is converted into chemical energy that can later on be used for different processes taking place in living cells.

To understand the role of supramolecular architectures in these fundamental processes, scientists got motivated to design artificial counterparts that can mimic highly complex natural systems. Therefore, highly organized and well-defined porous cavities that are capable to encapsulate particular guest molecules were synthesized to provide a unique environment for the investigation of such non-covalent interactions.[1] Associated with these artificial host-guest systems numerous applications were developed, such as drug delivery and release,[2] chemosensing and imaging,[3] nanomachines,[4] ion transport,[5] metallo-enzyme mimics,[6] stabilization of reactive compounds,[7] catalysis[8] and even nuclear waste treatment.[9]

This clearly elucidates, why host-guest chemistry was intensively developed in the past, starting with the Dianin´s compound,[10] crown ethers[11] and macrobicyclic amines[12] in the 60´s. These initial studies on host-guest phenomena were concerned with the complexation of relatively small molecules and ions and were later on continued with the development of several new host systems, like cryptands,[13] spherands,[14] carcerands,[15] hemicarcerands,[16] cyclodextrins,[17] calixarenes,[18] pillararenes[19] and curcurbiturils.[20] Recent publications, however, focus on the incorporation of larger functionalized compounds, such as fullerenes[21] and other aromatic hydrocarbons.[22] Regarding the latter, cyclophanes containing two parallelly arranged aromatic subunits in a well-defined distance, which were first reported by Cram *et al.* 1951,[23] have evolved as particularly versatile host molecules to intercalate planar aromatic guests by non-covalent π-π interactions. Thus, several reports on neutral covalently linked cyclophanes composed of pyromellitic or naphthalene bisimides have been published that are suitable to host a variety of small aromatic compounds.[24] Furthermore, recent examples are concerned with multiple charged systems, such as the "ExBox" introduced by the group of Stoddart, which can be used as a scavenger for polycyclic aromatic hydrocarbons (up to the size of coronene) in both aqueous and organic media.[25] Moreover, multicomponent cyclophanes were self-assembled by non-covalent metal ligand interactions and applied in host-guest chemistry.[26] Regarding their potential applications in catalysis,[27] sensing,[28] or transport processes,[29] macrocycles derived from perylene bisimides (PBIs) should be of particular interest as host systems. Due to their unique photophysical properties that are highly sensitive to environmental changes these systems should be useful to gather information about the corresponding host-guest complexes. It is to note that among all PBI-based cyclophanes reported so far there is no example in which the encapsulation of aromatic hydrocarbons into the porous cavity could be achieved.[30] A reasonable explanation for that can easily be provided based on the fact that the length of the spacer unit between both chromophores determines the size of the accessible void. Short π-π distances certainly provide insufficient space,[30c, 30e] whereas long and flexible spacer units facilitate an intramolecular PBI-PBI self-aggregation process that efficiently prevents guest intercalation.[30a, 30b, 30d]

Therefore, the introduction of a more rigid spacer unit with an appropriate length seems to be essential to overcome both of these shortcomings. Pleasingly, the syntheses of the *para*-xylylene bridged PBI cyclophanes **2PBI** that can be used for the selective

encapsulation of polycyclic aromatic molecules could successfully be accomplished and is presented in this work. Moreover, the photophysical properties of the corresponding host-guest complexes were investigated, which demonstrate that these cyclophanes serve as dual fluorescence probes that distinguish between electron-poor and electron-rich aromatic guests. Furthermore, larger macrocycles, composed of three to nine PBI subunits, were synthesized and their folding behavior in aromatic solvents and their self-assembly on highly ordered pyrolytic graphite (HOPG) was studied. Moreover, the cyclic trimer was used for the encapsulation of fullerene and the photophysical properties of this host-guest complex were investigated in detail (Figure 1).

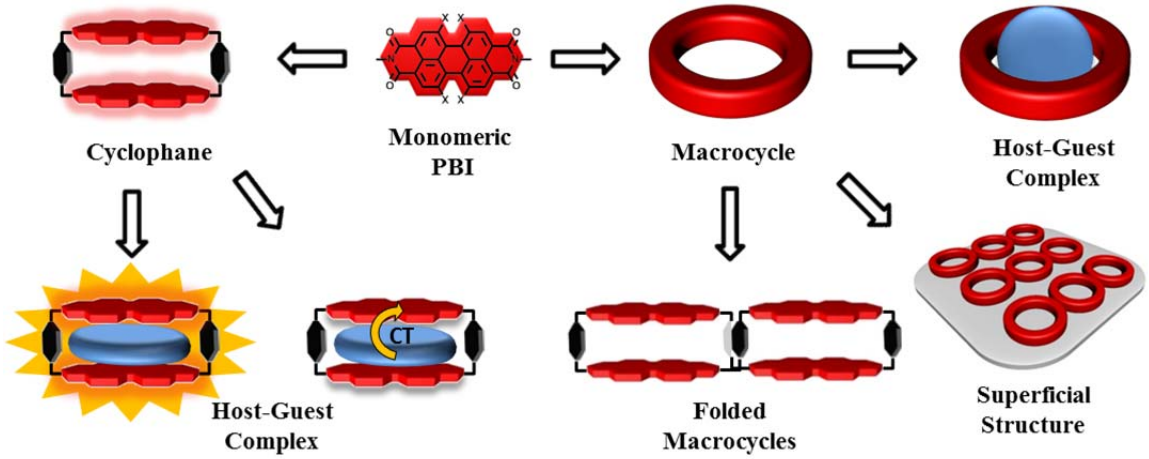

Figure 1. Illustration of the presented topics that are described in this thesis; left: Cyclophanes and their use for planar guest incorporation resulting in a change of the fluorescence behavior; right: Larger macrocycles, the complexation of fullerene, the self-assembly on HOPG surfaces and the folding in toluene.

Since the natural light harvesting system is the prototype for most of the subsequent studies **Chapter 2** gives an overview on the chromophores and their function in this assembly. Additionally, literature known macrocyclic systems composed of bisimide derivatives are presented and their main properties and applications are discussed.

Chapter 3 will focus on the own results that are discussed in detail. First, the syntheses will be described followed by host-guest studies of PBI cyclophanes that can be used as "turn-on" and "turn-off" fluorescence probes. Then, solvent and guest modulated photo-driven charge separation and triplet formation in the PBI cyclophane is presented. Furthermore, guest-promoted chirality transfer and studies on the effect of different bay substituents on the geometry of the cyclophanes are elucidated. Subsequently, the complexation of fullerene by the cyclic trimer and the energy transfer processes in the

supramolecular PBI-fullerene complex are shown. Finally, the folding of the larger macrocycles and the self-assembly on a HOPG surface is discussed.

Chapter 4 and **Chapter 5** give a summary of the work in English and German.

Chapter 6 explains the experimental details and includes all material and method information that were used for this work.

Chapter 2

—

Literature Survey

2.1 The Role of Chromophores in the Light-harvesting Systems

Life on earth is a result of sun energy that is used by plants in the photosynthesis to generate energy rich carbohydrates. These are the basis for nutrition of living organisms and oxygen generation and further provide the energy needed for technical applications. Thus, one of the major goals in science is to understand the biological processes in photosynthesis and to mimic these by artificial counterparts.

The photosynthesis can in principle be divided into two parts. The first one is the light-harvesting by photosystem complexes (PSII and PSI) that capture sunlight and transport this energy to a reaction center (RC) where charge separation takes place. The connection between the RC and membrane oxidoreductases, such as cytochrome bc_1 and b_6f is mediated by diffusion of quinones (Q), cytochrome *c* and plastocyanin (PC).[31] The electrons are thus transferred from PSII to PSI, which leads to an electrochemical potential gradient of protons that provides the driving force to generate adenosine triphosphate (ATP), while the electrons are further used to produce nicotinamide adenine dinucleotide phosphate (NADPH) (Figure 2). These high energetic compounds then convert carbon dioxide into carbohydrates and other energy containing molecules in the second part of photosynthesis, the dark reaction.

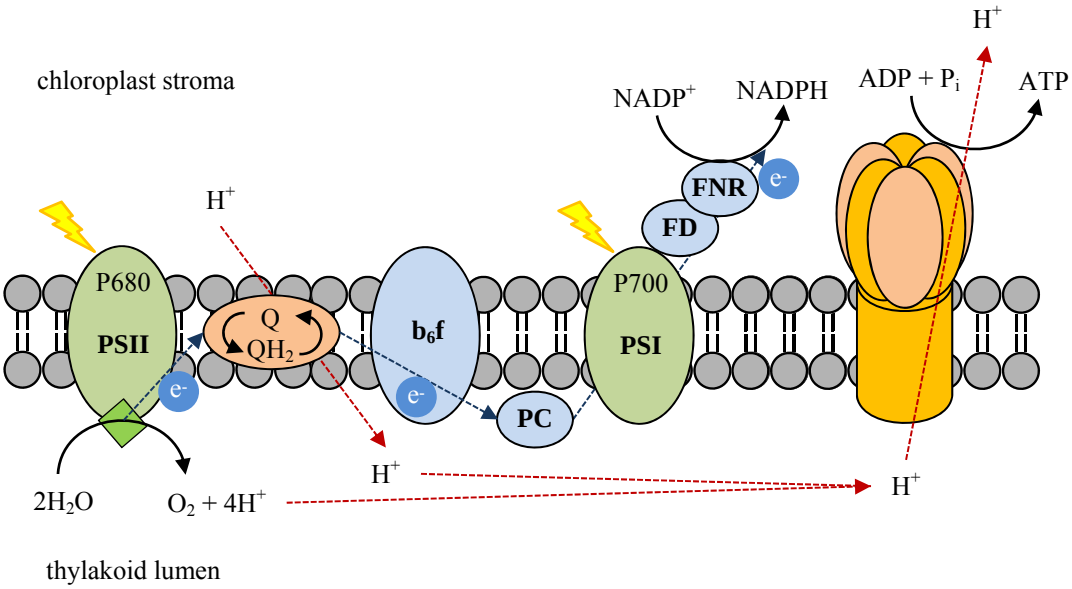

Figure 2. Photosynthetic thylakoid membrane of higher plants with photosystem PSII and PSI and cytochrome b_6f showing the electron transfer through electron carriers.

Obviously, one key step of photosynthesis is the light harvesting by the photosystems I and II that are large protein assemblies (up to 25 kDa of protein and 15 kDa of pigments)[32] located inside the thylakoid membranes. For an effective absorption of light, up to hundreds of pigments are embedded in these protein complexes that vary in structure and absorptivity.[33] Thereby, the weight percentage of chromophores can reach 40% of the photosystem.[34] Nature uses mainly assemblies of chlorophyll (Chl) and bacteriochlorophyll (BChl) dyes that absorb in the visible (vis) and near infrared (NIR) region of the solar spectrum. By using different substituents at the pyrrole rings and saturation of chemical bonds the energy levels of the chromophores are highly tunable (Figure 3).[35] Nevertheless, Chl *a* seems to be the most important pigment in oxygenic photosynthesis, since it is present in the RC and in antenna complexes, while other Chl pigments provide the flexibility that is needed to adapt differences in natural habitats and light quality.[33a] However, these other Chl pigments (Chl *b*, Chl *c*) often transfer their excitation energy to Chl *a* within 1 ps, why excitation energy transfer (EET) proceeds typically via Chl *a* chromophores.[32, 36] Organisms living underneath Chl *a* containing plants and thereby in visible light depleted regions mainly contain Chl *d* and Chl *f* pigments to absorb light from the NIR region.[37]

However, chlorophylls show only little absorption in the area of 500–650 nm, leading to the so called "green-gap" that is responsible for the green color of plants. Since penetration of light above 600 nm into water is negligible this gap has to be closed

especially in algae. This is achieved with the use of carotenoids, like *β*-carotene or fucoxanthin, and phycobilins that have broad absorption features between 400 and 700 nm (Figure 3).[35b, 35c, 38]

a)

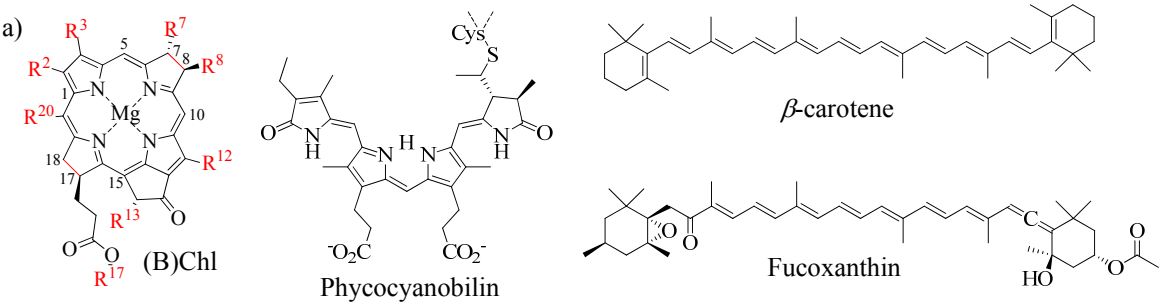

b)

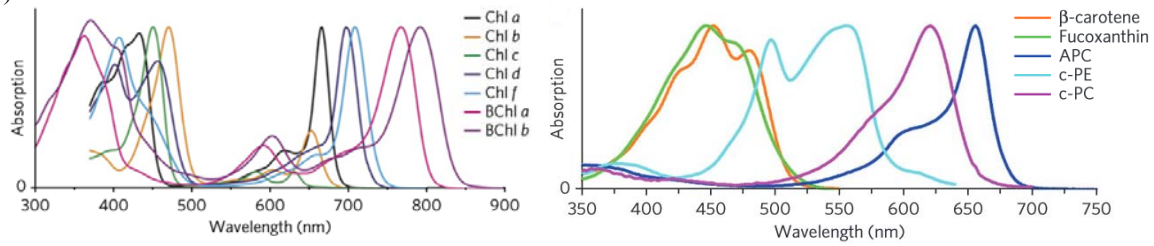

c)

Pigment	R^2	R^3	R^7	R^8	7-8 bond	R^{12}	R^{13}	17-18 bond	R^{20}	R^{17}
Chl *a*	CH_3	$CH{=}CH_2$	CH_3	C_2H_5	=	CH_3	$COOCH_3$	–	H	Phytol
Chl *b*	CH_3	$CH{=}CH_2$	CHO	C_2H_5	=	CH_3	$COOCH_3$	–	H	Phyol
Chl *c1*	CH_3	$CH{=}CH_2$	CH_3	C_2H_5	=	CH_3	$COOCH_3$	=	H	*
Chl *c2*	CH_3	$CH{=}CH_2$	CH_3	$CH{=}CH_2$	=	CH_3	$COOCH_3$	=	H	*
Chl *c3*	CH_3	$CH{=}CH_2$	$COOCH_3$	$CH{=}CH_2$	=	CH_3	$COOCH_3$	=	H	*
Chl *d*	CH_3	CHO	CH_3	C_2H_5	=	CH_3	$COOCH_3$	–	H	Phytol
Chl *f*	CHO	C_2H_5	CH_3	C_2H_5	=	CH_3	$COOCH_3$	–	H	Phytol
BChl *a*	CH_3	$COCH_3$	CH_3	C_2H_5	–	CH_3	$COOCH_3$	–	H	Phytol
BChl *b*	CH_3	$COCH_3$	CH_3	$=CHCH_3$	–	CH_3	$COOCH_3$	–	H	Phytol
BChl *c*	CH_3	$CHOHCH_3$	CH_3	Various	=	Various	H	–	CH_3	Various
BChl *d*	CH_3	$CHOHCH_3$	CH_3	Various	=	Various	H	–	H	Various
BChl *e*	CH_3	$CHOHCH_3$	CHO	Various	=	C_2H_5	H	–	CH_3	Various

Figure 3. a) Chemical structures of (bacterio)chlorophylls, phycocyanobilin and carotenoids; b) normalized UV-vis absorption spectra of different (bacterio)chlorophylls (left) and carotenoids (right) filling the "green-gap" (APC = allophycocyanin, c-PE = C-phyoerythrin, c-PC = C-phycocyanin); c) summary of the main (bacterio)chlorophylls (* Chls *c* have –CH=CH–COOH attached to the ring at R^{17}); reprinted with permission from ref.[39]. Copyright 2014 Nature Publishing Group.

Due to their short excited-state lifetimes of around 10 ps, these pigments need close contact to (B)Chls to enable fast EET (~1 ps) to store the absorbed light.[40] Furthermore, these dyes can rapidly quench triplet states within (B)Chl chromophores to prevent

oxidative cellular damage by singlet oxygen generation.[41] And indeed, (B)Chl *a* pigments are often close to carotenoids in the antenna complexes. To provide efficient EET nature uses both, local and overall funnel-principles. Herein, many pigments exchange excitations in a high energy pool, from where on the excitations cascade down in energy over lower energy pools to the RC. A stepwise decrease in number of chromophores per pool focuses the excitations near the RC.[39] Although, EET is often considered to take place in a funnel with a downhill energy gradient and the RC at the bottom, in plants and algae most of the pigments are more or less isoenergetic. In the PSII of plants the initial donor is the Chl *a* chromophore with an absorption maximum at 680 nm (P680, 175.9 kJ/mol). Interestingly, the primary donor in PSI is also a Chl *a* molecule, but with a different pigment-protein environment shifting its absorption maximum to 700 nm (P700, 170.9 kJ/mol).[39] This weak lowering in energy allows EET from PSII to PSI within equivalent chromophores. The role of the protein matrix gets more obvious by having a closer look on the light-harvesting system of bacteria, such as the well-studied purple bacteria (Figure 4).

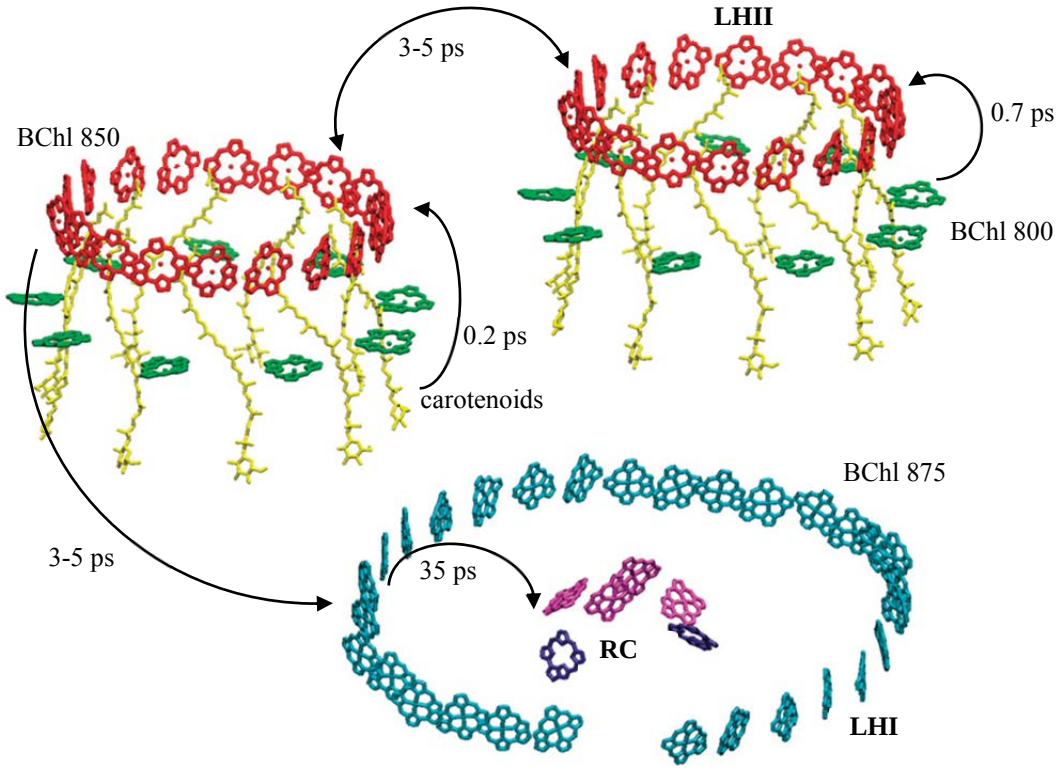

Figure 4. Schematic arrangement of chromophores in the photosynthetic apparatus of purple bacteria and energy transfer dynamics (yellow = carotenoids, green = BChl 800, red = BChl 850, cyan = BChl 875, purple = BChl 870, violet = BPheo); reprinted with permission from ref.[42]. Copyright 2013 The Royal Society of Chemistry.

Here, the cyclic arranged LHII complex contains two broad absorption bands in the NIR at 800 and 850 nm. Both are assigned to BChl *a* chromophores that vary in their absorption by a change in the pigment-pigment and pigment-protein environment caused by fixation of the BChl *a* molecules in the protein matrix.[43] The EET between BChl 800 and BChl 850 occurs within 0.7 ps and between two LHII complexes within 3–5 ps. Furthermore, each BChl *a* chromophore is located near to a carotenoid molecule that quenches triplet states and performs additional EET within 0.2 ps to BChl 850. A further EET to LHI occurs within 3–5 ps that again contains BChl *a* molecules, but this time with an absorption maximum at 875 nm. From the LHI complex a final EET appears in 35 ps to the RC located in the middle of the ring protein. In the RC the special pair of BChl 870 transfers an electron to bacterio-pheophytin *a* (BPheo; pheophytins are Chl molecules without the central Mg^{2+} ion) and further to a ubiquinone acceptor molecule that can diffuse to the RC through special ubiquinone channels in the LHI ring protein.[43b] This tuning of the absorption wavelength and width can be initiated through direct interaction to the protein, like charged protein residues[44] or H-bonds,[45] or indirect through stabilization of pigment conformations or pigment-pigment interactions.[43a]

Since the reaction center is highly specialized for charge separation with only few chromophores and thus is a weak absorber itself, efficient EET is needed.[39] To guarantee Förster resonance energy transfer (FRET) within the photosystems the orientation of dyes to each other has to be controlled.[46] With the typical (B)Chl fluorescence lifetime of ~1 ns and a critical Förster radius of 80 Å (r_0), at which EET is 50% efficient, the FRET is effective over distances of several nanometers.[46a] Furthermore, nearest neighbor distances (r) are limited to 10 Å due to light-absorption constraints. The large ratio r_0/r implies that EET is not limited to nearest neighbors in the LH complex, which enables interactions between multiple pigments and provides numerous pathways for the excitation energy to reach the RC rapidly.[34] And indeed, distances of less than 10 Å are avoided[47] in many LH complexes to circumvent self-quenching, whereas distances between 40 and 80 Å are favored.[46a] Especially the pigment-pigment distance between LHI and RC is with 40 Å ideal for FRET with a transfer quantum yield of 98.5% according to Förster´s equation (1),[48]

$$K_{\mathrm{EET}} = k_{\mathrm{r}} \left(\frac{r_0}{r}\right)^6 \qquad (1)$$

where k_r is the radiative rate constant of the donor. Thus, the EET rate is at least 64 times faster than the radiative decay rate.[34] Non-radiative decays can also be avoided by some unique relative orientations of chromophores at shorter distances as in photosynthetic bacteria, where BChl pigments are self-assembled in a head to tail arrangement of their transition dipoles. In such an arrangement EET is faster than 1 ps (Figure 4), due to strong dye interactions that lead to new excitonic levels, shared between the interacting chromophores.[39] In these cases, Förster´s point dipole approximation becomes unreliable and the excitation dynamics have to be described by Redfield theory that also considers the interactions with the surrounding.[49] These interactions are responsible for transitions between exciton levels and lead to net movement of excitations. The coherence of the excitations can persist for 0.1–1.0 ps in LH complexes[50] and is suggested to be responsible for the high efficiencies of LH. However, a rapid loss of coherence and fast incoherent diffusion of < 100 fs was reported with large pigment-pigment coupling.[51] Nevertheless, the excitations can still move over thousands of pigments in few picoseconds[52] suggesting that also strong interactions might be sufficient for EET. Thus, one photon can reach the RC within 100 ps after absorption by the antenna chromophores.[53]

After EET to the photoactive RC the light energy is converted into oxidation-reduction potential energy. This charge separated state has to live long enough (several μs) that the electrons can be extracted from the system mainly by diffusing quinones (Q). Therefore the RC is a composite of protein matrices with embedded cofactors, (B)Chl, (B)Pheo and quinones. From crystal structure the determination of the RC was achieved by Deisenhofer and Michel 1985,[54] who therefore received the Nobel Prize in chemistry along with Huber 1988. They found that the RCs of bacteria, PSII and PSI are similarly organized in a pseudo C_2 symmetry, which allows two pathways of electron transfer within the RC (Figure 5). In purple bacteria the excitons are transferred to a special pair of BChl 870 that reduces neighboring BPheo within 3 ps, which further reduces menaquinone in 200 ps. From there on the electron is given to ubiquinone in 100 μs that after a second reduction step and protonation leaves the RC complex and is replaced by a new ubiquinone molecule. The reduced ubiquinones are oxidized by cytochrome bc_1 in the membrane and the electrons are returned to BChl 870 in the RC. To enable an effective charge separation the BChl chromophores in the special pair have a close contact of 3.1–3.6 Å in a slipped cofacial arrangement.[54-55]

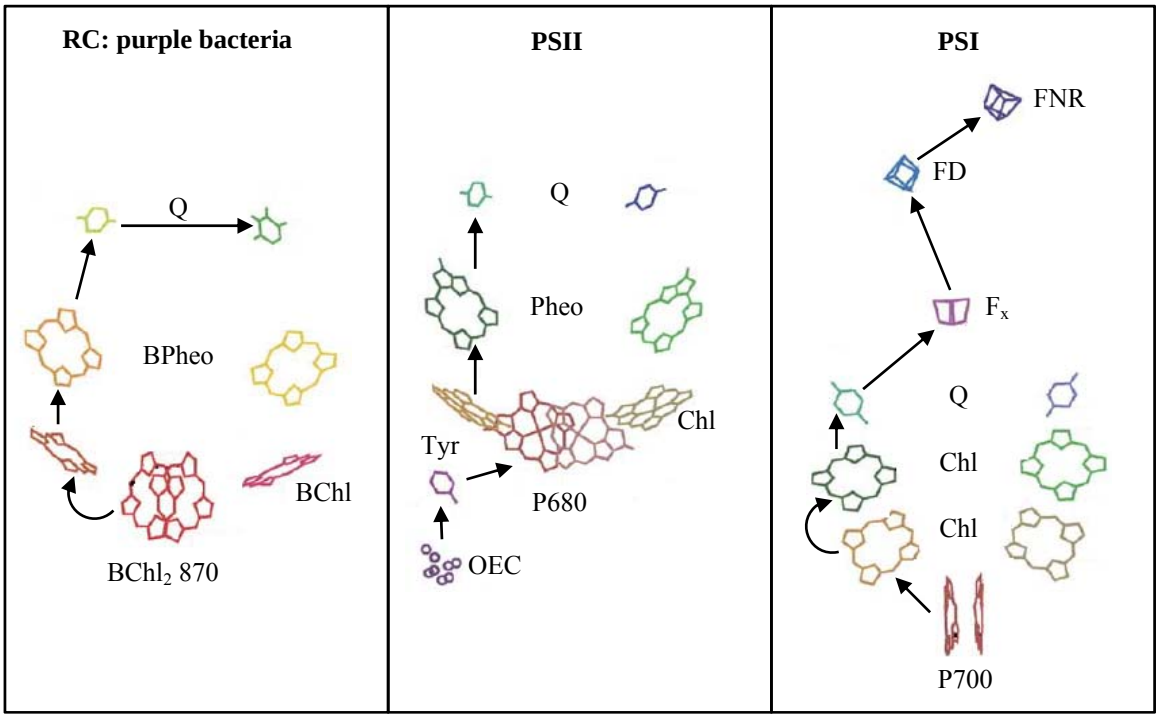

Figure 5. Arrangement of cofactors in the RC of purple bacteria, PSII and PSI; arrows indicate electron transfer reactions; reprinted with permission from ref.[34]. Copyright 2005 Elsevier.

In the PSII the number of Chl *a* molecules is with six chromophores higher than in the bacterial photosystem (four chromophores).[56] Here, the electron donor is a tyrosine (Tyr) residue on the D1 protein, instead of cytochrome as in bacteria. The electrons are taken from water molecules that are oxidized by inorganic clusters (oxygen-evolving complex: OEC) of ions (Mn^{2+}, Ca^{2+}, Cl^{-}) and shuttled to the oxidized special Chl *a* pair (P680) by Tyr. From there on, the electron transfer in PSII is very similar to that of bacterial systems reducing Pheo and quinones.

In the PSI a larger number of Chl *a* molecules were found, nevertheless, the actual electron transfer system is again comparable to the previously described RCs with a Chl *a* special pair (P700) at the beginning of the electron transfer chain. However, in this complex the electron acceptor is not a quinone molecule, but an iron sulfur protein, F_x. The electrons are now used to reduce ferredoxin (FD) that further transfers the electrons to the ferredoxin-NADP-reductase (FNR) and finally catalyze the reduction of $NADP^+$ to NADPH. The P700 special pair is reduced by a copper protein, called plastocyanin (PC) that mediates the electrons from PSII over cytochrome b_6f to PSI (Figure 2).

2.2 Deactivation Processes of Photoexcited Perylene Bisimide Dyes

This natural example impressively demonstrates how crucial the control of molecular arrangement in dye clusters is for the efficient light absorption, energy transfer and charge separation processes. All these processes occur within the assembly of the same type of chromophores, where only the conformation and position decide, which photophysical process prevails. Learning from nature, the design of artificial counterparts is one of the main targets in photosynthesis research to selectively address and control photophysical properties. Indeed, in the last decades multiple supramolecular and covalent dye arrays, including macrocycles, have been investigated with regard to their light-harvesting and photo-induced energy- and electron transfer processes.[57] As this work deals with perylene bisimide (PBI) based macrocycles, ring systems composed of bisimide-functionalized dye molecules are of particular interest. Since their optical and electrochemical properties are easily tunable, they are good candidates to study the photophysical processes in different structural arrangements. Thus, an overview of the literature known cyclic systems based on bisimide-functionalized dyes is given and their photophysical properties are discussed in the following section. Prior to addressing the individual cyclic systems, the major deactivation processes of photoexcited bisimide dyes, represented by perylene bisimide, are discussed, as they are important for the understanding of photophysical properties of cyclic dye arrays.

For an individual monomeric PBI upon photoexcitation a higher energy level S_n is populated, from which a very fast relaxation to the first excited state S_1 occurs according to Kasha´s rule.[58] From this excited state radiative and non-radiative deactivation processes back to the ground state (GS) take place. Since radiationless internal conversion (IC) to the ground state S_0 or intersystem crossing (ISC) to the triplet state T_1 are slow for monomeric PBIs, these processes are 10^6 times less favored than the radiative decay by emission (F), which leads to very high fluorescence quantum yields close to unity for this class of dyes. The non-radiative processes, however, get accessible in multichromophoric arrays in which several PBI units are in close proximity to each other (Figure 6).

Thus, bay-fused diperylene bisimides showed exceptional spin-orbit coupling induced intersystem crossing (SO-ISC) with triplet yields of > 90%.[59] With close contact of two PBIs in a cofacial arrangement the formation of an excited dimer (excimer) ^{1}(PBI-PBI)* can be observed that is usually weakly emissive with a broad and undefined red-shifted emission band.[60] In a close slip-stacked arrangement, however, the triplet states of the

chromophores can be reached effectively by singlet fission (SF) in which one excited singlet state converts into two triplet states ^{3}PBI-^{3}PBI with a theoretical triplet yield of 200%.[61] In this arrangement the excimer formation is surpressed. Theoretical studies on PBIs showed that the ideal stacking geometry is given with dX = 3.5–4.0 Å (long axis) and dY = 0.0–0.5 Å (short axis) and that only small changes in structure dramatically reduce the triplet yield.[62]

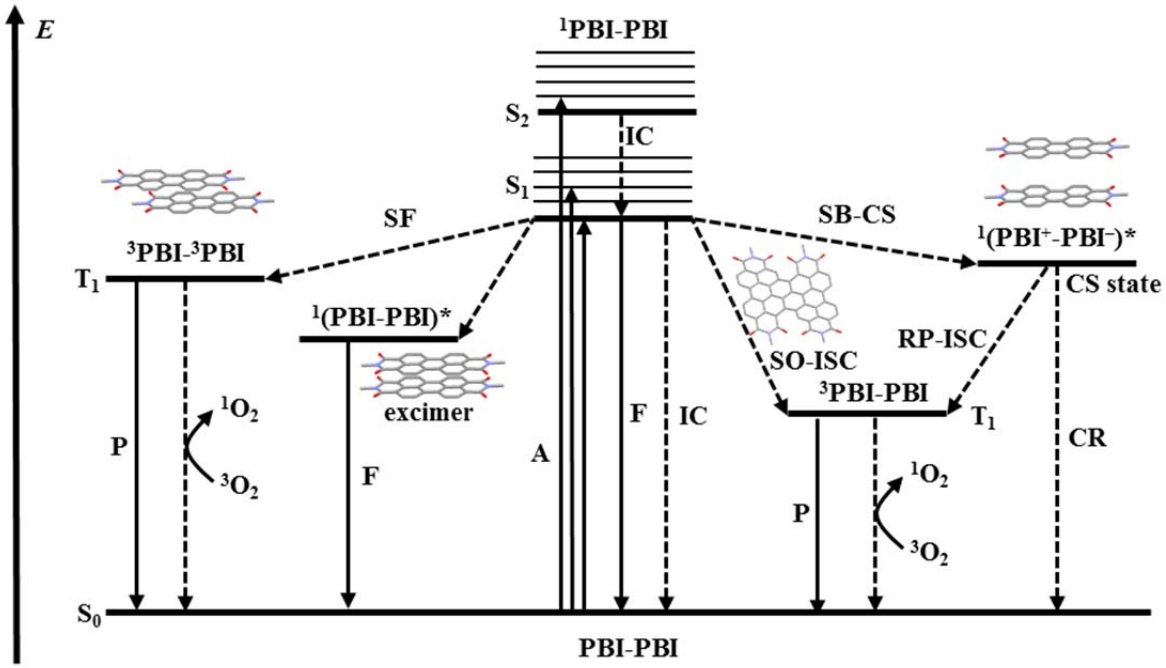

Figure 6. Jablonski-diagram of perylene bisimide (PBI) macromolecules with radiative (solid lines) and non-radiative (dashed lines) decay pathways after photoexcitation; molecular structures represent the required conformations for the individual photophysical processes.

With larger distance between the chromophores excitonic coupling is reduced and thus slow symmetry-breaking charge separation (SB-CS) can take place, similar to the special pairs in the reaction centers of natural light-harvesting systems.[63] Depending on the lifetime of the charge-separated state ^{1}(PBI$^+$-PBI$^-$)* the charge recombination occurs back to the ground state or to the triplet state ^{3}PBI-PBI via radical pair intersystem crossing (RP-ISC).[64] From the triplet states of the PBIs phosphorescence or energy transfer to molecular oxygen can occur, generating singlet oxygen.

Upon attachement or non-covalent contact with electron-rich molecules other non-radiative processes in the formed donor-acceptor complexes become facile. Thus, exiplex formation[65] or charge transfer[66] from the donor (guest) to the acceptor (PBI) can take place. The charge recombination of the CS state ^{1}(PBI$^-$-Guest$^+$)* is relatively fast

and thus typically occurs back to the ground state, but can also occur to the PBI triplet state via a spin-orbit charge transfer intersystem crossing mechanism (SOCT-ISC), if donor and acceptor are orthogonal to each other.[67]

On the other hand, energy transfer might take place, which can be devided into four different types. The first one is the trivial radiative mechanism in which the emitted light of the excited donor is reabsorbed by the acceptor. Therefore, a significant overlap between the emission band of the donor and the absorption band of the acceptor, as well as high concentrations are needed. The second process depends on similar overlap of absorption and emission bands, but is non-radiative by means of Förster resonance energy transfer (FRET). The energy transfer then arise through a coupling of the dipol moments of donor and acceptor through space with distances up to 50-100 Å.[68] For the third Dexter (exchange-) mechanism, an orbital overlap of the molecules is required, thus a very close contact between donor and acceptor is a prerequisite for this process.[69] Finally, energy (or exciton) hopping within the chromophore units can occur for closely stacked and excitonically coupled dyes, which was often observed in bisimide dye macromolecules.[70]

In the following, literature known macrocycles based on bisimide dyes are presented in which some of these photophysical processes were observed and related to the distinct structures that are given in the rigid cyclic arrays.

2.3 Pyromellitic Bisimide Containing Macrocycles

Pyromellitic bisimide (PyBI) based macrocycles were investigated in great detail by the group of Shinmyozu.[24b, 71] As smallest derivatives, PyBI containing ring systems are good model compounds to analyze the structure and conformational flexibility. Therefore, several PyBI macrocycles were synthesized and their ability for guest encapsulation was studied (Figure 7).

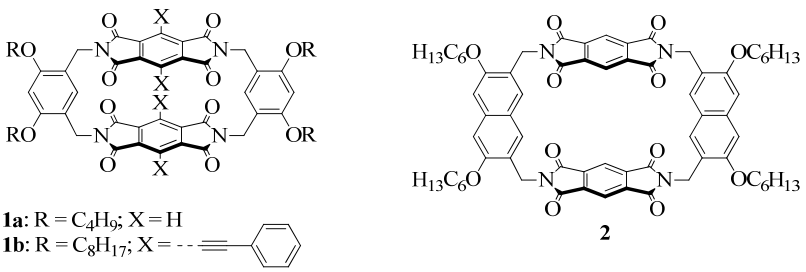

Figure 7. PyBI cyclophanes bridged with *meta*-xylylene (**1a**,**b**) or naphthalene units (**2**).

The *meta*-xylylene bridged cyclophanes **1a**,**b** provide an interplanar distance of ~5 Å that is too small to encapsulate aromatic hydrocarbons.[71a, 71c] Nevertheless, the interactions to electron rich guest molecules, naphthol, *p*-dimethoxybenzene and *p*-xylene were investigated. Upon addition of these molecules a CT band at higher wavelengths and the formation of 1:1 complexes in solution has been observed with low association constants of $K_a < 1\ M^{-1}$. From crystal structure analysis a packing of the aromatic guests on top of the PyBI cyclophane **1a** that is supported by CT interactions and H-bonding from the naphthol OH to the carbonyl groups of PyBI was concluded. Whereas the studies in solution always suggested the 1:1 complex formation, crystallographic analysis revealed a 1:2 ratio with α-naphthol forming a 1D supramolecular assembly. With the addition of phenylethynyl moieties at the 3,6-positions of PyBI **1b** the extension of the π-surface was realized. Herein the phenylethynyl groups have a parallel and slanted arrangement, shortening the interplanar distance of the PyBI moieties to ~4 Å. In the crystalline phase these phenyl subunits interlock with the neighboring molecules forming linear assemblies. Through the closer contact of the PyBI units excimer emission occurs in toluene and $CHCl_3$.

To enable the complexation of guest molecules between the PyBI moieties a larger spacer was introduced in **2**, namely a 2,7-bis(aminomethyl)naphthalene derivative.[24b, 71e] Now a cavity size of 7.3 Å is given that is ideal for the encapsulation of planar hydrocarbons ($K_a = 1.6–31.3\ M^{-1}$). And indeed the complexation of aniline leads to CT complexes with characteristic ^{1}H-NMR shifts. From crystal structure analysis 1:7 complexes were found in which one aniline molecule is encapsulated and six are coordinated to the outside. For the uptake of methoxybenzene derivatives multipoint interactions were concluded, such as CT, electrostatic, van der Waals, C–H··O and C–H··π interactions.

The larger macrocycles **3** have been realized with *p*-xylylene bridges that result in the molecular trimer (Figure 8), tetramer and pentamer.[71b, 71f] The cyclic trimer **3** was further used for the encapsulation of [2,2,2]-paracyclophane ($K_a = 30–40\ M^{-1}$) that fits perfectly inside the void with close CT contacts between the phenyl subunits and PyBIs.

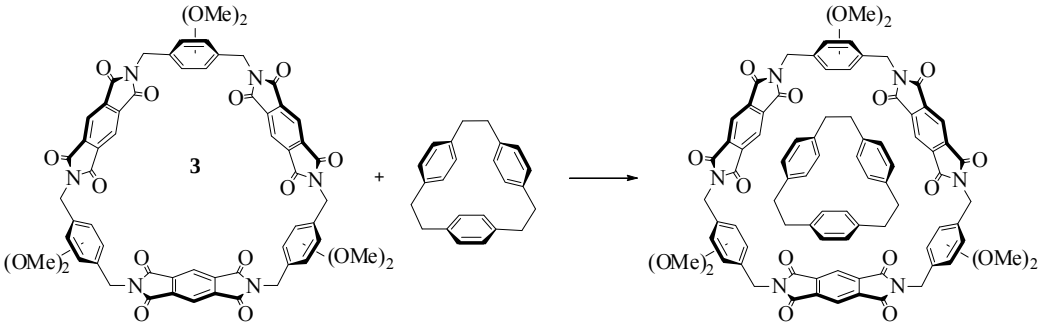

Figure 8. PyBI macrocyclic trimer **3** and the encapsulation of [2,2,2]-paracyclophane.

When this cycle is added to a hot *N*,*N*-dimethylanilin solution a deep-violet gel is formed upon cooling.[71d] The color was attributed to a CT from dimethylaniline to the PyBI. By drying in vacuum the dimethylaniline is removed and a yellow xerogel is maintained. With field emission scanning electron microscopy (FE-SEM) fibril structures in 3D networks were obtained that provides columnar pores in the xerogel with the diameter of one PyBI macrocycle. In this channel-type cavities other guest molecules can be inserted that further lead to a color change depending on the π-donating ability of the individual guest (Figure 9).

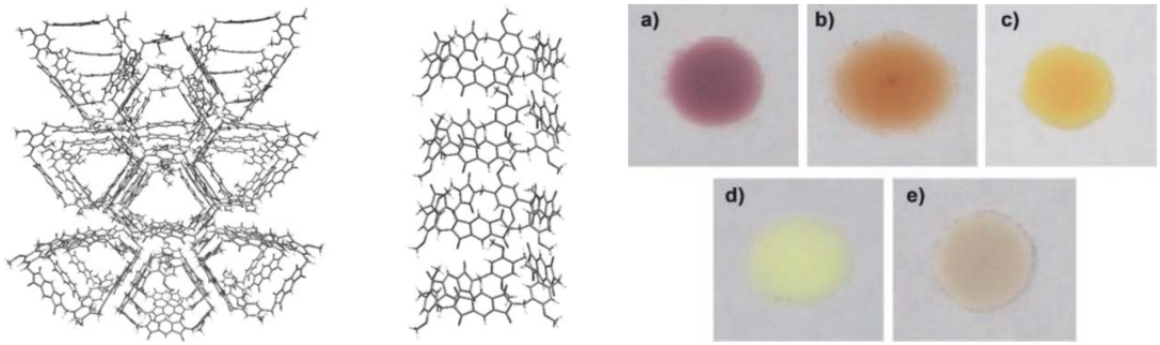

Figure 9. Crystal structure of **3** obtained from *N*,*N*-dimethylaniline (left) and photographs of the xerogel after adsorption of *N*,*N*-dimethylaniline (a), *N*-methylaniline (b), aniline (c), 1,3-dimethoxybenzene (d) and without a guest (e); reprinted with permission from ref.[71d]. Copyright 2010 Wiley-VCH Verlag GmbH & Co. KGaA, Weinheim.

With *trans*-1,2-cyclohexanediamine a shorter spacer between the PyBI units is introduced that leads to exciton coupling among them and to a blue shift of the UV-vis absorption band of 7 nm.[72] With the sign of the exciton split Cotton effects in conjunction with the exciton couplet due to the long-axis polarized π-π* transition at 240 nm, the individual electronic transitions could be assigned by CD spectroscopy of the cyclic trimer **4** (Figure 10). Thus, the n-π* electronic transitions at longer wavelengths of the UV absorption and

up to six π-π* transitions that are polarized in plane of the PyBIs along the symmetry axes (y,z) were identified. The experimental results have been further supported by computations.

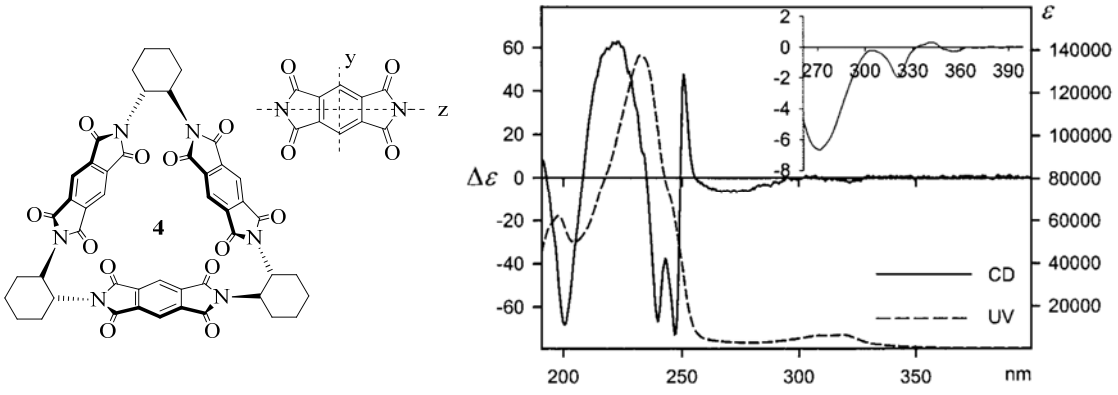

Figure 10. Molecular structure and CD and UV-vis absorptions spectra of PyBI trimer **4** in acetonitrile, 293 K, c = 1.5 x 10^{-4} M; reprinted with permission from ref.[72]. Copyright 2002 Wiley-VCH Verlag GmbH & Co. KGaA, Weinheim.

2.4 Covalently Bonded Naphthalene Bisimide Macrocycles

The next larger derivatives are naphthalene bisimides (NBI) and indeed a series of covalently bonded NBI macrocycles has been reported in the last decades in which the number of NBI subunits range from one to nine. The mononuclear cyclophanes were made with functional groups in the imide positions of the NBIs that can later on be intramolecularly bridged over the π-surface of the bisimides (Figure 11).

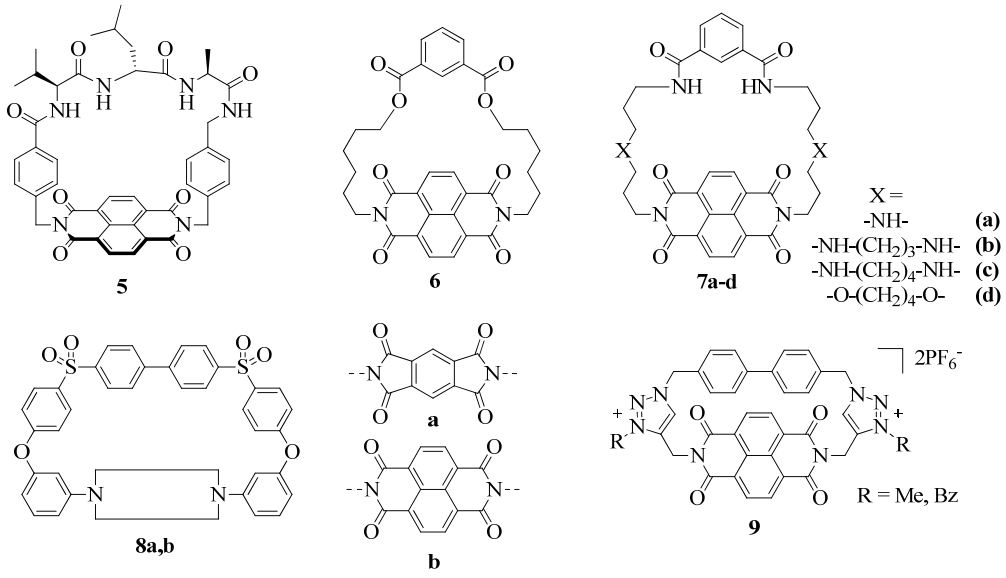

Figure 11. Mononuclear NBI cyclophanes **5**–**9**.

In the first reported example the NBI molecule **5** is bridged with a (*S*)-(valine-leucine-alanine) tripeptide unit that enables chiral hydrogen bonding to guest molecules.[24a] Upon addition of indole CT complexes are formed, however, with only a small association constant of 13 M^{-1} in chloroform at room temperature.

Fomine and coworkers studied with their NBI cyclophane **6** the tendency for cyclization or polymerization and showed that the cyclization reaction is driven by entropy and not by enthalpy, whereas the polymerization is the result of strain release on the ring-opening.[73] By replacing the isophthalic acid against isophthalamide and introducing spermidine- and spermine-like chains the NBI cyclophanes **7a-d** can be used as G-quadruplex binders. Through electrostatic interactions the G-quadruplex sequence can be stabilized, which occurs more effectively with increasing linker length. Furthermore, cancer cell growth inhibition activity was found for these cyclophanes **7** showing that bisimide macrocycles are promising candidates for medical applications.[74] The ether imide sulfones **8a**,**b** introduced by Colquhoun *et al.* provide a cavity size of 8.2 Å that is capable to encapsulate planar aromatic hydrocarbons. Since the ideal distance of π-surfaces for such host-guest phenomena is with ~7 Å somewhat smaller than in the NBI and PyBI cyclophanes **8a**,**b**, an induced-fit binding occurs. Thus, the cavity is flexible enough to provide close π-π interactions to the aromatic guests. As previously described, the encapsulation of electron rich molecules leads to strong color changes, indicative for intermolecular CT. Upon addition of guest molecules with large π-systems the 2:1 (host:guest) complexes are formed and were characterized by optical, as well as NMR spectroscopy and X-ray crystallography. By the encapsulation of molecules that can form hydrogen bonds (1,6-pyreneacetic acid), larger host-guest assemblies were realized (Figure 12). From UV-vis absorption titration experiments, the factors that dictate the binding have been elucidated with binding constants of up to 2.3 x 10^3 M^{-1}.[24c, 75]

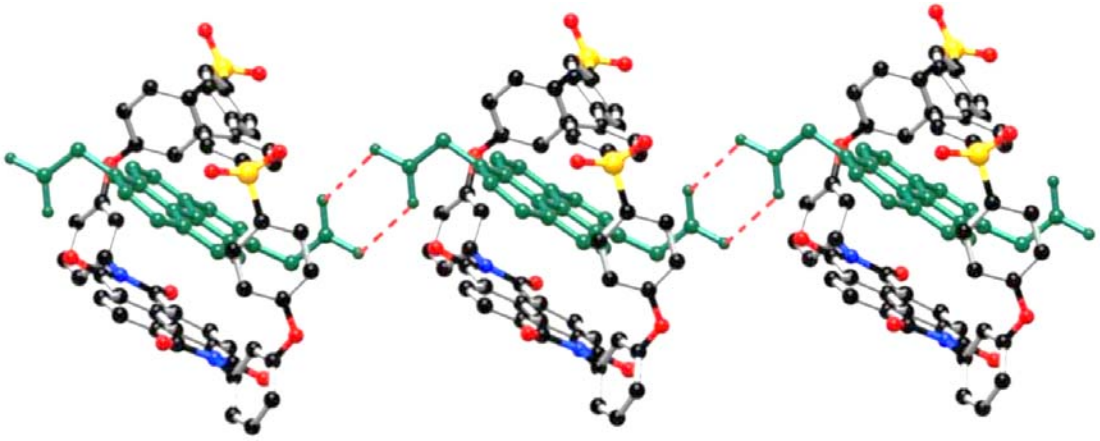

Figure 12. Polyrotaxane-type assembly by encapsulation of 1,6-pyreneacetic acid (shown in green) into **8b** and hydrogen bonding; reprinted with permission from ref.[24c]. Copyright 2009 Wiley-VCH Verlag GmbH & Co. KGaA, Weinheim.

In the NBI cyclophane **9** that was obtained by click-chemistry anion binding to the ring system was observed. Through methylation or benzylation of the triazole units positive charges were introduced to the cyclophane that support anion binding. Some selectivity was found regarding fluoride anions that induce the formation of the NBI radical anion through a SOMO-LUMO based electronic transition. In solid state highly porous networks were maintained in which an exchange of PF_6^- with halides can be achieved. Thus, different colored crystals of the so formed CT complexes were achieved.[76]
In the analog cyclophane **10** composed of two NBI moieties, metal ion interactions were studied (Figure 13).

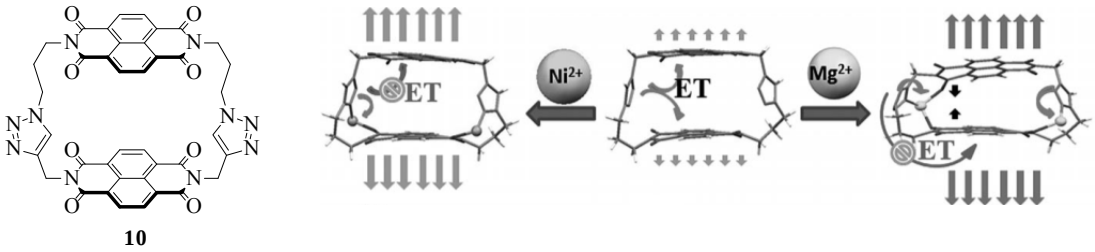

10

Figure 13. NBI cyclophane **10** composed of two NBI units and schematic representation of the different photophysical properties obtained by metal coordination; reprinted with permission from ref.[77]. Copyright 2012 Wiley-VCH Verlag GmbH & Co. KGaA, Weinheim.

In the free cyclophane **10** a photo-induced electron transfer from the triazole to the NBI moieties occurs that quenches the fluorescence of the macrocycle. Upon addition of divalent metal ions a binding to the triazole nitrogen and the carbonyl oxygen of the NBIs is observed that suppresses the ET process to the bisimides. Mainly two different

structures of the complexes were found depending on the metal ions that were used. With Mg^{2+}, Ba^{2+}, Hg^{2+}, Ca^{2+}, Zn^{2+} and Pb^{2+} a close packing of the NBIs is maintained that leads to excimer emission, whereas with Fe^{3+}, Co^{2+}, Ni^{2+} and Mn^{2+} an expanded conformation and monomer-like emission is observed.[77]

Already in the first example of NBI cyclophanes composed of two NBI moieties (**11**) that was reported by Lehn and Pascard in 1987, the encapsulation of nitrobenzene was monitored by fluorescence quenching (Figure 14).[78] In further studies on these cyclophanes **11**, excimer emission was observed and attributed to the close packing of the NBIs in the free host.[79]

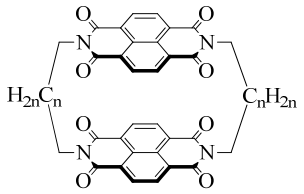

n = 8, 12

11

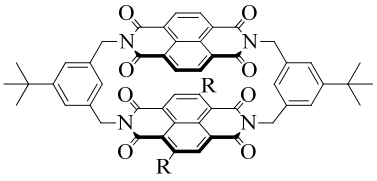

R = H, Cl, S*t*Bu, OMe, N(CH$_2$)$_5$

12

Figure 14. Molecular structures of cyclophanes **11** and **12** with two NBI units.

The group of Mayor synthesized a *meta*-xylylene bridged NBI cyclophane **12** and sublimed it on an Au(111) substrate in ultrahigh vacuum. With STM the structure has been visualized, showing that one NBI unit is weakly interacting with the Au(111) surface, while the second NBI has no interaction with the substrate at all.[80] In a stepwise synthesis, asymmetric NBI cyclophanes **12** were made composed of one unsubstituted and one core substituted NBI moiety. With excitation of these macrocycles an intramolecular FRET takes place from the unsubstituted to the 2,6-dimethoxy substituted NBI units, whereas for the other derivatives such a FRET is increasingly suppressed from S*t*Bu to N(CH$_2$)$_5$ caused by the stronger red shift of the absorbance, which results in less spectral overlap with the bare NBI.[81] While the cavity is too small for the incorporation of electron rich guest molecules, the binding of anions is still observable by ESI mass spectrometry. Thus, the binding of oxyanions (NO_3^- > ClO_4^- > SO_4^{2-} > AcO^-) was stronger than of halides and other anions, whereas monomers and linear oligomers bind strongest to halides.[82]

Such anion-π interactions were also observed in the NBI macrocycles **13** introduced by the groups of Stoddart and Wasielewski. Herein NBI molecules were connected with a chiral *trans*-1,2-cyclohexanediamine bridge that results in a molecular triangular prism

(Figure 15) similar to the PyBI triangle **4** reported by Gawroński *et al.*.[72] Through the close NBI-NBI contact at the bridging unit, intramolecular through-space electron sharing among all three NBIs takes place upon mono-reduction of **13** that was confirmed by DFT calculations, cyclic voltammetry, as well as EPR and ENDOR spectroscopy. This electronic communication between the redox centers increases the electron affinity of the NBIs and thus also enhances CT interactions to anions. Accordingly, this rigid tube-like cavity can be used as a receptor for linear I_3^- anions. In the corresponding crystal structure of these complexes helical assemblies of the I_3^- loaded cycles have been found (Figure 15).[83]

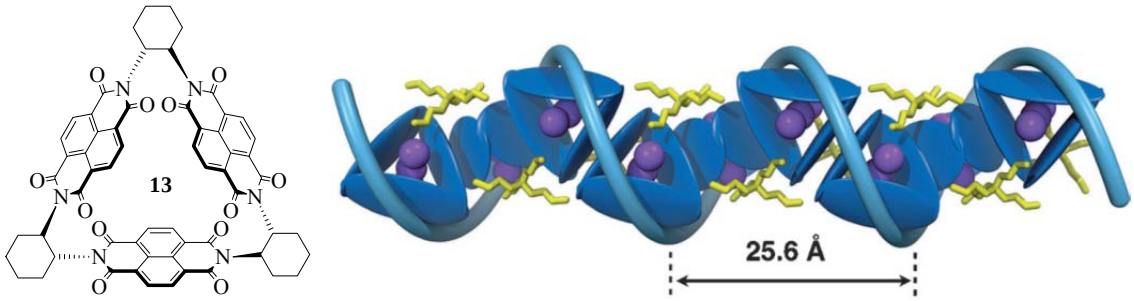

Figure 15. Molecular triangular prism **13** composed of three NBI units and schematic representation of the helical assembly of the corresponding I_3^-@**13** complexes; reprinted with permission from ref.[83]. Copyright 2013 Wiley-VCH Verlag GmbH & Co. KGaA, Weinheim.

As a further consequence of the electron sharing, six individually accessible redox states are present in the macrocycle **13** (Figure 16). These redox processes were used to reversibly load lithium ions on the NBI moieties in a stepwise manner. Together with the high porosity that allows the lithium ions to diffuse also in solid state and the low solubility in many solvents, which provides electrode stability, these cyclic trimers **13** are good candidates for rechargeable lithium-ion batteries.[84] With PyBI/NBI mixed trimers **14** and **15** they showed that with increasing the number of NBI subunits the electrochemical cell performance of the batteries are improved. Nevertheless, the individual redox states remain distinct in the studied triangles **4**, **13**, **14** and **15** (Figure 16).[85]

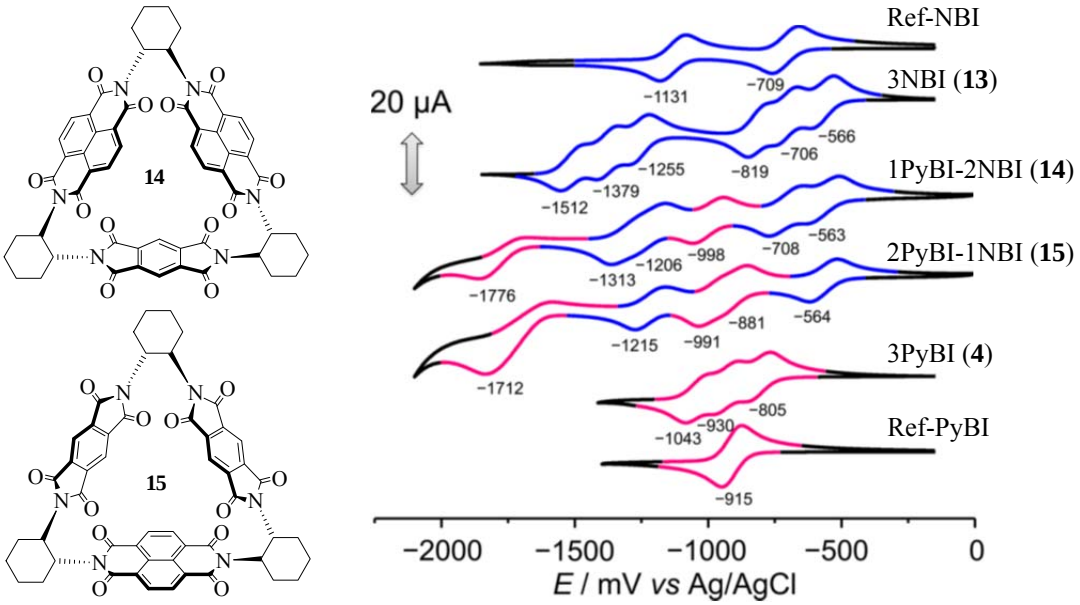

Figure 16. Molecular structures of the PyBI/NBI mixed trimers **14** and **15** and cyclic voltammograms of the cyclic trimers **4**, **13**, **14** and **15** (0.5 mM in DCM, TBAHFP, half-wave peak potentials $E_{1/2}$ are shown in mV); reprinted with permission from ref.[85]. Copyright 2016 American Chemical Society.

When the triangle is dissolved in 1,2-dihalohydrocarbons supramolecular nanotubes are formed in which the individual solvent molecules are penetrating the cavities and influence the exact structure of the tubes (Figure 17). In dichloroethene flexible infinite nanotubes are formed in the gel state, which is caused by the electron rich C=C double bond of the solvent. On the other hand rigid non-helical nanotubes in the solid state occur in $BrCH_2CH_2Br$, $ClCH_2CH_2Br$ and $ClCH_2CH_2I$ and only $ClCH_2CH_2Cl$ generates helical infinite nanotubes in the solid state. In all cases a columnar stack with a 60–65° rotation between each macrocycle is formed that is a result of cooperative [C–H··O], directed [X··X] solvent chains and lateral [X··π] interactions.[86] Although the [C–H··O] interactions are responsible for the rotation, the enantiomeric pure samples, forming the *R*,*R*- or *S*,*S*-dimers do not provide the optimal conformation for the hydrogen bonding (Figure 17 bottom). That is why the nanotubes are only observed in solid state and not as a gel. However, in a racemic mixture of both enantiomers, ideal assemblies with 12 weak [C–H··O] hydrogen bonds are maintained in the *R*,*S*-dimer. Thus, the racemic mixture of *R*-**13** and *S*-**13** forms supramolecular gels out of columnar stacks in $ClCH_2CH_2Cl$.[87]

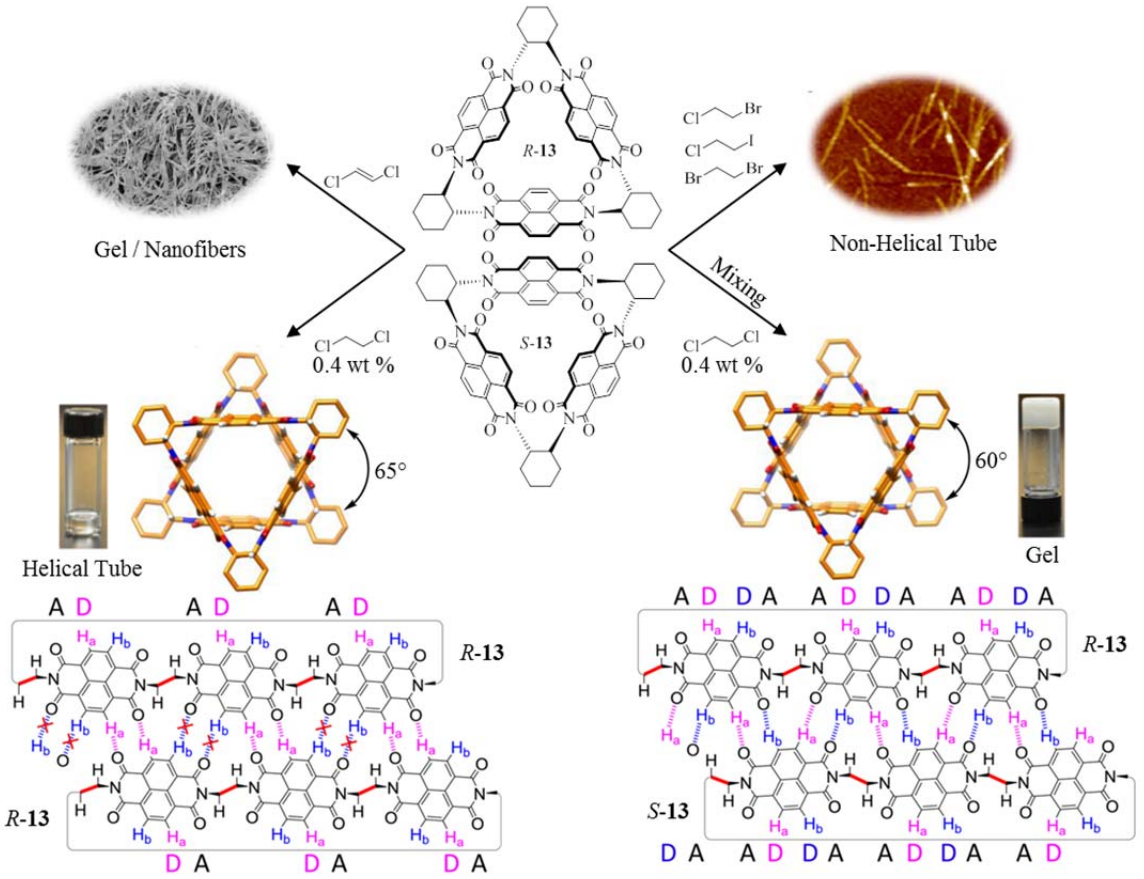

Figure 17. Schematic representation of the individual nanostructures obtained by self-assembly of the pure *R*-**13** and *S*-**13** in 1,2-dihalohydrocarbons and of the racemic mixture in $ClCH_2CH_2Cl$; illustrations of the hydrogen bonds in the columnar stacks are given at the bottom; reprinted with permission from ref.[86-87]. Copyright 2014/2016 American Chemical Society.

Beside the cyclic trimer, the analog dimer[88] and tetramer[89] were synthesized in which the electron delocalization was further studied. Thus, four electronic states have been isolated and characterized, namely the ground state, the exciton coupled singlet excited state, the radical anion and the radical dianion. In the neutral excited state the strong exciton coupling leads to a long-lived emissive species. The monoreduced state is a paramagnetic mixed-valance species with a very fast electron migration rate ($> 10^7\ s^{-1}$), whereas the radical dianion is diamagnetic and shows extensive π-electron delocalization interaction upon spin-pairing.

Whereas in the just described macrocycles, no preferences in the formed ring size were observed by changing from PyBI to NBI, Gawroński and coworkers found an unprecedented selectivity in their cyclic systems **16**.[90] In the cyclocondensation of PyBI and NBI diamines with dialdehydes macrocyclic dimers and trimers were achieved in yields of 65–82% (Figure 18). While the cyclization with isophthalaldehyde results in

both cases (PyBI and NBI) in the cyclic dimers **16a** and **16b**, the reaction with terephthalaldehyde differentiates between the two bisimides. Thus, PyBI and terephthalaldehyde form the cyclic dimer **16d**, whereas with NBIs the twisted [3+3] product **16c** is formed, caused by a rotation of one imide substituent. However, the explanation for these different thermodynamic products is not yet found.

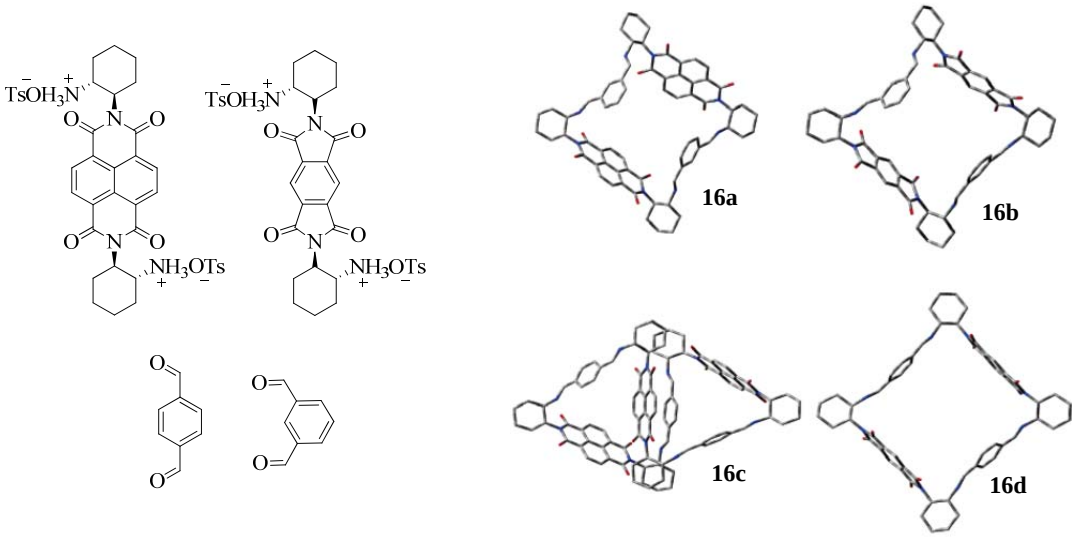

Figure 18. Starting compounds for cyclocondensation with aldehydes and the thermodynamic products **16a**–**d**; reprinted with permission from ref.[90]. Copyright 2006 American Chemical Society.

With reversible covalent bonding Sanders and coworkers were able to amplify the formation of one specific ring size of a NBI macrocycle that is templated by electron rich guest molecules.[91] Without any template the individual dimeric, trimeric and tetrameric cycles were formed from the dithiol building block **17** in yields of 50, 35 and 15%, respectively, through a disulfide bonding (Figure 19). Upon addition of dialkoxynaphthalenes **18** and **19**, donor-acceptor complexes are formed and the yields of trimer (**18**, 49%) or tetramer (**19**, 80%) are significantly increased, whereas the cyclic dimer is too small to encapsulate these guest molecules. Starting from the open NBI trimer larger cycles have been realized (Figure 19b). In a 1 mM water solution at pH 8 the cyclic trimer and hexamer were observed as the main products. At higher concentration of 5 mM also a trefoil molecular knot composed of nine NBI units was formed in acceptable yields as a result of a hydrophobic effect. Thus, with addition of a salt $NaNO_3$ the hydrophobic effect is enhanced and the selective formation of the knot is obtained as the thermodynamic product in almost quantitative yield. With the choice of Bu_4NNO_3 as additive salt that can solvate the NBI π-surface the unfolded cyclic hexamer and nonamer are generated, while the formation of the knot is suppressed.[92]

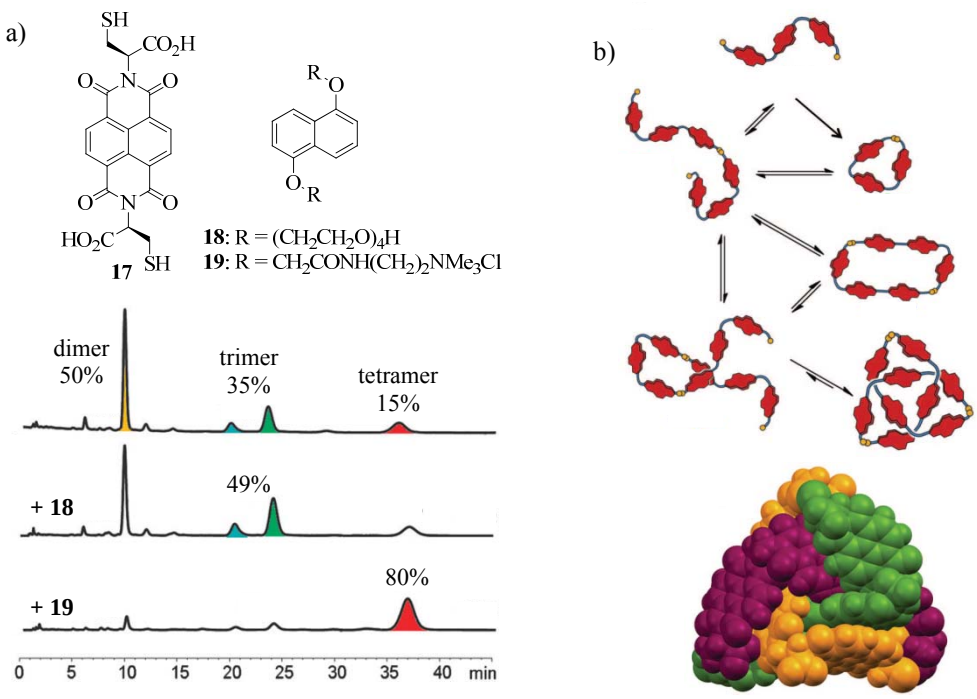

Figure 19. a) HPLC runs of templated amplification of NBI macrocycles upon addition of **18** or **19** to **17**; b) synthesis of larger cycles and of the molecular knot starting from an open trimer; reprinted with permission from ref.[91-92]. Copyright 2009 The Royal Society of Chemistry. Copyright 2016 American Association for the Advancement of Science.

The group of Stefankiewicz continued this work of dynamic combinatorial chemistry with NBI dithiols and connected them with various dithiol donor molecules. This led to a series of seventeen different donor-acceptor cycles and catenanes that were separable by HPLC.[93]

2.5 Perylene Bisimide Containing Macrocycles

A further increase of the molecular bisimide building blocks is achieved with the higher homologue of NBI, the perylene bisimide (PBI). However, parent PBIs are rather insoluble pigments and accordingly, functionalization by solubilizing substituents is a prerequisite to accomplish macrocyclic architectures. Towards this goal Würthner and coworkers utilized bay-tetraphenoxy-substituted PBIs, which are brilliant red emitters with fluorescence quantum yields close to unity.

While in the large PBI macrocycles excitonic coupling among the chromophores is rare, in PBI cyclophanes (Figure 20) dye-dye interactions are often seen due to close contact between the PBI moieties. The latter are enforced by the strong π-π-interactions between PBI dyes that are also responsible for self-assembly of these dyes already in quite dilute

solutions and their often insoluble pigment character. PBI cyclophanes are accordingly suitable model compounds to study electronic interactions between the PBI chromophores, since they often provide a well-defined structure with strictly preorganized dyes.

Langhals and coworkers reported on the first covalently coupled PBI cyclophane **20** already in 1998 in which bay unsubstituted PBI chromophores were connected by a flexible dodecyl chain in the imide position (Figure 20).[30a] In the absorption spectra a hypsochromic shift of the maximum, compared to the monomeric PBI, was observed, which reveals an intramolecular H-type stacking. Furthermore, the fluorescence spectrum is bathochromically shifted with relatively high fluorescence quantum yields of 40%. In the report they suggest a J-type stacking of the chromophores by a slipping of the PBI moieties after excitation. However, due to the broad and undefined structure of the fluorescence spectrum emissive excimer formation might also be an explanation for the detected optical features.[94]

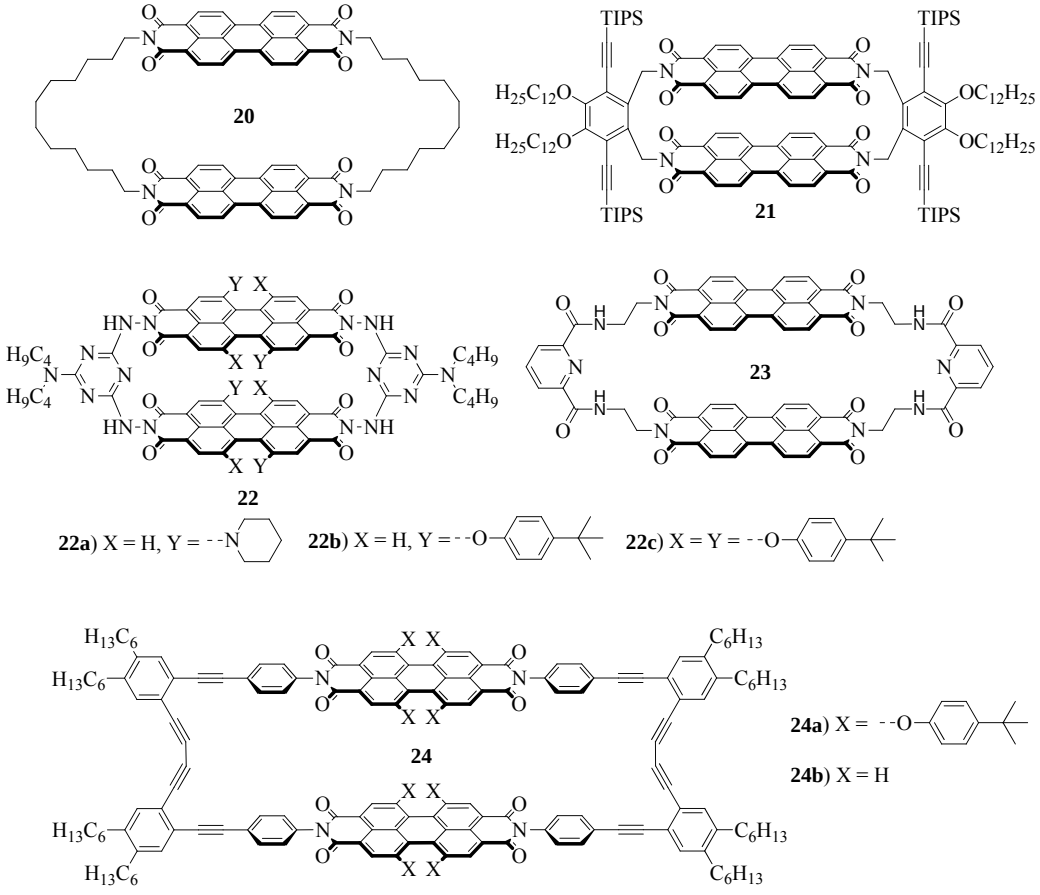

Figure 20. Chemical structures of PBI cyclophanes **20**–**24**.

Such excimer states have later on been reported in rigid tethered PBI cyclophanes **21** and **22** by Wasielewski[30e] and Jiang[30c], respectively. In the latter different PBI derivatives were connected through a 2,4-diamino-1,3,5-triazine linker.

Here the close contact between the chromophores and the high rigidity provided by the cyclophane **22** afford a defined electronic coupling between the dyes. By using 1,7-substituted PBI derivatives (**22a**,**b**) two different isomers were yielded in which the bay substituents of the individual chromophores are on opposite site (transoid) or on top of each other (cisoid). With 2D-ROESY NMR spectroscopy the isomers were assigned, confirming that the transoid conformation is the favored one due to steric effects. Similar to **20**, these cyclophanes experience a blue shift in the absorption by virtue of their face-to-face stacked geometry. The isomerisation of *trans*-**22b** and *cis*-**22b** has some effect on the absorption, shifting the maximum from 632 to 617 nm, which is caused by differences in the π-π interactions between the PBI chromophores according to DFT calculations. For cyclophane **22b** no emission was observed indicating the presence of efficient non-radiative decay pathways such as charge separation within the chromophores similar to noncyclic dimers composed of similar PBI dyes.[95] In contrast, **22a** shows weak structureless excimer emission with low quantum yields of 1–6% depending on the solvent, whereas **22c** has only weak monomer-like emission.[30c]

Similar to these studies the Wasielewski group approached bay unsubstituted PBI cyclophanes **21** that were connected with a rigid *ortho*-xylylenediamine spacer providing a close packing of the chromophores in a face-to-face arrangement. Thus, the absorption spectrum reveals H-type stacking of the chromophores and weak excimer emission with a fluorescence quantum yield of 0.1%. The very strong red shift of the fluorescence emission maximum was related to distance-dependent Frenkel-charge transfer exciton mixing.[30e, 96]

By the linkage of two chromophores with 2,6-bis(aminomethyl)pyridine (**23**) the highly selective and sensitive detection of mercury(II) was enabled. Nevertheless, the PBI chromophores are in this example not directly involved in the binding process and serve mainly as structural backbone, whereas the bridging units bind to the Hg^{2+} ions. However, after binding of Hg^{2+} the PBI emission is quenched, presumably due to the heavy metal effect. Unfortunately, no detailed discussions of the emission features, quenching mechanism or fluorescence quantum yields are given.[97]

The PBI cyclophane **24a**,**b** reported by Würthner and coworkers has very similar optical properties with the H-type stacking of the chromophores and an excimer emission with a fluorescence quantum yield of 0.4–6%. Since the excimer emission of **24b** is in THF ten-fold higher than in $CHCl_3$, efficient non-radiative decay channels are present in chlorinated solvents, which were further investigated by TA spectroscopy. It was found that in chlorinated solvents excimer-mediated intramolecular symmetry-breaking charge separation (SB-CS) takes place within 36 ps. The charge recombination then occurs back to the ground state in 1.1 ns. In contrast, in THF the excimer emission prevails with a long live time of 16 ns.[98] The major focus of **24a** was, however, on the stepwise reduction of the two bisimide dyes (Figure 21). Here a reversible widening of the cycle occurred with reduction of the PBI moieties due to electrostatic repulsion in the –4 charged molecules. This "breathing" of the cyclophane **24a** was monitored by cyclic voltammetry (CV) and spectroelectrochemistry suggesting intervalence charge transfer (IV-CT) character of the monoreduced species and a quasi-CT process in the biradical dianion.[30d]

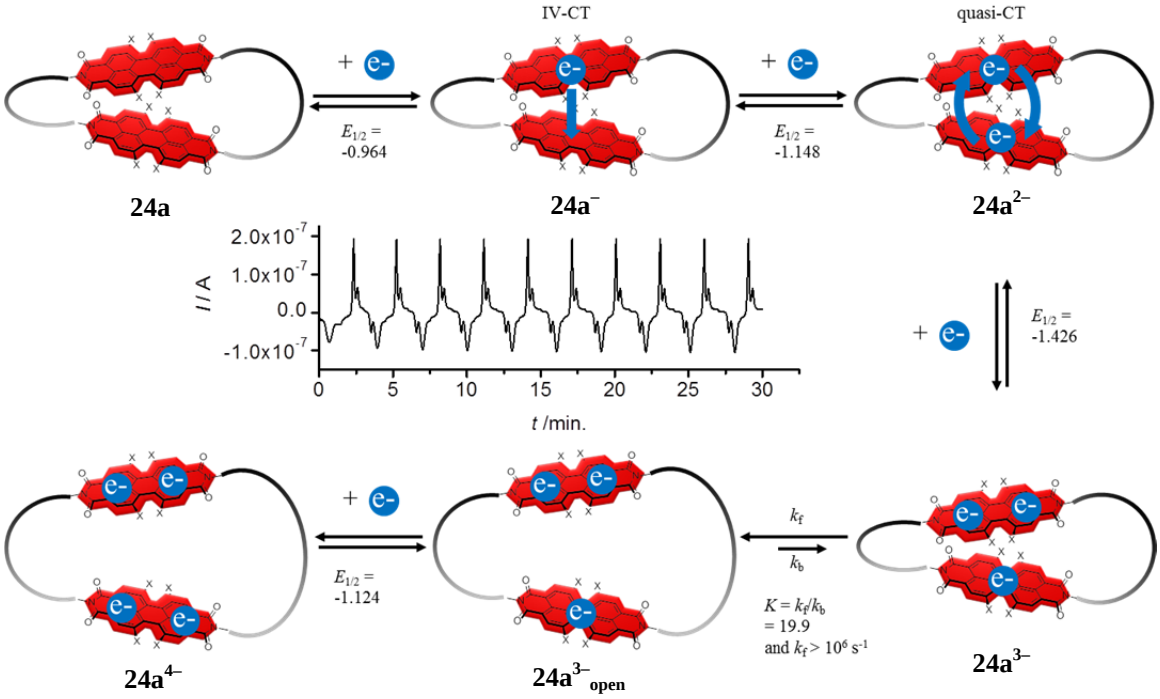

Figure 21. Schematic illustration of the "breathing" of the macrocycle **24a** by reversible reduction; reprinted with permission from ref.[30d]. Copyright 2013 WILEY-VCH Verlag GmbH & Co. KGaA, Weinheim.

As already demonstrated by the Langhals group, PBI cyclophanes can easily form PBI-PBI contacts in a helical arrangement.[30a] While in this early example a chiral solvent was employed to induce chirality to the PBI cyclophane, Li and coworkers

established macrocycles with flexible ethylene glycol chains and reversible disulfide bonding showing chiral features (Figure 22). In the synthesis of **25** the main products were found to be the cyclic dimer (39% yield) and the catenane (36% yield) that were formed by a dynamic self-assembly mechanism through π-π stacking of the PBI chromophores. However, under dilute conditions the monochromophoric cycle is formed in which an intramolecular disulfide bonding takes place.[99] The optical properties show similar behavior as the previously shown cyclophanes with a strong 0-1 transition band in the absorption spectra that was examined by time-dependent density functional theory (TDDFT).[100] To this type of macrocycle, chirality can be induced with tetra-substitution of the PBI core. Thus, the tetrachloro PBI cyclophane was synthesized in which a twist of the PBI core is present leading to different enantiomers of the chromophores, *P* and *M*.[101]

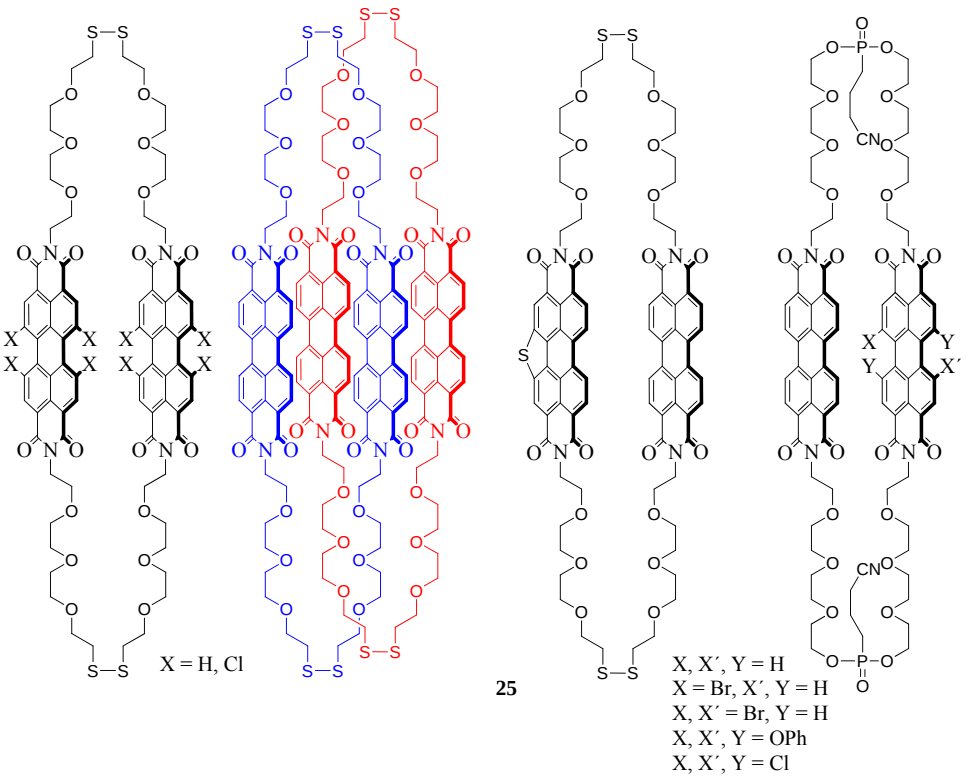

Figure 22. Chemical structures of cyclophanes and catenanes **25** reported by Li and coworkers.

Due to close contact of the PBI units only the homochiral dimers (*M*,*M*) or (*P*,*P*) are formed, while the heterochiral dimer (*M*,*P*) is sterically hindered.[102] It was furthermore shown that the transition between the homo- and heterochiral diastereomers is rather slow and that the system equilibrates within 24 h to a 1:1 ratio, which allows the separation of the individual cyclophanes **25**. The transition was monitored by NMR spectroscopy and

HPLC and the diastereomers were characterized by UV-vis absorption and fluorescence spectroscopy. Thus, the homochiral dimer is the kinetically favored macrocycle, whereas all diastereomers are equally thermodynamically favored.[30b] With increasing the size of the bay-substituents to phenoxy, the interactions between the chromophores are significantly reduced. Thus, dynamic self-assembly does not take place within the cyclization reaction resulting in a ring closure of the monomers.[103] With the help of hetero dimeric cycles composed of a bay-unsubstituted and a bay-substituted PBI chromophore, the effect of the core twist on the dynamic self-assembly was studied. Thus, with increasing the core twist the yield of product formation drops down due to decreasing binding strength between the two different chromophores.[104]

While all previously shown PBI macrocycles were connected via the imide positions, Nuckolls and coworkers reported on a new type of cyclophanes **26**, in which the cyclization in the bay position of the PBI chromophores has been carried out (Figure 23).

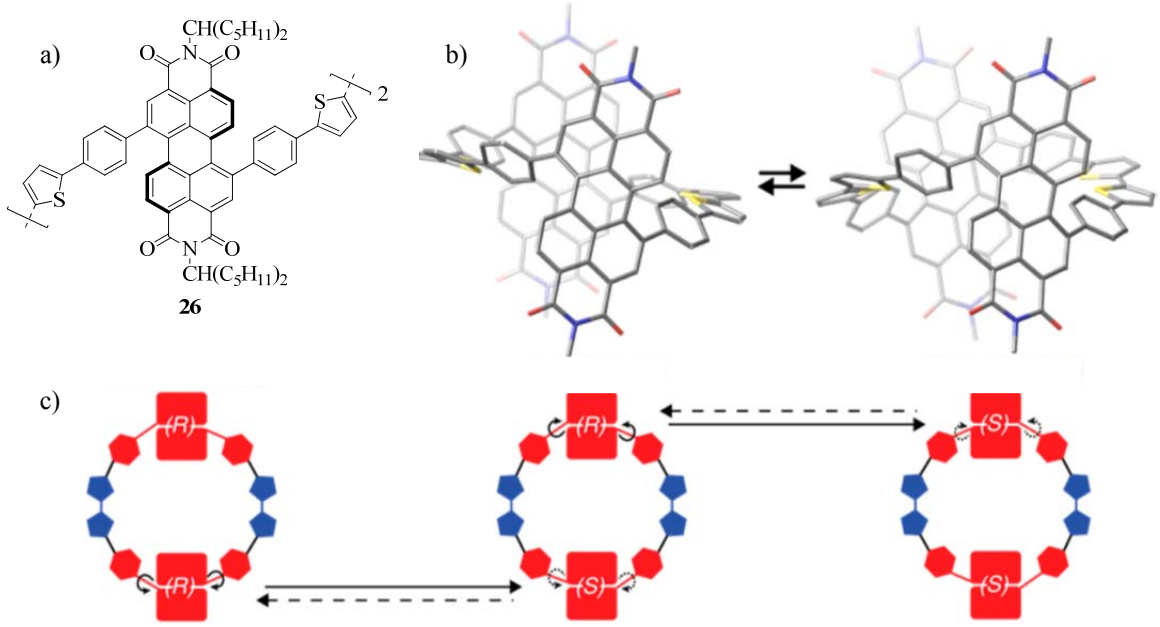

Figure 23. a) Chemical structure of the fully conjugated cyclophane **26**; b) DFT calculations of the homo and hetero dimer and schematic representation of the transition between the different diastereomers (c); reprinted with permission from ref.[105]. Copyright 2015 American Chemical Society.

Herein, bithiophene bridges serve as electron donor subunits, while the PBI chromophores are the electron poor acceptors, which leads to a –D–A–D–A– pattern within the cycle **26**. As bay-substituents, directly bonded phenyl groups were used and the bithiophene linkers were introduced by a Stille-type coupling reaction.[106] Thus, a fully conjugated black macrocycle was gained with a broad absorption feature from 300

to 700 nm. Through the linkage in the 1,7-position of the PBIs, chirality is induced to the PBI core. This leads to the formation of diastereomers in a ratio of 6:1 that were separated with chiral HPLC. The transition between these isomers was monitored by HPLC and takes place within 2 h by an intramolecular "somersault" of the PBI units (Figure 23c). From DFT calculations it appears that the homo dimers are the favored ones by virtue of less conformational strain of the bithiophene bridges.[105]

Acetylene-linked PBI macrocycles **27** (Figure 24a) containing three to six chromophores have been achieved by oxidative Glaser homo coupling under high dilution conditions at –30 °C of monomeric PBI molecules bearing terminal acetylene groups at the imide positions. The crude product mixture of the PBI macrocycles **27** was purified by recycling GPC and the separated molecules characterized by NMR spectroscopy and mass spectrometry, as well as cyclic voltammetry and optical spectroscopy. The absorption spectrum and the high fluorescence quantum yield of 91% (in CH_2Cl_2) of the cyclic trimer indicate that no significant electronic interactions between the PBI chromophores are present within the macrocycles. AFM images of the cyclic timer on HOPG showed the formation of donut-like 2D nanopatterns with a hexagonal arrangement in sizes of 8.2–8.6 nm.[107] Steady state fluorescence excitation anisotropy measurements were performed, showing the same spectra for the macrocycles **27** (trimer – hexamer) with absolute anisotropy values at the S_1 transition band of 0.022–0.015. Thus, excitation energy hopping (EEH) between adjacent transition dipole moments within the macrocycles was concluded.[108] Transient absorption spectroscopy revealed exciton-exciton annihilation due to exciton-exciton recombination between the individual PBI units of the cycles. This annihilation process indicates Förster-type incoherent energy transfer from an excited donor to an excited acceptor forming a doubly excited state that relaxes rapidly to the singly excited state.[109] The EEH times of the macrocycles **27** decrease with increasing ring size from 3.6 ps to 10.3 ps, which was rationalized to structural distortion and higher flexibility of the larger cycles and was further analyzed by molecular dynamics simulations.[108] In compliance with this distortion, no ordered nanostructures were observed on HOPG for the cyclic pentamer and hexamer (Figure 24b).

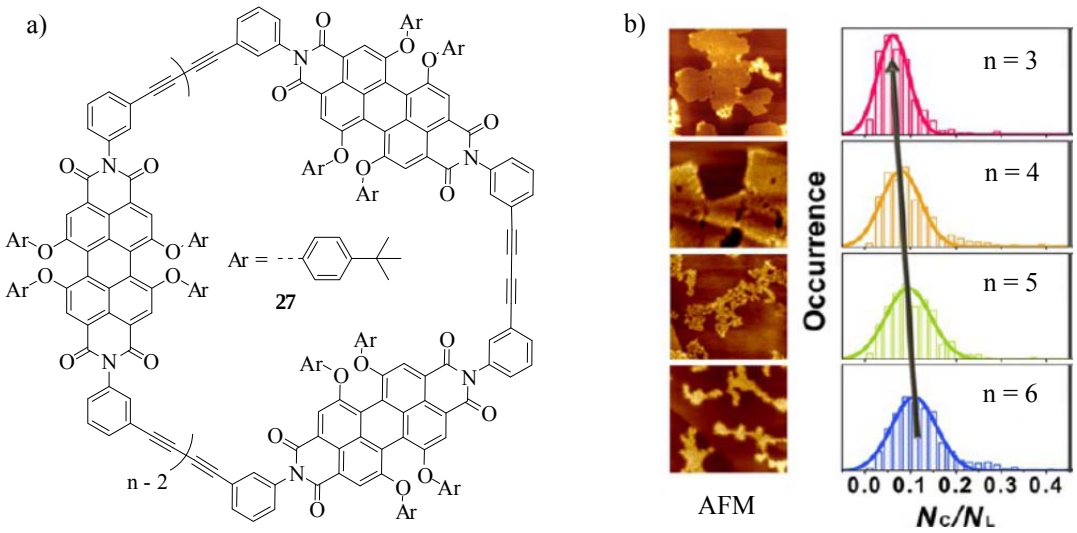

Figure 24. a) Chemical structure of acetylene linked PBI macrocycles **27**; b) AFM images and fluorescence lifetime plots observed by single-molecule fluorescence spectroscopy of the macrocycles **27** with ring sizes from n = 3–6; reprinted with permission from ref.[110]. Copyright 2013 American Chemical Society.

Furthermore, single-molecule fluorescence spectroscopy showed that the fluorescence lifetimes became shorter and their distribution broader with increasing structural flexibility of the macrocycles.[110] From single-molecule defocused wide-field imaging the orientation of the transition dipole moments of the PBI subunits in the cycles and the angle between each chromophore was determined. Thus, the molecular structures of the cycles were reconstructed confirming the higher distortion with increasing ring size.[111]

With shorter linkage between the individual PBI chromophores excitonic coupling within a cyclic trimer **28** is observed. This molecular triangle contains three PBI chromophores that were connected with (*R*,*R*)-*trans*-1,2-cyclohexanediamine, similar to the formerly discussed NBI triangles **13** (Figure 25a). In the absorption spectrum an enhanced 0-1 transition band was observed as well as a significantly reduced fluorescence (Φ_{fl} = 0.002) in comparison to a monomeric reference PBI (Φ_{fl} = 1.0). Transient absorption spectroscopy revealed a symmetry-breaking charge separation (SB-CS) within 12 ps despite of a low free energy of ΔG_{CS} = –0.19 eV for the charge separation (Figure 25b). Thereby, the PBI radical cation and the PBI radical anion are formed as confirmed by comparison of the transient absorption spectra with the UV-vis spectra obtained by oxidative and reductive titration experiments. EPR and ENDOR spectroscopy suggested that the unpaired electrons are delocalized among all three PBI chromophores in the cyclic triangle before charge recombination takes place within 1.12 ns (Figure 25c).[112]

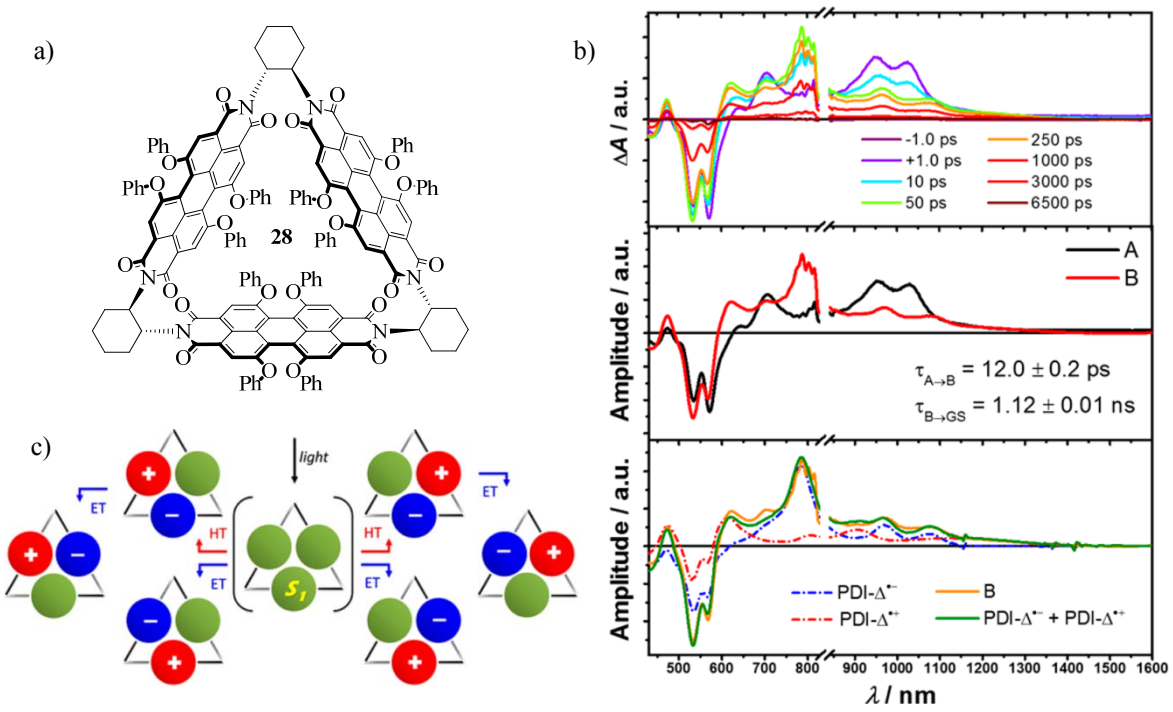

Figure 25. Chemical structure (a) and transient absorption spectra (b) of the cyclic trimer **28**; c) schematic representation of the charge separation and delocalization; reprinted with permission from ref.[112]. Copyright 2015 American Chemical Society.

2.6 Bisimide Containing Catenanes

For many macrocycles the formation of catenanes and rotaxanes has been demonstrated that enable new applications, like nanomachines and switches.[4b, 113] Also from bisimide containing cyclophanes such supramolecular assemblies are literature known and are shortly presented here.

The first studies in this regard have been reported by Sanders and coworkers.[114] The previously described inclusion phenomena of electron rich aromatics into electron deficient bisimide cyclophanes and the co-crystallization of PyBIs with dialkoxynaphthalenes in alternating stacks[115] encouraged them to synthesize a series of hetero catenanes through oxidative coupling of terminal acetylenes.[116] With the butadiyne linkers an ideal distance for π-π interactions with encapsulated guests of 7 Å is present in the bisimide cyclophanes. As second macrocycle, the crown ether bridged dialkoxynaphthalenes were chosen. Upon addition of the PyBI and NBI monomeric building blocks to these crown ether macrocycles a color change was observed, indicative for the formation of CT complexes by encapsulation of the bisimides. However, these CT

interactions seem not to be the major driving force for the strong binding, but hydrogen bonding between both bridging units (Figure 26b).

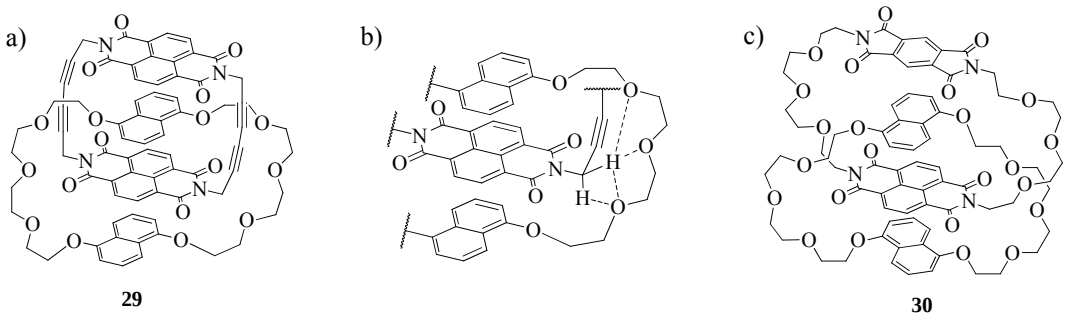

Figure 26. Chemical structures of the catenanes **29** (a) and **30** (c) reported by Sanders and coworkers and illustration of the hydrogen bonds within the catenane **29** (b).

After the coupling reaction, the individual catenanes **29** have been observed in reasonable yields of 30–50%. In additional studies Fallon *et al.* showed that these high yields can also be used for an improvement of the synthesis of free cyclophanes.[117] Interestingly, the corresponding catenane derivatives with the crown ether chains on the bisimides and the acetylene groups on the naphthalene cyclophane were not formed. This was explained by weaker binding strength in the complex formation, probably caused by an intramolecular self-aggregation of the bisimide moieties enabled by the flexible crown ether linkers. However, the asymmetric catenane **30** composed of one NBI and one PyBI unit in which both macrocycles bear the crown ether linkers is formed due to weaker self-aggregation between PyBI and NBI.[116e] In other attempts flexible linkers were successfully introduced by using two PyBI moieties[118] or by post-assembly modification of the acetylene bridges.[116c] In asymmetric PyBI/NBI systems the electrochemical and conformational properties have been correlated.[116d] Although in the neutral state the NBI is more likely to be in the inside of the catenane, a conformational change occurs upon the first reduction that brings the PyBI to the inside (Figure 27). With the second reduction process both bisimides get electron rich and thus cannot form the donor-acceptor complexes anymore. This leads to a second change of conformation in which neither of the bisimides is in the inside of the catenane. The next two reduction processes occur in this uncomplexed conformation forming the dianions of NBI and PyBI. Thus, the complexation behavior of the bisimide cyclophane can be tuned by a stepwise reduction of the system (Figure 27).

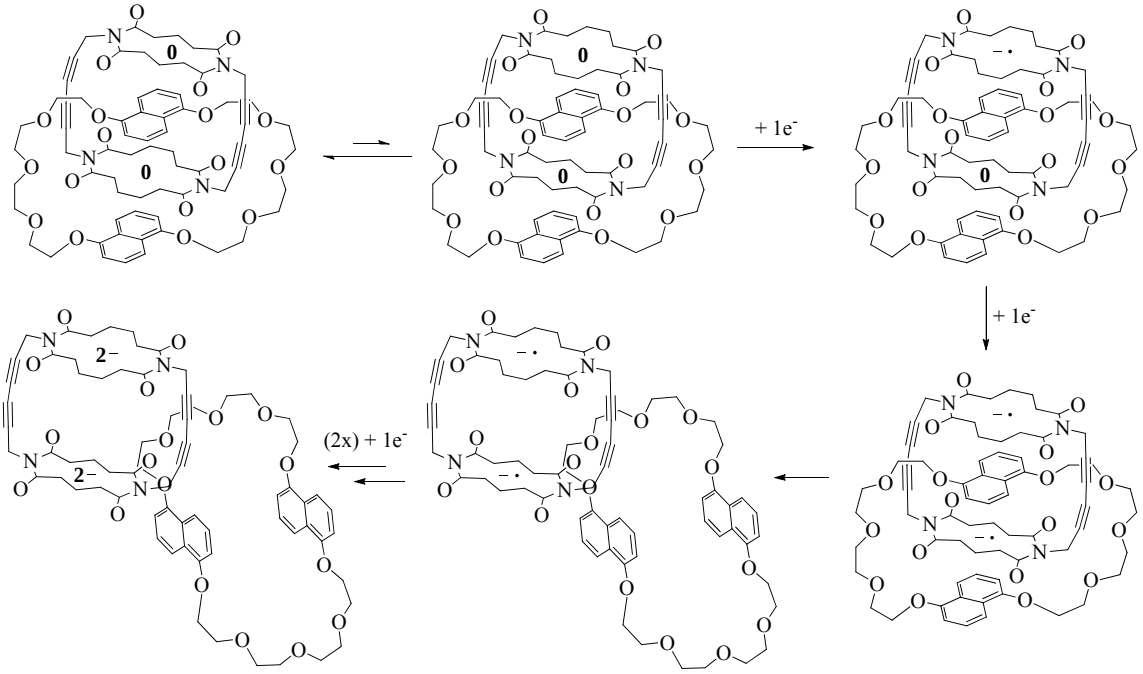

Figure 27. Schematic representation for the electrochemical and translational changes occurring upon stepwise reduction of a NBI/PyBI mixed catenane.

Similar switching processes have been observed in a series of desymmetrized catenanes **31** composed of different donor and acceptor units (Figure 28). Upon reduction of bipyridine and the bisimide or oxidation of TTF conformational changes were detected in which the encapsulated moieties vary to form the respective strongest donor-acceptor pairs. The structural changes were monitored by ^{1}H-NMR, CV and optical spectroscopy, as well as X-ray single crystal analysis.[119]

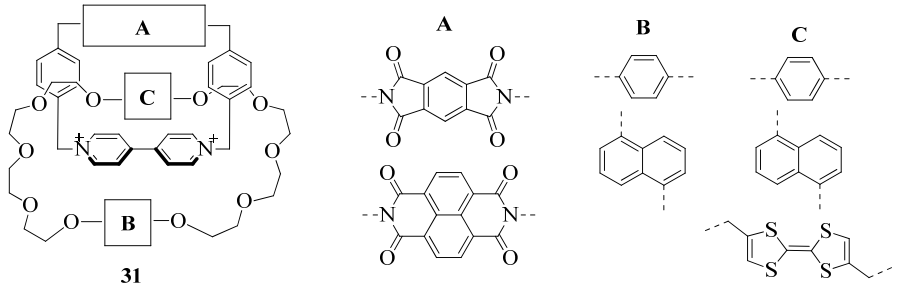

Figure 28. Desymmetrized catenanes **31** composed of different building blocks.

Encouraged by these systems further functional NBI and PBI catenanes have been synthesized bearing porphyrins (**32**),[120] fullerenes (**33**)[121] or charged expanded viologen-moieties (**34**) (Figure 29).[69]

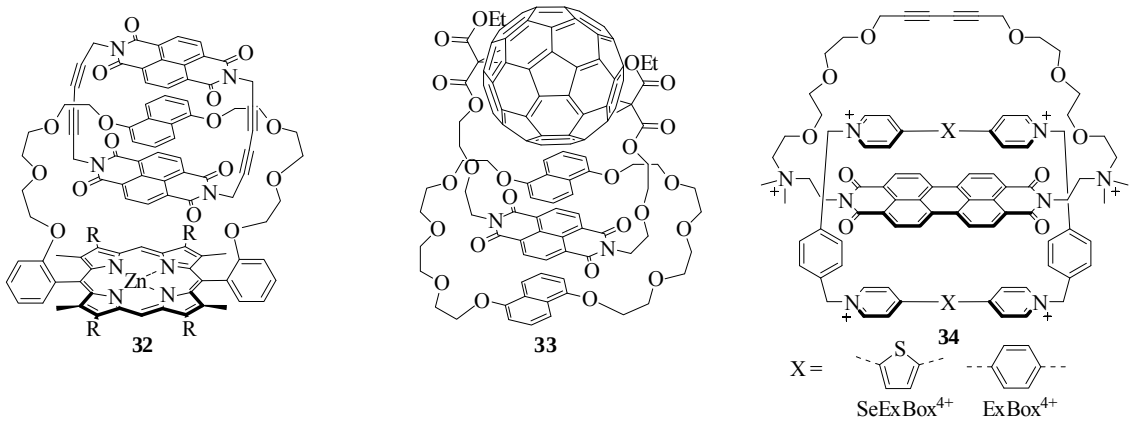

Figure 29. Functional donor-acceptor catenanes **32**–**34**.

In the PBI system **34** ($SeExBox^{4+}$) energy transfer was corroborated from the absorption and fluorescence excitation spectra, whereas in the free $ExBox^{4+}$ derivatives charge separation by an electron transfer or triplet formation (for $SeExBox^{4+}$) takes place. The EnT efficiencies from the $ExBox^{4+}$ derivatives to the PBIs are in all catenanes larger than 96%, which is caused by the close contact between donor and acceptor. With this EnT the PBI triplet state is populated very effectively in water within a few nanoseconds, although the antenna molecules **34** are barely fluorescent.[69]

Turner and coworkers demonstrated how catenanes can be used to generate larger molecular assemblies in 1D, 2D and 3D nanostructures (Figure 30).[122]

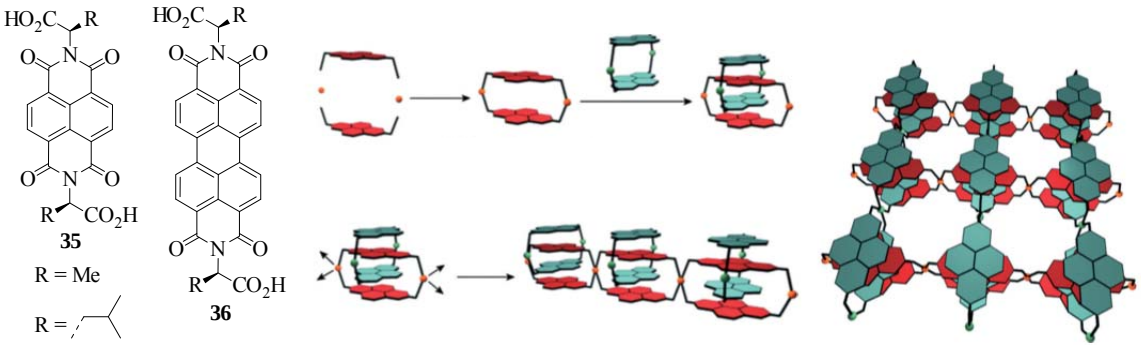

Figure 30. Chemical structures of NBI **35** and PBI **36** and illustration of the formed cyclophanes, catenanes and 1D and 2D nanopatterns; reprinted with permission from ref.[122]. Copyright 2013 The Royal Society of Chemistry.

Therefore, the NBI **35** and PBI **36** molecules have been equipped with alanine or leucine moieties in the imide positions that are capable to coordinate to metal centers. Hereby, the carboxylate groups can be attached to Cd(II) ions to form the corresponding cyclophanes $[Cd_2(AlaNBI)_2]$ that can further be extended to linear polymeric chains of the alanine

derivatives. With the interpenetration of two cyclophanes catenanes are formed that then result in 2D sheets. With the bulkier leucine groups the catenane formation is sterically hindered and thus only 1D polymers were observed. When the cyclophanes are connected with 4,4´-bipyridine forming the extended 1D chains, the encapsulation of the bipyridine moieties can occur. Now a 3D pattern is formed through the combination of the linear NBI cyclophane chains. With the PBI derivatives and their larger cavities the catenane formation is also with the leucine groups enabled that results in the formation of the 2D sheets again.

2.7 Bisimide Metallomacrocycles

Beside the covalently bonded macrocycles, cyclic squares **37** were generated by coordination of monomeric PyBI moieties to Pd(II) metal ions (Figure 31).[123] Herein the PyBIs represent the walls of the chiral box-like square **37**.

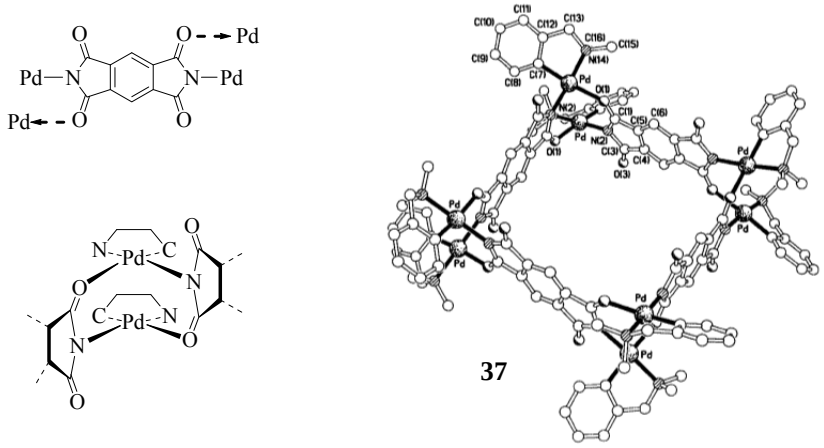

Figure 31. Molecular substructures and crystal structure of the coordinative assembled square **37**; reprinted with permission from ref.[123]. Copyright 1999 The Royal Society of Chemistry.

Such an approach towards functional supramolecular metallomacrocycles has widely been used taking advantage of thermodynamic equilibration to accomplish higher yields. One important example was presented by Harding and coworkers in 1995, in which the NBI **38** was equipped with bipyridine units in the imide position (Figure 32a).[124] Interestingly, the addition of an aromatic guest was necessary to exclusively direct the [2+2] metallomacrocycle **39** with Zn(II) ions. Upon addition of dimethoxybenzene a charge transfer occurs that changes the solution color from yellow to red, similar to the previously described CT complexes. Furthermore, it was shown that a short and rigid linking unit promotes the formation of the helical, guest-induced [2+2] cycles.[125]

In related studies metal (Zn(II), Cd(II), Cu(I)) coordination of NBI monomers **40** leads to close contact among them and thus excimer emission is observed (Figure 32b,c). Upon further addition of metal ions the cyclophane disassembles, the 1:2 (NBI:M) complex is formed and the monomer emission is regained.[126]

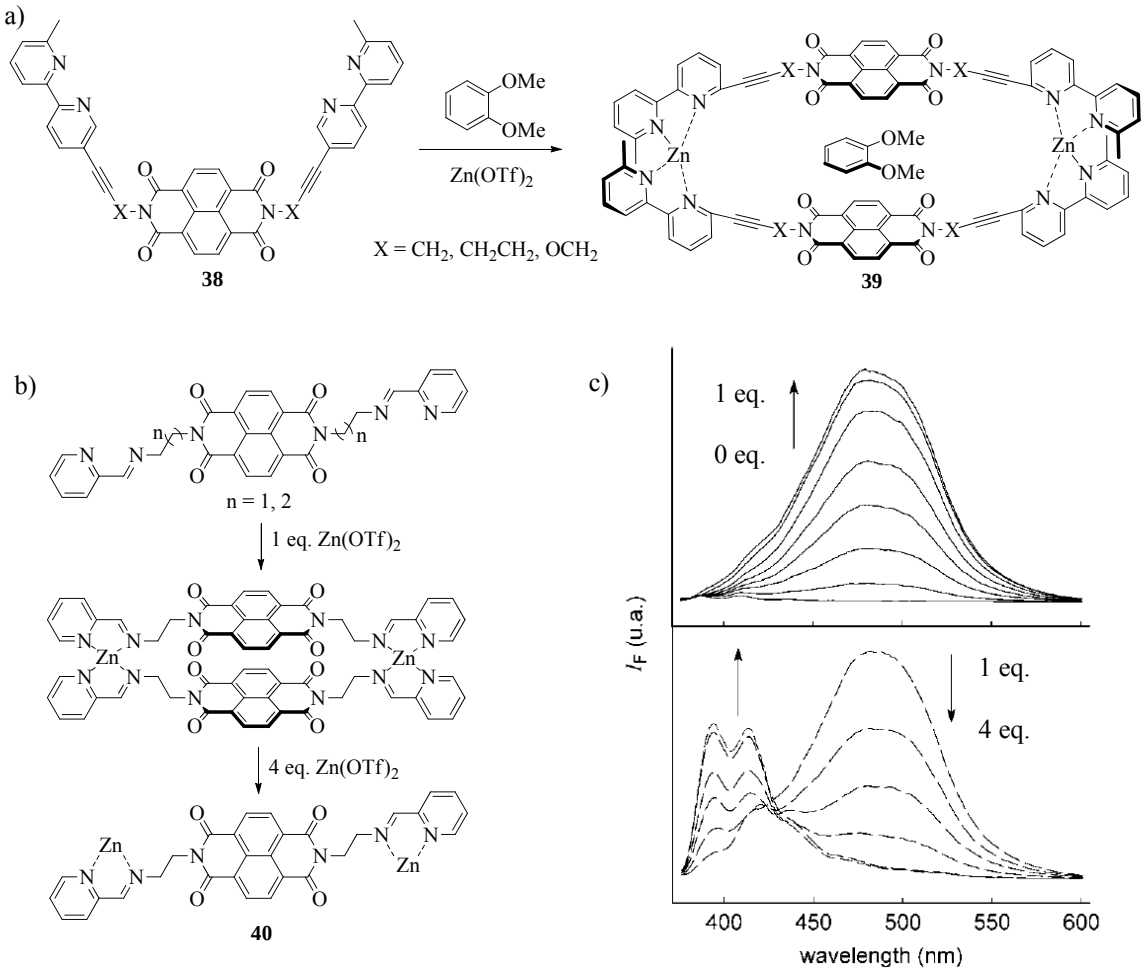

Figure 32. a) Guest-induced assembly of the NBI monomer **38** to the [2+2] NBI cyclophane **39**; b) assembly of the NBI monomers **40** to the corresponding cyclophane and further disassembly to the monomeric metal complex upon addition of Zn(II); c) fluorescence spectra of **40** upon addition of Zn(II) demonstrating the appearance and disappearance of the excimer emission band; reprinted with permission from ref.[126]. Copyright 2002 WILEY-VCH Verlag GmbH & Co. KGaA, Weinheim.

The appearance of excimer emission in condensed NBI cyclophanes upon addition of coordinating units has also been used to selectively detect pyrophosphate in aqueous solution at physiological pH. In the presence of pyrophosphate (PPI) the coordination to metal ion equipped NBIs **41** occurs and a closely packed NBI cyclophane is formed that changes its emission properties (Figure 33a).[127]

With the weak-link approach, conformational changes of NBI cycles **42** have been realized. Thereby, the metal ions are coordinated to a strong (–PPh_2) and a weak (–S–) binding ligand that results in a condensed NBI (or PyBI) cyclophane **42c**.[26a] Upon addition of ancillary pyridine ligands the M–S bond breaks apart, which causes the cyclophanes to open (**42o**) and thus increases the distance between the bisimides (Figure 33b). Along with this opening process the redox properties of the bisimides are changed and a 60 mV shift of the reduction waves is observed. No optical spectroscopy or host-guest studies for the condensed or open cycles have been carried out.

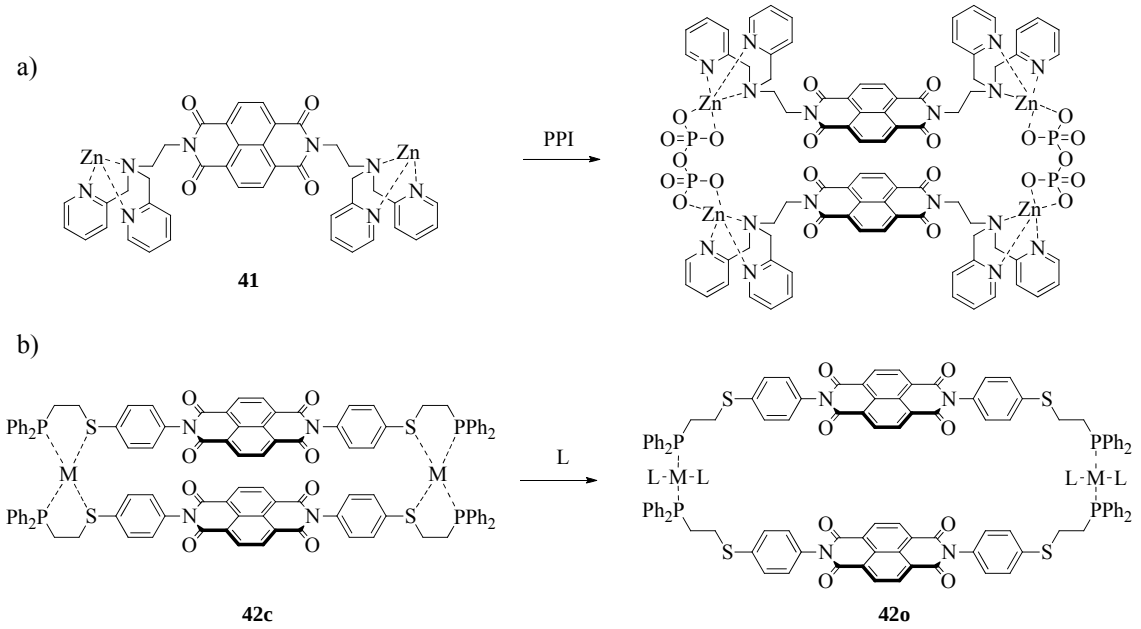

Figure 33. a) Self-assembly of metal ion equipped NBI monomers **41** to the closely packed cyclophane upon addition of pyrophosphate (PPI); b) opening process upon addition of an ancillary ligand to a NBI cyclophane **42c** that is self-assembled in a weak-link approach.

By introducing larger rigid bridges the bisimides are no longer cofacially arranged, but display a side-to-side conformation as in the cyclophanes **43** and **44** (Figure 34).[128] Thus, the conformation of the bisimides does not result in an accessible void. Nevertheless, small cavities are present that at least are large enough for solvent molecules, like DCM (indicated by the blue area in Figure 34). Furthermore, the binding of pyrene on the outer sphere of the rectangles **43** and **44** was observed, derived by π-π interactions with the NBI subunits.

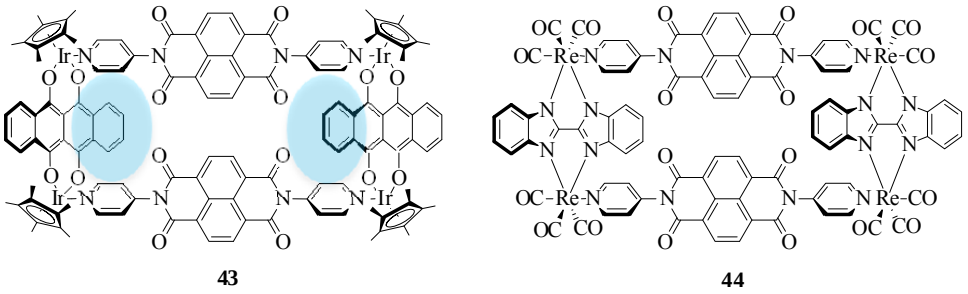

Figure 34. NBI cyclophanes **43** and **44** bridged by a large and rigid linker through metal coordination.

The metallo-supramolecular approach was also used for the synthesis of PBI containing macrocycles. In the first studies self-assembly by Pd(II) and Pt(II) coordination of monomeric chromophores bearing pyridine units in the imide position was studied. With the right combination of ligands and metal ions, defined macrocyclic arrays have been realized composed of two to four chromophores (Figure 35).

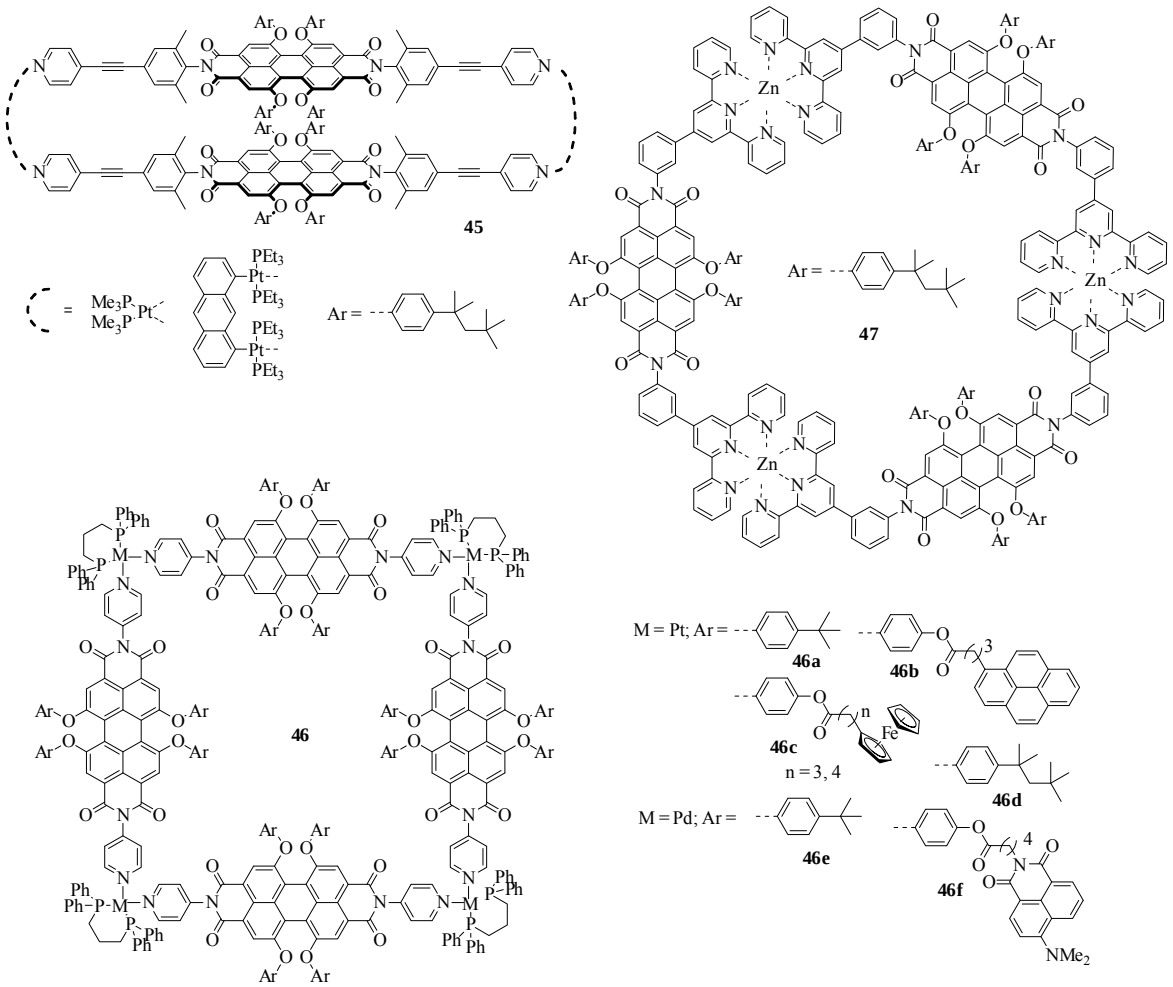

Figure 35. Chemical structures of PBI macrocycles **45–47** obtained by metal coordination of monomeric chromophore units.

With PBIs bearing pyridine ligands in the imide positions and with Pt(II) or Pd(II) ions the cyclophanes **45** containing two chromophores or the squares **46** out of four dyes were achieved, depending on the free coordination position in the metal ions and the length of the ligands. Thus, a rhomboid and rectangle supramolecular cyclophane **45** was synthesized from *cis*-$(PMe_3)_2Pt(OTf)_2$ or an anthracene clip along with a large and flexible PBI ligand.[129] On the other hand, the right-angled tetramer **46a-f** was maintained from $dppM(OTf)_2$ (M = Pt(II) or Pd(II), dpp = 1,3-bis(diphenyl-phosphino)propane) and a short and rigid bipyridine equipped PBI in almost quantitative yields. The optical and electrochemical properties of the tetramer **46** are almost unaffected by the coordination to the metal ions due to an electronic decoupling of the 4-pyridine units from the HOMO and LUMO of the PBI chromophores, resulting in highly fluorescent squares with quantum yields up to 88% (in $CHCl_3$). From isosbestic points in spectroelectrochemical investigations it appears that no interactions between the dyes are present in the supramolecular square. The complete disappearance of the absorption bands of the neutral state suggests a reversible switch of the framework from 0 to +12 in steps of four electrons.[130]

Attachment of pyrene antenna dyes in the bay position of the PBI cores afforded upon Pd(II) addition metallo-supramolcular squares **46b** bearing 16 pyrene antenna dyes at the periphery (Figure 36).

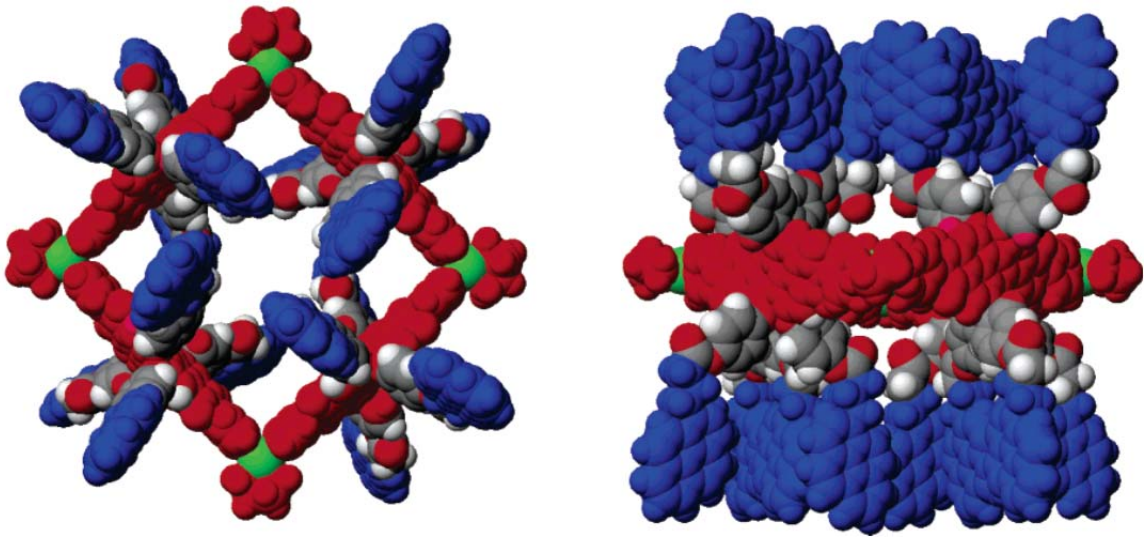

Figure 36. Top (left) and side view (right) of square **46b** with pyrene substituents obtained by geometry optimization (MD-MM2); pyrene = blue, PBI = red; reprinted with permission from ref.[131]. Copyright 2005 American Chemical Society.

Upon excitation of the pyrene units mainly PBI emission is observed suggesting energy transfer from the outer pyrene to the inner PBI with efficiencies > 90%.[131] However, the fluorescence quantum yields of the PBI dyes are significantly reduced to 5% indicating competing electron transfer from the donor pyrene to the PBI acceptor shortening the excited state lifetime from 5.5 ns to 930 ps. In transient absorption (TA) spectroscopy an electron transfer within 2 ps and a charge recombination in 1.2–1.8 ns was observed.[132]

To increase emission by energy transfer the electron transfer has to be suppressed. Therefore, a proper spectral overlap between the fluorescence emission of the donor and the absorption of the acceptor is required to optimize Förster-type resonance energy transfer (FRET). This was achieved by using 4-dimethylamino-1,8-naphthalimide as outer antenna chromophores (**46f**), which increases the fluorescence quantum yield by a factor of eight to 37% compared to the pyrene functionalized derivative **46b**.[133]

Beside the light-harvesting squares, multiredox active macrocycles **46c** with 16 ferrocene groups linked to the perylene cores were synthesized. Upon photoexcitation reductive electron transfer to the PBI chromophores takes place that quenches the fluorescence to < 1%. The redox properties of the ferrocenyl subunits are strongly affected by the supramolecular structure in the squares leading to a splitting of the reductive and oxidative waves in cyclic voltammetry, which was not observed for the monomeric PBI compound. This splitting can be explained by the position of the ferrocene units in which eight groups are pointing to the hydrophobic inside and the other eight groups to the outside of the square **46c**, where they are stabilized by the polar electrolyte. The electrochemical, as well as chemical oxidation with thianthrenium pentachloroantimonate was monitored by spectrophotometry, showing disassembling of the +24 charged molecular squares due to Coulomb repulsion.[134]

By using terpyridine equipped PBIs and Zn(II) ions, cyclic dye arrays with three chromophores (**47**) were synthesized in which the optical properties of the PBI dyes are not affected by the coordination to the metal ions. The macrocycles were characterized by NMR spectroscopy and mass spectrometry confirming the formation of [3+3] cycles. With spin coating onto highly ordered pyrolytic graphite (HOPG) two-dimensional networks were observed and studied by atomic force microscopy (AFM) showing linearly ordered or honeycomb structures with center-to-center distances of 4.7 and 4.3 nm, respectively (Figure 37).[135]

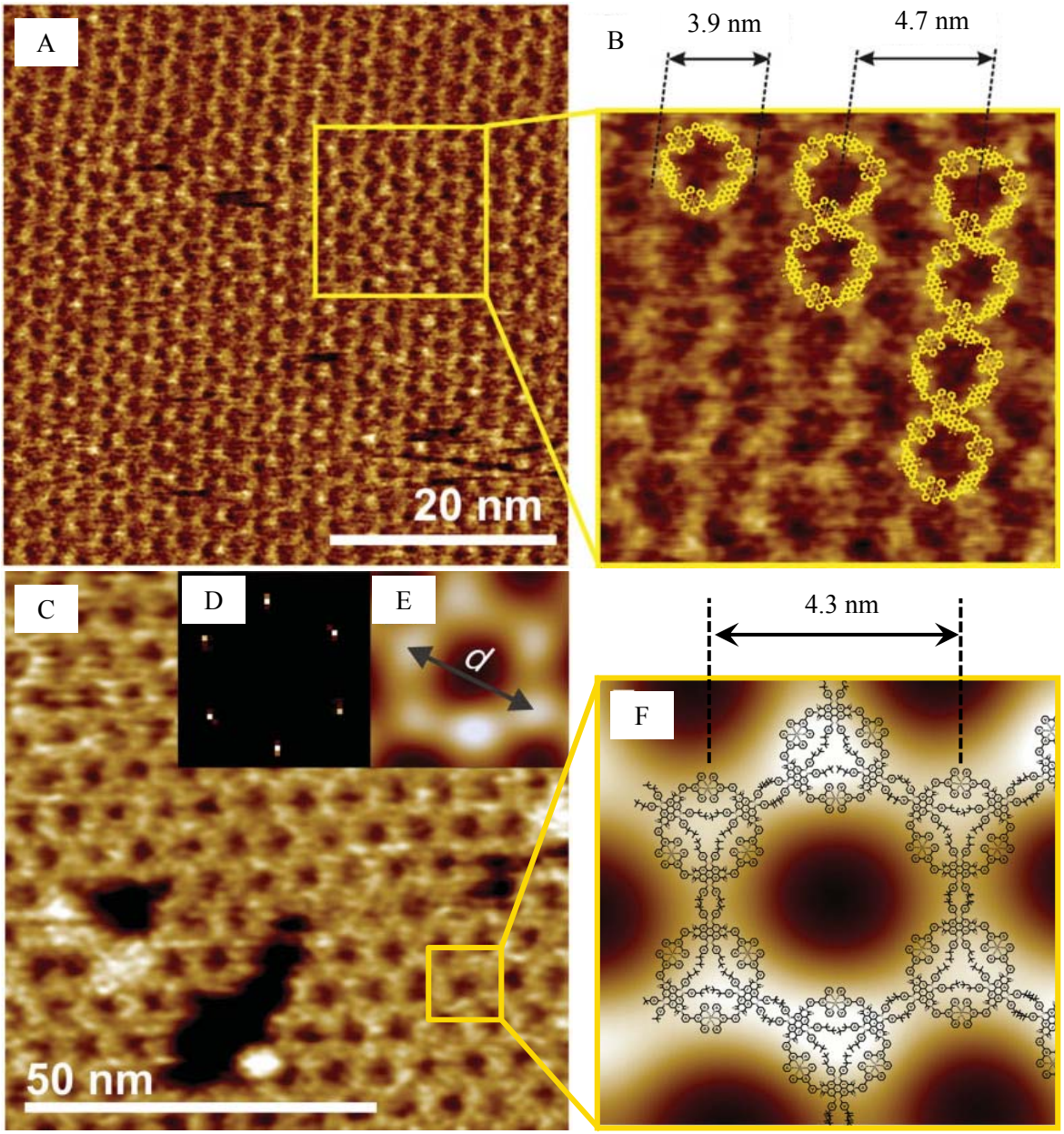

Figure 37. Tapping-mode AFM images and model of molecular arrangement of spin-coated films from DMF solutions of **47** (c = 2.4 x 10^{-5} M) onto HOPG; A and B show the linearly ordered and C–F the honeycomb nanostructures (D: FFT analysis of image C); reprinted with permission from ref.[135]. Copyright 2008 WILEY-VCH Verlag GmbH & Co. KGaA, Weinheim.

Also mixed metallomacrocycles have been reported in the past in which different donor-acceptor building blocks were connected. In these cycles long-lived charge separated states are one main advantage. In this regard Wasielewski and coworkers reported on a cyclic tetramer composed of PyBI, NBI and chlorophyll (Figure 38).[136] Through the coordination of the pyridine equipped PyBI subunit to the Zn(II) ion of the Chl self-assembly towards a defined molecular square **48** occurs.

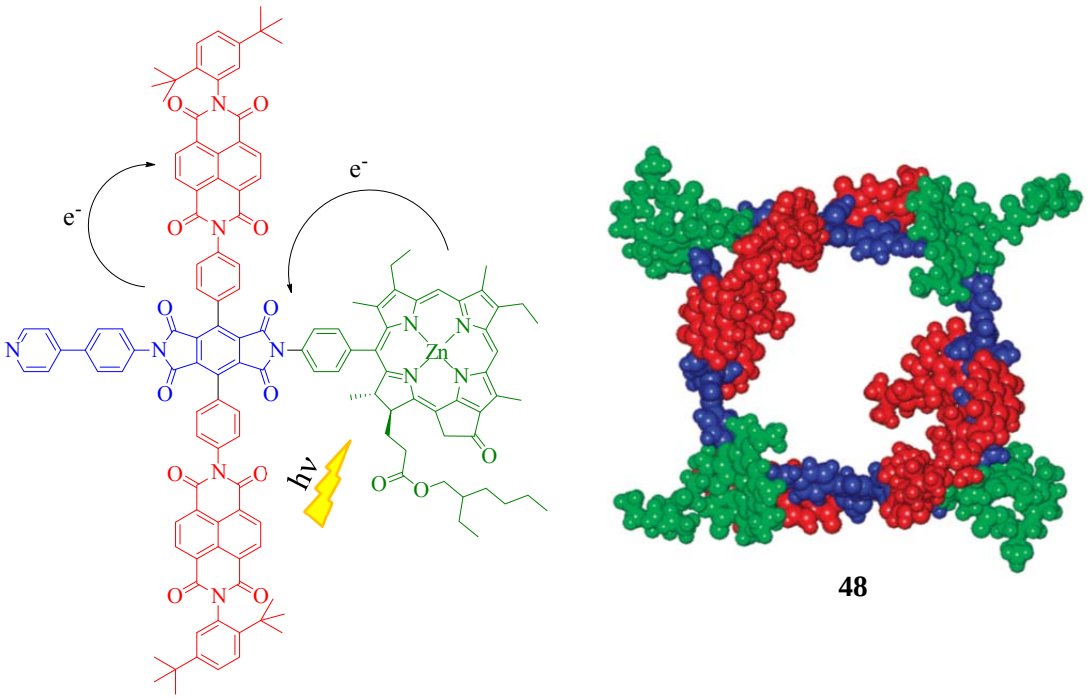

Figure 38. Chemical structure of the donor-acceptor building block and model of the self-assembled tetrameric square; reprinted with permission from ref.[136]. Copyright 2012 American Chemical Society.

TA spectroscopy revealed an electron transfer from Chl to the PyBI upon selective photoexcitation of the Chl moiety. Afterwards an further electron shift from the $Chl^{+\bullet}$-$PyBI^{-\bullet}$-NBI species to $Chl^{+\bullet}$-PyBI-$NBI^{-\bullet}$ takes place before charge recombination (CR) back to the ground state. The Gibbs free energies for the two charge separation processes are with –0.09 and –0.17 eV in the thermodynamically favored regime and occur within 8 and 827 ps, respectively. Hereby, quantum yields for the final $NBI^{-\bullet}$ of > 56% were observed. The charge recombination time τ_{CR} is in the cycle **48** with 30 ns singnificantly slower by a factor of three than in the monomeric compound (with 1% pyridine in toluene).

Similar electron transfer processes have also been observed in cyclic arrays **49** in which the NBI acceptor is directly coordinated to porphyrin donor units (Figure 39).[137] In this sytem the charge separation occurs within 80 ps (in toluene) and is thus much faster than in **48**. No values were reported for the charge recombination.

With the coordination of pyridine equipped PBIs to porphyrin multi-chromophores the dimeric **50a**,**b** or trimeric boxes **51** were achieved (Figure 39). In case of the tetraphenoxy substituted PBIs **50a** charge transfer occurs within 60 ps, forming the $PBI^{-\bullet}$-$porphyrin^{+\bullet}$ state with a short life time of 440 ps. On the other hand, pyrrolidinyl substituted PBIs **50b** show singlet excitation energy transfer from the photoexcited Zn porphyrin to the PBIs in

14 ps with a high efficiency of 70%, which is caused by a lowerd PBI singlet state and a lifted charge transfer state making the charge separation less favored. However, the competing charge separation process still lowers the quantum yield of the energy transfer. As a result of this energy transfer mainly PBI emission is maintained.[138]

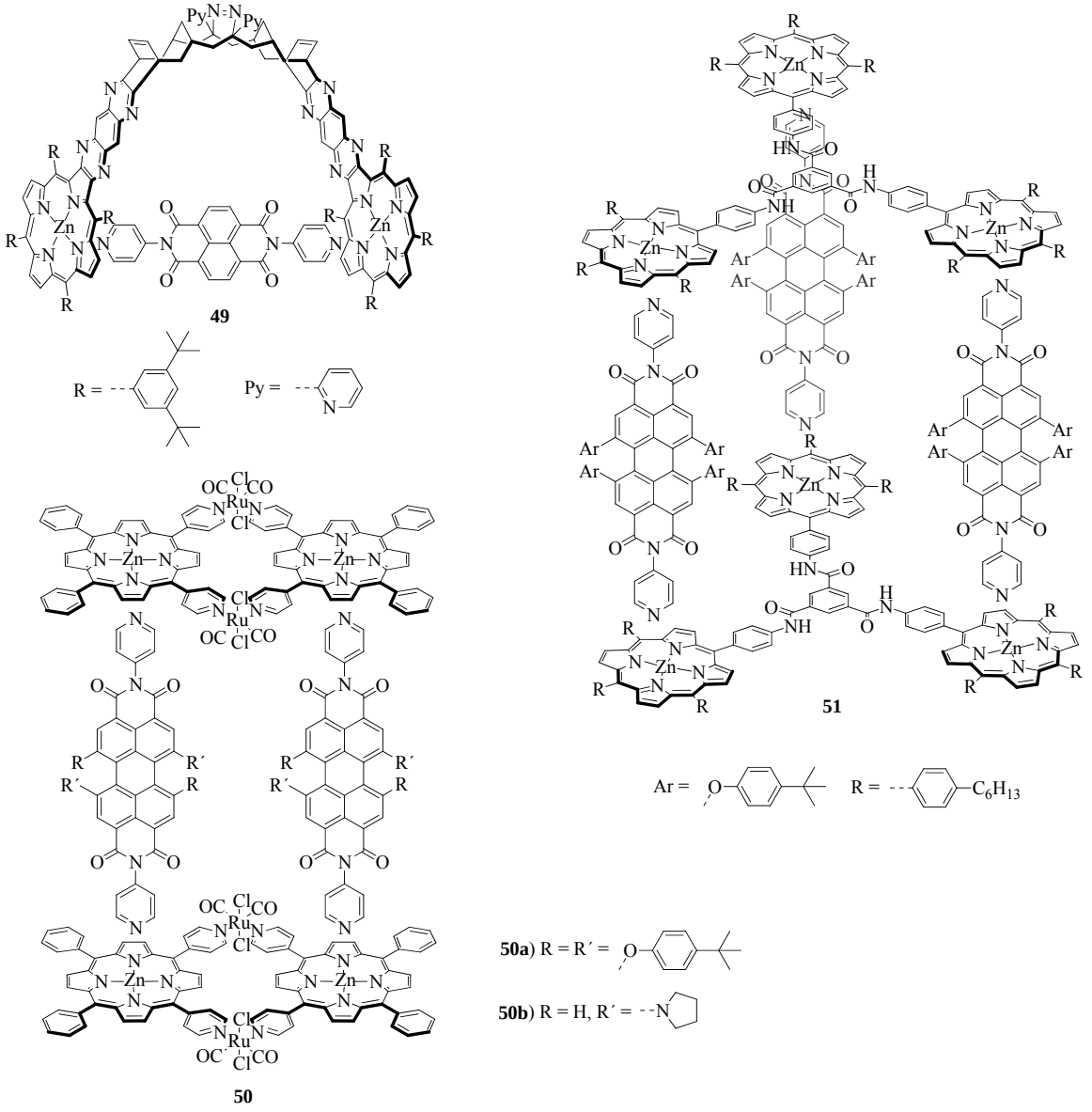

Figure 39. Macrocycles and cages **49**–**51** by coordination NBI/PBI to Zn porphyrins.

In the trimeric cage **51** Flamigni and coworkers studied the effect of solvent polarity on the charge recombination.[139] In polar solvents like DCM the CR occurs within 110 ps, whereas in less polar toluene this process is with ~6 ns significantly slower. The charge separation, however, is in both solvents equally fast with 17 and 30 ps, respectively.

To obtain large and well-defined cavities within the cages the coordination of formylpyridine equipped monomeric NBI units **52** to Zn(II) ions was used to form the corresponding tetrahedron Zn_4L_6 (Figure 40).[140] In these structures the NBI units **52** represent the edges of the tetrahedron with a length of ~21 Å.

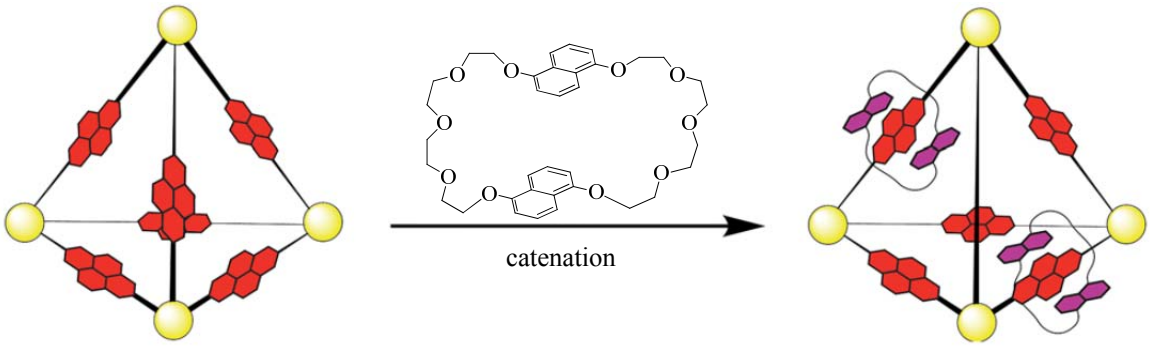

Figure 40. Chemical structure of monomeric NBI **52** that can be self-assembled to the corresponding tetrahedron by coordination to Zn(II) and further functionalized by catenation; reprinted with permission from ref.[140]. Copyright 2016 The Royal Society of Chemistry.

As described in chapter 2.6 the NBI moieties can be used for further functionalization by catenation with crown ether like cyclophanes. In this tetrahedron only two subunits undergo the catenation by sterically-control of the cavity size.

To further enlarge the cavity, PBIs **53** were used in a similar approach to form tetrahedra with an edge length of ~40 Å (Figure 41). This enables the complexation of functional guest molecules like coronene and fullerene into these $Fe(II)_4L_6$ tetrahedral hosts. With the six PBI units a reversible 34 electron cycling between a +18 and a –16 charged species was observed, enabled by the high porosity of the tetrahedron that allows the counterions to flow in and out of the host. However, the fluorescence of the tetrasubstituted PBIs gets quenched through the coordination to the Fe(II) ions.[141] To overvome this shortcoming a tetrahedron **54a** with Zn(II) ions has been made that reduces the excited-state intersystem crossing and fluorescence quenching. Upon dilution, however, this tetrahedron equilibrates to the Zn_2L_3 helicate and finally disassembles.[142] To stabilize the Zn_4L_6 tetrahedron a *tris*(2-aminoethyl)amine bridge has been introduced to covalently link each PBI edge in the cage **54b**. And indeed the stabilized Zn(II) tetrahedron could be obtained in 92% yield with a fluorescence quantum yield of 67%.

This strong emission can now be used for fluorescence sensing upon addition of aromatic guest molecules, such as perylene and coronene (Figure 41).[143]

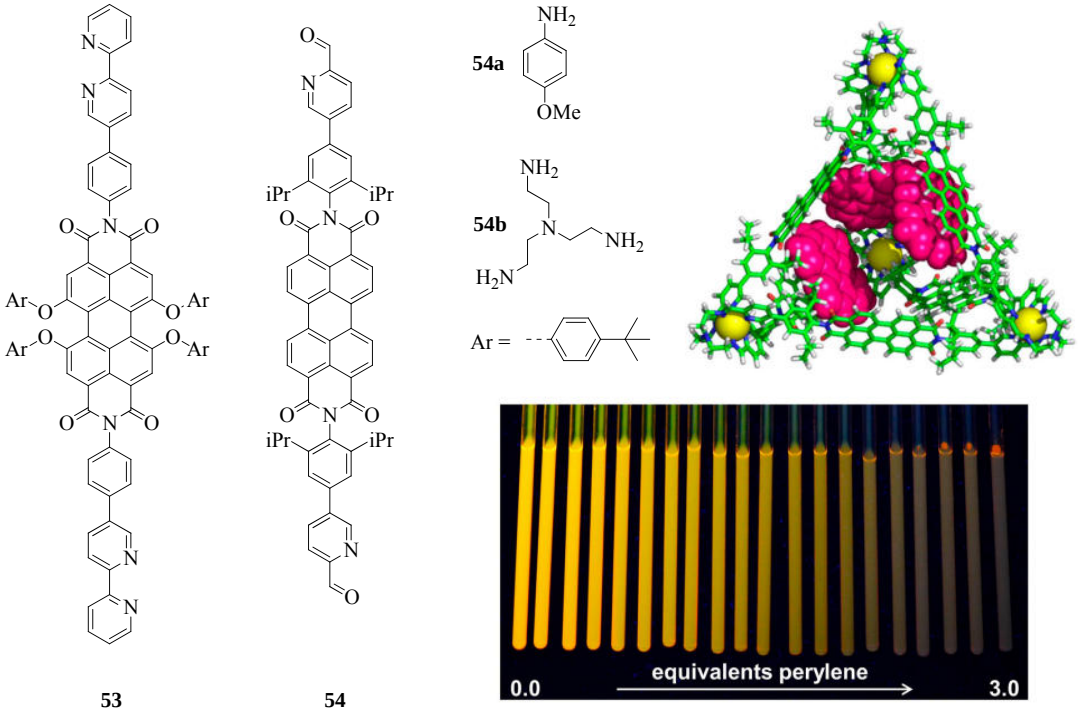

Figure 41. Chemical structure of the PBI building blocks **53** and **54a**,**b** for the formation of PBI tetrahedra by self-assembly to Fe(II) or Zn(II) ions. Geometry optimized structure of the perylene$_3$@**54b** complex and fluorescence quenching upon addition of perylene to **54b**; reprinted with permission from ref.[143]. Copyright 2015 WILEY-VCH Verlag GmbH & Co. KGaA, Weinheim.

Chapter 3

–

Results and Discussion

3.1 Synthesis and Characterization[1]

Inspired by the intriguing function of the natural light-harvesting dye arrays and the just discussed bisimide macrocycles the synthesis of *para*-xylylene bridged perylene bisimide macrocycles and cyclophanes was carried out following the procedure described in Figure 42.

Starting from literature known PBIs **PBI$_{(4\text{-}t\text{Bu})4}$**,[144] **PBI$_{(2,6\text{-}i\text{Pr})2}$**[145] and **PBI$_{(2,6\text{-Ph})2}$**[146] bearing cyclohexane in the imide positions alkaline hydrolysis was performed to get the perylene bisanhydrides **PBA$_{(4\text{-}t\text{Bu})4}$**, **PBA$_{(2,6\text{-}i\text{Pr})2}$** and **PBA$_{(2,6\text{-Ph})2}$** in yields of 86, 72 and 76%. While the addition of a small excess of potassium hydroxide (~10 eq.) is sufficient for **PBA$_{(4\text{-}t\text{Bu})4}$** and **PBA$_{(2,6\text{-}i\text{Pr})2}$**, 200 equivalence of KOH are necessary to convert **PBI$_{(2,6\text{-Ph})2}$** into its PBA derivative. The latter serve as precursors for both, the synthesis of the monomeric reference compounds **1PBI** bearing benzylamine in the imide positions and the *para*-xylylene bridged cyclophanes and macrocycles **nPBI**.

The monomeric PBIs **1PBI$_{(4\text{-}t\text{Bu})4}$**, **1PBI$_{(2,6\text{-}i\text{Pr})2}$** and **1PBI$_{(2,6\text{-Ph})2}$** could thus be synthesized in yields of 85–89% under standard imidization reaction conditions[147] with benzylamine in imidazole and pyridine at 120 °C and were purified by column chromatography.

[1] The syntheses of **PBA$_{(2,6\text{-}i\text{Pr})2}$**, **PBA$_{(2,6\text{-Ph})2}$**, **2PBI$_{(2,6\text{-}i\text{Pr})2}$** and **2PBI$_{(2,6\text{-Ph})2}$** were performed by Andreas Sieblist, Bachelor Thesis, Universität Würzburg, **2014**.

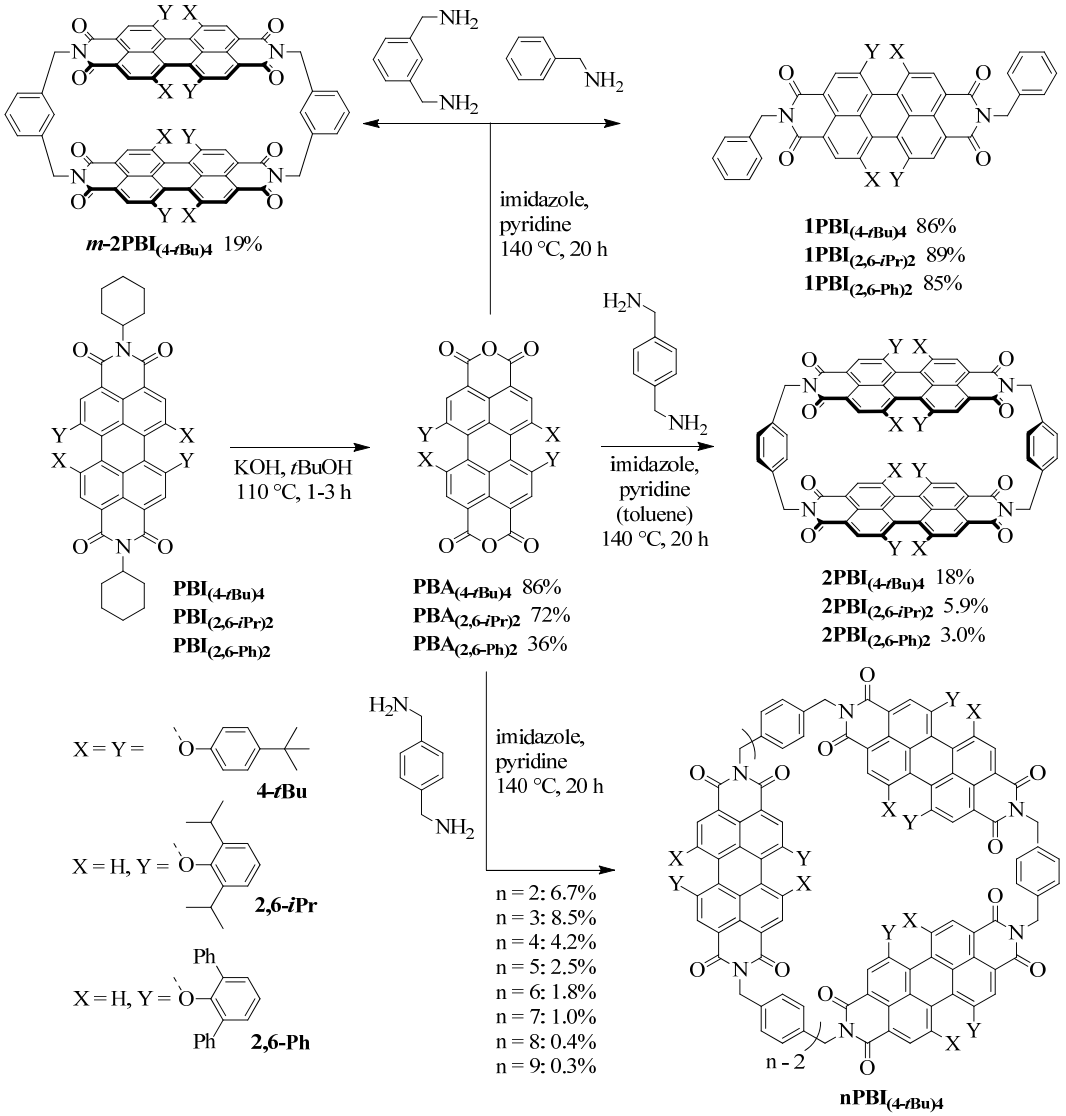

Figure 42. Synthesis route from the literature known PBI derivatives to the corresponding PBA precursor and the final products, the reference compounds **1PBI**, the cyclophanes **2PBI** and the bigger macrocycles **3PBI**–**9 PBI**.

Analog, the cyclophanes **2PBI$_{(4\text{-}t\text{Bu})4}$**, **2PBI$_{(2,6\text{-}i\text{Pr})2}$** and **2PBI$_{(2,6\text{-Ph})2}$** were obtained with *para*-xylylenediamine (1 eq.), however, only in low yields of 6.7, 5.9 and 3.0% after purification by column chromatography and recycling GPC (gel permeation chromatography). The cyclophane ***m*-2PBI$_{(4\text{-}t\text{Bu})4}$** was obtained from **PBA$_{(4\text{-}t\text{Bu})4}$** and *meta*-xylylenediamine in higher yields of 19%, which can be related to an optimized preorganization of the PBI subunits in the open dimers before ring closure. Despite the low yields it was possible to fully characterize the target molecules by NMR, UV-vis absorption, fluorescence spectroscopy and mass spectrometry and to perform host-guest

studies in chloroform and toluene, which allows the comparison of bay substituent effects on the binding strength (see chapter 3.4).

In addition to the PBI cyclophanes **2PBI$_{(4\text{-}t\text{Bu})4}$** the larger macrocycles **nPBI$_{(4\text{-}t\text{Bu})4}$** were obtained from the same reaction. Already the MALDI-TOF mass spectrum of the crude product mixture of **nPBI$_{(4\text{-}t\text{Bu})4}$** showed nicely the formation of macrocycles with different ring sizes starting with the dimer **2PBI$_{(4\text{-}t\text{Bu})4}$**, containing two PBI units, to the nonamer **9PBI$_{(4\text{-}t\text{Bu})4}$** with nine covalently linked chromophores (Figure 43).

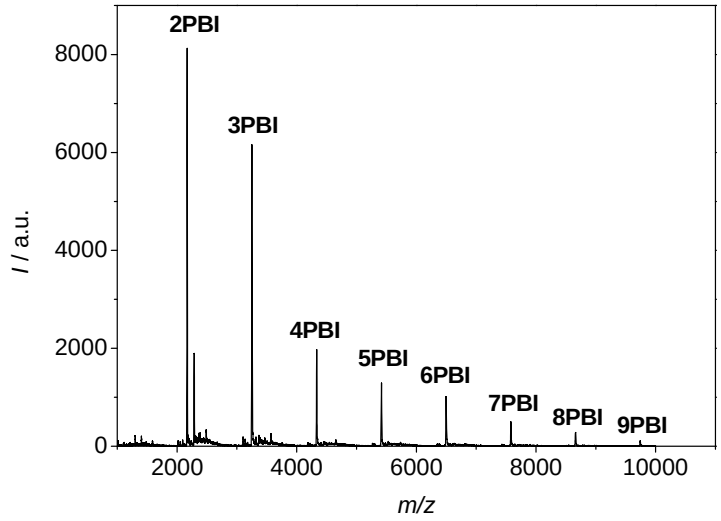

Figure 43. MALDI-TOF mass spectrum of the crude product mixture of **nPBI$_{(4\text{-}t\text{Bu})4}$** prior to separation of the individual macrocycles (pos. mode, DCTB in chloroform 1:1).

With column chromatography the separation of the cyclic dimer from the larger macrocycles and open oligomers was achieved, but not the separation of each macrocycle. Therefore, recycling GPC in chloroform, a method that was already used in the past to separate another class of PBI macrocycles,[107] was used to purify each individual macrocycle **nPBI$_{(4\text{-}t\text{Bu})4}$**. Thus, **nPBI$_{(4\text{-}t\text{Bu})4}$** were isolated in yields of 6.7, 8.5, 4.2, 2.5, 1.8, 1.0, 0.4 and 0.3%, respectively. The relatively low total yield of all macrocycles (~25%) and the decrease of the yield with increasing ring size (trimer to nonamer) is due to the fact that the macrocycles are formed by intramolecular ring closure of the respective open-chain intermediates, which becomes less favored with increasing ring size. Despite the low isolated yields, the individual macrocycles could be satisfactorily characterized by mass spectrometry, ^{1}H- and ^{13}C-NMR and optical spectroscopy. The ^{1}H-NMR spectra of **nPBI$_{(4\text{-}t\text{Bu})4}$** (n = 2–9) show in chloroform one set of signals confirming the high symmetry of the molecules. In comparison to the monomeric reference compound **1PBI$_{(4\text{-}t\text{Bu})4}$** a slight upfield shift of the PBI core protons

occur, which is strongest for **2PBI$_{(4\text{-}t\text{Bu})4}$** due to closer contact of the chromophores and gets smaller with increasing ring size and angle between the dyes (Figure 44). This indicates that with increasing ring size the contact between the PBI chromophores in chloroform is reduced in the way that the dyes in the bigger cycles behave more like the monomer **1PBI$_{(4\text{-}t\text{Bu})4}$**.

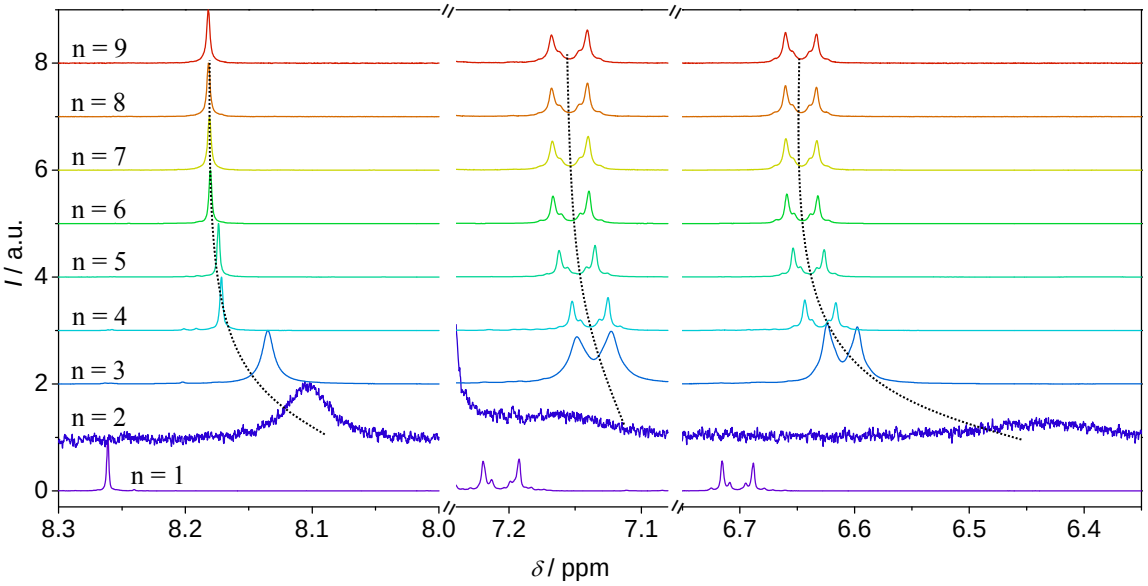

Figure 44. Aromatic region in ^{1}H-NMR spectra ($CDCl_3$; 400 MHz) of the monomeric reference **1PBI$_{(4\text{-}t\text{Bu})4}$** and macrocycles **2PBI$_{(4\text{-}t\text{Bu})4}$** – **9PBI$_{(4\text{-}t\text{Bu})4}$**. **2PBI$_{(4\text{-}t\text{Bu})4}$** has very broad signals due to slower interconversion of *P*- and *M*-atropoenantiomers at the NMR time scale; dotted lines indicate the signal shifts with increasing ring size.

Also for the derivatives **nPBI$_{(2,6\text{-}i\text{Pr})2}$** and **nPBI$_{(2,6\text{-Ph})2}$** larger macrocycles were observed in the crude reaction mixture by mass spectrometry. However, due to the very low yields already for the cyclic trimer of < 1%, these cycles were not further investigated.

To increase the yield of the desired cyclophane, the reaction conditions were optimized, which afforded the best results by dilution with toluene (c(**PBA$_{(4\text{-}t\text{Bu})4}$**) = 0.5 mM), which obviously facilitates the intramolecular dimerization by a template effect (for rationale see chapter 3.2). Remarkably, the yield of cyclophane **2PBI$_{(4\text{-}t\text{Bu})4}$** could thus be improved to 18%. However, similar optimization attempts for **2PBI$_{(2,6\text{-}i\text{Pr})2}$** and **2PBI$_{(2,6\text{-Ph})2}$** were not successful and did not improve the yield.

In the following the different properties of the synthesized cyclophanes and macrocycles will be discussed in detail. First the encapsulation of aromatic hydrocarbons in **2PBI$_{(4\text{-}t\text{Bu})4}$** will be presented, followed by a discussion on the guest and solvent

modulated photophysics of this cyclophane. Afterwards, it will be shown how the guest binding is optimized in disubstituted PBIs, whereas the substitution pattern of **2PBI$_{(4\text{-}t\text{Bu})4}$** can be used to induce chirality to the PBI core. Then, the encapsulation of fullerene into the larger cyclic trimer **3PBI$_{(4\text{-}t\text{Bu})4}$** is illustrated and finally the folding properties and self-assembly on HOPG of the macrocycles will be discussed.

3.2 A PBI Cyclophane as "Turn-on" and "Turn-off" Fluorescence Probe[2]

3.2.1 Optical Spectroscopy and Molecular Modelling

The optical properties of the PBI cyclophane **2PBI$_{(4\text{-}t\text{Bu})4}$** were studied by fluorescence and UV-vis absorption spectroscopy. A significantly decreased fluorescence quantum yield of 21% (in $CHCl_3$) was observed for **2PBI$_{(4\text{-}t\text{Bu})4}$** in comparison to 97% for the monomeric PBI **1PBI$_{(4\text{-}t\text{Bu})4}$** (Figure 45).

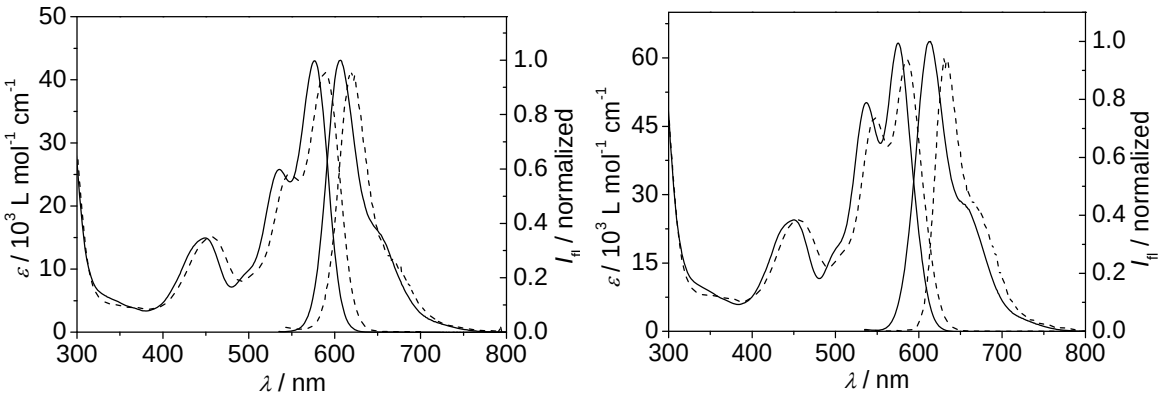

Figure 45. UV-vis absorption and fluorescence spectra of the monomeric reference compound **1PBI$_{(4\text{-}t\text{Bu})4}$** (left) and the PBI cyclophane **2PBI$_{(4\text{-}t\text{Bu})4}$** (right) in chloroform (dashed line) and toluene (solid line); emission spectra are normalized to the corresponding UV-vis maxima; c = 5.0 x 10^{-6} M; RT.

This can be explained on the basis of spatial proximity of the PBI units in the cyclophane **2PBI$_{(4\text{-}t\text{Bu})4}$** giving rise to a weak interchromophoric interaction that obviously opens new non-radiative decay channels. In compliance with this, the ratio of the 0-0 and 0-1 vibronic transition ($A_{0\text{-}0}/A_{0\text{-}1}$) for cyclophane **2PBI$_{(4\text{-}t\text{Bu})4}$** is considerably reduced to 1.25 in contrast to 1.66 for **1PBI$_{(4\text{-}t\text{Bu})4}$**, suggesting exciton-vibrational couplings.[148] On the other hand, molecular modelling (Figure 46a) suggests that the interchromophoric distance of approximately 6.5 Å should be properly suited for the encapsulation of planar aromatic guest molecules, and indeed the fluorescence quantum yield of **2PBI$_{(4\text{-}t\text{Bu})4}$** is substantially increased to 64% in the aromatic solvent toluene (**1PBI$_{(4\text{-}t\text{Bu})4}$**: Φ_{fl} = 99%). This can be explained in terms of intercalation of toluene molecules between both PBI chromophores leading to a reduced exciton coupling between the two PBI chromophores.

[2] This chapter has been published: P. Spenst, F. Würthner, *Angew. Chem. Int. Ed*. **2015**, *54*, 10165-10168; *Angew. Chem*. **2015**, *127*, 10303-10306.

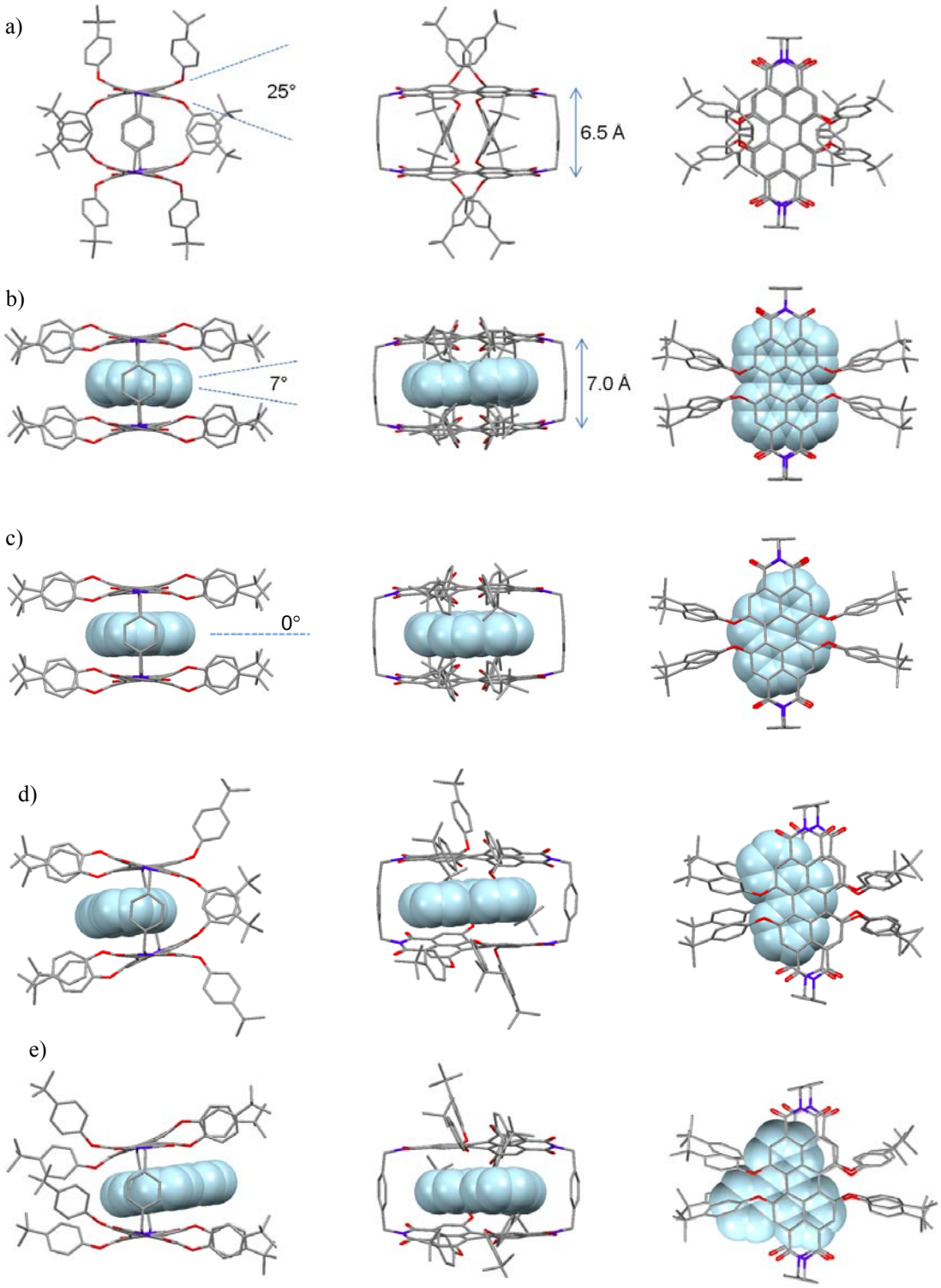

Figure 46. Geometry optimized structures of the free PBI cyclophane **2PBI$_{(4\text{-}t\text{Bu})4}$** (a) and of the 1:1 complexes perylene@**2PBI$_{(4\text{-}t\text{Bu})4}$** (b), pyrene@**2PBI$_{(4\text{-}t\text{Bu})4}$** (c), phenanthrene@**2PBI$_{(4\text{-}t\text{Bu})4}$** (d) and triphenylene@**2PBI$_{(4\text{-}t\text{Bu})4}$** (e) in the front- (left), side- (middle) and top-view (right) obtained by force field optimization; Maestro 9.3, MacroModel 9.8, $CHCl_3$, MM2*.

Obviously, embedding of toluene between two PBIs is also the reason for increased yields of cyclophane **2PBI$_{(4\text{-}t\text{Bu})4}$** in this particular solvent (see chapter 3.1).

3.2.2 Host-Guest Studies

To investigate the capability of **2PBI$_{(4\text{-}t\text{Bu})4}$** to serve as a host for other more complex aromatic hydrocarbons UV-vis absorption and fluorescence (λ_{ex} = 530 nm) titration experiments were performed by adding an excess of the particular guest to a solution of **2PBI$_{(4\text{-}t\text{Bu})4}$** in chloroform ($c$(**2PBI$_{(4\text{-}t\text{Bu})4}$**) = 5.8 x 10^{-5} M) (Figure 98 – Figure 102 in the appendix). Therefore, different rigid and flexible aromatic substrates were applied to determine the factors that influence the complexation behavior.

The titration of cyclophane **2PBI$_{(4\text{-}t\text{Bu})4}$** with rather electron-poor guest molecules like naphthalene, biphenyl, 9-fluorenone, anthraquinone, phenanthrene, phenylnaphthalene and triphenylene resulted in only small changes of the PBI absorbance (Figure 47a). Several isosbestic points indicated the formation of single well-defined host-guest complexes. Most interestingly, the intercalation of the guest molecules between the cofacially arranged π-surfaces of the PBI chromophores significantly increased the emission intensity up to 100% by virtue of a reduced electronic coupling between the two PBIs (*vide supra*) (Figure 47a and Figure 48a, red squares). In contrast, the complexation of more electron-rich substrates like carbazole, anthracene, pyrene and perylene further quenches the PBI fluorescence due to charge transfer (CT) interactions between the guest and the electron-poor PBI chromophores (Figure 47b and Figure 48a, blue squares).[21b] Additionally, the emission maxima of the host-guest complexes are strongly red-shifted to 650, 657 and 690 nm for carbazole, pyrene and anthracene, which can presumably be attributed to emissions originating from CT states. Since the oxidative fluorescence quenching is related to an intermolecular charge transfer from the HOMO of the guest molecule to the HOMO of the photoexcited host (inset Figure 48a), cyclophane **2PBI$_{(4\text{-}t\text{Bu})4}$** can be used as both “turn-on” and “turn-off” fluorescence probe depending on the electronic character of the encapsulated aromatic hydrocarbon.

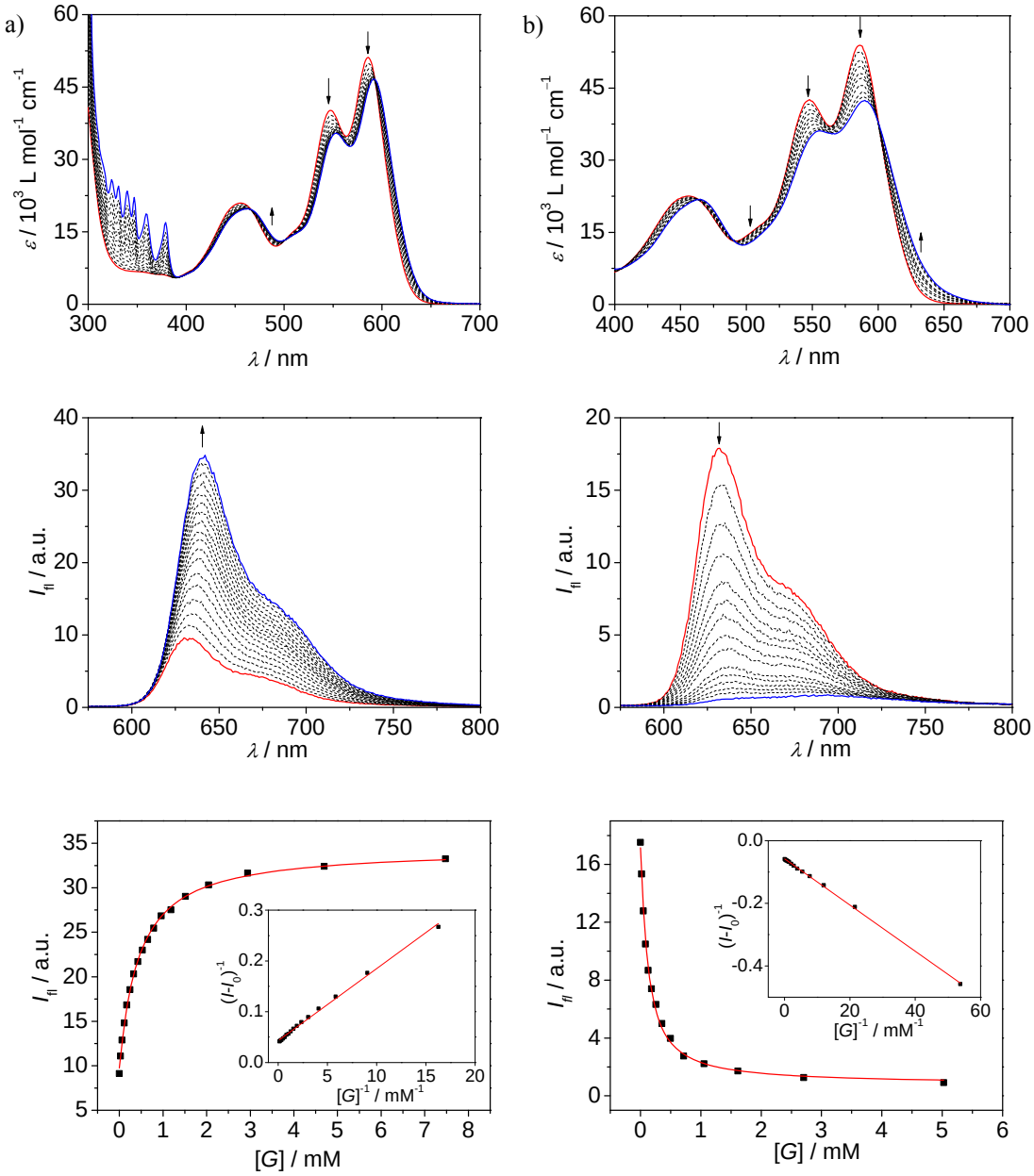

Figure 47. Changes in the UV-vis absorption (top) and emission spectra (middle) of PBI cyclophane **2PBI$_{(4\text{-}t\text{Bu})4}$** upon titration with the individual guest molecules on the examples of phenanthrene (a) and anthracene (b); c(**2PBI$_{(4\text{-}t\text{Bu})4}$**) = 5.8 x 10^{-5} M in $CHCl_3$; red line: spectra before titration; blue line: spectra after the individual guest is completely added; arrows indicate spectral changes; bottom: non-linear least square fitting curves of the fluorescence intensities vs. the guest concentration (inset: Benesi-Hildebrand plot confirming the 1:1 stoichiometry).

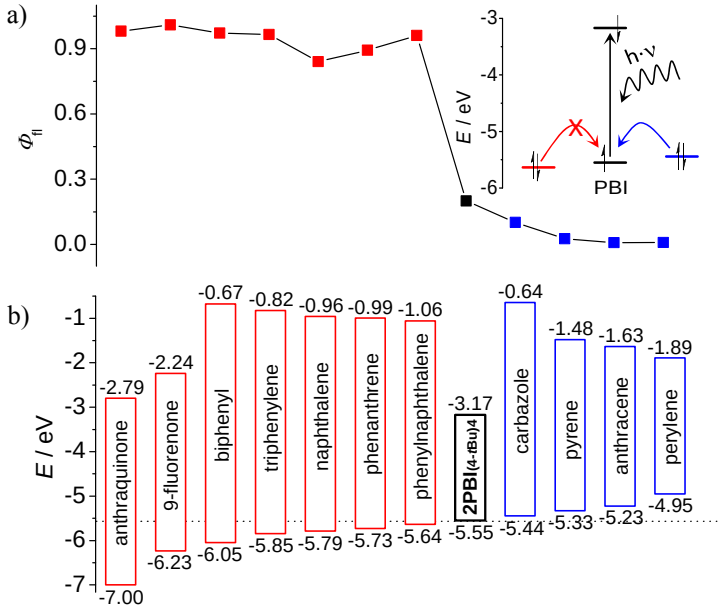

Figure 48. (a) Plot of the fluorescence quantum yield Φ_{fl} of the host-guest complexes. Electron-poor guests (red), electron-rich guests (blue) and the free cyclophane **2PBI$_{(4\text{-}t\text{Bu})4}$** (black); inset: schematic representation of the oxidative fluorescence quenching mechanism; (b) calculated HOMO and LUMO levels of the guest molecules; DFT calculations, Gaussian09W, B3LYP/6-31G(d).

Considering the energy level of ferrocene/ferrocenium with respect to the vacuum level[149] and the oxidation potential of cyclophane **2PBI$_{(4\text{-}t\text{Bu})4}$** ($E_{1/2}^{ox}$ (**1**/**1**$^+$) = 0.84 V, Figure 51b in chapter 3.3), the HOMO level of **2PBI$_{(4\text{-}t\text{Bu})4}$** can readily be estimated as –(4.8+0.84) eV = –5.64 eV (DFT calculations: –5.55 eV). Thus, guest molecules with a HOMO that is higher in energy than the one of cyclophane **2PBI$_{(4\text{-}t\text{Bu})4}$** will quench the PBI emission. Whilst aromatic hydrocarbons with a lower lying HOMO level obviously increase the cyclophane fluorescence because the guest molecules keep the two PBIs at distance, preventing structural relaxation in the excited state towards increased intermolecular PBI-PBI coupling that constitutes a common fluorescence quenching pathway of these dyes.[94b] Furthermore, new bathochromically shifted CT-bands at higher wavelengths can be observed for electron-rich guest molecules by UV-vis spectroscopy beside the original PBI absorption maxima (Figure 47b). As a consequence of the particularly strong interaction between perylene and PBI host **2PBI$_{(4\text{-}t\text{Bu})4}$** the corresponding perylene@**2PBI$_{(4\text{-}t\text{Bu})4}$** complex could also be confirmed by mass spectrometry (MALDI-MS, Figure 103 in the appendix).

According to Benesi and Hildebrand, who developed a simple mathematical approach for the determination of equilibrium constants of non-covalent host-guest complexes ΔI_{fl}^{-1}

was plotted versus $[G]^{-1}$ suggesting the formation of 1:1 complexes for all applied guests (Figure 98 – Figure 102 in the appendix).[150] The respective binding constants were accordingly determined using a 1:1 binding model (2) by non-linear least square fitting:[151]

$$I_{\text{obs}} = I_{\text{A}} + \frac{I_{\text{AB}} - I_{\text{A}}}{2c_{\text{A}}^{0}}\left(c_{\text{A}}^{0} + c_{\text{B}}^{0} + \frac{1}{K_{\text{a}}} \pm \sqrt{\left(c_{\text{A}}^{0} + c_{\text{B}}^{0} + \frac{1}{K_{\text{a}}}\right)^{2} - 4c_{\text{A}}^{0}c_{\text{B}}^{0}}\right) \qquad (2)$$

where I_{A}, I_{AB} and I_{obs} are the fluorescence intensities at a selected wavelength of the free host, the 1:1 complex and the measured intensity. ${c_{\text{A}}}^{0}$ and ${c_{\text{B}}}^{0}$ are the total concentrations of the host and the guest. K_{a} is the respective binding constant. From the binding constant K_{a} the Gibbs free energy $\Delta {G^{0}}_{298}$ can be calculated according to equation (3):

$$\Delta G_{298}^{0} = -RT \ln K_{\text{a}} \qquad (3)$$

The results are summarized in Table 1.

Table 1. Binding constants K_{a} [M^{-1}] and Gibbs free energies $\Delta {G^{0}}_{298}$ [kJ mol^{-1}] for the 1:1 complexes of aromatic hydrocarbons by PBI cyclophane **2PBI$_{(4\text{-}t\text{Bu})4}$** in $CHCl_3$ at c = 5.8 x 10^{-5} M.

guest	K_{a}	R^2	$-\Delta {G^{0}}_{298}$
naphthalene	26.8 ± 0.6	0.999	8.15
9-fluorenone	(1.6 ± 0.1) x 10^3	0.997	18.1
carbazole	944 ± 110	0.991	17.0
anthraquinone	(1.5 ± 0.1) x 10^3	0.998	18.0
biphenyl	(7.1 ± 0.4) x 10^3	0.997	20.0
anthracene	(9.9 ± 0.6) x 10^3	0.997	22.8
phenanthrene	(2.4 ± 0.1) x 10^3	0.999	19.3
phenylnaphthalene	(1.1 ± 0.1) x 10^4	0.996	23.1
pyrene	114 ± 2.0	0.999	11.7
triphenylene	(1.2 ± 0.1) x 10^3	0.998	17.5
perylene	(4.6 ± 0.4) x 10^4	0.997	26.6

For a presumed prevalence of dispersion interactions in these host-guest complexes it is reasonable to assume that the affinity of **2PBI$_{(4\text{-}t\text{Bu})4}$** towards aromatic guest molecules correlates to the host-guest π-surface that is in direct contact by the non-covalent interaction (Figure 49).[152]

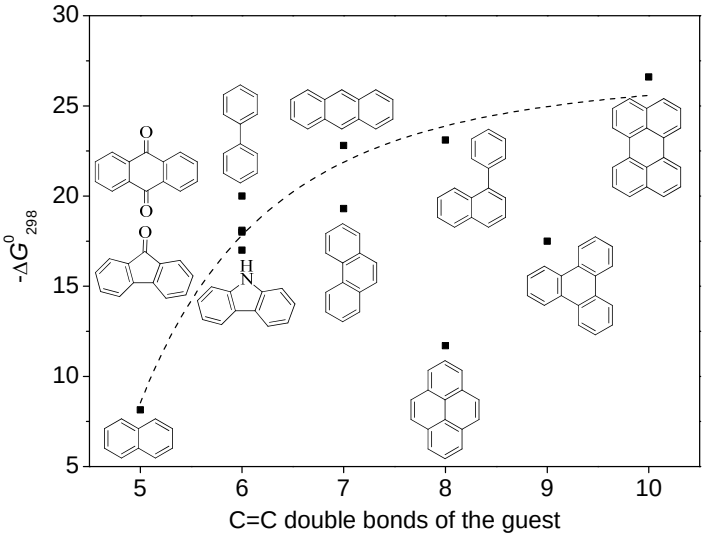

Figure 49. Plot of $-\Delta G^0_{298}$ versus the number of C=C double bonds of the guests´ π-scaffold; the dotted line visualizes the trend between binding strength and interacting π-orbitals that maximize for perylene in $CHCl_3$.

Thus, the dimension of the PBI π-surface apparently defines the maximal binding strength and increasing number of C=C double bonds within the substrate should result in larger binding constants until the aromatic PBI core becomes completely covered and the guest molecule too extended to be encapsulated.[153] This tendency can be corroborated considering that the binding constant K_a continuously increases in the order naphthalene ($26.8\ M^{-1}$) << carbazole ($940\ M^{-1}$) ≈ anthraquinone ($1.5 \times 10^3\ M^{-1}$) ≈ 9-fluorenone ($1.6 \times 10^3\ M^{-1}$) < anthracene ($9.9 \times 10^3\ M^{-1}$) < phenylnaphthalene ($1.1 \times 10^4\ M^{-1}$) < perylene ($4.6 \times 10^4\ M^{-1}$) where the binding strength reaches its maximum (marked as dotted line in Figure 49). The similar values for similarly sized electron-rich and electron-poor guest molecules (e.g. carbazole and 9-fluorenone) also corroborate the view that the binding energy is indeed governed by dispersion and not by charge transfer forces. Considering the number of C=C double bonds that should be involved in the complexation of phenanthrene and triphenylene the observed binding constants are apparently lower than one might expect. However, regarding the geometry optimized structures of phenanthrene@**2PBI$_{(4\text{-}t\text{Bu})4}$** and triphenylene@**2PBI$_{(4\text{-}t\text{Bu})4}$** this observation seems to be rather reasonable since both guest molecules are partially displaced from the cavity due to the core twisting of bay-substituted PBIs (Figure 46d, e).[154] Therefore, the number of C=C double bonds that contribute to the binding interaction in both complexes is reduced to approximately six, which is consistent with our experimental findings. Due

to the twist of the aromatic PBI core, the cavity of cyclophane **2PBI$_{(4\text{-}t\text{Bu})4}$** is indeed somewhat distorted and consequently exhibits a certain selectivity towards more flexible guest molecules, which are capable to screen the surface of the inner void.

Therefore, the binding constant between **2PBI$_{(4\text{-}t\text{Bu})4}$** and pyrene (114 M^{-1}), which acts as a representative for relatively rigid and more discoid aromatic hydrocarbons is significantly decreased (K_a is 100 times lower than that for phenylnaphthalene). In contrast, substrates with a high intrinsic flexibility like biphenyl can readily adapt the geometry of the cavity resulting in a comparatively high equilibrium constant of $K_a = 7.1 \times 10^3$ M^{-1} that is four times higher than the ones for the planarized analogues 9-fluorenone, carbazole and anthraquinone. Molecules like 1,1'-binaphthyl and 1,1'-binaphthole, which are axially too twisted, or substrates like tetracene and *trans*-stilbene, which are larger than the cavity of the PBI cyclophane itself could not be encapsulated by **2PBI$_{(4\text{-}t\text{Bu})4}$**. This provides further evidence that the complexation indeed takes place within the cavity and not at the outer PBI π-surface. It should be pointed out that all host-guest studies were carried out in chloroform, which is a solvent with excellent solvation properties for PBI π-scaffolds.[155] Thus, far higher binding constants are expected in other solvents.

In summary, the rigid *para*-xylylene bridged cyclophane **2PBI$_{(4\text{-}t\text{Bu})4}$** exhibits an ideal interchromophoric distance for the encapsulation of aromatic hydrocarbons with binding constants up to 4.6×10^4 M^{-1}. Since the emission properties of the complexes are highly dependent on the electronic structure of the substrate, cyclophane **2PBI$_{(4\text{-}t\text{Bu})4}$** could be used as both "turn-on" and "turn-off" fluorescence probe distinguishing electron-rich and electron-poor aromatic molecules (Figure 50).

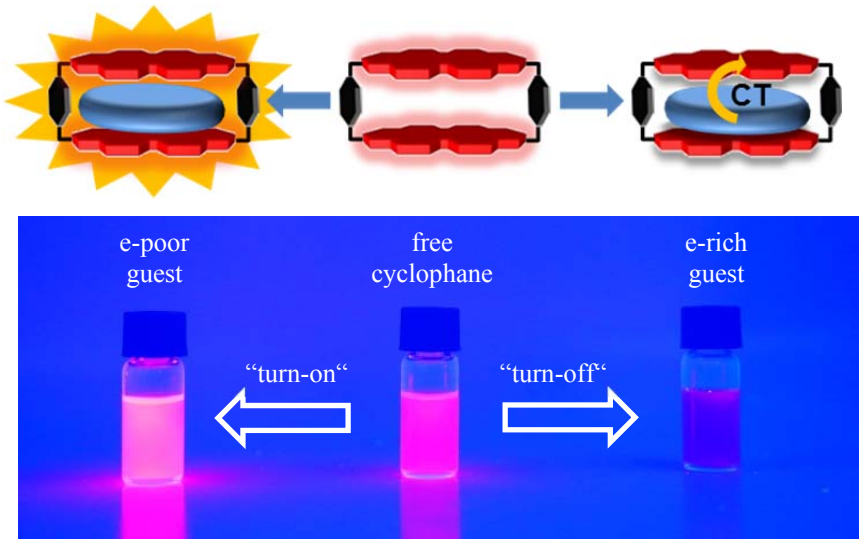

Figure 50. Schematic illustration (top) and representative photograph (bottom) for the “turn-on” (phenylnaphthalene@**2PBI$_{(4\text{-}t\text{Bu})4}$**) and “turn-off” (carbazole@**2PBI$_{(4\text{-}t\text{Bu})4}$**) fluorescence sensing of electron-poor and electron-rich aromatic hydrocarbons of the PBI cyclophane **2PBI$_{(4\text{-}t\text{Bu})4}$**.

3.3 Guest and Solvent Modulated Photo-driven Charge Separation and Triplet Generation in a PBI Cyclophane[3]

As described in chapter 2.1 the precise positioning of the light absorbing chlorophylls and their associated redox cofactors in photosynthetic reaction center proteins using weak van-der-Waals interactions and metal-ligand and hydrogen bonds results in optimized electronic interactions between them that result in efficient charge separation to form radical ion pairs (RPs).[42, 156] For example, photoexcitation of the chlorophyll special pair dimer in some reaction center proteins leads to symmetry-breaking charge separation (SB-CS),[157] which has motivated researchers to develop synthetic analogues and to investigate the fundamental photophysics behind SB-CS.[95, 158]

One factor thus far limiting studies of non-covalent supramolecular ensembles has been the lack of suitable dye-based hosts bearing sufficiently large cavities to complex redox-active guest molecules. In recent work this challenge was approached with the cyclic PBI trimer **28** (see chapter 2.5) for which biomimetic intramolecular symmetry-breaking charge separation (SB-CS) could be observed in τ_{CS} = 12 ps, although the free energy of charge separation, ΔG_{CS}, is barely negative.[112] The charge recombination (CR) back to the PBI ground state (GS) is much slower (τ_{CR} = 1.12 ns), despite the larger ΔG_{CR} of this process. According to Marcus theory,[159] ET can occur in the normal region ($-\Delta G_{ET} < \lambda$) or in the inverted region ($-\Delta G_{ET} > \lambda$) depending on the relative magnitudes of the Gibbs free energy ($-\Delta G_{ET}$) and the reorganization energy (λ).[158a, 160] The PBI trimer **28** data imply that its charge recombination reaction is in the Marcus inverted region.[159, 161] Unfortunately, no guest encapsulation could be achieved within the PBI trimer **28**, in contrast to the PBI cyclophane, **2PBI$_{(4\text{-}t\text{Bu})4}$**, whose fluorescence is quenched by the encapsulation of electron rich aromatic guests (chapter 3.2). Accordingly, the electronic interactions of **2PBI$_{(4\text{-}t\text{Bu})4}$** and its corresponding host-guest complexes are elucidated by steady-state absorption, fluorescence and transient absorption (TA) spectroscopy to identify the ET processes and the individual lifetimes of the states formed.

[3] This chapter has been published: P. Spenst, R. M. Young, M. R. Wasielewski, F. Würthner, *Chem. Sci.* **2016**, *7*, 5428-5434.

3.3.1 Steady state Spectroscopy and Electrochemistry

The steady-state UV-vis absorption spectrum of **2PBI$_{(4\text{-}t\text{Bu})4}$** has its maximum at 582 nm in dichloromethane, which is comparable to the tetraphenoxy-substituted monomeric PBI **1PBI$_{(4\text{-}t\text{Bu})4}$**. Similar to other multi-chromophoric PBI systems, the 0-1 vibronic band of **2PBI$_{(4\text{-}t\text{Bu})4}$** at 543 nm is significantly enhanced with respect to the 0-0 transition that can be related to the excitonic coupling of the two cofacial arranged PBI units (Figure 51a).[30d, 112, 148d] The corresponding fluorescence spectrum has its maximum at 627 nm, which is bathochromically shifted by 12 nm and has a significantly quenched 7% fluorescence quantum yield compared to **1PBI$_{(4\text{-}t\text{Bu})4}$** ($\Phi_{fl}$(**1PBI$_{(4\text{-}t\text{Bu})4}$**) = 75% in DCM), indicative of an efficient nonradiative decay process. No long-lived and red-shifted excimer-like emission[30d, 148d] was observed, which is attributed to the stiff linkage and the relatively long 6.5 Å interplanar distance between the two PBI chromophores.

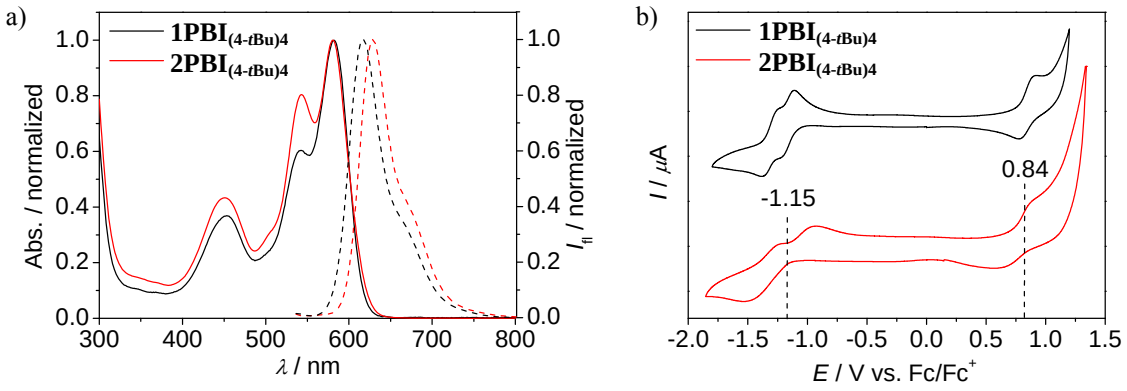

Figure 51. Normalized UV-vis absorption (solid line) and fluorescence (dashed line) spectra (a) of **2PBI$_{(4\text{-}t\text{Bu})4}$** (red) and **1PBI$_{(4\text{-}t\text{Bu})4}$** (black); DCM, RT, c = 5 x 10^{-5} M; cyclic voltammograms (b) in DCM of **2PBI$_{(4\text{-}t\text{Bu})4}$** and **1PBI$_{(4\text{-}t\text{Bu})4}$**; reference electrode: Ag/AgCl, working and auxiliary electrode: Pt; 0.1 M TBAHFP, Fc/Fc$^+$, RT, c = 2 x 10^{-4} M.

To get information with regard to the thermodynamic driving force for photo-driven charge separation ΔG_{CS} cyclic voltammetry was performed on **2PBI$_{(4\text{-}t\text{Bu})4}$** and **1PBI$_{(4\text{-}t\text{Bu})4}$** in dry dichloromethane under argon (Figure 51b). **2PBI$_{(4\text{-}t\text{Bu})4}$** shows similar behavior to the monomer with two reversible reduction and one reversible oxidation waves, which are slightly cathodically shifted by 20 mV compared to **1PBI$_{(4\text{-}t\text{Bu})4}$**. The broadening of the **2PBI$_{(4\text{-}t\text{Bu})4}$** voltammogram can be related to multi-electron processes.[30d] To quantify the driving force for the charge separation and recombination for the cyclophane the Weller equation was applied (Eq. (4) and (5)):[162]

$$\Delta G_{CS} = e\left[E_{ox(D)} - E_{red(A)}\right] - E_{00} - \frac{e^2}{4\pi\varepsilon_0\varepsilon_S r_{DA}} - \frac{e^2}{8\pi\varepsilon_0}\left(\frac{1}{r_D} + \frac{1}{r_A}\right)\left(\frac{1}{\varepsilon_{ref}} - \frac{1}{\varepsilon_S}\right) \quad (4)$$

$$\Delta G_{CR} = -(\Delta G_{CS} + E_{00}) \quad (5)$$

where $E_{ox(D)}$ and $E_{red(A)}$ are the first oxidation and reduction potential of PBI, respectively, E_{00} is the excited state energy, r_{DA} is donor-acceptor center-to-center distance and r_D and r_A are the effective ionic radii, respectively. The dielectric constants of the spectroscopic solvent and of the solvent used in electrochemistry are given with ε_S and ε_{ref}.

Since dichloromethane has been used in both, spectroscopy and cyclic voltammetry studies, the Born ionic solvation energy (final) term in the Weller equation (4) can be neglected. The oxidation and reduction potentials are 0.84 V and –1.15 V vs. Fc/Fc^+, the excited state energy calculated from the average value of absorption and emission maxima of **2PBI$_{(4\text{-}t\text{Bu})4}$** is 2.06 eV, and the 0.65 nm distance between the two PBI units in **2PBI$_{(4\text{-}t\text{Bu})4}$** is obtained from the DFT calculated structure (Figure 46a). Thus, the Gibbs free energy for the intramolecular charge separation and recombination in **2PBI$_{(4\text{-}t\text{Bu})4}$** is calculated to ΔG_{CS} = –0.32 eV and ΔG_{CR} = –1.74 eV, respectively, confirming that both electron transfer processes for charge separation and subsequent charge recombination are thermodynamically favorable.

3.3.2 Transient Absorption Spectroscopy of the Free Host 2PBI$_{(4\text{-}t\text{Bu})4}$

To elucidate the excited state dynamics in the PBI cyclophane **2PBI$_{(4\text{-}t\text{Bu})4}$** femtosecond (fs) and nanosecond (ns)TA studies were performed (Figure 52). The fsTA spectra (Figure 52a) show the ground state bleach (GSB) at 461, 543 and 583 nm and the stimulated emission (SE) at 611 and 664 nm as shoulders in the spectra. The excited singlet state ^{1}*PBI absorption (ESA) has a positive signal at 710 nm and the two characteristic strong maxima in the NIR region at 959 and 1035 nm. While the TA spectra and the high fluorescence quantum yield for ^{1}***1PBI$_{(4\text{-}t\text{Bu})4}$** indicate that it decays back to the ground state primarily by emission (Figure 104 in the appendix), the PBI cyclophane **2PBI$_{(4\text{-}t\text{Bu})4}$** shows very different excited state dynamics with a fast decay of the ^{1}*PBI state in 161 ± 4 ps to a new transient species. Here the SE and ESA signals fully disappear, while new bands arise in the visible region at 486 and 628 nm, in the NIR region at 797, 993 and 1100 nm and a broad feature at ~1220 nm. By comparison to the PBI radical cation and anion absorption spectra these bands can clearly be attributed to $PBI^{+\bullet}$ (486, 628, 1220 nm) and the $PBI^{-\bullet}$ (797, 993, 1100 nm).[112, 130b] From these

ultrafast transient dynamics data it can be concluded that photo-driven intramolecular SB-CS occurs in the PBI cyclophane with a high quantum yield.

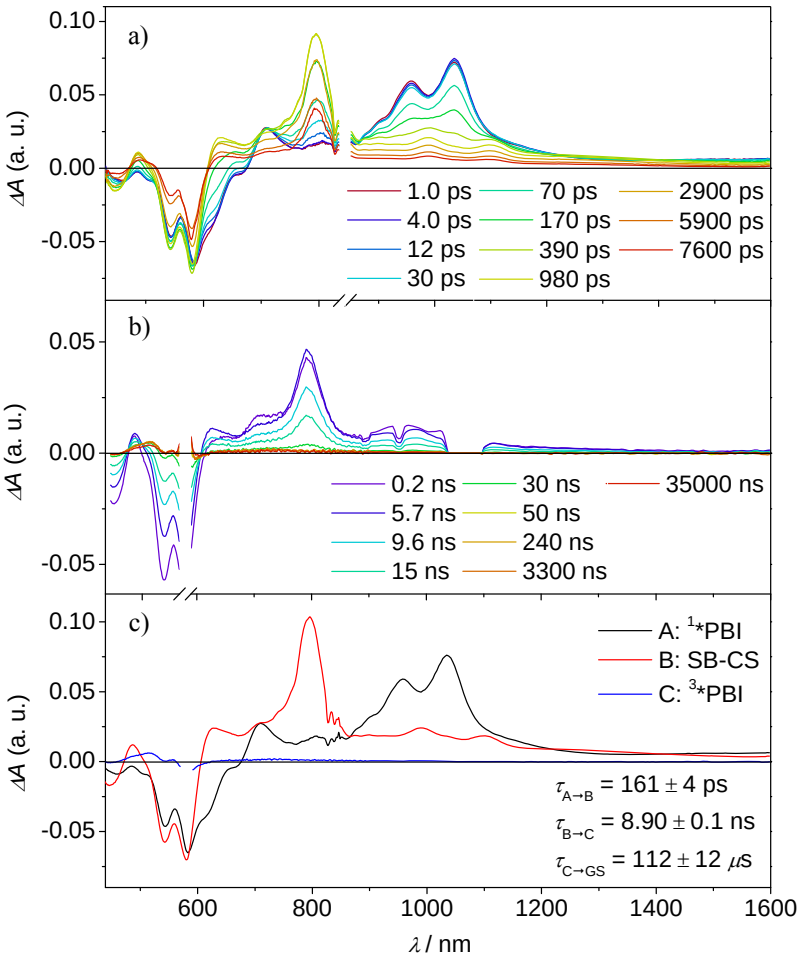

Figure 52. Femtosecond (a) and nanosecond (b) transient absorption spectra of **2PBI$_{(4\text{-}t\text{Bu})4}$** showing the excited state dynamics after photoexcitation. Species-associated spectra (c) reconstructed from global fits to the sequential A → B → C → ground state model, where A is ^{1}*PBI, B is SB-CS state and C is ^{3}*PBI (λ_{ex} = 580 nm, 1.0 μJ/pulse, dichloromethane, 298 K, degassed for nsTA). The C → ground state time was determined from nsTA.

Most interestingly and presumably caused by the long distance between the PBI moieties, CR between $PBI^{+\bullet}$ and $PBI^{-\bullet}$ in **2PBI$_{(4\text{-}t\text{Bu})4}$** occurs only slowly with 8.90 ± 0.06 ns to produce a significant yield of the PBI triplet state (^{3*}PBI) characterized by positive absorptions at 515 and 556 nm, a bleach at 579 nm and a weak positive and broad absorption at 734 nm (Figure 52b).[163]

3.3.3 Triplet Formation Mechanism

Spin-orbit coupling induced intersystem crossing (SO-ISC) is slow in PBIs, leading to very low triplet quantum yields for common PBIs (< 1%).[164] Thus, formation of $PBI^{+\bullet}$-$PBI^{-\bullet}$ is obviously a prerequisite for populating ^{3*}PBI, either by spin-orbit charge transfer intersystem crossing (SOCT-ISC) or by radical pair intersystem crossing (RP-ISC). The SOCT-ISC mechanism requires large changes in orbital angular momentum upon formation of $PBI^{+\bullet}$-$PBI^{-\bullet}$, which would require the π-systems of the two PBI molecules to be nearly orthogonal,[165] which is not the case in **2PBI$_{(4\text{-}t\text{Bu})4}$**. In contrast, the RP-ISC mechanism requires a relatively weak magnetic interaction between the two PBI radicals within $PBI^{+\bullet}$-$PBI^{-\bullet}$.[166] Photoexcitation of **2PBI$_{(4\text{-}t\text{Bu})4}$** produces $^1(PBI^{+\bullet}\text{-}PBI^{-\bullet})$, whose spin dynamics depend strongly on the isotropic spin-spin exchange interaction, $2J = E_S - E_T$, where E_S and E_T are the energies of $^1(PBI^{+\bullet}\text{-}PBI^{-\bullet})$ and $^3(PBI^{+\bullet}\text{-}PBI^{-\bullet})$, respectively.[167] Due to the long through-space and through-bond distances between the PBI subunits, $2J$ for $PBI^{+\bullet}$-$PBI^{-\bullet}$ should be small enough to enable RP-ISC of $^1(PBI^{+\bullet}\text{-}PBI^{-\bullet})$ to $^3(PBI^{+\bullet}\text{-}PBI^{-\bullet})$.[166] Moreover, since $2J \propto V^2$,[167] and $k_{ET} \propto V^2$ (equation 6), the relatively long 8.90 ns CR time is also consistent with a small value of $2J$. The subsequent CR process is spin selective in that $^1(PBI^{+\bullet}\text{-}PBI^{-\bullet})$ recombines back to the singlet ground state, whereas $^3(PBI^{+\bullet}\text{-}PBI^{-\bullet})$ recombines to ^{3*}PBI within **2PBI$_{(4\text{-}t\text{Bu})4}$**.[168] The experimental findings thus indicate that RP-ISC is the most likely mechanism producing ^{3*}PBI within **2PBI$_{(4\text{-}t\text{Bu})4}$**. Unfortunately, the 8.90 ns $PBI^{+\bullet}$-$PBI^{-\bullet}$ lifetime is too short to observe this RP directly by time-resolved EPR spectroscopy.

The lifetime of ^{3*}PBI within **2PBI$_{(4\text{-}t\text{Bu})4}$** is very long ($\tau \geq 112$ μs) in a degassed solution at room temperature. Isolating **2PBI$_{(4\text{-}t\text{Bu})4}$** in a glassy solvent matrix is necessary to prohibit quenching by diffusion; however, this also prohibits the SB-CS process and thus, the intrinsic triplet lifetime could not be investigated. To estimate the quantum yield for the triplet formation, singlet oxygen emission was measured and compared to that of a methylene blue standard (MB).[169] From this experiment, the singlet oxygen quantum yield is determined to $\Phi_\Delta = 0.27$, which also serves as the lower limit of the ^{3*}PBI yield and is consistent with the weak triplet signal in the TA spectra (Figure 52c). This result and the low fluorescence quantum yield indicate that the main pathway back to the ground state is by singlet RP recombination. Furthermore, no photobleaching of **2PBI$_{(4\text{-}t\text{Bu})4}$** with singlet oxygen was observed, verifying the great photostability of PBIs against oxidation. The SB-CS process is disfavored in non-polar solvents such as toluene

as evidenced by the increase in **2PBI$_{(4\text{-}t\text{Bu})4}$** fluorescence quantum yield to 64%.[170] Consistent with the increased emission, the transient absorption spectra of **2PBI$_{(4\text{-}t\text{Bu})4}$** in toluene show only singlet excited state decay directly back to the GS in $\tau = 4.5 \pm 0.6$ ns without the population of other transient species (Figure 105 in the appendix).

3.3.4 Transient Absorption Spectroscopy of the Host-Guest Complexes

By adding electron-rich guests, such as carbazole, pyrene, anthracene, and perylene to **2PBI$_{(4\text{-}t\text{Bu})4}$**, host-guest complexes are formed, leading to a slight bathochromic shift of the **2PBI$_{(4\text{-}t\text{Bu})4}$** absorption maximum and the appearance of a new band at longer wavelength that can be attributed to a charge transfer transition. Furthermore, the PBI fluorescence is almost fully quenched in the presence of these guests (chapter 3.2). The oxidation potentials of carbazole, pyrene, anthracene, and perylene are 0.64,[171] 0.91,[172] 0.88,[173] and 0.59 V[174] vs. Fc/Fc$^+$, respectively. Using these data in equations (4) and (5), and the calculated 0.35 nm PBI-guest distance in the complex, we calculate $\Delta G_{CS} = -0.73$, –0.46, –0.49 and –0.78 eV, respectively, and $\Delta G_{CR} = -1.33$, –1.60, –1.57 and –1.28 eV for the host-guest complexes (guest@**2PBI$_{(4\text{-}t\text{Bu})4}$**), which clearly show that the electron transfer processes in the complexes are highly favored thermodynamically.
In the fsTA spectra, ultrafast CS components of $\tau_{CS} = 6.7 \pm 0.2$, 3.6 ± 0.3, 1.1 ± 0.2 and 0.9 ± 0.1 ps were observed for **2PBI$_{(4\text{-}t\text{Bu})4}$** complexed with carbazole, pyrene, anthracene and perylene, respectively (Figure 53 and Figure 106 – Figure 108 in the appendix). The fsTA spectra of the perylene@**2PBI$_{(4\text{-}t\text{Bu})4}$** complex in Figure 53 show the PBI$^{-\bullet}$ absorptions along with a strong positive absorption at 542 nm that can be attributed to perylene$^{+\bullet}$.[175] The radical cation features of the other hydrocarbons are much weaker in the observed spectral window and strongly overlap with the GSB and PBI$^{-\bullet}$ absorption changes, and were thus not observed. However, no PBI$^{+\bullet}$ bands were detected, confirming that the CS now takes place between **2PBI$_{(4\text{-}t\text{Bu})4}$** and the guest molecule alone.

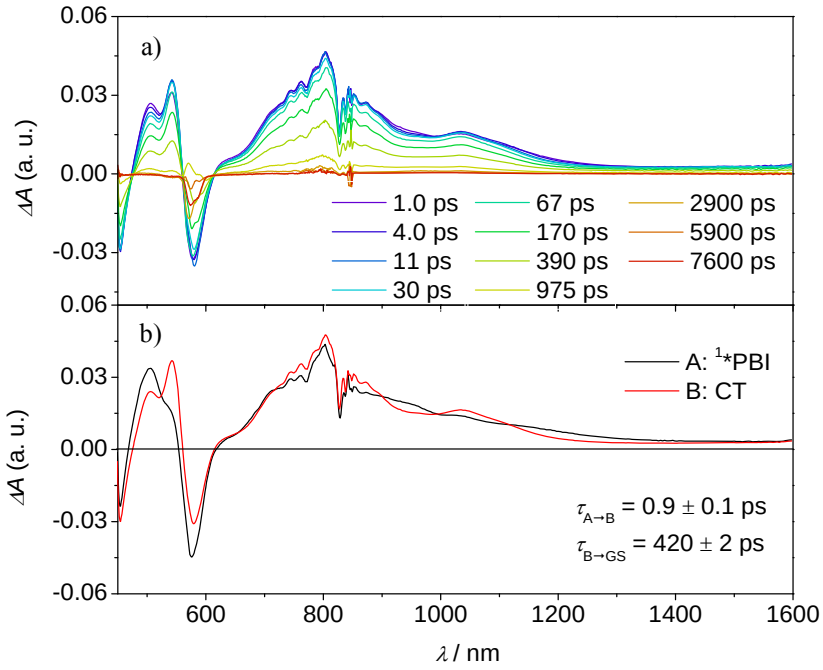

Figure 53. Femtosecond (a) transient absorption spectra of the perylene@**2PBI$_{(4\text{-}t\text{Bu})4}$** complex showing the excited state dynamics after photoexcitation. Species-associated spectrum (b) reconstructed from global fits to the sequential A → B → ground state (GS) model, where A is ^{1}*PBI and B is CT state (λ_{ex} = 580 nm, 1.0 μJ/pulse, dichloromethane, 298 K, air equilibrated).

The ultrafast charge separation processes in the complexes are close to our detection limit (~200 fs); thus the spectra of ^{1}*PBI are difficult to observe for the perylene and anthracene complexes, but are clearer for pyrene and carbazole. The second time constant gives the CR lifetime directly back to the GS of PBI without any indication of triplet formation. This is consistent with a large 2J in the guest$^{+\bullet}$-PBI$^{-\bullet}$ RP, which precludes RP-ISC. The corresponding CR times using the carbazole, pyrene, anthracene and perylene guests are τ_{CR} = 892 ± 46, 593 ± 42, 1140 ± 120 to 420 ± 2 ps, respectively.

The data show that the CS rate increases with increasing ΔG_{CS} for ET from the HOMO of the respective electron-donating guest to the photo-excited electron-accepting PBI. Using τ_{CS} and τ_{CR} obtained from the transient absorption kinetics and the corresponding values of ΔG_{CS} and ΔG_{CR}, the total reorganization energy $\lambda = \lambda_S + \lambda_I$, where λ_S and λ_I are the solvent and internal reorganization energies, respectively, and the electronic coupling matrix element V can be calculated according to Marcus theory by applying equation (6):[159b]

$$k_{ET} = \sqrt{\left(\frac{4\pi^3}{h^2 \lambda k_B T}\right)} V^2 \exp\left[-\frac{(\Delta G_{ET} + \lambda)^2}{4\lambda k_B T}\right] \qquad (6)$$

where k_{ET} is the electron transfer rate constant calculated from the transient absorption spectra, and ΔG_{ET} is the Gibbs free energy for charge separation or recombination. Given that the difference in λ between the GS and the excited singlet state for rigid aromatic molecules like PBI is very small, a single curve is drawn through both the CS and CR data, even though, strictly speaking, they represent two different reactions: 1) excited singlet state → RP and 2) RP → GS (Figure 54). The experimental data of k_{ET} were fitted by equation (6), giving a reorganization energy $\lambda = 0.75$ eV and an electronic coupling matrix element $V = 15$ cm^{-1}. The relatively high value of λ is consistent with a large λ_S resulting from reorientation of polar CH_2Cl_2 in response to the formation or decay of the RP charges.[158c] Furthermore, the data show that the CS lies in the Marcus normal region and reaches the peak of the Marcus parabola for the perylene@**2PBI$_{(4\text{-}t\text{Bu})4}$** complex, where $-\Delta G_{ET} \cong \lambda$. In contrast, the CR lies far in the Marcus inverted region, where the ET rates decrease with increasing free energy changes. The slow recombination observed in the Marcus inverted region is in general considered advantageous because long-lived charge separated states offer the possibility to utilize their stored energy for desired purposes such as artificial photosynthesis.[42, 156, 158a, 158c, 158e-g]

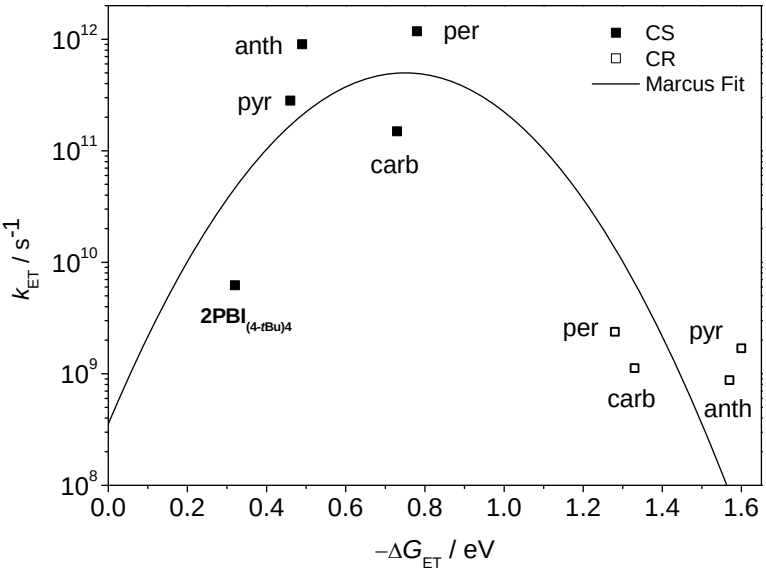

Figure 54. Plot of electron transfer rate constants in the PBI cyclophane **2PBI$_{(4\text{-}t\text{Bu})4}$** and the corresponding host-guest complexes vs. the thermodynamic driving force ($-\Delta G_{ET}$) for charge separation (solid squares) and charge recombination (open squares); the line represents the fit according to equation (6) with $\lambda = 0.75$ eV and $V = 15$ cm^{-1}.

In summary, it could be shown that the PBI cyclophane **2PBI$_{(4\text{-}t\text{Bu})4}$** undergoes intramolecular symmetry-breaking charge separation and slow charge recombination, which is accompanied by RP-ISC leading to ^{3}*PBI that can be used to generate singlet oxygen with a 27% quantum yield (Figure 55).

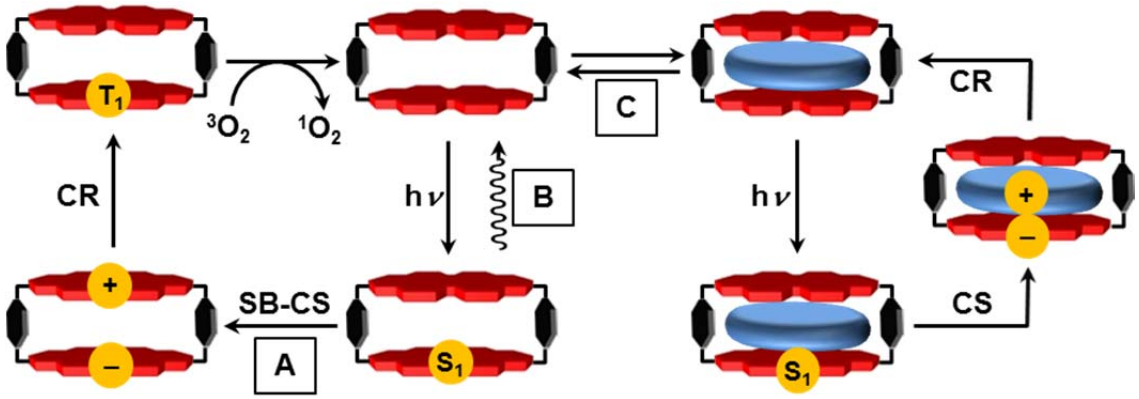

Figure 55. Schematic illustration of the different excited state photophysics upon excitation; A: symmetry-breaking charge separation and recombination to the PBI triplet within the PBI cyclophane **2PBI$_{(4\text{-}t\text{Bu})4}$** in dichloromethane that can be used for singlet oxygen generation and oxidation reactions; B: emission in toluene; C: encapsulation of aromatic guests and charge separation between guest and **2PBI$_{(4\text{-}t\text{Bu})4}$** and charge recombination to the ground state.

Since ^{3}*PBI is not accessible by conventional SO-ISC,[176] the RP-ISC pathway to ^{3}*PBI offers the possibility of developing an entirely new set of PBI applications, as demonstrated here with singlet oxygen generation. In contrast, the CS reaction within **2PBI$_{(4\text{-}t\text{Bu})4}$** is endergonic in a non-polar solvent like toluene, resulting in a high fluorescence quantum yield. Binding electron-rich guest molecules within the **2PBI$_{(4\text{-}t\text{Bu})4}$** host affords a complete change of the photoexcited state relaxation pathway leading to intermolecular charge separation within a few picoseconds with formation of the radical cation of the guest and the PBI radical anion. These findings show that the PBI cyclophane **2PBI$_{(4\text{-}t\text{Bu})4}$** is indeed a special dye pair whose excited state properties are effectively modulated by its solvent environment as well as host-guest complex formation with electron donors.

3.4 "Self-encapsulation" of Side Arms in Perylene Bisimide Cyclophanes

As described in chapter 3.2 the tetrasubstitution pattern of the PBI units in the cyclophane **2PBI$_{(4\text{-}t\text{Bu})4}$** induce a rather strong core twist of the π-skeleton of ~25°, which markedly influence the binding of planar aromatic hydrocarbons. Accordingly, complexation of rather stiff molecules like pyrene, which resist distortion into the twisted conformations, occurs with a much lower binding constant than that of flexible ones (see chapter 3.2). Therefore, a new class of perylene bisimide cyclophanes **2PBI$_{(2,6\text{-}i\text{Pr})2}$** and **2PBI$_{(2,6\text{-Ph})2}$** was synthesized in which tweezer-like bay-substituents were introduced. These side groups should planarize the PBI scaffold and with that the hole cavity.[145-146] Furthermore, this new bay-substituents may point inside the void and are according to molecular modelling somewhat "self-encapsulated", changing the available space for guest molecules in the cavity. With these features, the side groups have a significant influence on the binding of aromatic hydrocarbons.

3.4.1 NMR and Optical Spectroscopy

In the cyclisation reaction to the corresponding cyclophanes of the disubstituted PBIs two different isomers can in principle be formed in which the bay-substituents are either on the same side (cisoid) or on opposite side (transoid) with respect to each other.[30c] This was observed for both derivatives **2PBI$_{(2,6\text{-}i\text{Pr})2}$** and **2PBI$_{(2,6\text{-Ph})2}$** resulting in two sets of signals in the ^{1}H-NMR spectra for the particular isomers in ratios of 4:1 and 12:1, respectively. Similar to literature known derivatives these isomers could not be separated by standard chromatographic methods.[30c] From 2D-ROESY NMR the individual proton signals can be assigned to the corresponding isomer. Here, a cross signal between PBI core protons of the two chromophores can be seen for the transoid derivative due to spatial proximity, which is not given in the cisoid form (Figure 56).

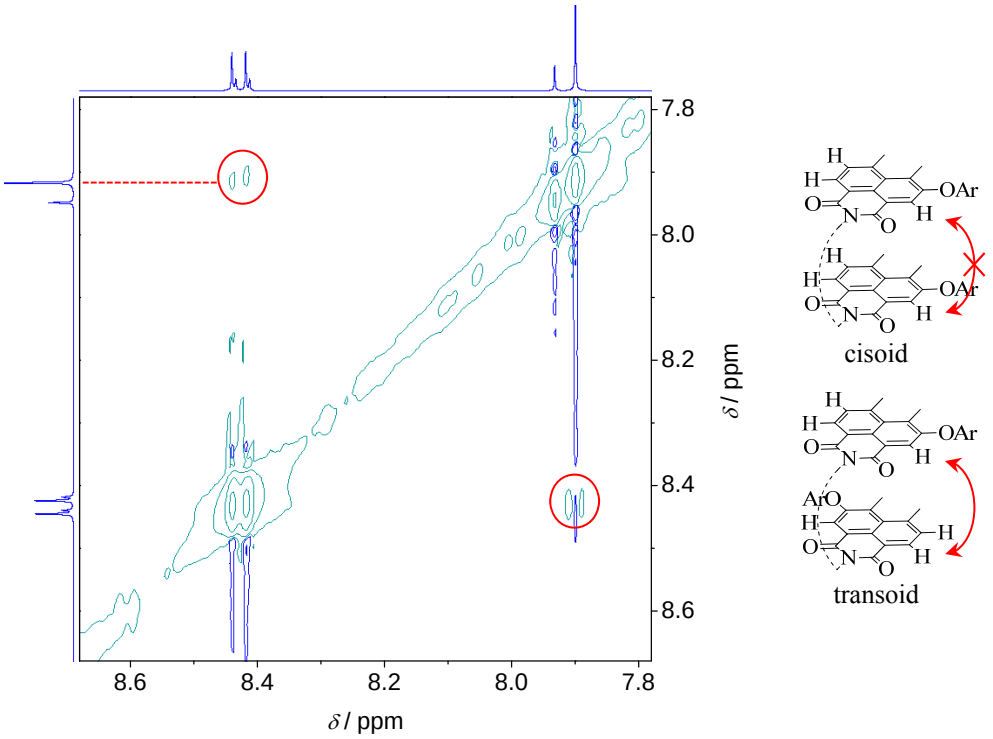

Figure 56. 2D-ROESY NMR spectrum of **2PBI$_{(2,6\text{-}i\text{Pr})2}$** in $CDCl_3$ (400 MHz); red circles and molecule substructures indicate the cross signal observed in the transoid isomer.

According to this, the transoid isomer is the favored conformation, which might be rationalized by a sterical congestion of the bulky substituents in the cisoid arrangement. This also explains why such different ratios are present for **2PBI$_{(2,6\text{-}i\text{Pr})2}$** and **2PBI$_{(2,6\text{-Ph})2}$**. Thus, increasing the size of the bay-substituents from *iso*-propyl to phenyl, the sterically hindrance is enhanced. While in the monomeric compounds **1PBI$_{(2,6\text{-}i\text{Pr})2}$** and **1PBI$_{(2,6\text{-Ph})2}$** the protons of the individual side groups are chemically equivalent, they get distinguishable in the corresponding cyclophanes, since parts of this tweezer-like groups are pointing inside the cavity. Thus, the *iso*-propyl units split up from two doublets in the monomer to 2 x 4 doublets in the cyclophane distinguishing between each methyl unit inside and outside the cavity and between both isomers. From 2D-COSY NMR spectroscopy each proton of the individual *iso*-propyl groups can be identified (Figure 57). However, with the small proton shifts and similar cross signals in the 2D-ROESY NMR spectra it cannot be clarified, which groups are inside or outside the cavity in **2PBI$_{(2,6\text{-}i\text{Pr})2}$**.

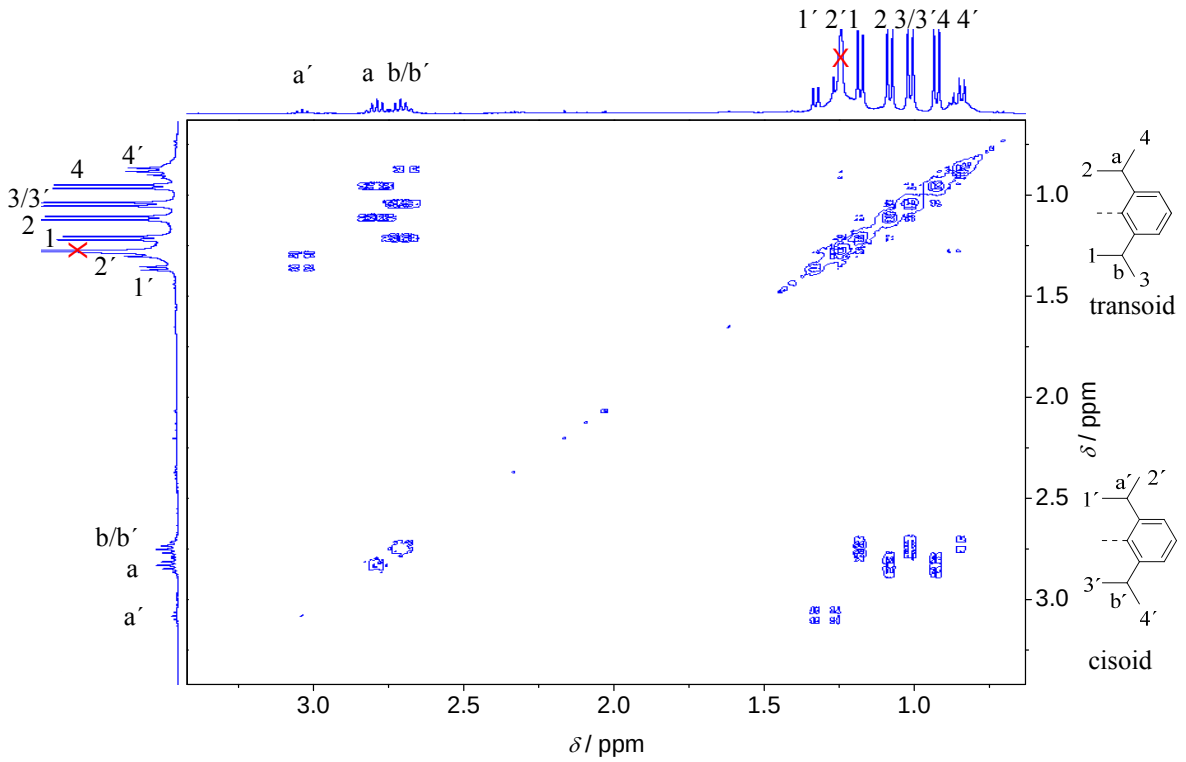

Figure 57. 2D-COSY NMR spectrum of **2PBI$_{(2,6\text{-}i\text{Pr})2}$** in $CDCl_3$ (400 MHz) with assignment of the single protons of the *iso*-propyl groups in the individual isomers.

In the phenyl derivative the aromatic substituents are not only pointing inside the cavity, but are indeed "self-encapsulated" through weak π-π interactions with the PBI cores. Thus, they experience a strong upfield shift of 0.48 (proton b) and 0.73 ppm (proton a) in the ^{1}H-NMR spectrum with respect to the protons of the phenyl groups on the outside of the cyclophane due to shielding effects inside the cavity (Figure 58). Although molecular modelling suggests that the void is only accessible for two phenyl groups of the substituents at the same time (Figure 59b), ^{1}H-NMR signal integration indicates the incorporation of all four aromatic subunits. Furthermore, the proton signals are quite broad at room temperature, which is indicative for a fast in-out exchange. Thus, temperature dependent ^{1}H-NMR studies were performed showing a stronger broadening at higher temperature and a clear sharpening upon cooling, which can be explained by a decelerated motion of the bay-substituents (Figure 58). Furthermore, the protons a and b of the "self-encapsulated" groups are slightly downfield shifted by 0.13 ppm with decreasing temperature. Additionally, the protons c/c´ and d/d´ become distinguishable at low temperature. Interestingly, also at 245 K the spectrum suggests the encapsulation of all four side arms, which might be indicative for a different conformational preference from the one obtained by force field calculations.

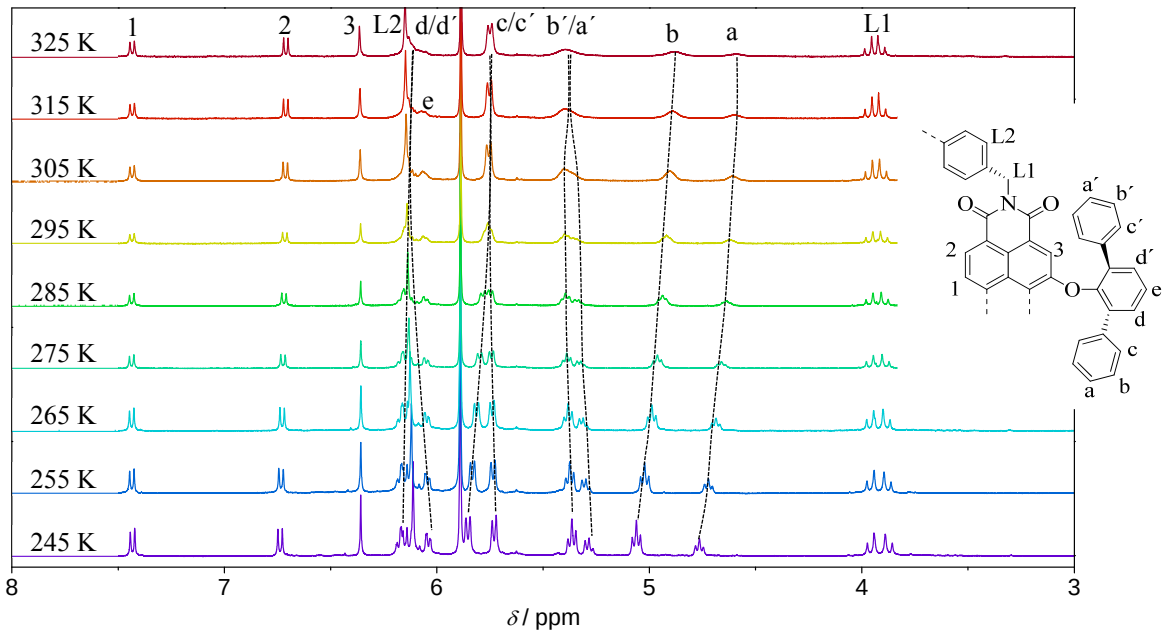

Figure 58. Temperature dependent ^{1}H-NMR spectra of **2PBI$_{(2,6\text{-Ph})2}$** from 325 K (red line) to 245 K (blue line) in steps of 10 K with assignment of the single protons of the individual phenyl groups; $CDCl_3$, 400 MHz.

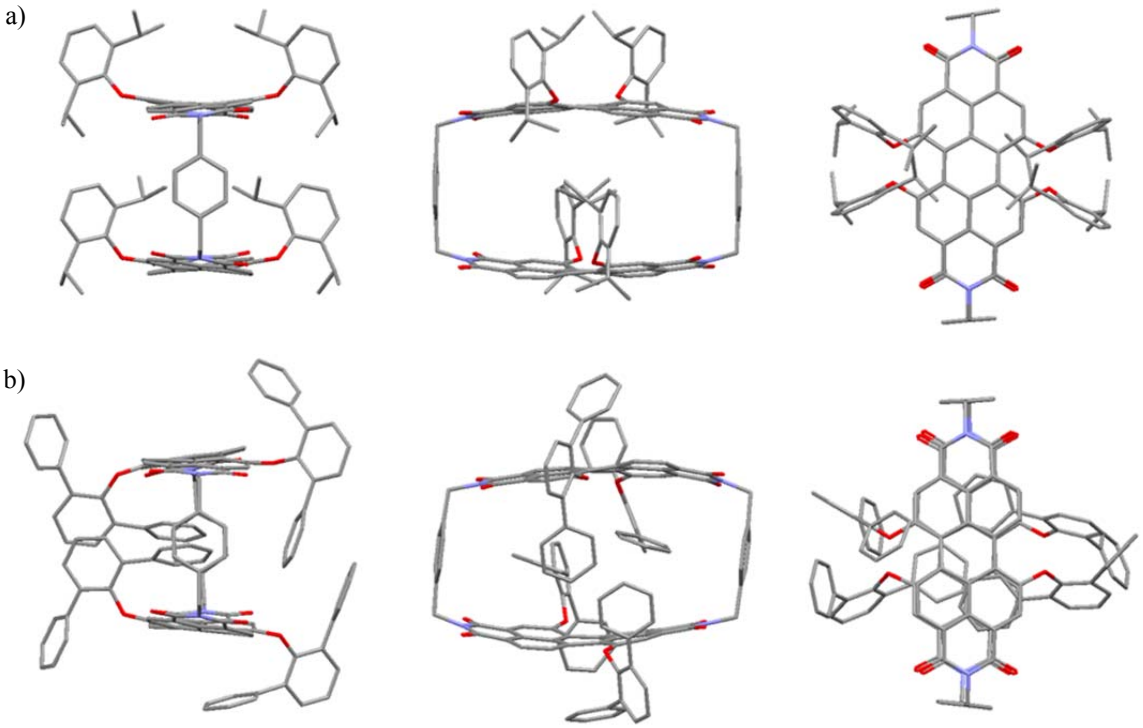

Figure 59. Geometry optimized structures of the PBI cyclophane **2PBI$_{(2,6\text{-}i\text{Pr})2}$** (a) and **2PBI$_{(2,6\text{-Ph})2}$** (b) in the front- (left), side- (middle) and top-view (right) obtained by force field optimization; Maestro 9.3, MacroModel 9.8, MM2*.

The conformational restrictions imparted in **2PBI$_{(2,6\text{-}i\text{Pr})2}$** and **2PBI$_{(2,6\text{-Ph})2}$** lead also to a sharpening of the absorption bands compared to **2PBI$_{(4\text{-}t\text{Bu})4}$** with a clear vibronic pattern. Along with the sharpening of the absorption band the extinction coefficients of **2PBI$_{(2,6\text{-}i\text{Pr})2}$** and **2PBI$_{(2,6\text{-Ph})2}$** are increased to 93000 and 95000 M^{-1} cm^{-1} with maxima at 557 and 563 nm compared to the tetra-substituted cyclophane **2PBI$_{(4\text{-}t\text{Bu})4}$** with 54000 M^{-1} cm^{-1} (λ_{max} = 585 nm). For all PBI cyclophanes **2PBI** the 0-1 transition band is more pronounced than in the corresponding monomeric reference compounds **1PBI**, which indicates an excitonic coupling of the PBI units, which is typical for cofacially arranged PBI systems (Figure 60).[148]

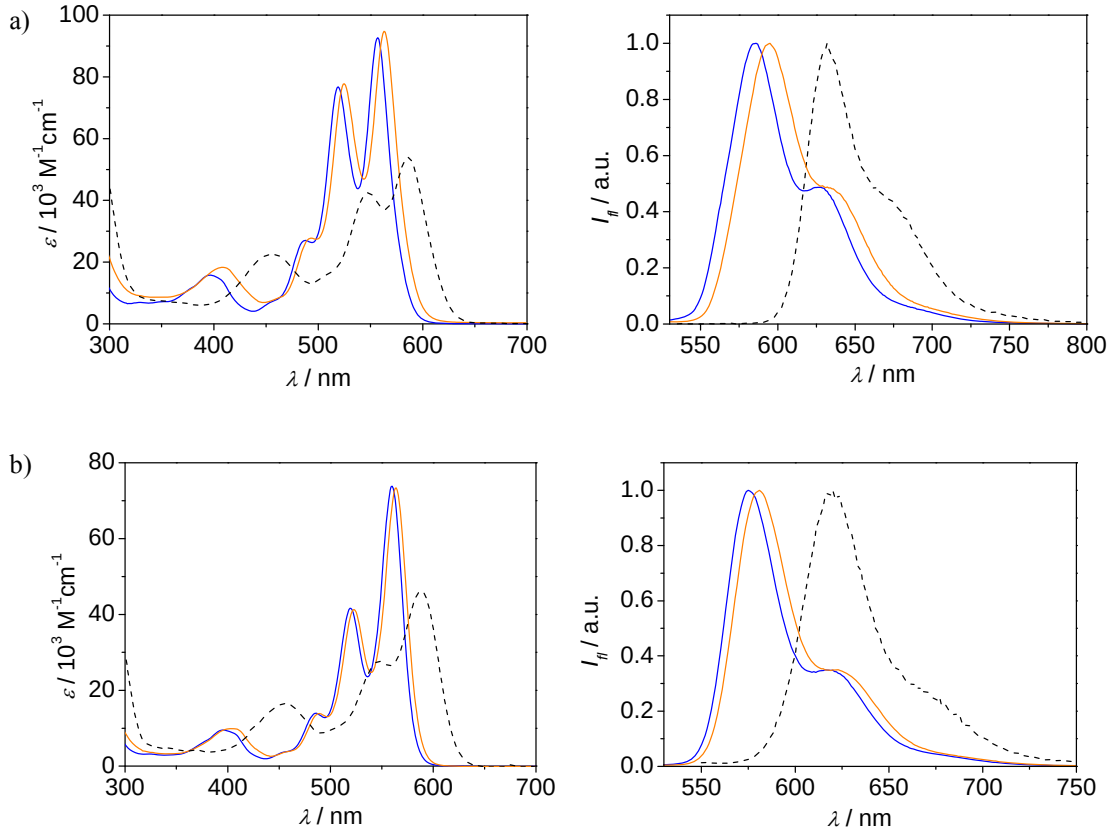

Figure 60. UV-vis (left) and normalized fluorescence spectra (right) of the cyclophanes **2PBI** (a) and the monomeric PBIs **1PBI** (b) in chloroform; **nPBI$_{(4\text{-}t\text{Bu})4}$**: black dotted line; **nPBI$_{(2,6\text{-}i\text{Pr})2}$**: blue line; **nPBI$_{(2,6\text{-Ph})2}$**: orange line; c = 5 x 10^{-5} M.

The fluorescence spectra are the mirror images of the vibronic patterns of the absorbance with their maxima at 584, 594 and 632 nm for **2PBI$_{(2,6\text{-}i\text{Pr})2}$**, **2PBI$_{(2,6\text{-Ph})2}$** and **2PBI$_{(4\text{-}t\text{Bu})4}$**, respectively. Whereas the Stokes´ shifts of **1PBI$_{(4\text{-}t\text{Bu})4}$** and **2PBI$_{(4\text{-}t\text{Bu})4}$** are in the same range with 944 and 1092 cm^{-1}, the monomers **1PBI$_{(2,6\text{-}i\text{Pr})2}$** and **1PBI$_{(2,6\text{-Ph})2}$** show remarkable small Stokes´ shifts of 496 and 489 cm^{-1}. However, this is nearly doubled in

the corresponding cyclophanes **2PBI$_{(2,6\text{-}i\text{Pr})2}$** and **2PBI$_{(2,6\text{-Ph})2}$** to 830 and 927 cm^{-1}. As discussed in chapter 3.2 the encapsulation of electron-poor guests hinders the electronic interaction between the two PBI units and thus increases the fluorescence quantum yield up to 100%. This effect can also be seen for the "self-encapsulation" of the bay-substituents leading to fluorescence quantum yields of 97% and 99% in chloroform for **2PBI$_{(2,6\text{-}i\text{Pr})2}$** and **2PBI$_{(2,6\text{-Ph})2}$**, whereas the cyclophane **2PBI$_{(4\text{-}t\text{Bu})4}$** has a low quantum yield of 21%.

3.4.2 Host-Guest Studies

Due to the high fluorescence quantum yields of the cyclophanes **2PBI$_{(2,6\text{-}i\text{Pr})2}$** and **2PBI$_{(2,6\text{-Ph})2}$** only the encapsulation of the electron-rich guest molecules carbazole, anthracene, pyrene and perylene was studied.

To exclude an isomer effect on the binding strength a ^{1}H-NMR titration experiment of perylene to **2PBI$_{(2,6\text{-}i\text{Pr})2}$** was performed. Due to the strong binding the in-out guest exchange process is slower than the NMR timescale, which leads to a separation of the protons of free host and of the corresponding host-guest complex. This enables a direct measurement of the ratios between the cisoid and transoid cyclophane in the free host and its complex during the encapsulation process (Figure 61).

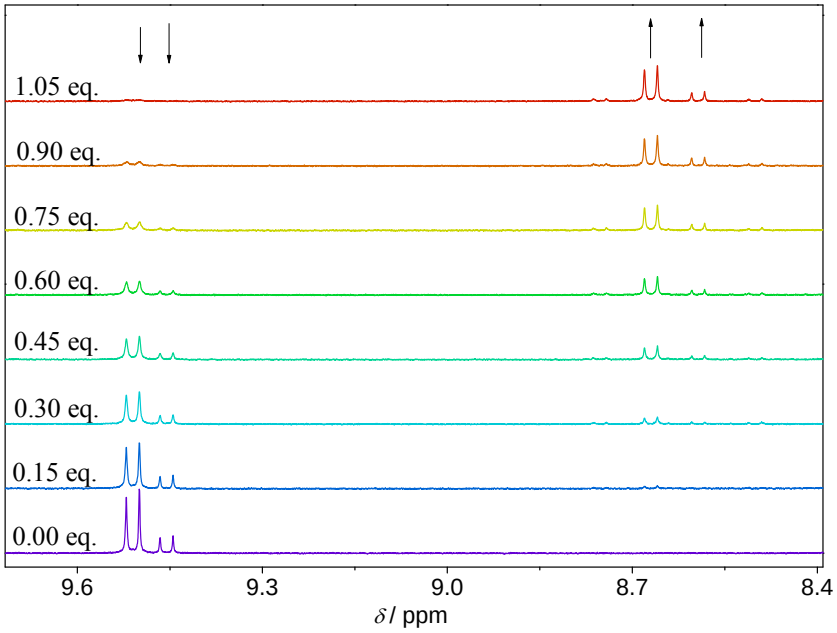

Figure 61. ^{1}H-NMR spectra of **2PBI$_{(2,6\text{-}i\text{Pr})2}$** in $CDCl_3$ (c = 1 x 10^{-3} M) with successive addition of perylene; arrows indicate the spectral changes upon increasing the amount of guest molecule.

In this experiment no changes in the isomer ratio were observed during any titration step and as the signals of the free host disappear, the signals for the complex appear in the same rate of 4:1, confirming that the binding strength for perylene is identical in both isomers. Furthermore, the PBI protons are upfield shifted up to 0.84 ppm with the complexation of perylene. The same can be seen for the intercalated guest molecules whose proton chemical shift values are displaced by 1.46–2.21 ppm due to strong shielding effects inside the cavity. 2D-NMR spectroscopic measurements confirm the predicted structure of the complex obtained by molecular modelling (Figure 62).

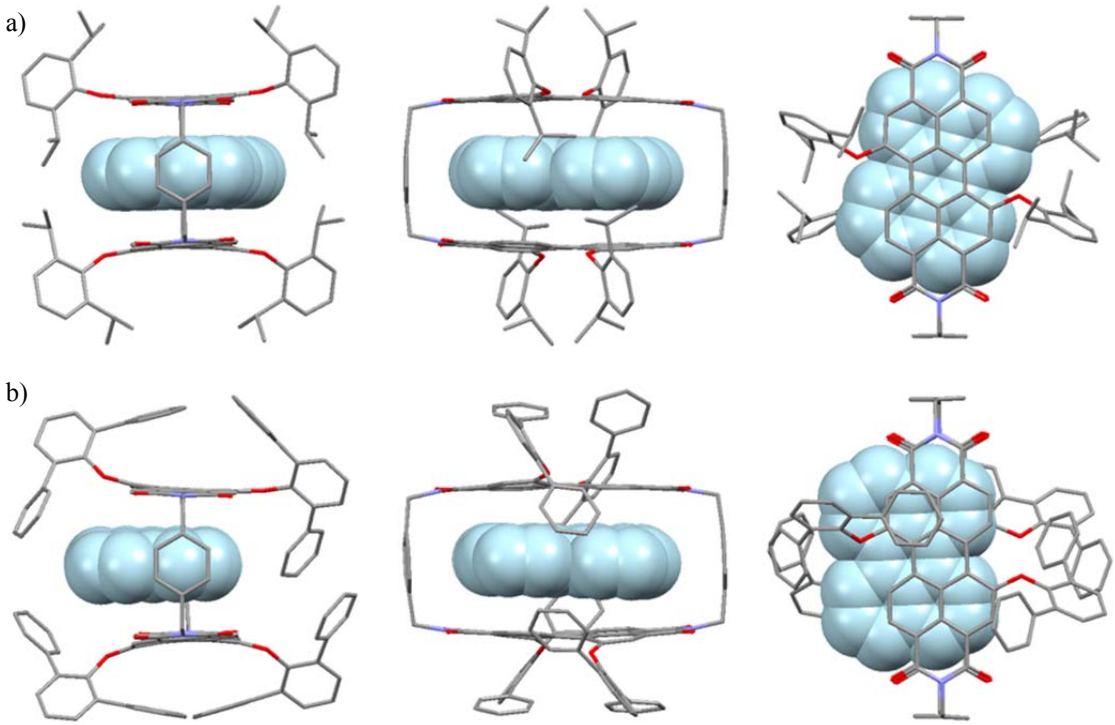

Figure 62. Geometry optimized structures of the complexes perylene@**2PBI**$_{(2,6\text{-}i\text{Pr})2}$ (a) and perylene@**2PBI**$_{(2,6\text{-Ph})2}$ (b) in the front- (left), side- (middle) and top-view (right) obtained by force field optimization; Maestro 9.3, MacroModel 9.8, $CHCl_3$, MM2*.

While for the free host the final assignment of the *iso*-propyl groups that are inside or outside the cavity was not possible, it is in the complex due to cross signals with the encapsulated guest (red circles in Figure 63). From the 2D-ROESY NMR spectrum it is obvious that not only the rotation of the whole 2,6-diisopropyl-phenoxy group is hindered but also the rotation of the individual *iso*-propyl groups themselves. Accordingly, each methyl unit of one isopropyl group has a cross signal to a different PBI core proton.

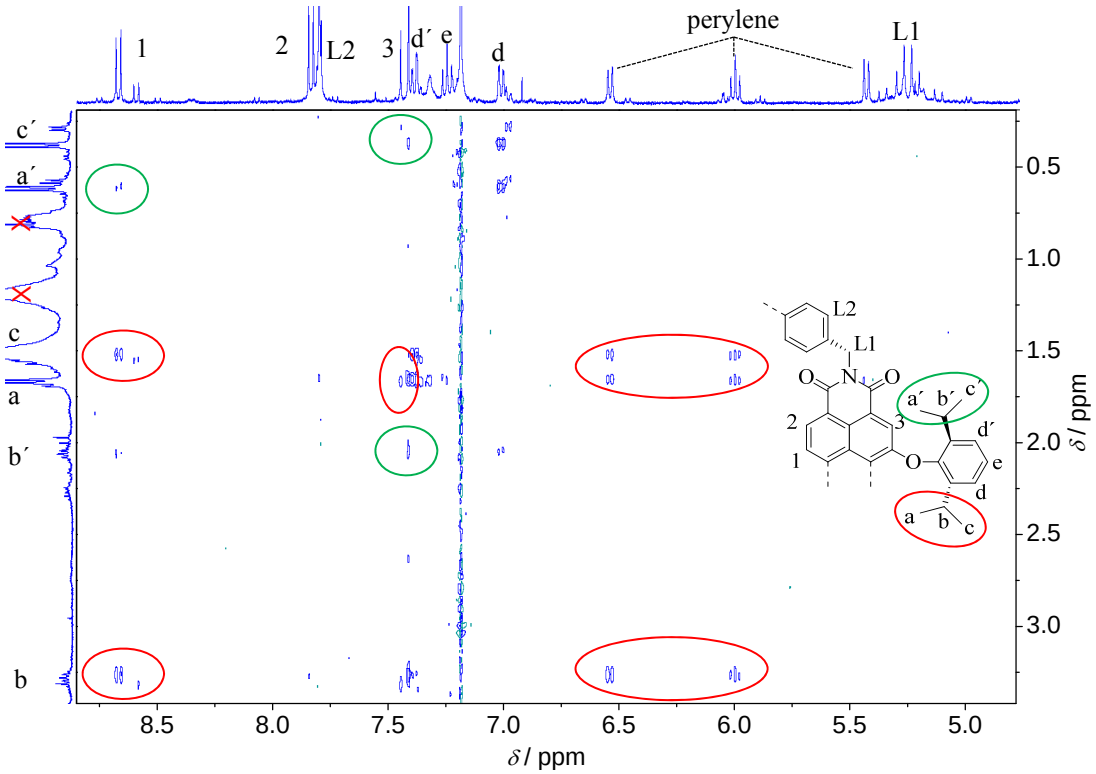

Figure 63. 2D-ROESY NMR spectrum of the perylene@**2PBI$_{(2,6\text{-}i\text{Pr})2}$** complex in $CDCl_3$ with highlighted cross signals and assignment of the *iso*-propyl groups pointing inside (red) and outside (green) the cavity, c(**2PBI$_{(2,6\text{-}i\text{Pr})2}$**) = 1 x 10^{-3} M.

In the formed complexes a charge transfer from the guest to the PBI chromophores takes place and the fluorescence gets quenched, which allows the determination of the binding constants by UV-vis absorption and fluorescence titration experiments (Figure 64 and Figure 109 – Figure 112 in the appendix). With the complexation of guest molecules a change in the PBI absorption bands is observed. In addition, a new band or shoulder arises at higher wavelengths that can be assigned as the charge transfer band. Several isosbestic points indicate the formation of defined host-guest complexes. With the formation of the charge transfer complexes the fluorescence of **2PBI$_{(2,6\text{-}Ph)2}$** gets completely quenched, whereas the complexes of **2PBI$_{(2,6\text{-}i\text{Pr})2}$** show weak CT emission with maxima at 611, 660 and 639 nm for carbazole, anthracene and pyrene, similar to the complexes of **2PBI$_{(4\text{-}t\text{Bu})4}$** as described in chapter 3.2. By plotting the inverse changes of the emission vs. the inverse guest concentration (Benesi-Hildebrand plot) the formation of 1:1 complexes in all host-guest systems is confirmed.

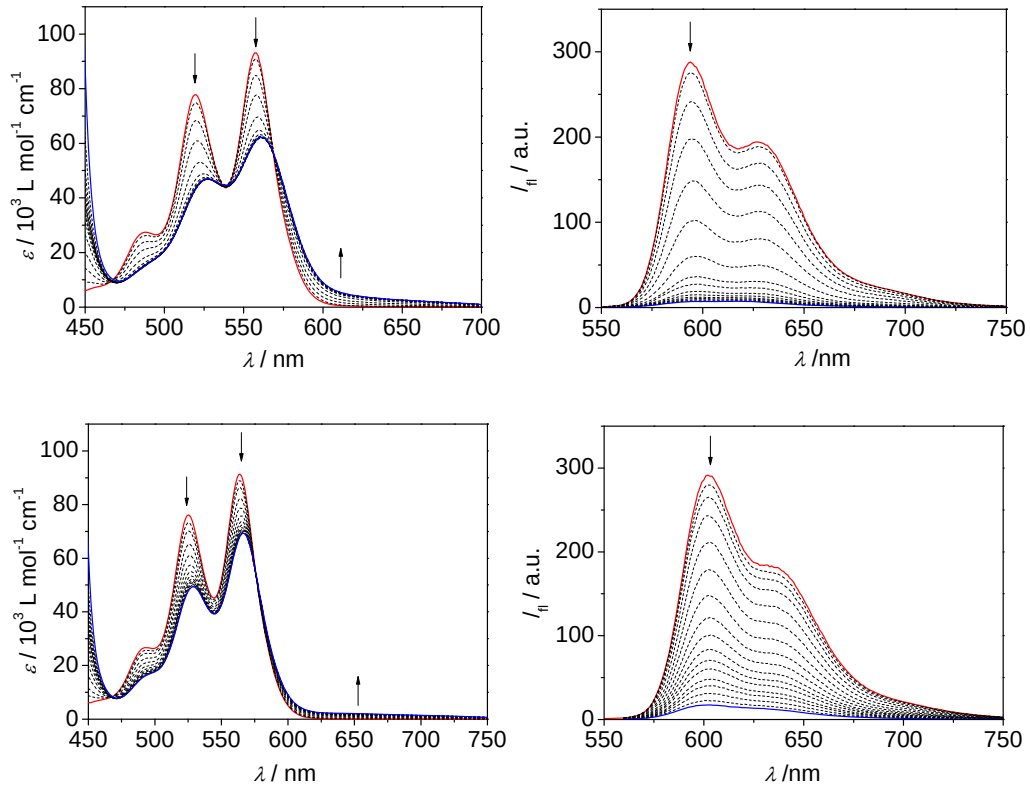

Figure 64. Changes in the UV-vis absorption (left) and emission spectra (right) of PBI cyclophane **2PBI$_{(2,6\text{-}i\text{Pr})2}$** (a) and **2PBI$_{(2,6\text{-Ph})2}$** (b) upon titration with perylene; c(**2PBI**) = 5.0 x 10^{-5} M in $CHCl_3$; red line: spectra before titration; blue line: spectra after the guest is completely added; arrows indicate spectral changes.

By comparing the respective binding strengths of the complexes with **2PBI$_{(2,6\text{-}i\text{Pr})2}$**, **2PBI$_{(2,6\text{-Ph})2}$** and those of the formerly discussed **2PBI$_{(4\text{-}t\text{Bu})4}$** the effects of the substituents and planarization of the PBI cores on the binding of aromatic guests can be seen (Table 2). With the introduction of *iso*-propyl groups in the 2,6-positions of the PBI bay-substituents the sterically hindrance inside the cavity is only slightly increased, but the PBI core is planarized and thus provides a planar cavity for effective π-π interactions with planar aromatic hydrocarbons. Because carbazole is too small to be affected by these factors it has similar binding strength in **2PBI$_{(2,6\text{-}i\text{Pr})2}$** as in the previously discussed **2PBI$_{(4\text{-}t\text{Bu})4}$** (chapter 3.2; K_a = 2.0 x 10^3 M^{-1}). By increasing the size of the guest to anthracene, pyrene and perylene the binding constant increases to 1.4 x 10^4, 7.0 x 10^4 and 1.6 x 10^6 M^{-1} due to the addition of interacting C=C double bonds in the guest molecules. While the strong PBI core twist in **2PBI$_{(4\text{-}t\text{Bu})4}$** effects especially the binding of the rigid pyrene and reduces the binding constant significantly, **2PBI$_{(2,6\text{-}i\text{Pr})2}$** provides with its planarized cavity an ideal environment for the binding of stiff molecules. Accordingly,

the encapsulation of pyrene occurs with a much higher binding constant than in **2PBI$_{(4\text{-}t\text{Bu})4}$** with a value that lies perfectly between anthracene and perylene and thus is as expected for its number of C=C bonds. With this, the planarity of the PBIs leads to an almost linear enhancement of the Gibbs free energy with the size of the intercalated molecule in **2PBI$_{(2,6\text{-}i\text{Pr})2}$**.

Table 2. Binding constants K_a [M^{-1}] and Gibbs free energies ΔG^0_{298} [kJ mol^{-1}] calculated from fluorescence data for the 1:1 complexes of aromatic hydrocarbons by PBI cyclophanes **2PBI$_{(2,6\text{-}i\text{Pr})2}$**, **2PBI$_{(2,6\text{-Ph})2}$** and **2PBI$_{(4\text{-}t\text{Bu})4}$** in $CHCl_3$; c(**2PBI**) = 5 x 10^{-5} M.

guest	host	K_a ($CHCl_3$)	R^2	$-\Delta G^0_{298}$
carbazole	**2PBI$_{(2,6\text{-}i\text{Pr})2}$**	(2.0 ± 0.9) x 10^3	0.998	18.8
	2PBI$_{(2,6\text{-Ph})2}$	449 ± 18	0.999	15.1
	2PBI$_{(4\text{-}t\text{Bu})4}$	944 ± 110	0.991	17.0
anthracene	**2PBI$_{(2,6\text{-}i\text{Pr})2}$**	(1.4 ± 0.1) x 10^4	0.994	23.7
	2PBI$_{(2,6\text{-Ph})2}$	(1.1 ± 0.03) x 10^3	0.999	17.4
	2PBI$_{(4\text{-}t\text{Bu})4}$	(9.9 ± 0.6) x 10^3	0.997	22.8
pyrene	**2PBI$_{(2,6\text{-}i\text{Pr})2}$**	(7.0 ± 0.2) x 10^4	0.999	27.7
	2PBI$_{(2,6\text{-Ph})2}$	278 ± 9.5	0.999	13.9
	2PBI$_{(4\text{-}t\text{Bu})4}$	114.2	0.999	11.7
perylene	**2PBI$_{(2,6\text{-}i\text{Pr})2}$**	(1.6 ± 0.5) x 10^6	0.998	35.4
	2PBI$_{(2,6\text{-Ph})2}$	(1.8 ± 0.3) x 10^5	0.996	29.9
	2PBI$_{(4\text{-}t\text{Bu})4}$	(4.6 ± 0.4) x 10^4	0.997	26.6

In the phenyl derivative **2PBI$_{(2,6\text{-Ph})2}$** the sterically hindrance inside the cavity is increased due to the large phenyl groups that are pointing into the void. This "self-encapsulation" by the aromatic side arms lowers indeed the binding constant for the complexation of carbazole, anthracene and perylene by about one order of magnitude, since the phenyl groups have to be replaced by the aromatic guests (Table 2).

Due to the bulkiness of the large bay substituents in **2PBI$_{(2,6\text{-Ph})2}$** the PBI cores still experience some twisting of ~7.8° (taken from calculated structure, Figure 62) that dramatically affects the complexation of pyrene and reduces its binding constant to 278 M^{-1}.

Assuming that the *iso*-propyl groups have no real interactions inside the cyclophane **2PBI$_{(2,6\text{-}i\text{Pr})2}$**, this cavity can be seen as formally empty, whereas **2PBI$_{(2,6\text{-Ph})2}$** is filled with the "self-encapsulated" bay-substituents. Thus, the binding strength of the phenyl

moieties can roughly be estimated to ΔG^0_{298}(Ph) = ΔG^0_{298}(**2PBI$_{(2,6\text{-}i\text{Pr})2}$**) – ΔG^0_{298}(**2PBI$_{(2,6\text{-}Ph)2}$**) = –5.2 kJ/mol, which is the average difference of the individual binding strengths of **2PBI$_{(2,6\text{-}i\text{Pr})2}$** and **2PBI$_{(2,6\text{-}Ph)2}$** to the aromatic guest molecules carbazole, anthracene and perylene.

To further analyze the "self-encapsulation" of the bay-substituent phenyl units host-guest complexation studies were performed in toluene (Figure 111 – Figure 112 and Table 7 in the appendix). Now, both voids are filled with the aromatic solvent molecules and thus, in both cases the solvent has to be replaced. For **2PBI$_{(2,6\text{-}Ph)2}$** there should not be a large difference replacing the phenyl units of the bay-substituents or of the solvent, and indeed there is nearly no solvent effect observed for the encapsulation of aromatic guests (Figure 65b). However, in the case of **2PBI$_{(2,6\text{-}i\text{Pr})2}$** a new competing molecule is introduced with the aromatic solvent that significantly lowers the binding strength of other aromatic guest molecules (Table 7 in the appendix). This competition can especially be seen for carbazole, pyrene and perylene that have a reduced Gibbs free energy by 4.2, 2.2 and 4.5 kJ/mol, which is close to the previously calculated binding strength of the bay-substituent phenyl subunits in chloroform (Figure 65a).

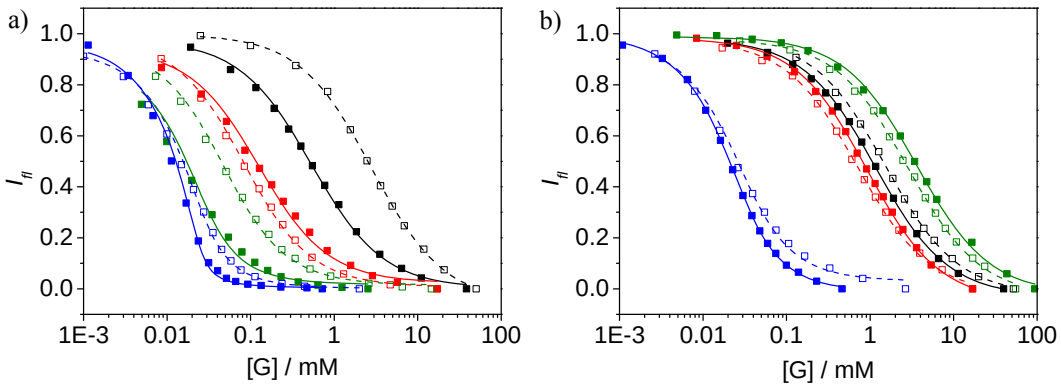

Figure 65. Plots of the fluorescence intensity upon titration of the individual guests to **2PBI$_{(2,6\text{-}i\text{Pr})2}$** (a) and **2PBI$_{(2,6\text{-}Ph)2}$** (b); least square fits in $CHCl_3$ (solid line) and toluene (dashed line); black: carbazole, red: anthracene; green: pyrene; blue: perylene; c(**2PBI**) = 5 x 10^{-5} M.

In summary, the synthesis of a new series of PBI cyclophanes was shown that can be used as "turn-off" fluorescence probes with very high binding constants of up to 1.6 x 10^6 M^{-1}. By using the tweezer-like substituents a "self-encapsulation" was observed that leads to a strong increase of the fluorescence quantum yields close to 100%. Furthermore, the twice substituted PBI cyclophanes **2PBI$_{(2,6\text{-}i\text{Pr})2}$** and **2PBI$_{(2,6\text{-}Ph)2}$** showed isomerization in which the side groups have a transoid or cisoid conformation in ratios of 4:1 and 12:1,

respectively. These were not separable but also do not differ in strength of binding guest molecules. By UV-vis absorption and fluorescence titration studies the formation of charge transfer complexes was proven that quenches the fluorescence. With comparison of the binding strengths the effect of sterics and the PBI core twist was analyzed showing that already a slight core twist of ~8° has a strong influence for rigid guest molecules, reducing their binding strength. Furthermore, the effect of "self-encapsulation" was studied by solvent variation that sugggests a binding energy for the bay-phenyl groups of ~5 kJ/mol.

3.5 Guest-mediated Chirality Transfer

One of the central topics in chemistry and biology is the chirality of molecules that can be used for chiral recognition,[177] enantioselective catalysis,[178] nonlinear optics[179] and molecular switches.[180] Especially drug research is strongly focused on chiral compounds since stereoisomers, particularly enantiomers of a molecule may show entirely different biological activities. Chirality has also some implication in technical applications, like photo- and electroluminescence devices for stereoimaging that typically contain chiral polymeric emitters or chiral dopants in nematic liquid crystals.[181] The most prominent chiral units for such applications are biphenyl,[182] binaphthyl[183] or helicenes and helicene-like compounds.[184] In most of these cases the required twisting of π-surfaces to impart chirality is achieved by attaching sterically demanding groups that hinder free rotation.[185] However, such twisted aromatic systems are often not conformationally stable and undergo dynamic racemization at a certain temperature. The activation energy for such dynamic processes can be tuned by changing the substituents that modulate the energy barrier for conformational interconversion.

The substitution of PBIs at bay-positions leads to such a twist of the perylene core, resulting in inherent conformational chirality (inset Figure 66). Depending on the number and size of the attached groups a torsion angle of 4–37° was reported for bay-substituted PBI chromophores. In general, the atropisomers created by such core-twisting undergo fast racemization at room temperature due to low barriers for the interconversion.[101a] Therefore, several strategies have been introduced to force the chromophores into a specific, stable conformation. Indeed, self-assembly of core-substituted PBI dyes bearing homochiral side chains showed an enrichment of one enantiomer in the helical assembly as evidenced by CD effects, indicating chirality transfer from side chains to the helical assembly.[186] Ionic self-assembly of PBI dyes containing homochiral counter ion groups leads to helical aggregates with single-handed helicity exhibiting chiral excitonic coupling of PBI chromophores in CD spectra, which is indicative of chirality transfer from the homochiral counter ion to the PBI molecule.[187] Another successful approach to achieve conformationally stable PBIs is the bridging of the bay-substituents with ethylene glycol chains to restrict the dynamic racemization, and hence the individual enantiomers could be resolved by chiral HPLC.[101b, 102, 188] Also multi-chromophoric cyclic PBI systems have been established in which chirality was observed by a decelerated racemization process[30b, 105] or by a solvent-induced chirality transfer.[30a]

In this chapter, a new strategy has been explored to induce chirality to a core-twisted PBI molecule (Figure 66). For this purpose, the encapsulation of homochiral guest molecules into the tetraphenoxy-substituted, core-twisted PBI cyclophane **2PBI$_{(4\text{-}t\text{Bu})4}$** bearing *para*-xylylene bridges was used to force the two PBI units into a specific conformation, forming host-guest complexes of homochiral PBI dimers (*M*,*M*) or (*P*,*P*), depending on the absolute configuration (*R*) or (*S*) of the guest molecule. In the cyclophane ***m*-2PBI$_{(4\text{-}t\text{Bu})4}$** that contains shorter *meta*-xylylene bridges, however, the encapsulation of guest molecules is not possible due to smaller PBI-PBI distance and thus guest-mediated chirality transfer was not observed. The guest encapsulation and chirality transfer properties of **2PBI$_{(4\text{-}t\text{Bu})4}$** have been investigated by UV-vis absorption, fluorescence, NMR and circular dichroism (CD) spectroscopy and further analyzed by molecular modelling.

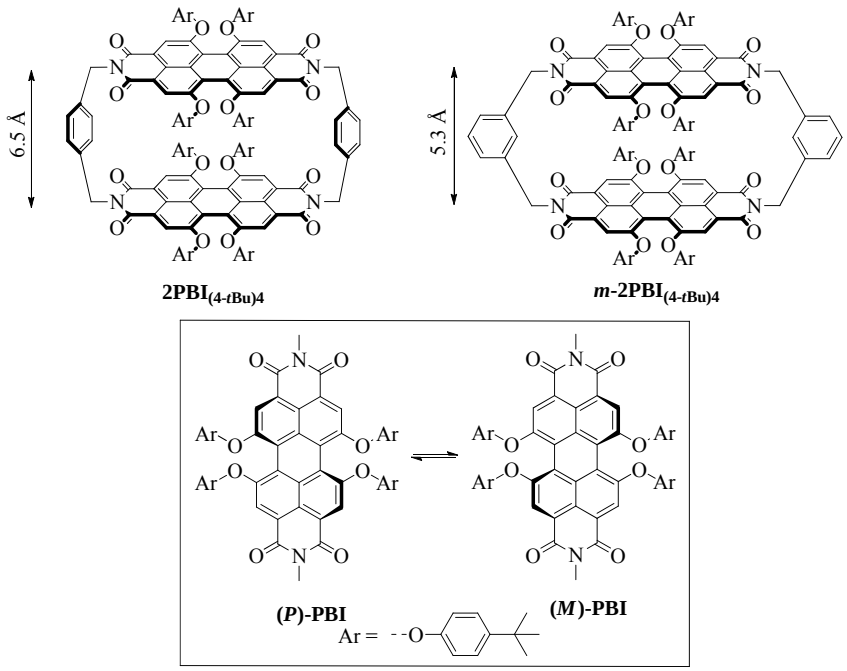

Figure 66. Chemical structures of the two cyclophanes **2PBI$_{(4\text{-}t\text{Bu})4}$** and ***m*-2PBI$_{(4\text{-}t\text{Bu})4}$** with different distances between the PBI subunits that lead to distinctive chiral recognition behavior by guest-mediated chirality transfer; inset: illustration of the interconversion of atropo-enantiomers (*P*)- and (*M*)-PBI.

3.5.1 UV-vis Absorption, Fluorescence and NMR Spectroscopy of PBI Cyclophanes

As described in chapter 3.2, the PBI cyclophane **2PBI$_{(4\text{-}t\text{Bu})4}$** shows in chloroform an enhanced 0-1 transition band in the absorption spectrum ($A_{0\text{-}0}/A_{0\text{-}1}$ = 1.25) with respect to the monomeric reference compound **1PBI$_{(4\text{-}t\text{Bu})4}$**, which is indicative of weak exciton

coupling between the PBI chromophores in this cyclophane (Figure 67a). The fluorescence is drastically quenched to a quantum yield of 21% compared to 97% of the monomeric reference **1PBI$_{(4\text{-}t\text{Bu})4}$**. The optical properties of cyclophane ***m*-2PBI$_{(4\text{-}t\text{Bu})4}$** differ slightly from those of **2PBI$_{(4\text{-}t\text{Bu})4}$** with a $A_{0\text{-}0}/A_{0\text{-}1}$ ratio of 1.12 and a fluorescence quantum yield of 9% in chloroform (Figure 67b). The smaller $A_{0\text{-}0}/A_{0\text{-}1}$ ratio and quantum yield reveal a bit stronger exciton coupling in ***m*-2PBI$_{(4\text{-}t\text{Bu})4}$** than in **2PBI$_{(4\text{-}t\text{Bu})4}$** caused by a closer contact between the PBI units of 5.3 Å (**2PBI$_{(4\text{-}t\text{Bu})4}$**: 6.5 Å, taken from calculated structures in Figure 67c,d).

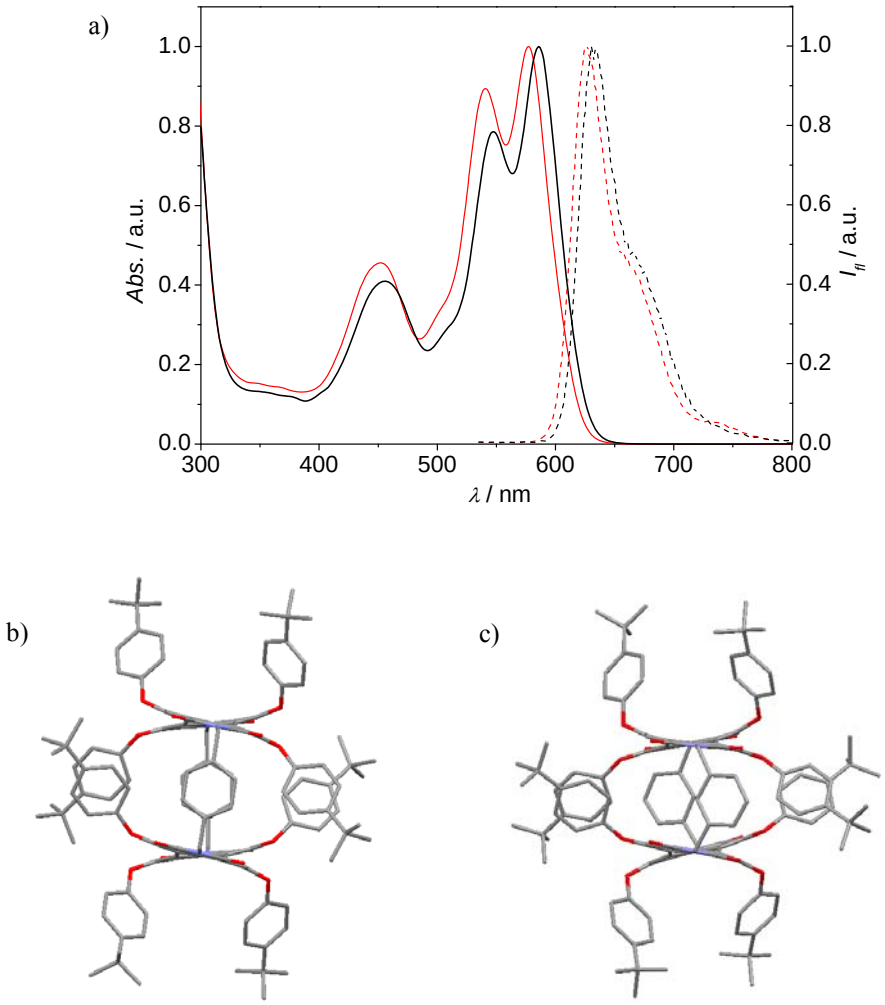

Figure 67. UV-vis absorption (solid line) and normalized emission spectra (dashed line) of **2PBI$_{(4\text{-}t\text{Bu})4}$** (black) and ***m*-2PBI$_{(4\text{-}t\text{Bu})4}$** (red) in $CHCl_3$, c = 5 x 10^{-5} M; 298 K; geometry optimized structures of the homochiral PBI cyclophanes **2PBI$_{(4\text{-}t\text{Bu})4}$** (b) and ***m*-2PBI$_{(4\text{-}t\text{Bu})4}$** (c) in the front-view obtained by force field optimization; Maestro 9.3, MacroModel 9.8, AMBER.

In the ^{1}H-NMR spectrum of ***m*-2PBI$_{(4\text{-}t\text{Bu})4}$** in chloroform at 298 K two sets of strongly separated signals are observed, particularly for the PBI core protons ($\Delta\delta$= 0.15 ppm) as

well as phenylring protons of the bay-substituents ($\Delta\delta$ = 0.32 and 0.75 ppm) and benzyl CH_2 protons ($\Delta\delta$ = 0.80 ppm), which show a geminal coupling (13.5 Hz) due to their diastereomeric nature caused by the chiral PBI core (Figure 68).

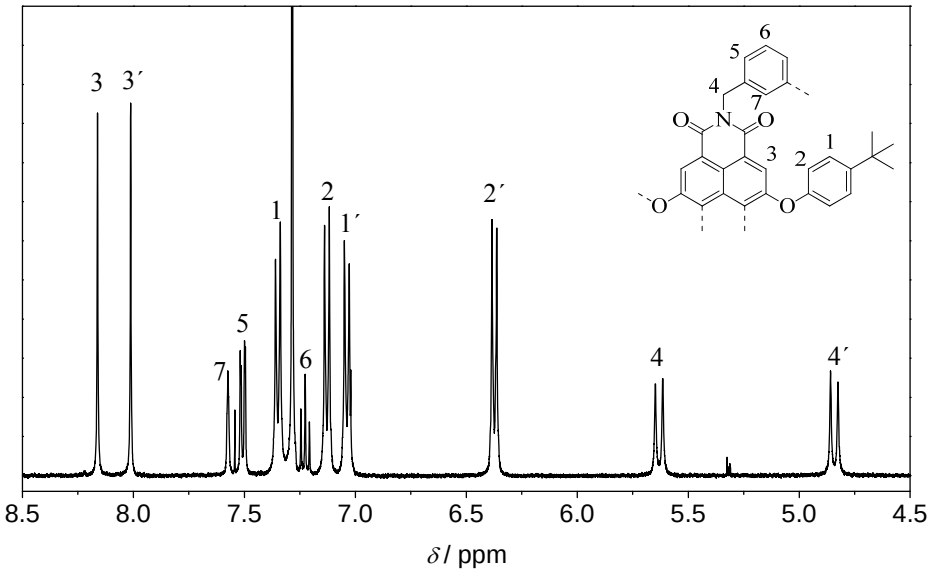

Figure 68. ^{1}H-NMR spectrum of ***m*-2PBI$_{(4\text{-}t\text{Bu})4}$** in $CHCl_3$ (298 K, 400 MHz) with the assignment of individual protons.

With increasing the temperature to 360 K, the signal splitting is not observable anymore and one single set of signals is maintained (Figure 113; in tetrachloroethane-d_2). From the coalescence temperature T_c = 320 K and the splitting of the proton signals in the NMR spectra the activation energy for the observed dynamic process can be calculated according to equation (7):

$$\Delta G^{\neq} = RT_C \ln\left(\frac{RT_C\sqrt{2}}{\pi N_A h \Delta\nu}\right) \qquad (7)$$

An activation energy of –62 kJ/mol was estimated for ***m*-2PBI$_{(4\text{-}t\text{Bu})4}$** that is in good agreement with literature known values for the (*M*)-(*P*) chirality inversion of atropo-isomers of tetraphenoxy-substituted PBIs.[189]

Now the question arises, what is the reason for the appearance of the two sets of signals for this cyclophane? The fact that each of the core-tetrasubstituted PBI units in the cyclophane can possess (*M*) and (*P*) atropo-enantiomers through twisting of the perylene core,[101b] the PBI dimer in the cyclophane can have four stereoisomers, namely (*M*,*M*) and (*P*,*P*) homochiral dimers and (*M*,*P*) and (*P*,*M*) heterochiral dimers. Because of the same symmetry, the protons of each enantiomeric pair are equivalent and thus can not be

distinguished by NMR spectroscopy. However, in (*M*,*M*) and (*M*,*P*) (or (*P*,*P*)/(*P*,*M*)) diastereomers the protons are not equivalent, and accordingly two sets of proton signals can be expected. Moreover, each proton in the individual diastereomers, i.e. (*M*,*M*) and (*M*,*P*), should result in two signals distinguishing the protons that are pointing inside the cavity or to the outside. That means, in the presence of (*M*,*M*) and (*M*,*P*) diastereomers four sets of signals are to expect (*vide infra*).

Since this cyclic PBI dimer ***m*-2PBI$_{(4\text{-}t\text{Bu})4}$** shows only two sets of nicely resolved sharp signals in a 1:1 ratio, the observed signal splitting can be attributed to the presence of (*M*,*M*) and (*P*,*P*) homochiral diastereomers. In these, the conformational exchange between the enantiomeric units is obviously restricted by the close PBI-PBI contact and the signal splitting is caused by the shielding effect of the protons oriented inside the cavity. Indeed, it has been reported that chiral recognition of core-twisted PBI molecules leads to homochiral PBI dimer assemblies.[30b, 102] Thus, we assume that in the cyclophane ***m*-2PBI$_{(4\text{-}t\text{Bu})4}$** with congested cavity only the homochiral dimers (*M*,*M*) and (*P*,*P*) are present, an outcome of such chiral recognition.

In **2PBI$_{(4\text{-}t\text{Bu})4}$** the distance between the two PBI chromophores is larger, which should allow conformational flexibility and thus all the possible stereoisomers can be in dynamic equilibrium at particular temperature. Indeed, at room temperature, only broad signals are observed in the ^{1}H-NMR spectrum, indicating a fast dynamic process at NMR time scale. Therefore, temperature-dependent ^{1}H-NMR spectroscopy was performed to study the conformational changes in this cyclophane. For this purpose, a 0.8 mM solution of **2PBI$_{(4\text{-}t\text{Bu})4}$** in tetrachloroethane-$d_2$ was prepared and ^{1}H-NMR spectra were measured at different temperatures reaching from 360 to 260 K in steps of 10 K (Figure 69 and Figure 114 in the appendix).

At a high temperature of 360 K, only one set of relatively sharp proton signals are observed (Figure 69 red spectrum). Thus, at high temperature the cyclophane **2PBI$_{(4\text{-}t\text{Bu})4}$** shows high symmetry with a dynamic interconversion process that is faster than the NMR time scale. With this fast conformation flipping of the PBI core the diastereomers are not distinguishable by NMR. Upon cooling down the sample gradually, the proton signals get broader until the coalescence temperature T_c is reached at ~320 K. Here, the proton signals are hardly visible, since the rate of conforamtional exchange is identical to the difference in the peak frequency. Upon further cooling, a signal splitting and sharpening is observed, which indicates that the conformational interconversion is now slower than

the NMR time scale (Figure 69 blue spectrum). According to equation (7) the activation energy for **2PBI$_{(4\text{-}t\text{Bu})4}$** was calculated to –62 kJ/mol that is similar to ***m*-2PBI$_{(4\text{-}t\text{Bu})4}$**.

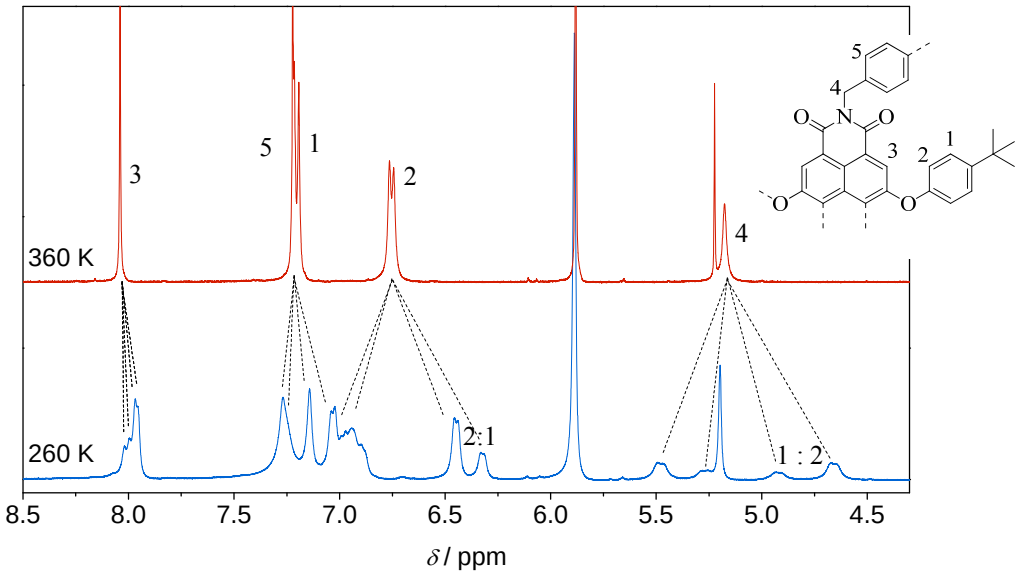

Figure 69. ^{1}H-NMR (400 MHz) spectra of **2PBI$_{(4\text{-}t\text{Bu})4}$** at 360 K (red) and 260 K (blue) and assignment of the individual protons; tetrachloroethane-d_2; c = 0.8 mM; dotted lines indicate the splitting of the proton signals at low temperature.

As mentioned in the previous section, due to same symmetry of the two possible homochiral dimers (*M*,*M*) and (*P*,*P*) or heterochiral dimers (*M*,*P*) and (*P*,*M*), each of these pairs constitute an enantiomeric pair, they are not distinguishable by NMR spectroscopy. However, the protons in diastereomers (*M*,*M*) and (*M*,*P*) are not equivalent and thus have different NMR shifts and the protons of each diastereomer should split in two sets due to the shielding effect. Therefore, in total four sets of signals are observed at low temperature (260 K) for the two diastereomers. In the absence of chirality transfer between the chromophores, the two diastereomers should appear in a 1:1 ratio. However, at 260 K a ratio of ~2:1 for each of the significant proton signals is observed, revealing a slight preference for one diastereomer through chiral recognition (Figure 69 blue spectrum). From this signal ratio the equilibrium constant at 260 K can be estimated to $K_{eq} = 2$ according to the equations 8 and 9 for the (*M*,*M*) and (*M*,*P*) diastereomers.

$$(M,M) \leftrightharpoons (M,P) \qquad (8)$$

$$K_{eq} = \frac{[(M,P)]}{[(M,M)]} \qquad (9)$$

With this, the difference in the potential energy between the diastereomers can be estimated to ΔG = 1.4 kJ/mol. Since at 260 K the proton signals in the NMR spectrum are still somewhat broadened, which is indicative for remaining conformational exchange dynamics of the PBIs, this energy difference should be considered as the upper limit.

From geometry optimized structures obtained by force field calculations (Maestro 9.3, MacroModel 9.8, AMBER) the individual diastereomers of **2PBI$_{(4\text{-}t\text{Bu})4}$** were compared. In both homochiral and heterochiral dimers of **2PBI$_{(4\text{-}t\text{Bu})4}$**, four of the bay-phenoxy-substituents (two of each PBI unit) are oriented upwards or downwards of the cyclophane, whereas the other four phenoxy groups are closing the sides of the cavity. Thereby, a π-π interaction between the phenoxy groups occurs that is present in the homochiral diastereomer within transoid substituents and in the heterochiral diastereomer between cisoid substituents (Figure 46a and Figure 70). The calculated potential energies are with –387.6 (homochiral) and –388.6 kJ/mol (heterochiral) nearly identical and in agreement with the small difference estimated based on the NMR spectra. Although in closely stacked assemblies of conformationally fixed monomeric PBIs the homochiral dimers prevail,[102] these calculations suggest that the heterochiral dimer of PBIs in cyclophane **2PBI$_{(4\text{-}t\text{Bu})4}$** is slightly thermodynamically favored.

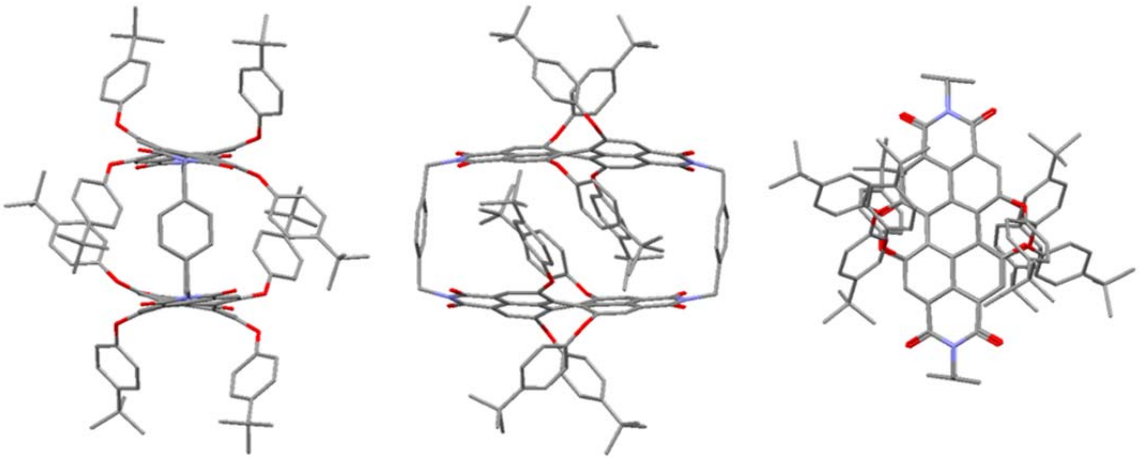

Figure 70. Geometry optimized structure of the heterochiral PBI cyclophane **2PBI$_{(4\text{-}t\text{Bu})4}$** in the front- (left), side- (middle) and top-view (right) obtained by force field optimization; Maestro 9.3, MacroModel 9.8, AMBER.

3.5.2 NMR Spectroscopic Studies on Guest Encapsulation

While in ***m*-2PBI$_{(4\text{-}t\text{Bu})4}$** the interplanar distance of 5.3 Å does not provide enough space between the chromophores to accommodate guest molecules, encapsulation of aromatic

hydrocarbons might be used to influence the chirality transfer in **2PBI$_{(4\text{-}t\text{Bu})4}$** due to close contact between the aromatic guest and both chromophores. To study the transfer of chiral information in this system, temperature-dependent ^{1}H-NMR spectroscopy was performed with a mixture of **2PBI$_{(4\text{-}t\text{Bu})4}$** and perylene (8 eq.), a strong binding guest (Figure 115 in the appendix). At high temperature of 360 K, one set of sharp signals was observed for the **2PBI$_{(4\text{-}t\text{Bu})4}$** with a small upfield shift of 0.07–0.28 ppm compared to the free host (Figure 71 red spectrum). The proton signals of the perylene guest molecule are significantly broadened due to fast guest in-out exchange and do not allow to distinguish between host-embedded and free perylene molecules.

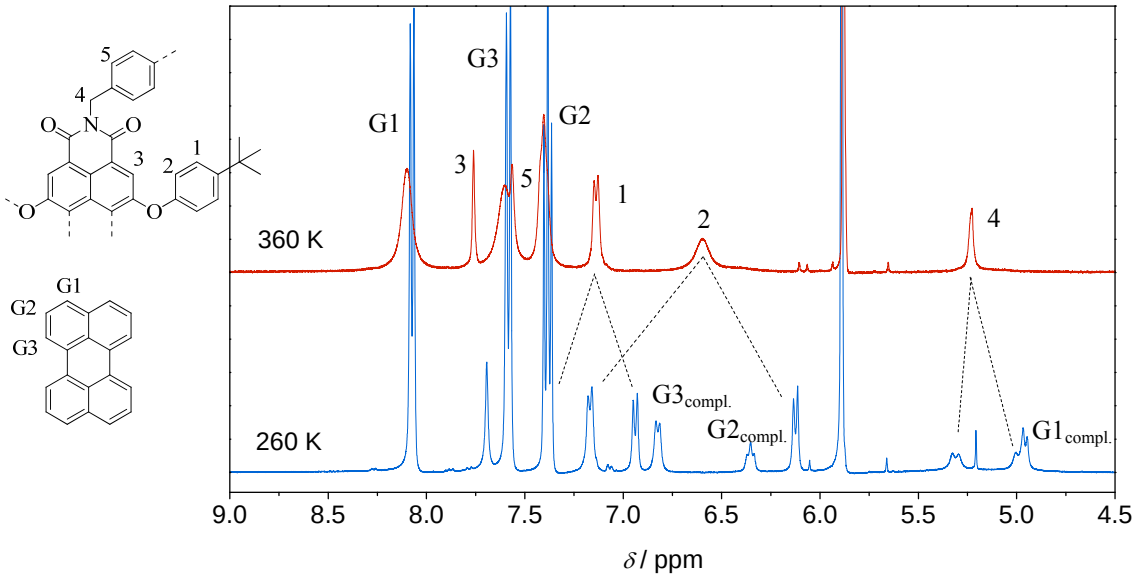

Figure 71. ^{1}H-NMR spectra (400 MHz) at 360 K (red) and 260 K (blue) of perylene@**2PBI$_{(4\text{-}t\text{Bu})4}$** and assignment of the individual protons; tetrachloroethane-d_2; c = 0.8 mM; 8 eq. of perylene; dotted line indicate the splitting of the individual proton signals at low temperature.

With decreasing the temperature to 260 K a sharpening of the perylene protons is observed and encapsulated guest molecules can be distinguished from those dissolved in the solvent (Figure 71 blue spectrum). The proton signals of encapsulated guests experience a strong upfield shift of ~1 ppm for G2 and G3 protons and 2.6 ppm for G1 protons due to the aromatic shielding effect provided by the cavity. Furthermore, the signal integrals confirm the formation of 1:1 complexes. Concomitantly, the proton signals of the host split in a pattern (indicated by the dotted line in Figure 71) that is reminiscent of the homochiral dimers (*M*,*M*) and (*P*,*P*) observed for the free host at

260 K. The fact that no signals for the (*M*,*P*) and (*P*,*M*) heterochiral dimers can be observed anymore indicates a guest-mediated transfer of chiral information between the chromophores. From the coalescence temperature of ~320 K and the signal splitting an activation energy of –64 kJ/mol was calculated according to equation (7) that is close to the activation energy of the free host.

3.5.3 Circular Dichroism Studies

Due to the fact that perylene is an achiral guest molecule, chirality transfer mediated by this guest molecule leads to a racemic mixture of homochiral dimers. Therefore, in another experimetn host-guest complexation with homochiral guest molecules (*R*)-naphthylethylamine or (*S*)-naphthylethylamine was examined using circular dichroism (CD) spectroscopy. First, UV-vis spectra were measured that show similar features as previously seen for the encapsulation of electron-poor achiral guests with a decreased and slightly bathochromically shifted UV-vis absorption band (Figure 72, lower panel).

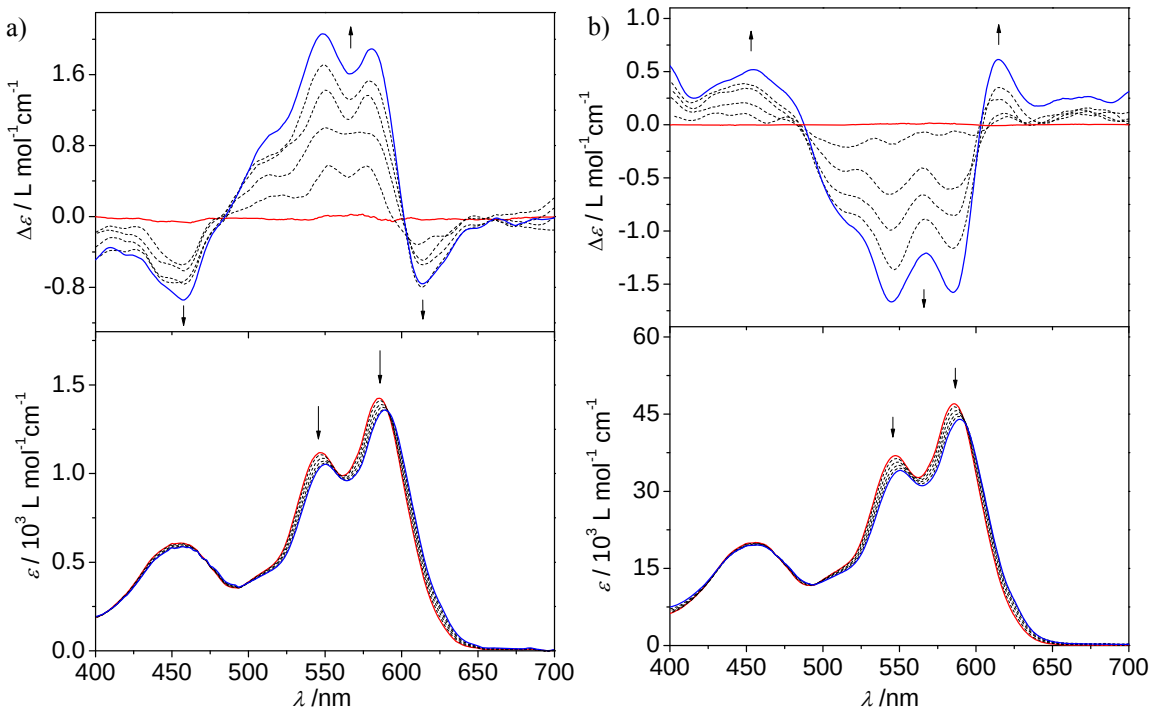

Figure 72. CD and UV-vis absorption spectra of **2PBI$_{(4\text{-}t\text{Bu})4}$** upon addition of (*S*)-naphthylethylamine (a) and (*R*)-naphthylethylamine (each 9000 eq.) (b); c(**2PBI$_{(4\text{-}t\text{Bu})4}$**) = 6 x 10^{-5} M in $CHCl_3$, 298 K; red line: spectra before titration; blue line: spectra after the individual guest is completely added; arrows indicate spectral changes upon addition of guest molecules.

Furthermore, fluorescence spectroscopy revealed an increase of emission upon addition of the chiral guest (Figure 116 in the appendix). From the titration experiments a binding constant in chloroform was calculated to be 16.5 M^{-1}. The pretty low binding constant can probably be related to the rather tight cavity that is only ideal for truly planar aromatic compounds, but not for those bearing bulky chiral groups.

More interestingly, upon binding of the chiral guests into the cyclophane **2PBI$_{(4\text{-}t\text{Bu})4}$** a Cotton effect is observed for the optical transitions of the PBIs (Figure 72, upper panel) that is in part attributable to the PBI core twist and to chiral exciton coupling between the chromophores in a helical arrangement,[186-187] as evidenced by a bisignate feature in the CD spectra with a zero crossing at 601 nm similar to homochiral dimer aggregates of PBI dyes.[102, 190] The addition of (*S*)-naphthylethylamine or (*R*)-naphthylethylamine results in mirror image CD signals. By comparison of the detected CD spectra with literature known homochiral dimers of conformationally fixed PBIs,[102] it appears that the encapsulation of (*S*)-naphthylethylamine favors the homochiral (*P*,*P*)-dimer, whereas (*R*)-naphthylethylamine favors the (*M*,*M*)-dimer of PBI units in cyclophane **2PBI$_{(4\text{-}t\text{Bu})4}$**. The absolute $\Delta\varepsilon$ values for the transition at 591 nm of the two diastereomers of **2PBI$_{(4\text{-}t\text{Bu})4}$** are +1.86 and –1.58 M^{-1} cm^{-1}, giving an absorption dissymmetry factor $g = \Delta\varepsilon/\varepsilon$ of 2.91 x 10^{-5}. This value is indeed rather small compared to conformationally fixed (*P*)- or (*M*)-PBI molecules[101b] and suggests that the chiral guest molecules could only weakly bias the equilibrium between (*M*,*M*)- and (*P*,*P*)-host molecules. The additional negative sign of the exciton couplet at higher wavelengths for the (*P*,*P*)-dimer indicates a left-handed helical arrangement ((*M*)-helicity) of the two PBIs in the cyclophane according to exciton chirality method (opposite helicity for the (*M*,*M*)-dimer).[102, 191] It is to note that upon addition of homochiral naphthylethylamine to ***m*-2PBI$_{(4\text{-}t\text{Bu})4}$** with smaller cavity no Cotton effect was observed, indicating on the one hand, that no guest encapsulation into this smaller cyclophane takes place and, on the other hand, that the CD effect observed for **2PBI$_{(4\text{-}t\text{Bu})4}$** is indeed imparted by chirality transfer from the homochiral guest to the PBI chromophores.

A much stronger Cotton effect for **2PBI$_{(4\text{-}t\text{Bu})4}$** was observed in enantiomerically pure solvent (*R*)- or (*S*)-limonene (Figure 73a). Similar to the CD signals with homochiral naphthylethylamine, a bisignate feature was observed in enantiomerically pure limonene. Moreover, a solvent-induced chirality transfer, that is an environmental influence on the cyclophane, is also observable for ***m*-2PBI$_{(4\text{-}t\text{Bu})4}$** (Figure 73b). It is to note that no CD

signals were observed neither for the monomeric reference compound **1PBI$_{(4\text{-}t\text{Bu})4}$** in chloroform or chiral limonene nor for the free host **2PBI$_{(4\text{-}t\text{Bu})4}$** in chloroform or upon addition of the achiral guest perylene.

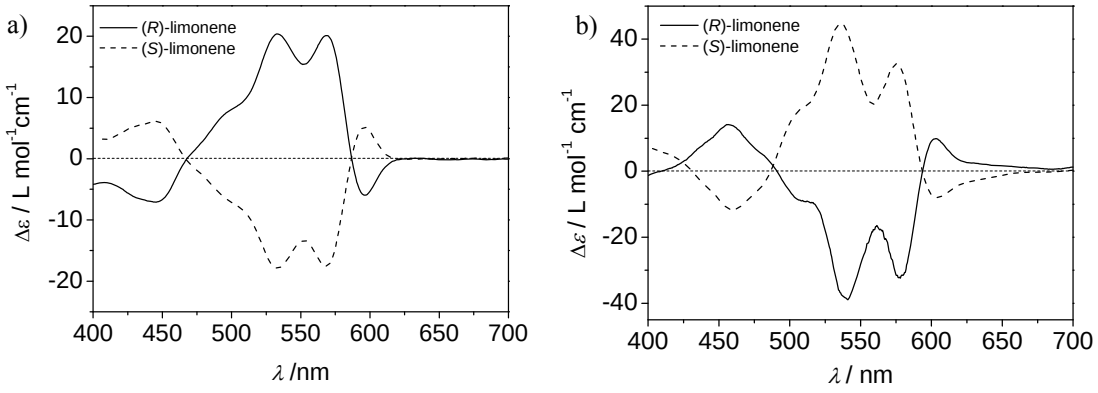

Figure 73. CD spectra of **2PBI$_{(4\text{-}t\text{Bu})4}$** (a) and ***m*-2PBI$_{(4\text{-}t\text{Bu})4}$** (b) in (*R*)-limonene (solid line) and (*S*)-limonene (dotted line); c = 5 x 10^{-5} M; 298 K.

In comparison to **2PBI$_{(4\text{-}t\text{Bu})4}$**, the signs of the CD signals for ***m*-2PBI$_{(4\text{-}t\text{Bu})4}$** are inverted in (*R*)- and (*S*)-limonene, respectively. Although the encapsulation of limonene into **2PBI$_{(4\text{-}t\text{Bu})4}$** can hardly be observed by UV-vis absorption and fluorescence spectroscopy, this change in the sign of the CD signals indicates different interactions between the chiral solvent molecules and the cyclophane **2PBI$_{(4\text{-}t\text{Bu})4}$** than in ***m*-2PBI$_{(4\text{-}t\text{Bu})4}$**. Whereas in ***m*-2PBI$_{(4\text{-}t\text{Bu})4}$** the chirality transfer is surely induced by the surrounding, in **2PBI$_{(4\text{-}t\text{Bu})4}$** it seems to be dictated by limonene molecules inside the cyclophane cavity. The lower intensity of the CD signal in **2PBI$_{(4\text{-}t\text{Bu})4}$** can probably be explained by competing processes between the solvent-induced and guest-mediated chirality transfer in this particular system.

As shown in the preceding studies, the addition of enantiomerically pure guest molecules to the cyclophane **2PBI$_{(4\text{-}t\text{Bu})4}$** bearing two core-twisted PBI chromophores leads to the formation of homochiral host-guest complexes with specific CD spectral signature. For related biological systems, in particular protein (enzyme)-ligand binding processes, two different mechanistic models, namely induced fit and conformational selection, are discussed in literature.[192] According to the induced fit mechanism the interaction between a protein and a ligand induces conformational changes in the protein to adopt a conformation best suited to the ligand (Koshland-Nemethy-Filmer induced fit).[193] On the othe hand, in the conformational selection mechanism the protein adopts different conformations prior to binding that are in equilibrium, and the ligand selects the most

compatible one for binding and shifts the equilibrium to the binding site (Monod-Wyman-Changeux conformational selection).[194] For our present chemical system, i.e. binding of homochiral guest molecules to the cyclophane **2PBI$_{(4\text{-}t\text{Bu})4}$**, both mechanisms should be taken into account. The guest molecule either selects the conformation best compatible for binding from the dynamically equilibrating conformations, or first binds to the host and then induces a conformational change leading to homochiral complexes (Figure 74). Since at room temperature conformational dynamics have been observed for **2PBI$_{(4\text{-}t\text{Bu})4}$**, it appears to be reasonable that the conformational selection mechanism is present in this particular system. However, detailed mechanistic and molecular dynamic simulation studies will be required to make a conclusive mechanistic proposal.

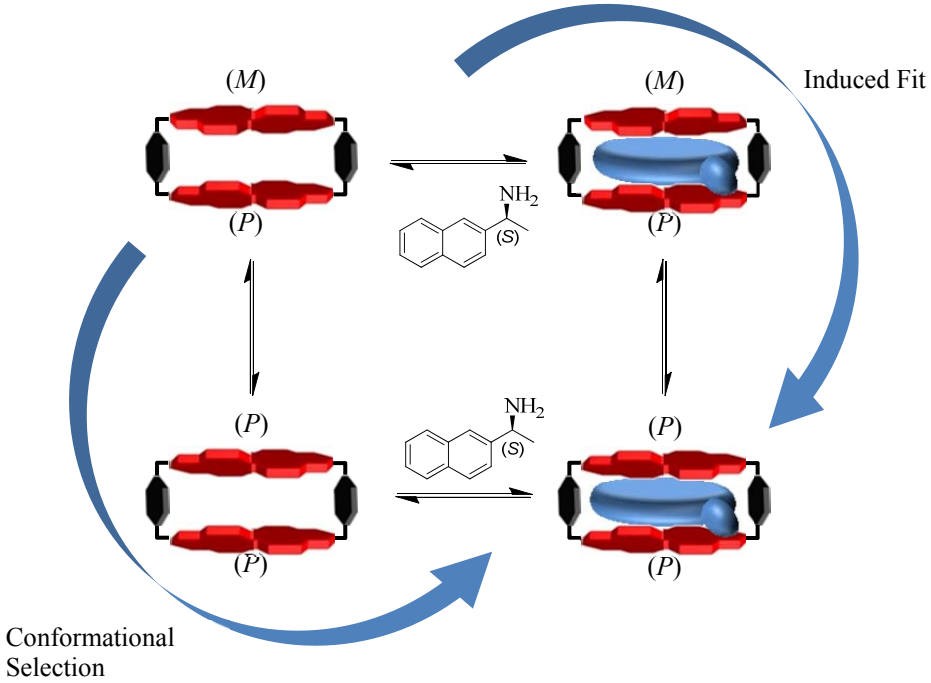

Figure 74. Illustration of the two different guest-mediated chirality transfer mechanisms, i.e. induced fit and conformational selection.

In summary, it could be shown in this chapter that in PBI cyclophane **2PBI$_{(4\text{-}t\text{Bu})4}$** only weak interactions between the chromophores are present due to a large distance of 6.5 Å. This facilitates conformational flexibility leading to different stereoisomers depending on the (*M*)- and (*P*)-conformation of each of the two core-twisted PBI chromophores. A weak conformational template effect between the PBI units is revealed by low-temperature NMR spectroscopy with slight preference for heterochiral dimers. Although the cavity is not ideal for the encapsulation of sterically demanding chiral molecules,

2PBI$_{(4\text{-}t\text{Bu})4}$ can be used as a model compound to get in-depth insight into the mechanism of chirality transfer in a host-guest complex, which might lead to the development of new cyclophane systems for potential applications in chiral recognition and imaging.

3.6 Complexation of Fullerene into the Cyclic Trimer

Since the discovery of fullerenes by Kroto *et al*.,[195] the search for molecular receptors to study convex-concave π-interactions started.[196] The main focus in this research field is the selective recognition of specific fullerene derivatives for purification from complex mixtures[197] and the self-assembly of electroactive nanostructures.[198] Therefore, host-guest complexes with high association constants in solution are needed. The design of suitable hosts is thus one major task to achieve these assemblies. In this regard *para*-phenylacetylenes were intesivley investigated as proper hosts for different fullerene derivatives that provide a nanoring structure optimized for the ball-shaped fullerenes.[21a, 21c, 199] But also other host systems have successfully been utilized for the complexation of fullerenes, like calixarenes,[200] corannulenes[201] and π-extended tetrathiafulvalenes.[21b, 202] Furthermore, electron-rich porphyrine containing host systems showed to have high binding constants to the acceptor fullerenes of up to 10^8 M^{-1} (in benzene)[203], which is facilitated by the metalions in the porphyrine centers.[204]

Although a series of PBI macrocycles has been reported in the last decades (see chapter 2.5), non-covalent PBI-fullerene complexes are rare in literature.[141, 205] However, the combination of an electron-poor PBI and fullerene, resulting in an acceptor-acceptor system, showed to be an interesting candidate to study EnT processes.[206] Recent studies on covalently linked PBI-fullerene systems showed that an EnT from the excited PBI moiety to the fullerene unit takes place. Afterwards, the fullerene populates its triplet state enabling a second EnT back to the PBI to form the PBI triplet state.[206-207]

In the herein discussed *para*-xylylene bridged PBI macrocycels, the cyclic trimer **3PBI$_{(4\text{-}t\mathrm{Bu})4}$** composed of three PBI units has a structure of a molecular tube with an optimal size for the encapsulation of fullerene C_{60} and C_{70}. These complexes where studied by UV-vis absorption, fluorescence and transient absorption spectroscopy to investigate the EnT processes from the PBI unit to the fullerene and back.

3.6.1 Optical Spectroscopy

The UV-vis absorption spectrum of **3PBI$_{(4\text{-}t\mathrm{Bu})4}$** in toluene shows very similar spectral features compared to the monomeric PBI **1PBI$_{(4\text{-}t\mathrm{Bu})4}$** with a maximum at 573 nm and the 0-1 transition band located at 535 nm (Figure 75a). The fluorescence spectrum exhibits a maximum at 610 nm and is the mirror image of the absorption spectrum (Figure 75b, red line). The relatively high fluorescence quantum yield of 79% is similar to the one of

reference compound **1PBI$_{(4\text{-}t\text{Bu})4}$** with 86% and thus indicates only minor electronic interactions between the chromophores in toluene.

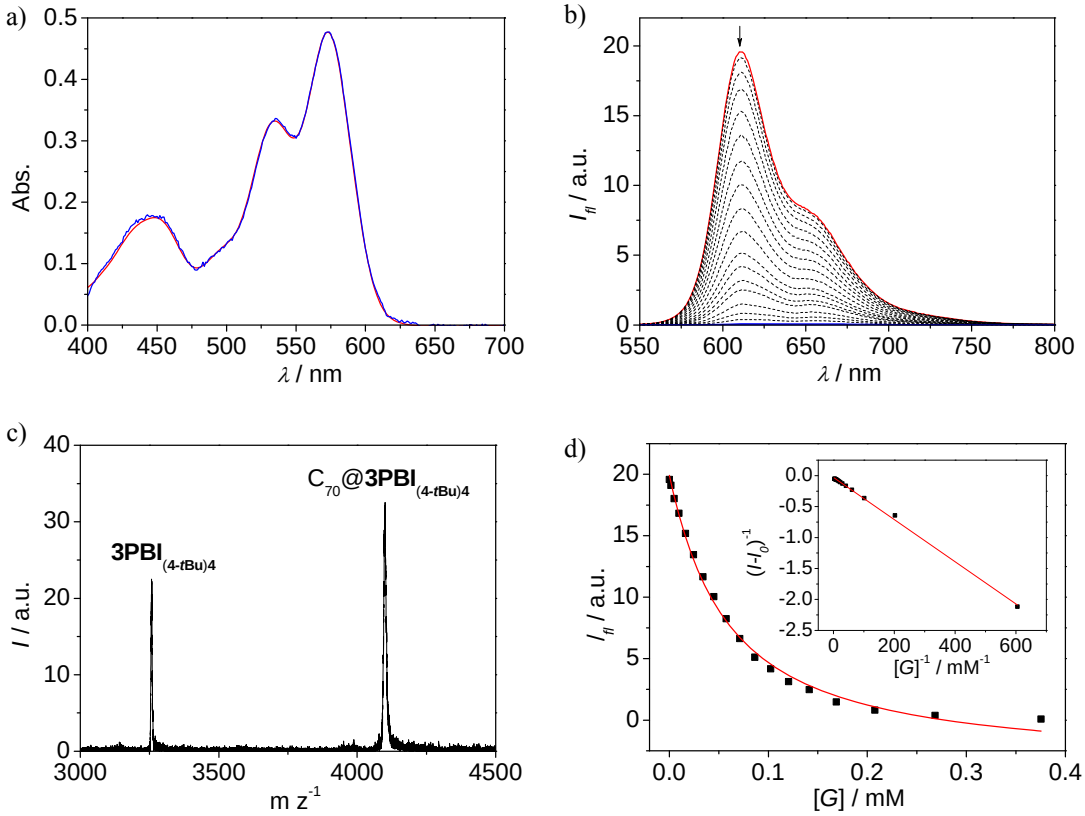

Figure 75. UV-vis absorption (a) and fluorescence (b) spectra of **3PBI$_{(4\text{-}t\text{Bu})4}$** upon the addition of fullerene C_{70} in toluene (c(**3PBI$_{(4\text{-}t\text{Bu})4}$**) = 5 x 10^{-5} M, RT); red line: spectra before titration; blue line: spectra after the guest is completely added (the fullerene absorption is substracted from the measured spectrum); arrow indicates spectral changes; c) MALDI-TOF mass spectrum of the C_{70}@**3PBI$_{(4\text{-}t\text{Bu})4}$** complex (pos. mode, DCTB in $CHCl_3$); d) least square fitting of the fluorescence data according to equation (2) (inset: Benesi-Hildebrand plot confirming the 1:1 stoichiometry).

The addition of fullerene C_{60} or C_{70} leads to a successive quenching of the fluorescence through complexation into the cyclic trimer (Figure 75b). Although fullerene has only weak absorption between 500 and 600 nm, changes of the PBI absorption are not directly visible due to the lack of specific charge transfer bands – both molecules are acceptors – or conformational changes of the PBIs. However, subtracting the fullerene absorption from the measured spectra, the remaining PBI absorption can be visualized (Figure 75a, Figure 117a in the appendix, blue line). Thus, in contrast to the complexes of planar aromatic hydrocarbons in the analog cyclophane **2PBI$_{(4\text{-}t\text{Bu})4}$** (see chapter 3.2), no changes can be observed between the absorption of **3PBI$_{(4\text{-}t\text{Bu})4}$** and the corresponding fullerene complexes.

From the fluorescence data the formation of 1:1 complexes can be concluded applying the Benesi-Hildebrand plot (inset Figure 75d, Figure 117d in the appendix), which is also confirmed by MALDI-TOF mass spectrometry of the mixture between fullerene and **3PBI$_{(4\text{-}t\text{Bu})4}$** (Figure 75c, Figure 117c in the appendix). The respective binding constants were accordingly determined using a 1:1 binding model by non-linear least square fitting (equation (2)). Thus, binding constants of K_a = (1.85 ± 0.10) x 10^3 M^{-1} (R^2 = 0.998, ΔG^0_{298} = –18.6 kJ/mol) and (1.95 ± 0.15) x 10^4 M^{-1} (R^2 = 0.996, ΔG^0_{298} = –24.5 kJ/mol) were found for the complexation of C_{60} and C_{70}, respectively. The significantly higher binding strength of fullerene C_{70} can be explained by the geometry optimized structures of the corresponding complexes (Figure 76).

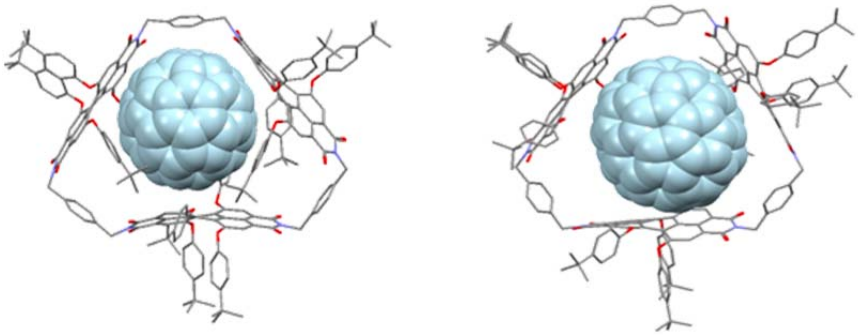

Figure 76. Geometry optimized structures of the 1:1 complexes C_{60}@**3PBI$_{(4\text{-}t\text{Bu})4}$** (left) and C_{70}@**3PBI$_{(4\text{-}t\text{Bu})4}$** (right) obtained by force field optimization; Maestro 9.3, MacroModel 9.8, MM2*.

From these structures it can nicely be seen that fullerene C_{60} is smaller than the cavity itself, which leads to a bending of one PBI unit to optimize the π-π interactions within the complex, whereas C_{70} perfectly fits inside the cavity.

3.6.2 Transient Absorption Spectroscopy

To elucidate the excited state dynamics in the PBI trimer and its fullerene complexes femtosecond (fs) and nanosecond (ns)TA spectroscopy on the free host **3PBI$_{(4\text{-}t\text{Bu})4}$** and the mixture with fullerene C_{60} were performed. The spectra of **3PBI$_{(4\text{-}t\text{Bu})4}$** in toluene show the expected signatures of single PBIs after excitation with the ground state bleach (GSB) at 454, 537 and 588 nm, the stimulated emission (SE) at 590 and 651 nm and the excited state absorption (ESA) at 705, 959 and 1038 nm (Figure 77). After 2.4 ± 0.5 ps a slight decrease in the GSB and an increase of the band at 1038 nm is observed. Based on the timescale and the similarity of the spectra this transition most likely represents

structural relaxation and solvent reorientation on the singlet excited state ^{1}*PBI of the chromophores.[188b, 208] After that, the excited PBI goes back to the GS within 6.60 ± 0.9 ns, which represents the decay by emission. No further transient states were observed ruling out long living species like triplet states in the free host (Figure 77).

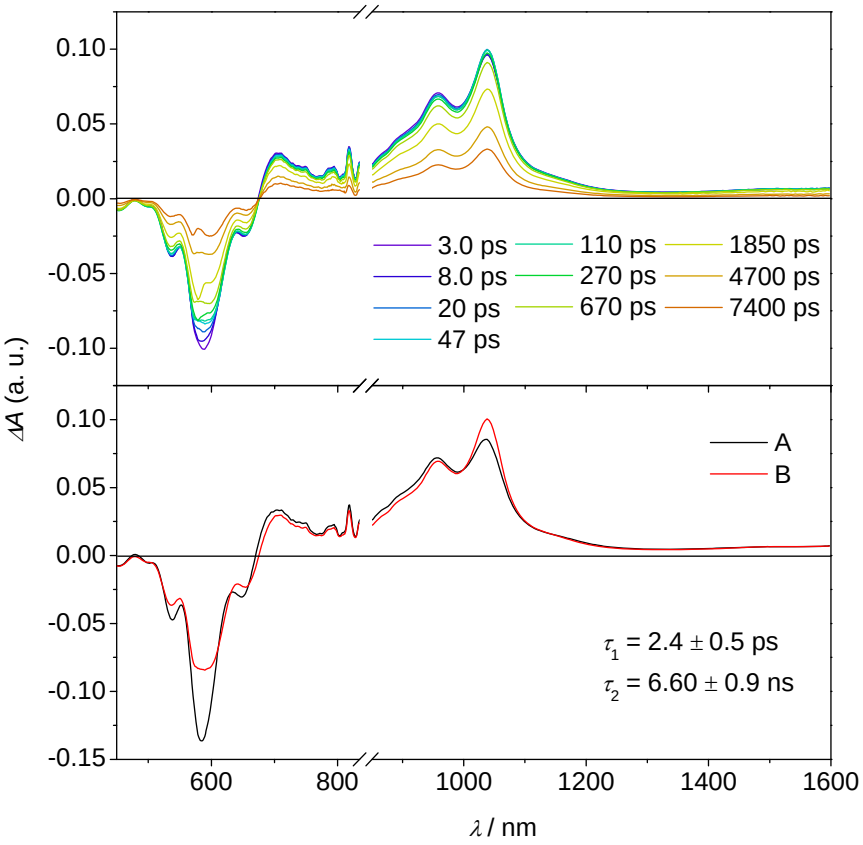

Figure 77. Femtosecond (top) transient absorption spectra of **3PBI$_{(4\text{-}t\text{Bu})4}$** in toluene showing the excited state dynamics after photoexcitation. Species-associated spectra (bottom) reconstructed from global fits to the sequential A → B → ground state model, where A and B are ^{1}*PBI, (A → B likely presents relaxation on the singlet state based on the timescale and the similarity of the spectra); λ_{ex} = 580 nm, 1.0 μJ/pulse, 298 K.

Based on the weak absorption of fullerene C_{60} at the excitation wavelength of 580 nm the TA features of the free guest were investigated (Figure 118 in the appendix). In the measured range of 450 to 1600 nm no GSB or SE were observed, but a relatively strong ESA at 506 and 980 nm. After 1.15 ± 0.01 ns these signals disappear and a new transient species is populated with a strong positive band at 750 nm (Figure 118b in the appendix), which is known to be the triplet state of the fullerene.[209] In an air-saturated solution the fullerene triplet state lives 303 ± 4 ns until it decays back to the GS.

In contrast, the mixture of **3PBI$_{(4\text{-}t\text{Bu})4}$** and fullerene shows totally different transient absorption properties (Figure 78a,b). Since the absorption of the PBI dyes at 580 nm is much stronger than of fullerene, the excitation of the guests in the mixture can be neglected. Furthermore, due to the relatively strong binding between host and guest and by using an excess of fullerene C_{60} an excitation of the free host is unlikely why the exclusive excitation of the host-guest complexes can be assumed. After excitation the transient spectra show the features of **3PBI$_{(4\text{-}t\text{Bu})4}$** with only weak SE features (Figure 78).

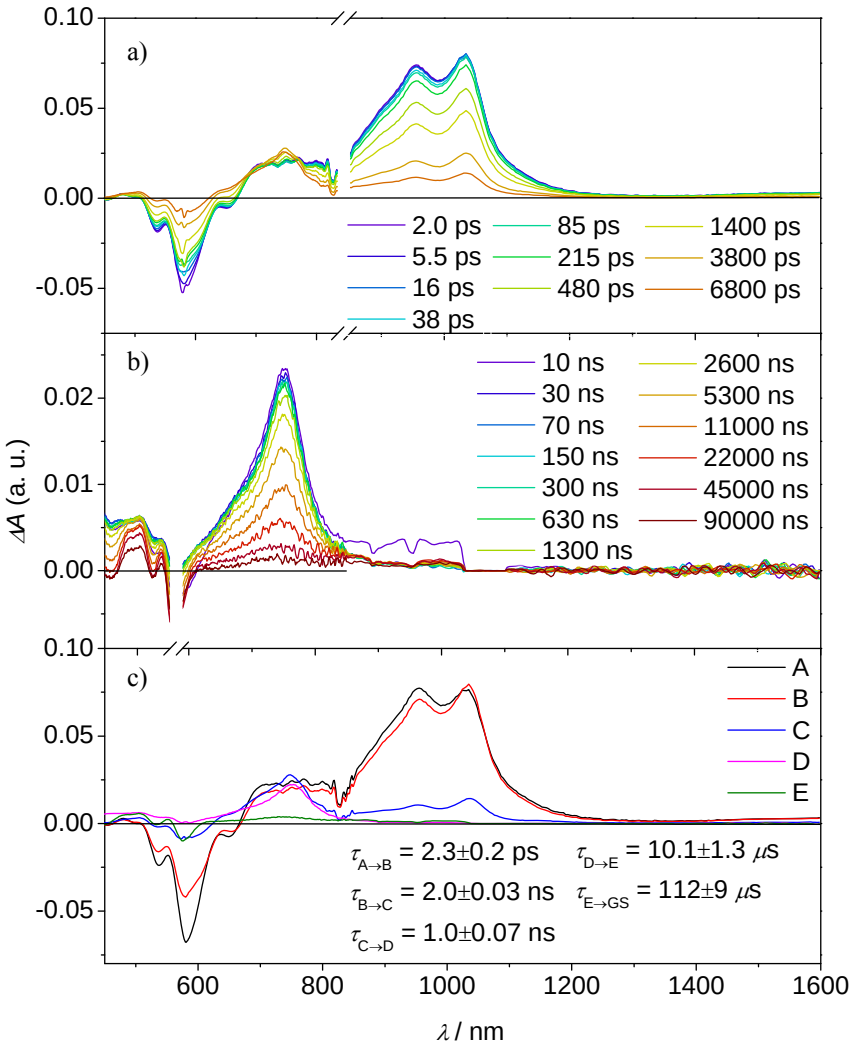

Figure 78. Femtosecond (a) and nanosecond (b) transient absorption spectra of the complex C_{60}@**3PBI$_{(4\text{-}t\text{Bu})4}$** showing the excited state dynamics after photoexcitation. Species-associated spectra (c) reconstructed from global fits to the sequential A → B → C → D → E → ground state model, where A is ^{1}*PBI-C_{60}, B is PBI-^{1}*C_{60}, C is PBI-$^{3*}C_{60}$, D and E are ^{3*}PBI-C_{60} (λ_{ex} = 580 nm, 1.0 μJ/pulse, toluene, 298 K, degassed for nsTA). The C → D → E → ground state times were determined from nsTA.

After 2.3 ± 0.2 ps a slight change in the TA spectrum is detected that is similar to the relaxation of the free host. However, it is known that the energy transfer from the singlet excited state of the PBI to the fullerene takes place in the same time range as the relaxation,[206] why this ultrafast decay could also be attributed to the energy transfer process. This assumption is strengthened by the fact that the next transient species, observed after 2.00 ± 0.03 ns shows the strong band of the fullerene triplet at 750 nm, whereas the signals of the PBI fully disappear. It is notable that the triplet formation of the fullerene is with ~2 ns in the complex slower compared to the free guest with 1.15 ns. Interestingly, the decay of the triplet state is not monoexponential but shows one fast component of 1.10 ± 0.07 ns and two long living features with 10 and 112 μs. Having a closer look on the species-associated spectra these different decays can be explained (Figure 78c).

After the first nanosecond the spectrum shows new bands at 505 and 550 nm that can be attributed to the triplet state of the PBIs. Since this was not observed for the free **3PBI$_{(4\text{-}t\text{Bu})4}$** the population of the triplet state surely happens via a second energy transfer from the fullerene triplet state to the PBI, which is with 1.1 ns in good agreement with literature known values.[206] However, the signal of the fullerene triplet state at 750 nm only fully disappears within the next 10 μs. Due to the fact that the host-guest complexes are formed through non-covalent bonding the transient spectra are taken from a dynamic system in which a guest in-out exchange might be possible at room temperature within the time range of the experiment. This allows a disassembly of the complexes and a release of the excited fullerene before the second energy transfer back to the PBI can take place. Thus, two different species of the excited fullerene exist in solution, the complexed one that can undergo energy transfer to the PBI and the free fullerene that decays back to its GS in 10 μs without energy transfer. After these 10 μs only the features of the PBI triplet remain in the spectra that decay to the PBI GS within 112 μs, which is the typical lifetime of ^{3}*PBIs (see chapter 3.3).

In summary, the cyclic PBI trimer **3PBI$_{(4\text{-}t\text{Bu})4}$** has a rigid tube like conformation with suitable size to act as a host for fullerenes. Due to the size of the cavity the encapsulation of fullerene C_{70} is around one order of magnitude stronger than of C_{60}. In both cases the complexation leads to a total quenching of the PBI fluorescence. To understand the decay of the excited state of the PBI, transient absorption spectroscopy of the free host, fullerene C_{60} and the corresponding host-guest complex was performed. While the free **3PBI$_{(4\text{-}t\text{Bu})4}$**

shows mainly the decay by emission the corresponding fullerene complex shows a series of steps after excitation. After a fast energy transfer from the PBI to the fullerene (2.3 ± 0.2 ps) the fullerene triplet state is populated within the next 2.00 ± 0.03 ns. During that process an in-out guest exchange can take place releasing the excited fullerene that afterwards decays back to the GS in 10 μs. On the other hand, the fullerene that remains in the complex can undergo a second energy transfer process generating the PBI triplet state with the expected long lifetime of 112 μs. With this, the PBI triplet state can effectively been reached by energy transfer processes with fullerene in a non-covalent system.

3.7 Folding of Perylene Bisimide Macrocycles

The organization of π-conjugated molecules into defined structures plays a unique role in chemistry and biology to create specific functions. Outstanding examples in nature are the self-organization of DNA into double helices[210] or the fixation of chlorophyll and bacteriochlorophyll arrays into macrocyclic structures in light-harvesting systems of purple bacteria (see chapter 2.1).[31, 211] Whereas in nature a sophisticated matrix of proteins and numerous non-covalent interactions force the dye subunits into defined arrangements, it is of interest to explore simpler approaches to direct the dye molecules to a desired organization in a specific environment.[212] Such a control of molecular structure is crucial also for artificial counterparts, knowing that the position of the dyes to each other defines the photophysical processes that occur in the composite because small changes can lead to quite different electronic interactions (see chapter 2.2).[62, 67c]

Perylene bisimide (PBI) dyes are well suited for such studies since they are easy to tune in their conformation and photophysical properties by substitution in the imide- or bay-positions.[213] Thus, multi-chromophoric PBI systems could be used to study electronic interactions in defined self-assembled or covalently tethered ensembles.[213-214] Indeed, covalent linkage of PBI chromophores has been used quite extensively for the preorganization of dyes to give arrangements with specific photophysical properties.[61b, 148c, 163, 215] Furthermore, in a smaller number of studies the transition between different conformations has been demonstrated by changing solvent polarity inducing folding of backbone-tethered PBI oligomers.[216] In these foldamers[217] with different backbone length π-π interactions between the dyes were used to create highly ordered assemblies with defined geometry that were explored by optical spectroscopy. Likewise, rigid PBI macrocycles[107-108, 112] and a variety of cyclophanes (see chapter 2.5) have been reported.[57b, 57c, 218] As previously discussed **2PBI$_{(4\text{-}t\mathrm{Bu})4}$** showed a variety of exciting and in part unprecedented properties: a) Ability to form strong host-guest complexes with binding constants up to ~10^5 M^{-1} with large aromatic π-systems such as perylene (chapter 3.2); b) Solvent- and guest-dependent excited state relaxation with intense fluorescence in toluene and in the presence of electron-poor guest molecules versus strongly quenched emission in the presence of electron-rich guests due to photo-induced electron transfer or in dichloromethane due to symmetry-breaking charge separation (SB-CS) and subsequent triplet state population (chapter 3.3). These features could be related to a well-shaped rather rigid cavity that enables the encapsulation of aromatic solvents or larger aromatic

π-systems that modulate the interaction of the two PBI chromophores in the photo-excited state.

Herein the subsequent study on the homologous oligomer series derived from **2PBI$_{(4\text{-}t\text{Bu})4}$**, i.e. PBI macrocycles **nPBI$_{(4\text{-}t\text{Bu})4}$** (n = 3–9) where numerous PBI chromophores (n) are covalently linked through *para*-xylylene bridges is presented. A folding of the macrocycles can be initiated with a significant odd-even effect regarding the number of PBI chromophores in aromatic solvents like toluene. The photophysical properties of folded and unfolded (in dichloromethane) PBI macrocycles have been studied by fluorescence, steady-state and transient absorption (TA) spectroscopy and femtosecond stimulated Raman spectroscopy (FSRS) revealing a folding-modulated excited state behavior. These results are rationalized by a templating effect of aromatic solvents that direct a conformational change of the odd-membered macrocycles (n = 4, 6, 8) from a wide-stretched conformation to a coiled double-string conformation. To the best of our knowledge such conformational changes by folding of macrocycles and with that changes in photophysical properties through solvent-specific intramolecular dye-dye interactions are to date unprecedented.

3.7.1 Steady-State UV-vis Absorption and Fluorescence Properties

The optical properties of dimer **2PBI$_{(4\text{-}t\text{Bu})4}$** have been reported previously (chapters 3.2 and 3.3) and thus will not be discussed here in detail. However, the relevant data for **2PBI$_{(4\text{-}t\text{Bu})4}$** are given to provide a complete picture of this series of macrocycles.

The investigation were started in dichloromethane, a solvent that is known for its excellent solvation properties for PBI dyes.[155] The steady-state absorption spectra (c = 5 x 10^{-6} M) of the macrocycles in this solvent display the typical bandshape of monomeric PBIs (Figure 79a). While the S_0-S_2 transition provides only a broad signal between 400 and 500 nm, a characteristic vibronic fine structure can be observed for the S_0-S_1 transition with maxima at around 580 ($A_{0\text{-}0}$) and vibronic progressions at 540 nm ($A_{0\text{-}1}$). The corresponding fluorescence spectra are the mirror images of the S_0-S_1 absorption spectra with maxima at 620 nm. These results suggest that in dichloromethane all macrocycles prevail in wide-stretched conformations where PBI-PBI interactions are absent. In contrast, upon changing the solvent to aromatic toluene some of the macrocycles reveal remarkable changes of their spectra. While the cycles with odd numbers of PBI units still show the typical monomer-type bandshape (Figure 79b left), a

strong increase of the 0-1 vibronic transition band for the others is observed indicating an increased interaction, i.e. exciton coupling between the molecules (Figure 79b right).[148]

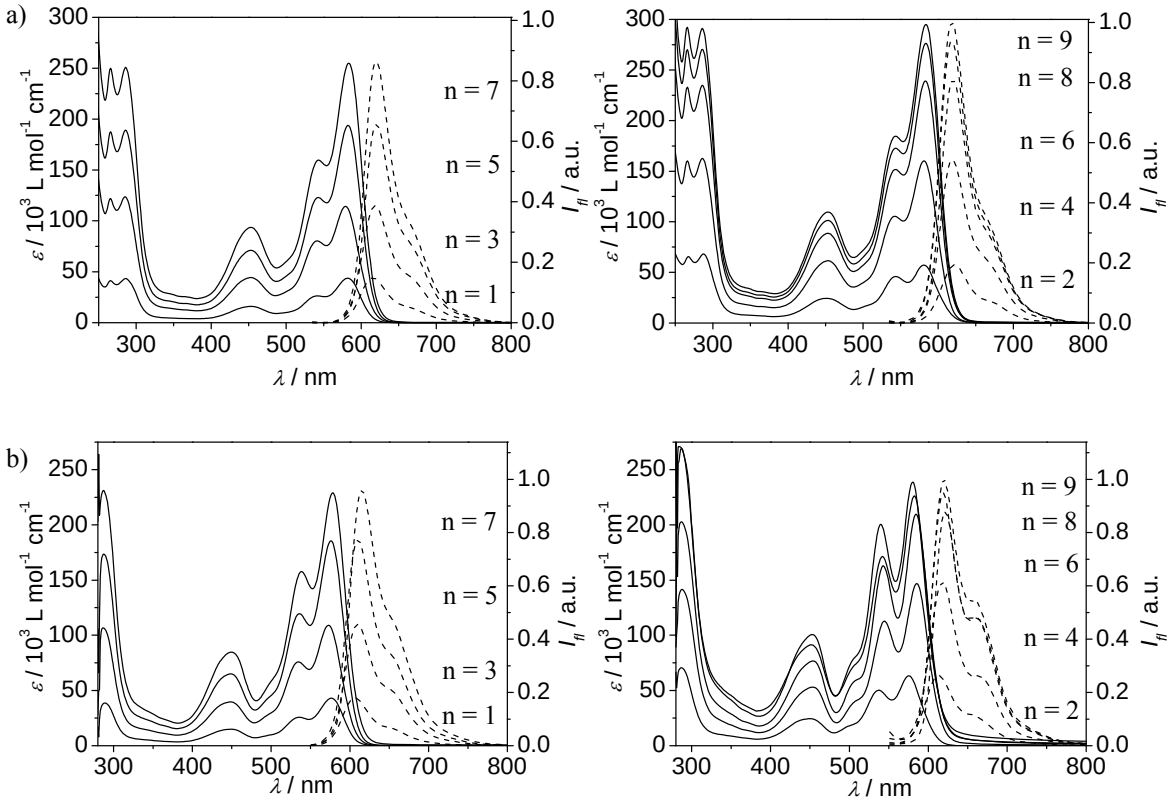

Figure 79. UV-vis absorption (solid line) and fluorescence spectra (dashed line) of **nPBI$_{(4\text{-}t\text{Bu})4}$** (n = 1–9) in DCM (a) and toluene (b); c = 5 x 10^{-6} M, fluorescence spectra are normalized to the corresponding maximum in the absorption.

To elucidate whether these spectral changes of the even-numbered macrocycles in the absorption bands originate from intermolecular or intramolecular couplings, i.e. PBI aggregation by self-assembly or folding, concentration-dependent UV-vis absorption studies of **4PBI$_{(4\text{-}t\text{Bu})4}$** were performed in toluene (2.5 x 10^{-5} M – 3.5 x 10^{-7} M) (Figure 119 in the appendix). With dilution of the sample no changes in the spectra occur, which excludes the formation of self-assembled larger aggregates of the macrocycles and corroborates an intramolecular folding in toluene.

The $A_{0\text{-}0}/A_{0\text{-}1}$ ratio in the UV-vis absorption spectra has been often used to distinguish between uncoupled monomer-like PBIs and those influenced by excitonic coupling among each other.[148] For the given series, values of ~1.60 are observed for **nPBI$_{(4\text{-}t\text{Bu})4}$** with n = 5–9 in dichloromethane that are very close to the reference monomer **1PBI$_{(4\text{-}t\text{Bu})4}$** ($A_{0\text{-}0}/A_{0\text{-}1}$ (**1PBI$_{(4\text{-}t\text{Bu})4}$**) = 1.66). With decreasing ring size the $A_{0\text{-}0}/A_{0\text{-}1}$ ratio is reduced to

1.52, 1.42 and 1.25 for **4PBI$_{(4\text{-}t\text{Bu})4}$**, **3PBI$_{(4\text{-}t\text{Bu})4}$** and **2PBI$_{(4\text{-}t\text{Bu})4}$**, respectively.[148d] In toluene the $A_{0\text{-}0}/A_{0\text{-}1}$ ratio for even-numbered **4PBI$_{(4\text{-}t\text{Bu})4}$**, **6PBI$_{(4\text{-}t\text{Bu})4}$** and **8PBI$_{(4\text{-}t\text{Bu})4}$** is markedly reduced to ~1.3 indicating a significant interchromophoric coupling within these cycles in their folded state. For the odd-numbered cycles the $A_{0\text{-}0}/A_{0\text{-}1}$ ratio diminishes from 1.55 to 1.45 and 1.19 for **5PBI$_{(4\text{-}t\text{Bu})4}$**, **7PBI$_{(4\text{-}t\text{Bu})4}$** and **9PBI$_{(4\text{-}t\text{Bu})4}$** suggesting partial folding with increasing ring size (all data are summarized in Table 3 and graphically visualized in Figure 80). Notably, for the two smallest and most rigid macrocycles **2PBI$_{(4\text{-}t\text{Bu})4}$** and **3PBI$_{(4\text{-}t\text{Bu})4}$** identical $A_{0\text{-}0}/A_{0\text{-}1}$ ratios are observed in dichloromethane and toluene, which suggests the presence of similar conformations in both solvents.

Table 3. Characteristic optical spectroscopic data of **nPBI$_{(4\text{-}t\text{Bu})4}$** (n = 1–9) in dichloromethane and toluene.

n	$A_{0\text{-}0}/A_{0\text{-}1}$ (CH_2Cl_2)	$A_{0\text{-}0}/A_{0\text{-}1}$ (Tol)	Φ_{fl} (CH_2Cl_2)	Φ_{fl} (Tol)	τ_{fl} [ns] (CH_2Cl_2)	τ_{fl} [ns] (Tol)
1	1.66	1.67	0.73	0.86	4.4 ± 0.1	4.2 ± 0.03
2	1.25	1.26	0.07	0.58	3.2 ± 0.01	5.3 ± 0.08
3	1.42	1.44	0.64	0.79	3.1 ± 0.2	5.2 ± 0.3
4	1.52	1.30	0.53	0.16	2.6 ± 0.1	2.7 ± 0.1
5	1.58	1.55	0.59	0.78	2.7 ± 0.1	5.5 ± 0.4
6	1.58	1.29	0.56	0.15	3.2 ± 0.08	1.0 ± 0.03
7	1.60	1.45	0.52	0.53	2.7 ± 0.08	5.7 ± 0.3
8	1.60	1.32	0.56	0.14	2.9 ± 0.1	0.67 ± 0.01
9	1.60	1.19	0.54	0.13	3.0 ± 0.07	3.1 ± 0.1

Concomitantly with the changes observed for the $A_{0\text{-}0}/A_{0\text{-}1}$ ratio in the UV-vis absorption spectra, the fluorescence is significantly quenched in toluene for even-membered macrocycles **4PBI$_{(4\text{-}t\text{Bu})4}$**, **6PBI$_{(4\text{-}t\text{Bu})4}$** and **8PBI$_{(4\text{-}t\text{Bu})4}$** with quantum yields of only Φ_{fl} ~ 15% compared to the monomer reference **1PBI$_{(4\text{-}t\text{Bu})4}$** ($\Phi_{fl}$ = 86%), indicating the presence of additional non-radiative decay channels due to the interacting PBI units. For the odd-numbered macrocycles the fluorescence quantum yields remain high for the cycles **3PBI$_{(4\text{-}t\text{Bu})4}$**, **5PBI$_{(4\text{-}t\text{Bu})4}$**, **7PBI$_{(4\text{-}t\text{Bu})4}$** and only decreases significantly for the largest **9PBI$_{(4\text{-}t\text{Bu})4}$** to 13%.

In dichloromethane with the exception of **2PBI$_{(4\text{-}t\text{Bu})4}$**, fluorescence quantum yields are only little affected and remain high for the whole series (Φ_{fl} = 52–64%). Accordingly, the changes in the fluorescence quantum yields follow exactly the same trend as observed for the $A_{0\text{-}0}/A_{0\text{-}1}$ ratios, confirming the presence of folded species for even membered

macrocycles and increasing amounts of folded species for odd membered macrocycles with increasing ring size (Figure 80b).

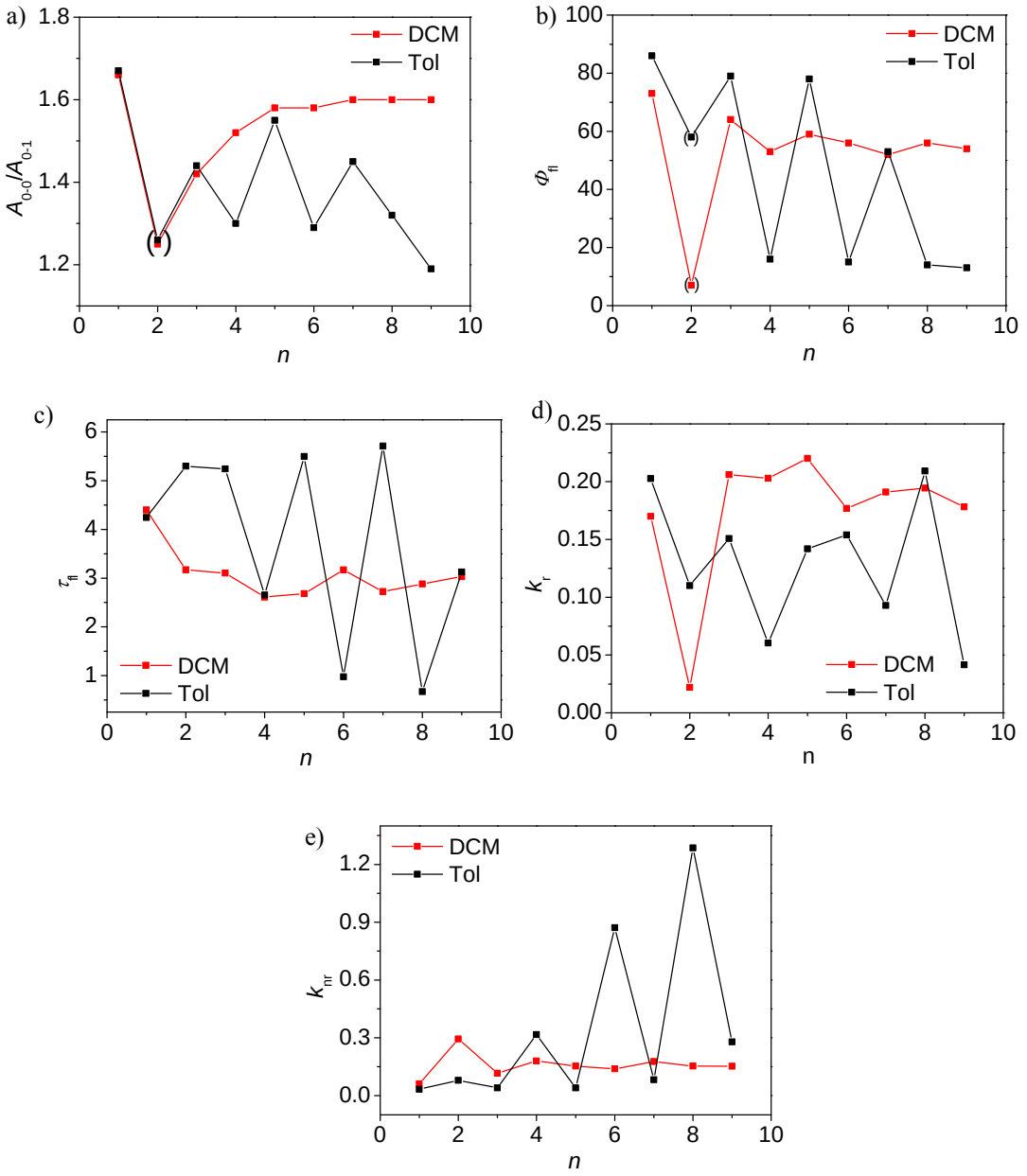

Figure 80. Plots of optical and photophysical data against the number of PBI units of macrocycles **nPBI$_{(4\text{-}t\text{Bu})4}$** (n = 1–9) in dichloromethane (DCM) and toluene. a) $A_{0\text{-}0}/A_{0\text{-}1}$ ratio of the transition bands in the absorption; b) fluorescence quantum yield; c) fluorescence lifetime; d) radiative rate constant k_r; e) non-radiative rate constant k_{nr}.

The experimental fluorescence lifetimes τ_{fl} in dichloromethane show little variation for all the cycles (2.6–3.2 ns), which are, however, reduced compared to **1PBI$_{(4\text{-}t\text{Bu})4}$** with a lifetime of 4.4 ± 0.1 ns. In toluene the fluorescence lifetimes reflect again the odd-even effect of the molecular folding (Figure 80c). For the odd-numbered cycles the

fluorescence lifetimes have values between 5.2 and 5.7 ns that are even higher than for the monomer (4.2 ns), whereas the even-numbered cycles have much lower lifetimes of 0.67–2.7 ns. The nonamer **9PBI$_{(4\text{-}t\mathrm{Bu})4}$** is again special and has a lifetime in-between (3.1 ± 0.1 ns) indicating the presence of folded units.

With the obtained fluorescence lifetimes τ_{fl} and the quantum yields Φ_{fl} the radiative and non-radiative rate constants can be estimated. The radiative rate constant is given with $k_r = \Phi_{fl} \times \tau_{fl}^{-1}$ and has in dichloromethane for all of the cycles except **2PBI$_{(4\text{-}t\mathrm{Bu})4}$** a value of ~0.2 ns^{-1} (Table 4). The non-radiative rate constant $k_{nr} = (1 - \Phi_{fl}) \times \tau_{fl}^{-1}$ is with ~0.17 ns^{-1} for all larger macrocycles **3PBI$_{(4\text{-}t\mathrm{Bu})4}$** to **9PBI$_{(4\text{-}t\mathrm{Bu})4}$** slightly lower than k_r.

Table 4. Radiative and non-radiative rate constants for **nPBI$_{(4\text{-}t\mathrm{Bu})4}$** (n = 1–9) in dichloromethane and toluene.

n	k_r [ns^{-1}] (CH_2Cl_2)[a]	k_{nr} [ns^{-1}] (CH_2Cl_2)[b]	k_r [ns^{-1}] (Tol)[a]	k_{nr} [ns^{-1}] (Tol)[b]
1	0.17	0.061	0.20	0.033
2	0.022	0.29	0.11	0.079
3	0.21	0.12	0.15	0.040
4	0.20	0.18	0.060	0.32
5	0.22	0.15	0.14	0.040
6	0.18	0.14	0.15	0.87
7	0.19	0.18	0.093	0.082
8	0.19	0.15	0.21	1.29
9	0.18	0.15	0.042	0.28

a) $k_r = \Phi_{fl} \times \tau_{fl}^{-1}$; b) $k_{nr} = (1-\Phi_{fl}) \times \tau_{fl}^{-1}$

In toluene the odd-even effect is consistently evident with $k_r > k_{nr}$ for cycles with odd numbers of PBI chromophores where the differences between both values gets smaller with higher flexibility from reference **1PBI$_{(4\text{-}t\mathrm{Bu})4}$** to cycles **3PBI$_{(4\text{-}t\mathrm{Bu})4}$**, **5PBI$_{(4\text{-}t\mathrm{Bu})4}$** and **7PBI$_{(4\text{-}t\mathrm{Bu})4}$**, and finally changes for **9PBI$_{(4\text{-}t\mathrm{Bu})4}$** to $k_r < k_{nr}$. On the other hand, for the even-numbered cycles k_r is always smaller than k_{nr} (Table 4) from 0.079 for **2PBI$_{(4\text{-}t\mathrm{Bu})4}$** to 1.29 ns^{-1} for **8PBI$_{(4\text{-}t\mathrm{Bu})4}$**. A somewhat different trend is found for the radiative rate constant where an increase occurs for the even-numbered cycles from 0.06 to 0.21 ns^{-1} with increasing ring size, but a decrease for the odd-numbered cycles from 0.20 to 0.042 ns^{-1} (Table 4, Figure 80d, e).

3.7.2 Solvent-dependent Folding Properties

To clarify the origin of the peculiar properties of PBI macrocycles in toluene their absorption properties were further analyzed in a series of non-aromatic solvents (acetone, THF, CH_2Cl_2, $CHCl_3$, Et_2O, dioxane and CCl_4, with ε_r = 20.7, 9.10, 7.60, 4.81, 4.30, 2.25 and 2.24, respectively). For all of these solvents characteristic monomer-like bandshapes and $A_{0\text{-}0}/A_{0\text{-}1}$ ratios were observed (Figure 120 in the appendix), corroborating the presence of unfolded wide-stretched conformations. Thus, solvent polarity can be excluded as the driving force for the folding process.

Since the folding so far was only observed in toluene, other aromatic solvents were next examined by UV-vis absorption spectroscopy. By comparison of the $A_{0\text{-}0}/A_{0\text{-}1}$ ratios to the previously discussed values of the corresponding CH_2Cl_2 solutions in which the macrocycles are in their unfolded state, the degree of folding in the individual aromatic solvent can be monitored (Figure 81). For the monomeric reference **1PBI$_{(4\text{-}t\text{Bu})4}$** a value of ~1.66 was found for all the applied solvents confirming that no intermolecular interactions between the solvent molecules and the given chromophore influence the band shape (Figure 81a black line). In the dimer **2PBI$_{(4\text{-}t\text{Bu})4}$** (red line) and trimer **3PBI$_{(4\text{-}t\text{Bu})4}$** (blue line), lower values of ~1.3 (dimer) and ~1.4 (trimer) are observed. The values are, however, rather independent of the respective solvent, which suggests solvent-independent conformations, i.e. rigid scaffolds (Figure 81a).

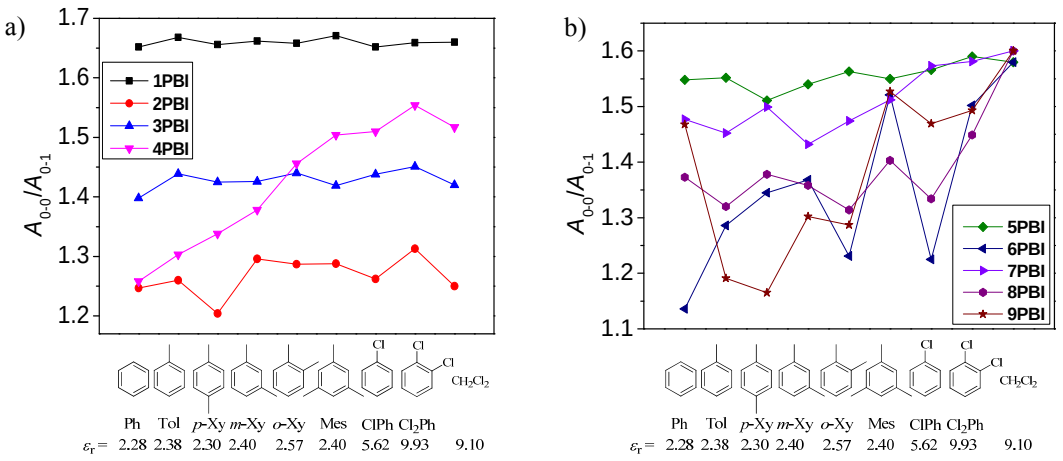

Figure 81. Plots of the $A_{0\text{-}0}/A_{0\text{-}1}$ ratios in different aromatic solvents and CH_2Cl_2 for **1PBI$_{(4\text{-}t\text{Bu})4}$**–**4PBI$_{(4\text{-}t\text{Bu})4}$** (a) and **5PBI$_{(4\text{-}t\text{Bu})4}$**–**9PBI$_{(4\text{-}t\text{Bu})4}$** (b).

In contrast, the $A_{0\text{-}0}/A_{0\text{-}1}$ ratios for **4PBI$_{(4\text{-}t\text{Bu})4}$** differ strongly depending on the type of aromatic solvents from 1.26 in benzene to 1.55 in *ortho*-dichlorobenzene (purple line).

This indicates a successive shift of the equilibrium towards the folded state in the order of Cl_2Ph < ClPh < Mes < *o*-Xy < *m*-Xy < *p*-Xy < Tol < Ph (Figure 81a). Similar trends can be observed for the folding of the larger macrocycles **6PBI$_{(4\text{-}t\text{Bu})4}$**, **8PBI$_{(4\text{-}t\text{Bu})4}$** and **9PBI$_{(4\text{-}t\text{Bu})4}$**, however, the order of the solvent that promotes the folding differs (Figure 81b). Clearly, also in this solvent series no relationship between folding tendency and solvent polarity can be deduced. Instead, these experiments indicate that the position and number of the methyl or chlorine groups in the aromatic solvent molecules plays a role for the conformational preference and PBI-PBI interactions of the macrocycles.

It is indeed particularly impressive that the $A_{0\text{-}0}/A_{0\text{-}1}$ ratio for **4PBI$_{(4\text{-}t\text{Bu})4}$** (and similarly other odd-numbered **nPBI**s, see Figure 81b) is able to distinguish the utilized aromatic solvents, giving specific values of 1.26 (Ph), 1.30 (Tol), 1.34 (*p*-Xy), 1.38 (*m*-Xy), 1.46 (*o*-Xy), 1.50 (Mes), 1.57 (ClPh), and 1.55 (Cl_2Ph) (all values are summarized in Table 5). Accordingly, **4PBI$_{(4\text{-}t\text{Bu})4}$** can be utilized as a molecular probe for the determination of the given aromatic solvent.

Table 5. Comparison of the $A_{0\text{-}0}/A_{0\text{-}1}$ ratios of macrocycles **nPBI$_{(4\text{-}t\text{Bu})4}$** (n = 2–9) and the monomeric reference compound **1PBI$_{(4\text{-}t\text{Bu})4}$** in different aromatic solvents and dichloromethane.

Solvent	n = 1	n = 2	n = 3	n = 4	n = 5	n = 6	n = 7	n = 8	n = 9
Ph	1.65	1.25	1.40	1.26	1.55	1.14	1.48	1.37	1.47
Tol	1.67	1.26	1.44	1.30	1.55	1.29	1.45	1.32	1.19
p-Xy	1.66	1.20	1.43	1.34	1.51	1.35	1.50	1.38	1.17
m-Xy	1.66	1.30	1.43	1.38	1.54	1.37	1.43	1.36	1.30
o-Xy	1.66	1.29	1.44	1.46	1.56	1.23	1.47	1.31	1.29
Mes	1.67	1.29	1.42	1.50	1.55	1.52	1.51	1.40	1.53
ClPh	1.65	1.26	1.44	1.51	1.57	1.23	1.57	1.33	1.47
Cl_2Ph	1.66	1.31	1.45	1.55	1.59	1.50	1.58	1.45	1.49
CH_2Cl_2	1.66	1.25	1.42	1.52	1.58	1.58	1.60	1.60	1.60

In the previous investigations for **2PBI$_{(4\text{-}t\text{Bu})4}$** we could demonstrate that this rigid cyclophane acts as a good host molecule in chloroform, which can bind various planar aromatic guest molecules with appreciable binding constants (chapter 3.2). For the larger macrocycles investigated here such binding properties are absent, which can be attributed to a lack of preorganization, i.e. the prevalence of wide-stretched conformations in the majority of solvents. This conformational preference obviously changes for the even-numbered macrocycles in aromatic solvents that exert a template effect to shift the conformational equilibrium towards conformations with pronounced PBI-PBI

interactions. The fact that identical $A_{0\text{-}0}/A_{0\text{-}1}$ ratios are observed for **2PBI$_{(4\text{-}t\text{Bu})4}$** and **4PBI$_{(4\text{-}t\text{Bu})4}$** in benzene (Figure 81a) indeed corroborates the perception that similar PBI-PBI contacts are given for **2PBI$_{(4\text{-}t\text{Bu})4}$** and folded **4PBI$_{(4\text{-}t\text{Bu})4}$** as suggested in Figure 82. Based on the in-depth studies for **2PBI$_{(4\text{-}t\text{Bu})4}$** it is accordingly reasonable to assume that one or more aromatic solvent molecules fill up the space between a PBI dye pair also for **4PBI$_{(4\text{-}t\text{Bu})4}$** as illustrated in Figure 82. Thus, under the template effect of the solvent molecules the PBI oligomer chain of odd-membered macrocycles coils into a double-string rope leading to the observed spectral features. Thereby subtle sterical differences of the respective incorporated solvent molecules modulate the $A_{0\text{-}0}/A_{0\text{-}1}$ ratio in a rather specific way.

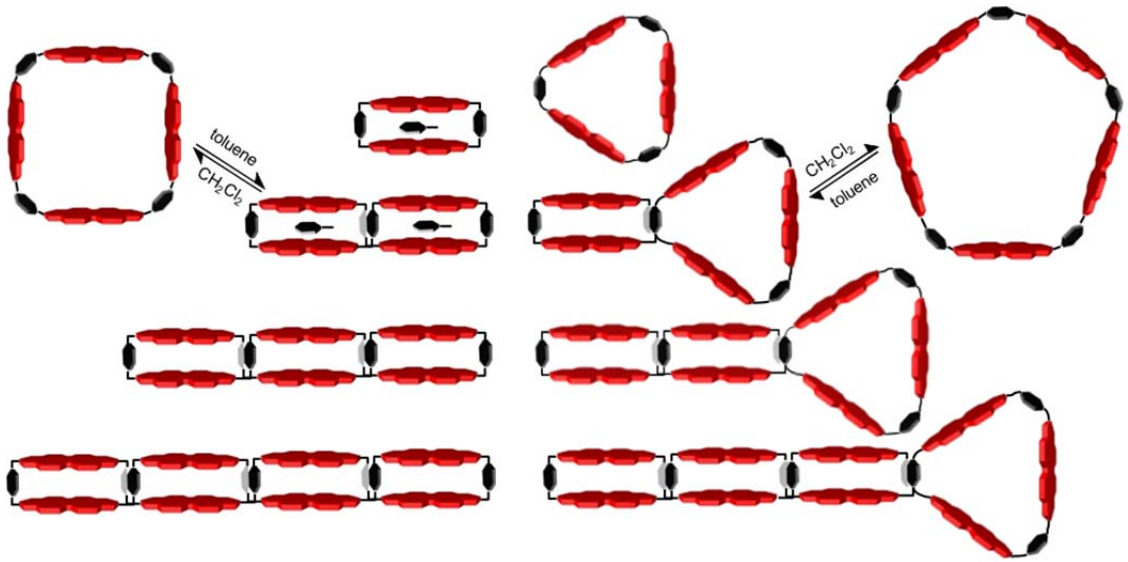

Figure 82. Schematic sketch of toluene-filled **2PBI$_{(4\text{-}t\text{Bu})4}$**, solvent-dependent conformational change of **4PBI$_{(4\text{-}t\text{Bu})4}$**, **6PBI$_{(4\text{-}t\text{Bu})4}$** and **8PBI$_{(4\text{-}t\text{Bu})4}$**, rather solvent-independent wide-stretched conformations of **3PBI$_{(4\text{-}t\text{Bu})4}$**, **5PBI$_{(4\text{-}t\text{Bu})4}$** and **7PBI$_{(4\text{-}t\text{Bu})4}$**, and the special partial folding transition of **9PBI$_{(4\text{-}t\text{Bu})4}$**.

To get a better understanding of the folded structures, molecular modelling of **4PBI$_{(4\text{-}t\text{Bu})4}$** was performed using force field calculations (Figure 83). The geometry optimized structure corroborates the presence of a pleated structure consisting of two PBI pairs whose interchromophore distance of around 6.8 Å appears ideally suited to embed aromatic solvent molecules. Because of the two crossing xylene linkers, the PBI dyes have a twisted arrangement of 15° to each other that directs two bay-substituents of each PBI molecule into the cavity of the neighbored PBI cores. This might explain why the folded macrocycles don't behave in all properties like the rigid **2PBI$_{(4\text{-}t\text{Bu})4}$** with its more rigid cofacial arrangement of the chromophores and why rather similar solvents afford

distinguishable optical signals. Thus, it is the conformationally rather flexible phenoxy-substitutent[208b] whose arrangement is governed by the respective embedded solvent molecules.

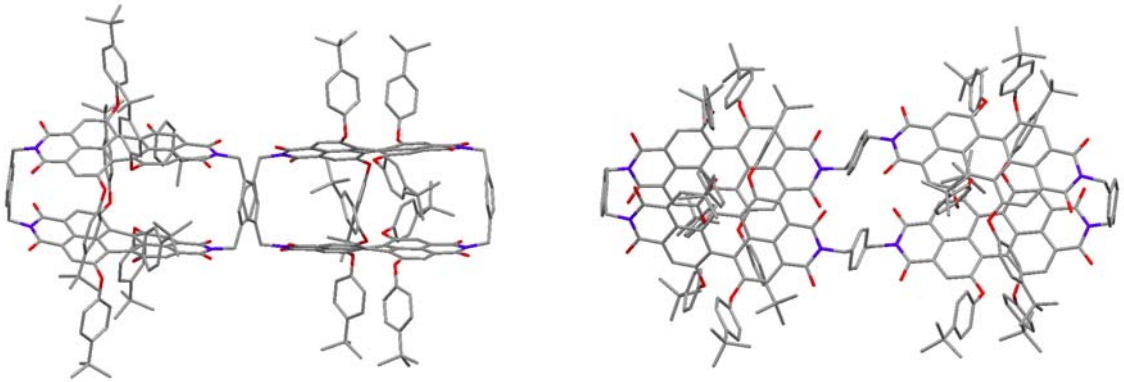

Figure 83. Geometry optimized structure of the folded **4PBI$_{(4\text{-}t\text{Bu})4}$** in side view (left) and top view (right) obtained by force field optimization; Maestro 9.3, MacroModel 9.8, MM2*.

Assuming that this structural motive can also be adapted to **6PBI$_{(4\text{-}t\text{Bu})4}$** and **8PBI$_{(4\text{-}t\text{Bu})4}$**, the observed similar optical properties of the even-numbered macrocycles can be explained, although with increasing flexibility other folded patterns might be possible as well. It is clear that the odd-numbered cycles cannot form such pairs of dimers including all the chromophore units and that the smaller trimer forms a rather rigid triangular structure (Figure 82). With higher flexibility partially folded motives might be implied for the larger macrocycles. Based on the $A_{0\text{-}0}/A_{0\text{-}1}$ ratio and the fluorescence quantum yield such partial folding appears to be absent for **5PBI$_{(4\text{-}t\text{Bu})4}$** but becomes more likely for **7PBI$_{(4\text{-}t\text{Bu})4}$**. Finally, for **9PBI$_{(4\text{-}t\text{Bu})4}$** both $A_{0\text{-}0}/A_{0\text{-}1}$ ratio and fluorescence quantum yield suggest the presence of a mostly pleated structure in toluene that might consist of three pairs of PBIs and one triangular arrangement (Figure 82).

Whilst a binding of aromatic molecules could not be observed by conventional titration experiments for macrocycles larger than **2PBI$_{(4\text{-}t\text{Bu})4}$**, the transition between unfolded and folded conformations could be easily monitored by UV-vis absorption spectra of the tetrameric cycle **4PBI$_{(4\text{-}t\text{Bu})4}$** in different mixtures of dichloromethane and toluene (Figure 84).

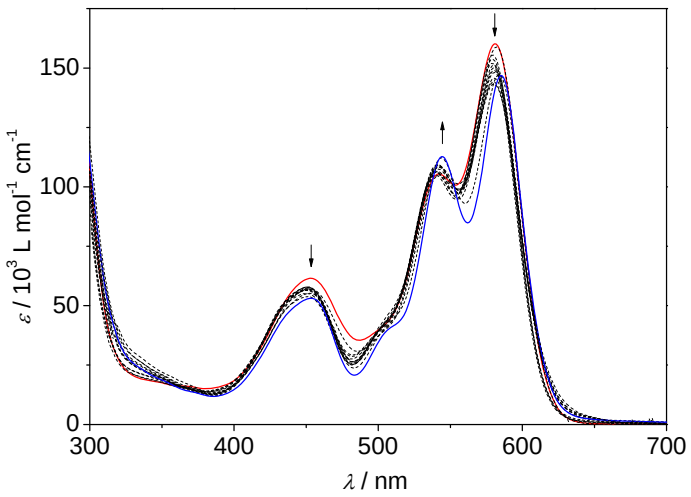

Figure 84. UV-vis absorption spectra of **4PBI$_{(4\text{-}t\text{Bu})4}$** in solvent mixtures of CH_2Cl_2 (red line) and toluene (blue line); arrows indicate the spectral changes with increasing CH_2Cl_2 content; c = 5 x 10^{-6} M; RT.

From these absorption spectra it is obvious that more than 70% of toluene is needed to induce the folding process which explains the failure of **4PBI$_{(4\text{-}t\text{Bu})4}$** to give host-guest complexes with aromatic guest molecules in well-solvating solvents such as chloroform as observed for the rigid and properly preorganized **2PBI$_{(4\text{-}t\text{Bu})4}$**. Nevertheless, the successive decrease of the $A_{0\text{-}0}/A_{0\text{-}1}$ ratio at higher toluene contents allows to estimate the free energy for the folding process in toluene according to the method of Moore and Ray (Figure 85).[219] For this determination two assumptions have to be made: 1) the extinction coefficient ε_U in CH_2Cl_2 solution corresponds to the entirely unfolded state and 2) the extinction coefficient ε_F found in toluene is related to the complete folded state.

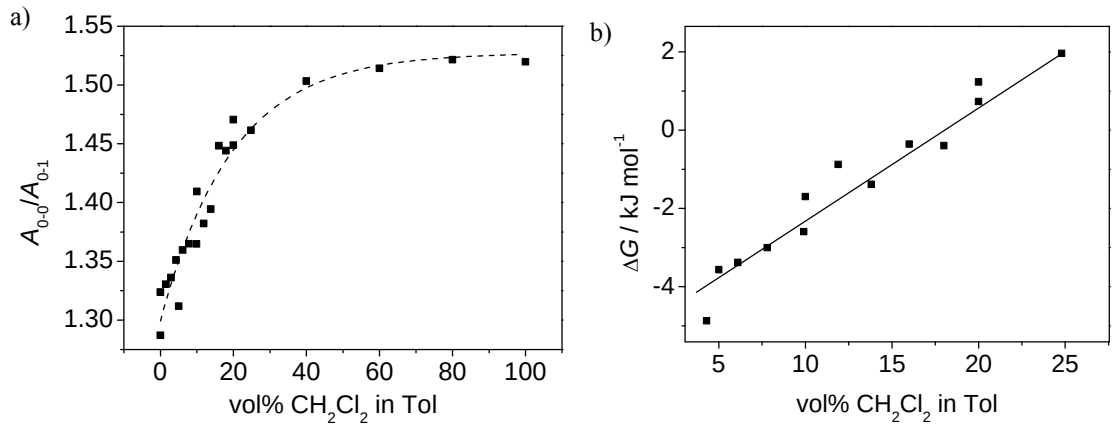

Figure 85. Changes in the $A_{0\text{-}0}/A_{0\text{-}1}$ ratio of **4PBI$_{(4\text{-}t\text{Bu})4}$** in CH_2Cl_2/toluene mixtures and plot of the ΔG values for the folding process derived from the spectral development at the 0-0 transition band. The solid line represents the fitting curve from linear regression according to equation (13).

From there on, the mole fraction α_U of chromophores in the unfolded state can be estimated for all solvent mixtures using equation (10):

$$\alpha_U = \frac{\varepsilon_F - \varepsilon_{obs}}{\varepsilon_F - \varepsilon_U} \qquad (10)$$

where ε_{obs} is the extinction value of the individual solvent mixture at the 0-1 or 0-0 transition band. The equilibrium constant K_{eq} and the Gibbs free energy changes ΔG for each solvent composition can then be calculated according to equations (11) and (12):

$$K_{eq} = \frac{c_F}{c_U} = \frac{1-\alpha_U}{\alpha_U} \qquad (11)$$

$$\Delta G = -RT \ln K_{eq} \qquad (12)$$

where c_F and c_U are the concentrations of the folded and unfolded species, respectively. In analogy to the solvent denaturation of proteins and peptide secondary structures, the free energy change between both conformations is assumed to behave linearly with the solvent composition.[220] This enables the estimation of the Gibbs free energy in pure toluene by extrapolation of the fitting line of the $A_{0\text{-}0}$ transition band to –5.3 ± 0.2 kJ/mol with a slope of $m[CH_2Cl_2]$ = 292 ± 13 kJ/mol (Figure 85b) according to equation (13):

$$\Delta G = \Delta G(tol) - m[CH_2Cl_2] \qquad (13)$$

The detailed thermodynamic data obtained by this analysis are given in Table 6.

3.7.3 Excited State Properties

There is one important issue to keep in mind when discussing UV-vis absorption and fluorescence spectroscopy data. The former data result from optical excitations of molecules in the ground state that exist in their thermally equilibrated conformational manifold. Upon excitation these molecules are promoted into their excited states that are on the other hand not equilibrated. Furthermore, at low to moderate light intensities only one molecule in the macrocycle is optically excited whilst the others prevail in the ground state. Such excited macrocycles may exhibit various relaxation pathways into energetically more favourable geometries and/or electronically more stable configurations, e.g. excimers, charge transfer states, etc. The respective states will finally determine the relaxation path back to the ground state via radiative and non-radiative pathways.

Table 6. Thermodynamic data obtained by the analysis of the $A_{0\text{-}0}$ transition band in absorption spectra of **4PBI$_{(4\text{-}t\text{Bu})4}$** in CH_2Cl_2/toluene mixtures.

vol% CH_2Cl_2 in Tol	ε_{obs} ($A_{0\text{-}0}$) / 10^3 L mol^{-1} cm^{-1}	α_U	K_{eq} / M^{-1}	ΔG / kJ mol^{-1}
100	160.20	1.00	0.00	--
80	159.97	0.99	0.015	10.4
60	158.93	0.92	0.092	5.92
40	156.28	0.74	0.35	2.60
25	155.49	0.69	0.45	1.96
20	153.75	0.57	0.75	0.73
18	152.04	0.46	1.17	-0.39
16	152.10	0.46	1.16	-0.36
14	150.58	0.36	1.75	-1.39
12	150.16	0.34	1.98	-1.70
10	149.02	0.26	2.85	-2.59
8	148.56	0.23	3.36	-3.00
6	148.17	0.20	3.92	-3.38
4	146.95	0.12	7.15	-4.87
2	145.23	0.01	12.2	-6.19
0	145.10	0.00	--	--

According to the data from steady-state fluorescence spectroscopy and the calculated radiative and non-radiative rates a quite uniform behavior for all cycles in dichloromethane except for **2PBI$_{(4\text{-}t\text{Bu})4}$** can be recognized. The exceptional behavior of the latter could be related to an unusually fast symmetry-breaking charge separation (SB-CS) in the previously discussed studies and will accordingly not be discussed here (see chapter 3.3). Instead, getting insights into the different relaxation pathways in dichloromethane and toluene for the larger macrocycles by time-resolved spectroscopy is the main goal for this chapter.

To elucidate the excited state dynamics of the macrocycles, femtosecond (fs) and nanosecond (ns) transient absorption (TA) spectroscopy was performed. Due to a low solubility of the larger macrocycles in toluene, these studies are restricted on **3PBI$_{(4\text{-}t\text{Bu})4}$**, **4PBI$_{(4\text{-}t\text{Bu})4}$** and **5PBI$_{(4\text{-}t\text{Bu})4}$**. In dichloromethane all of these macrocycles showed similar dynamics after photoexcitation at 580 nm (Figure 86 and Figure 121 – Figure 129) with the for tetraphenoxy-PBIs typical features of ground state bleach (GSB) at 458, 543 and 585 nm, stimulated emission (SE) at 610 and 658 nm and the excited state absorption

(ESA) at 707, 952 and 1031 nm.[112] After 3.06 ± 0.2 ns **3PBI$_{(4\text{-}t\text{Bu})4}$** reaches a new transient species that can be identified as the symmetry-broken charge separated state (SB-CS) similar to the previously discussed **2PBI$_{(4\text{-}t\text{Bu})4}$** (chapter 3.3) and other PBI macrocycles.[112] In this state new bands for the PBI radical anion and cation are present at 797, 993 and 1100 nm ($PBI^{-\bullet}$) and at 486, 628 and 1220 nm ($PBI^{+\bullet}$).[112]

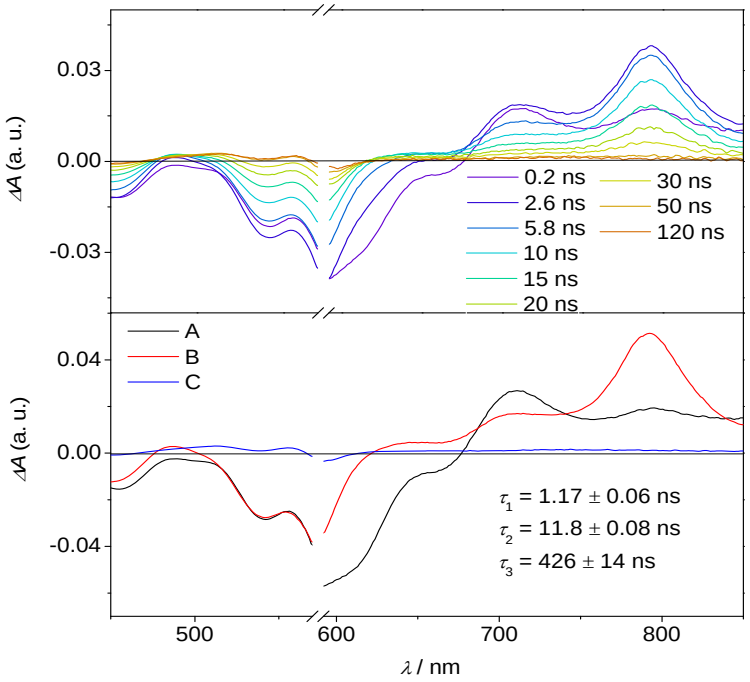

Figure 86. Nanosecond transient absorption spectra (top) of **4PBI$_{(4\text{-}t\text{Bu})4}$** in dichloromethane showing excited state dynamics after photoexcitation; species-associated spectra plots (bottom) reconstructed from global fits to the sequential A → B → C → ground state model, where A is the singlet excited state S_1, B is the charge separated state SB-CS and C is the PBI triplet T_1 (λ_{ex} = 580 nm, 1.0 μJ/pulse, 298 K).

The much slower charge separation in **3PBI$_{(4\text{-}t\text{Bu})4}$** (3.06 ± 0.2 ns) compared to **2PBI$_{(4\text{-}t\text{Bu})4}$** (161 ± 4 ps) is a clear indication that this process occurs through space between the PBI cores and not through bond and that the PBI dyes are further apart from each other in **3PBI$_{(4\text{-}t\text{Bu})4}$** compared to **2PBI$_{(4\text{-}t\text{Bu})4}$**. In **4PBI$_{(4\text{-}t\text{Bu})4}$** and **5PBI$_{(4\text{-}t\text{Bu})4}$** the charge separation is with 1.71 ± 0.06 and 2.25 ± 0.9 ns faster than in **3PBI$_{(4\text{-}t\text{Bu})4}$** (Figure 121 – Figure 129) that can be explained in terms of a higher flexibility of the larger cycles allowing the PBI molecules to approach each other in contrast to the rather rigid **3PBI$_{(4\text{-}t\text{Bu})4}$**. However, the charge separation is still much slower than in the conformationally fixed **2PBI$_{(4\text{-}t\text{Bu})4}$**, which suggests that also **4PBI$_{(4\text{-}t\text{Bu})4}$** and **5PBI$_{(4\text{-}t\text{Bu})4}$** prevail in wide-stretched conformations both in the ground and excited states.

The charges then recombine to a significant fraction to the PBI triplet state in 14.5 ± 0.1, 11.8 ± 0.08 and 12.7 ± 0.1 ns for **3PBI$_{(4\text{-}t\text{Bu})4}$**, **4PBI$_{(4\text{-}t\text{Bu})4}$** and **5PBI$_{(4\text{-}t\text{Bu})4}$** with a PBI triplet lifetime of 560 ± 18, 426 ± 14 and 403 ± 41 ns in an air-saturated solution (Figure 121 – Figure 129). The relatively short lifetimes of the triplet state can be explained by an energy transfer to molecular oxygen generating singlet oxygen. With this, the quantum yield of triplet formation can be estimated through the measurement of singlet oxygen emission at 1270 nm with methylene blue as literature known reference (Φ_Δ = 0.57 in dichloromethane).[169] Thereby, a quantum yield of ~20% was observed for **3PBI$_{(4\text{-}t\text{Bu})4}$**, **4PBI$_{(4\text{-}t\text{Bu})4}$** and **5PBI$_{(4\text{-}t\text{Bu})4}$**.

By switching the solvent to toluene, the symmetry-breaking charge separation gets energetically unfavored as elucidated in detail for **2PBI$_{(4\text{-}t\text{Bu})4}$** (chapter 3.3) and hence the triplet pathway is prevented. Now, the radiative pathway prevails after photoexcitation explaining the higher fluorescence quantum yields for the odd-numbered **3PBI$_{(4\text{-}t\text{Bu})4}$** and **5PBI$_{(4\text{-}t\text{Bu})4}$** in toluene (Figure 121 – Figure 129). In accordance with the fluorescence lifetimes (Table 3), the decay of the excited state of even-numbered **4PBI$_{(4\text{-}t\text{Bu})4}$** (Figure 87) is with 3.77 ± 0.6 ns much faster than that of the odd-numbered ones (6.60 ± 0.9, 6.44 ± 0.6 ns). Furthermore, an ultrafast decay of 2.4 ± 0.5, 2.7 ± 0.8 and 1.7 ± 0.2 ps was observed for **3PBI$_{(4\text{-}t\text{Bu})4}$**, **4PBI$_{(4\text{-}t\text{Bu})4}$** and **5PBI$_{(4\text{-}t\text{Bu})4}$**, respectively, which can be attributed to solvent and structural rearrangement.[208b]

Since the analysis based on species-associated spectra suggests that the excited state of **4PBI$_{(4\text{-}t\text{Bu})4}$** decays directly back to the ground state without passing through any other long living states such as an excimer,[94b] non-radiative internal conversion appears to be the most reasonable explanation for the pronounced fluorescence quenching in the folded conformation of this even-numbered macrocycle. If so, an increased vibrational coupling between the chromophores might be the reason and it is tempting to relate this coupling to the enhanced 0-1 transition band observed in the UV-vis absorption spectra.

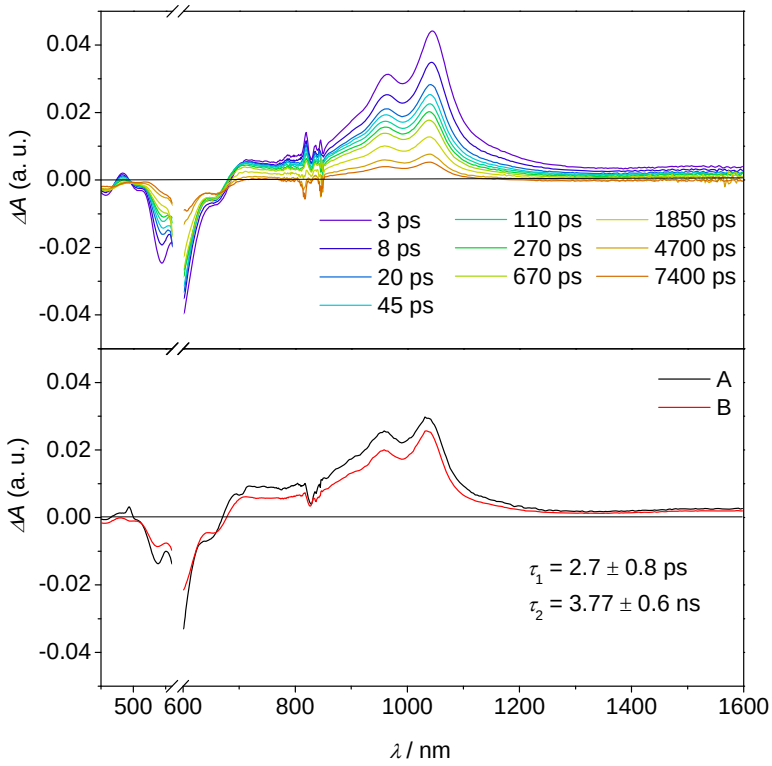

Figure 87. Femtosecond (top) transient absorption spectra of **4PBI$_{(4\text{-}t\text{Bu})4}$** in toluene showing the excited state dynamics after photoexcitation; species-associated spectra (bottom) reconstructed from global fits to the sequential A → B → ground state model, where A and B are ^{1}*PBI, (λ_{ex} = 580 nm, 1.0 μJ/pulse, 298 K).

3.7.4 Femtosecond Stimulated Raman Spectroscopy

To take a closer look on the vibrational coupling, femtosecond stimulated Raman spectroscopy (FSRS) measurements were performed on **nPBI$_{(4\text{-}t\text{Bu})4}$** (n = 1–5). Upon excitation at the very edge of the absorption band at 610 nm (0.6 μJ/pulse) the characteristic C-C stretching modes of the excited PBI core at 1360, 1394, 1458, 1549 and 1590 cm^{-1} were observed in dichloromethane (Figure 88).[221] From these studies it is obvious that the relative intensities of the Raman bands of the macrocycles do not change compared to monomeric reference **1PBI$_{(4\text{-}t\text{Bu})4}$** in dichloromethane, confirming that there is only subtle interchromophoric vibrational coupling within the macrocycles. In toluene, however, the Raman bands at higher energy are slightly shifted to 1551 and 1594 cm^{-1}. While for monomeric **1PBI$_{(4\text{-}t\text{Bu})4}$** and **3PBI$_{(4\text{-}t\text{Bu})4}$** bearing PBIs at fixed distances the ratio of these frequencies I_{1551}/I_{1594} is greater than one, it is changed for **4PBI$_{(4\text{-}t\text{Bu})4}$** to I_{1551}/I_{1594} < 1. Furthermore, two new shoulders at 1374 and 1584 cm^{-1} are detected for **4PBI$_{(4\text{-}t\text{Bu})4}$**. The Raman spectrum of **2PBI$_{(4\text{-}t\text{Bu})4}$** in toluene is similar to that of **4PBI$_{(4\text{-}t\text{Bu})4}$**, whereas **5PBI$_{(4\text{-}t\text{Bu})4}$** shows a behavior that is in-between of **3PBI$_{(4\text{-}t\text{Bu})4}$** and **4PBI$_{(4\text{-}t\text{Bu})4}$** with

I_{1551}/I_{1594} ~ 1. Thus, these findings confirm a strong exciton-vibrational coupling in the even-numbered cycles,[148] whereas the odd-numbered compounds show a weaker vibrational interaction in an unfolded state.

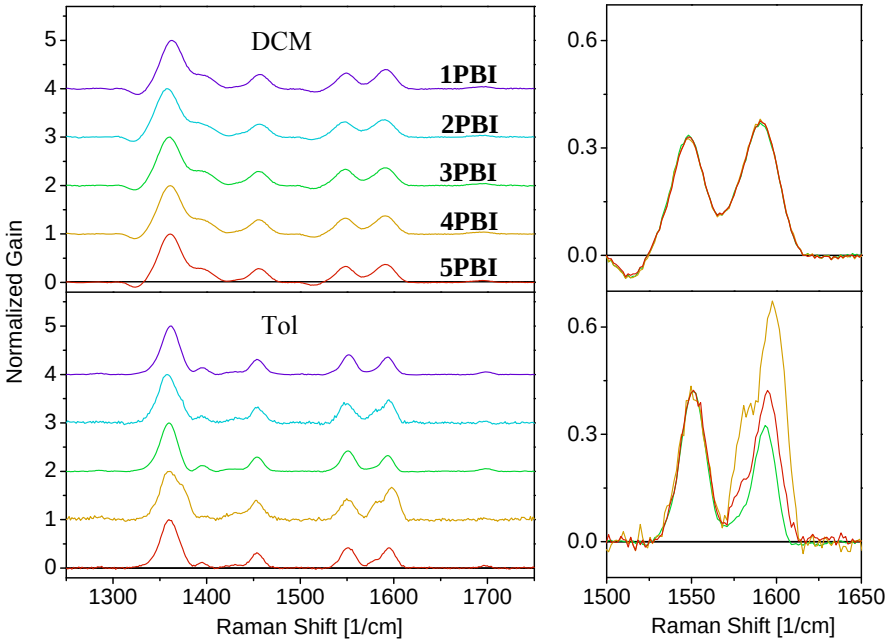

Figure 88. Normalized femtosecond stimulated Raman spectra of **1PBI$_{(4\text{-}t\text{Bu})4}$** to **5PBI$_{(4\text{-}t\text{Bu})4}$** in dichloromethane (top) and toluene (bottom); right: comparison of relative frequency intensities of **3PBI$_{(4\text{-}t\text{Bu})4}$**, **4PBI$_{(4\text{-}t\text{Bu})4}$** and **5PBI$_{(4\text{-}t\text{Bu})4}$**; λ_{RP} = 610 nm, 0.6 μJ/pulse, 298 K.

The behavior of **5PBI$_{(4\text{-}t\text{Bu})4}$** in the FSRS experiments can be explained based on the structural models shown in Figure 82, since it has a conformation that is in-between of the rigid unfolded **3PBI$_{(4\text{-}t\text{Bu})4}$** and the perfectly folded **4PBI$_{(4\text{-}t\text{Bu})4}$**. Furthermore, the dramatically increase of the non-radiative rate constants of the even-membered macrocycles seems to be an effect of the linear elongation of the dimer stacks. That implies an enhancement of the exciton-vibrational coupling with increasing ring size.

In this chapter a new series of PBI macrocycles with varied ring size from dimer to nonamer has been reported and their folding behavior has been elucidated in great detail by fluorescence, steady-state and transient absorption spectroscopy as well as femtosecond stimulated Raman spectroscopy. For these macrocycles a unique odd-even effect regarding the ring size could be established. The even-numbered macrocycles undergo intramolecular folding under the templating effect of aromatic solvents with concomitant fluorescence quenching to quantum yields as low as 14%, shortened fluorescence lifetimes and a pronounced exciton-vibrational coupling in the UV-vis

absorption spectra. In contrast, the macrocycles with odd number of chromophores show still the characteristic spectral features of monomeric reference **1PBI$_{(4\text{-}t\text{Bu})4}$** and converge to the folded cycles only for the largest and most flexible **9PBI$_{(4\text{-}t\text{Bu})4}$**. Transient absorption spectroscopy revealed symmetry-breaking charge separation and triplet formation for all investigated macrocycles in dichloromethane whilst an accelerated internal conversion through folding was observed for even-numbered macrocycles in toluene. Intensity changes of the Raman frequency at 1594 cm^{-1} in the excited PBI are attributed to vibrational couplings. The spectral features were supported by molecular modelling for **4PBI$_{(4\text{-}t\text{Bu})4}$** showing a folding to pairs of dimers that explains the to-date for macrocycles unprecedented odd-even effect in the conformational and photophysical properties. The latter could be utilized to distinguish eight aromatic solvents unambiguously based on intensity ratio of the exciton-vibronic transitions.

3.8 Self-Assembly of Perylene Bisimide Macrocycles on HOPG Surfaces

Although the interest on artificial dye containing macrocycles has grown tremendously, only few examples are reported on 2D networks of such cyclic systems that mimic the organization of photosynthetic membranes.[107, 135] To investigate such networks atomic force microscopy (AFM) is a powerful tool and is thus often used for imaging cyclic arrays. The control of structure is thereby an important step, since the orientation of the chromophores to each other defines their electronic interactions. To gather this control of structure the size of the macrocycles was varied in which small and rigid cycles show a more defined arrangement than large and flexible ones.[107] Furthermore, the coordination sphere of metal ions was used that forms in the right combination with ligands honeycomb or squaric nanopatterns.[135] Nowadays, also covalent bonding on surfaces, the so called SCOFs (surface covalent organic frameworks), becomes a prominent method to control the formed network in size and structure.[222]

In this chapter, superficial structures of supramolecular macrocycles, composed of four to nine perylene bisimides (PBIs) (**4PBI$_{(4\text{-}t\text{Bu})4}$**–**9PBI$_{(4\text{-}t\text{Bu})4}$**) are reported. These macrocycles were self-assembled on highly ordered pyrolytic graphite (HOPG) surfaces in a two-dimensional manner, which was confirmed by AFM. With these compounds the motives of self-assembly can be varied by changing the ring size in the macrocycles. Furthermore, **4PBI$_{(4\text{-}t\text{Bu})4}$** showed a special behavior with three different types of 2D networks on the surface.

To study the capability of the *para*-xylylene bridged PBI macrocycles to self-assemble into 2D networks the adsorption on HOPG was investigated by AFM. Therefore, dilute solutions of **nPBI$_{(4\text{-}t\text{Bu})4}$** ($c$ = 5 x 10^{-6} M) in dichloromethane were spin-coated onto HOPG under 3000 rpm. Surprisingly, the macrocycles **2PBI$_{(4\text{-}t\text{Bu})4}$**, **3PBI$_{(4\text{-}t\text{Bu})4}$** and **8PBI$_{(4\text{-}t\text{Bu})4}$** did not result in any ordered 2D structures and only amorphous material was visualized by AFM. On the other hand, for the other macrocycles ordered structures could be visualized.

For the macrocycles **6PBI$_{(4\text{-}t\text{Bu})4}$** and **9PBI$_{(4\text{-}t\text{Bu})4}$** single spherical particles were observed (Figure 89). The film thickness was found to be 0.55 ± 0.03 nm for **6PBI$_{(4\text{-}t\text{Bu})4}$** and 0.75 ± 0.05 nm for **9PBI$_{(4\text{-}t\text{Bu})4}$**. In both cases the film thickness indicates the formation of monolayers in which the larger macrocycles **9PBI$_{(4\text{-}t\text{Bu})4}$** have higher flexibility and stronger distortion in structure and thus lead to slightly thicker 2D networks. The diameters of the particles are with 3.0 ± 0.2 and 4.5 ± 0.5 nm in good agreement with the

calculated diameter of the unfolded cycles **6PBI$_{(4\text{-}t\text{Bu})4}$** (3.0 nm) and **9PBI$_{(4\text{-}t\text{Bu})4}$** (4.7 nm) from geometry optimized structures. Thus, the adsorption on the surface confirms our structural prediction of unfolded cycles in polar solvents from chapter 3.7. The orientation of the cycles in the 2D network can be described as close-packing of spheres in which one macrocycle is surrounded by six neighboring molecules. This type of packing typically occurs by geometry reasons and not through interactions between the molecules. This can easily be explained, considering that the tetra-substituted PBIs show only weak driving force for π-π contact[189] and the xylylene linkers are too small to control the self-assembly of the large and flexible macrocycles.

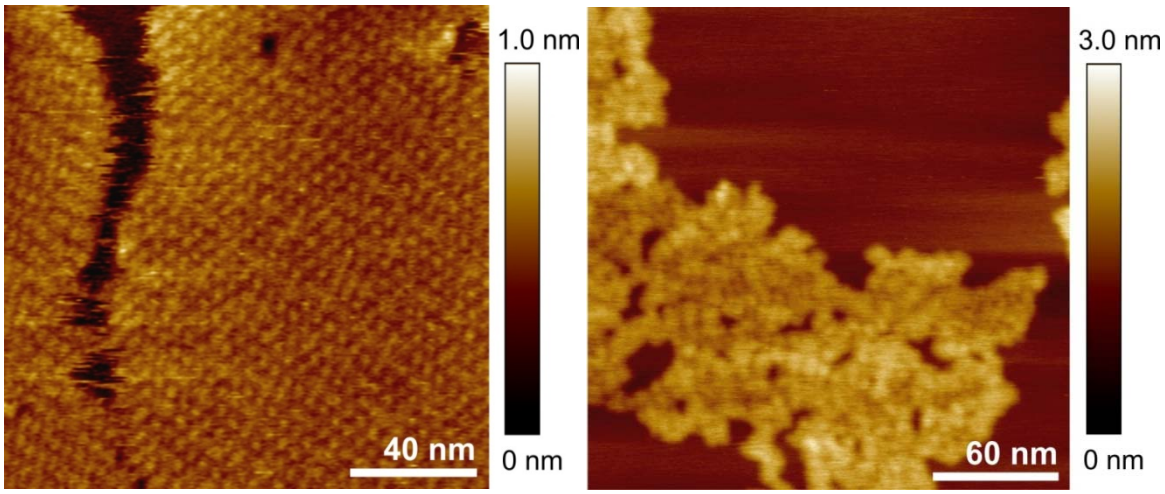

Figure 89. Tapping-mode AFM height images of **6PBI$_{(4\text{-}t\text{Bu})4}$** (left) and **9PBI$_{(4\text{-}t\text{Bu})4}$** (right) films spin coated onto HOPG; 3000 rpm; DCM; c = 5 x 10^{-6} M.

The cycles **5PBI$_{(4\text{-}t\text{Bu})4}$** and **7PBI$_{(4\text{-}t\text{Bu})4}$** appear to form lamellar structures of extended linear arrangements (Figure 90). Herein, the widths of these stripes are with 2.8 ± 0.4 and 3.5 ± 0.4 nm again in good agreement with the calculated ring diameters of the corresponding cycles in their open form (2.7 and 3.6 nm). The heights of the networks are 0.75 ± 0.1 and 0.49 ± 0.02 nm and thus suggest the formation of monolayers in which the macrocycles are lying flat on the graphite.

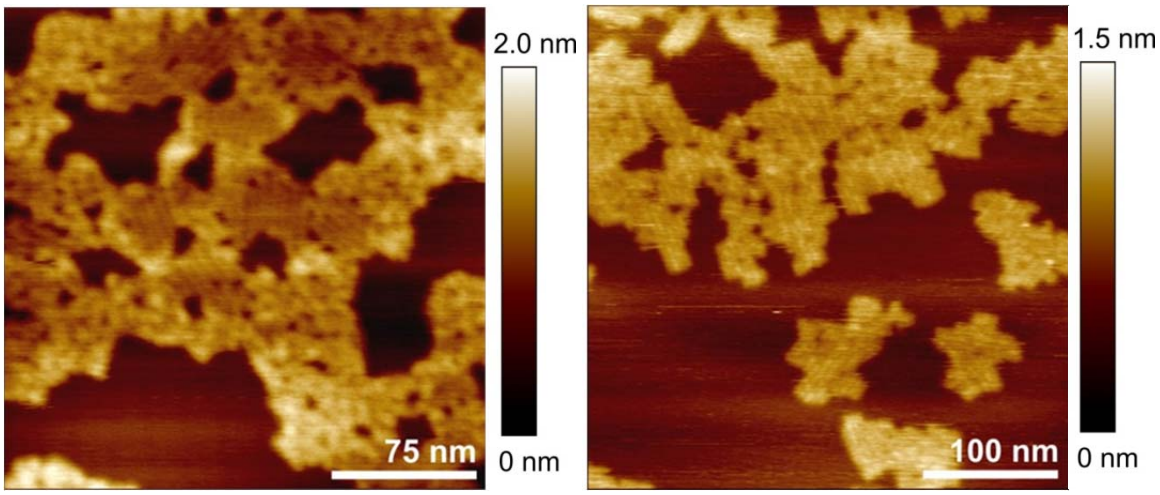

Figure 90. Tapping-mode AFM height images of **5PBI$_{(4\text{-}t\text{Bu})4}$** (left) and **7PBI$_{(4\text{-}t\text{Bu})4}$** (right) films spin-coated onto HOPG; 3000 rpm; DCM, c = 5 x 10^{-6} M.

The most interesting features were observed for the cyclic tetramer **4PBI$_{(4\text{-}t\text{Bu})4}$**, where three different types of structures were found on HOPG. By having a closer look on the AFM images the transitions between these structures can be observed (Figure 91, Figure 92). After spin-coating a lamellar arrangement with a thickness of 0.50 ± 0.05 nm and a diameter of 2.3 ± 0.4 nm (calculated: 2.0 nm) is formed, similar to **5PBI$_{(4\text{-}t\text{Bu})4}$** and **7PBI$_{(4\text{-}t\text{Bu})4}$**. The flat aligned macrocycles then spontaneously start to convert into quadratic patterns (Figure 91a).

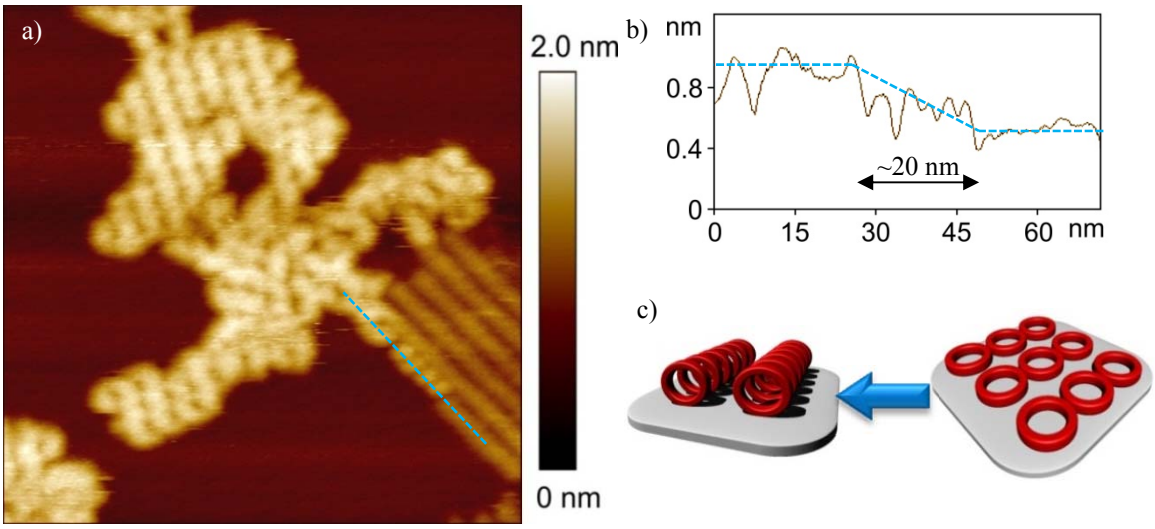

Figure 91. a) Tapping-mode AFM height image of a **4PBI$_{(4\text{-}t\text{Bu})4}$** film spin-coated onto HOPG; 3000 rpm; DCM, c = 5 x 10^{-6} M; b) cross-section along the dotted line in the AFM image; c) proposed model of the individual nanostructures.

With the height of 1.0 ± 0.1 nm, it is clear that these structures are no more flat lying macrocycles, but straightened up cycles that are slightly compressed and slipped in their conformation due to the empty void. The cross-section along the raising process inidcates a successive increase of the film thickness over a range of ~20 nm (Figure 91b). Also the width broadening to 1.7 x 2.9 nm confirms the compressed and slipped arrangement of the macrocycles. These data thus suggest that the macrocycles "stand" on the surface without any contact between the single multi-chromophores (Figure 91c). In these "standing" cycles only one core-twisted PBI subunit has contact with the surface resulting in weak interactions between the macrocycle **4PBI$_{(4\text{-}t\text{Bu})4}$** and HOPG. This weak adsorption on the surface allows a rearrangement of the molecules by mechanical force, using the tip of the microscope. Thus, by scanning the same area several times, the quadratic patterns can be scratched, moving the "standing" macrocycles (Figure 92).

After three scans the molecules start to approach each other and form tube like arrays with a width (3.0 ± 0.4 nm) and height (0.9 ± 0.1 nm) of one compressed macrocycle. During this process the flat lying and standing cycles with different orientation regarding the scan direction are not influenced in their position.

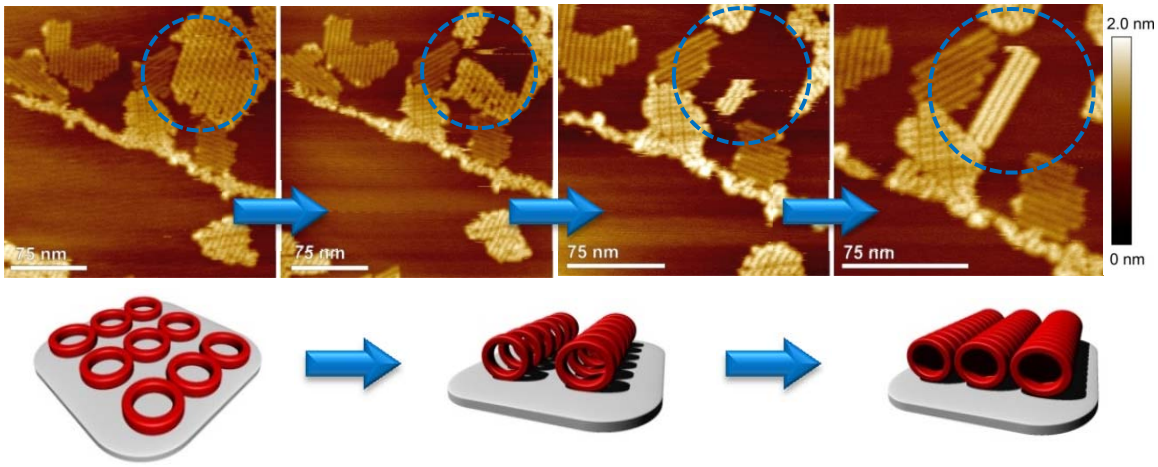

Figure 92. Tapping-mode AFM height images of a **4PBI$_{(4\text{-}t\text{Bu})4}$** film spin-coated onto HOPG; fist (left) to fourth (right) scan of the same area; 3000 rpm; DCM, c = 5 x 10^{-6} M; sketch at the bottom illustrates the transition between the individual 2D nanostructures.

Notably, no ordered structures were observed when the folded cycles were spin-coated out of toluene solutions on HOPG.

In summary, it was shown that different 2D nanopatterns can be achieved by changing the ring size of the PBI macrocycles. While **6PBI$_{(4\text{-}t\text{Bu})4}$** and **9PBI$_{(4\text{-}t\text{Bu})4}$** show close-packing of spheres without interactions between the chromophores, **5PBI$_{(4\text{-}t\text{Bu})4}$** and **9PBI$_{(4\text{-}t\text{Bu})4}$**

form lamellar monolayers of flat lying macrocycles. Moreover, **4PBI$_{(4\text{-}t\text{Bu})4}$** changes its structure from a lamellar arrangement with flat lying cycles to a quadratic structure with standing molecules. Due to weak interactions to the surface the standing macrocycles can be moved using the tip of the microscope to form supramolecular tubes. Thus, a spontaneous and a mechanically induced transition between nanostructures was observed.

Chapter 4

—

Summary

This work is concerned with the syntheses and photophysical properties of *para*-xylylene bridged macrocycles **nPBI** with ring sizes from two to nine PBI units, as well as the complexation of polycyclic aromatic guest compounds.

Starting from three different bay-substituted **PBIs** bearing cyclohexyl groups at the imide positions basic hydrolysis was performed to obtain the perylene bisanhydrides **PBA** in yields of 36–86%. These serve as the precursors for the macrocycles, cyclophanes as well as monomeric reference compounds (Figure 93). The latter were synthesized by imidization of the respective **PBA** building blocks with benzylamine in yields of 85–89%. Under the same conditions the cyclophanes could be obtained in yields of 3.0–6.7% and the larger macrocycles in 8.7–0.3%. In the case of **2PBI$_{(4\text{-}t\text{Bu})4}$** the dilution of the reaction mixture with toluene leads to an increase in the product formation to 18% yield. Hereby, the diluted conditions promote the intramolecular ring closure for small cycles. Furthermore, toluene has the additional feature to serve as a template, which preorganizes the PBI units into the cofacial arrangement. Based on this cofacial arrangement of the PBI subunits with an interplanar distance of ~7 Å the cyclophanes proved to be ideal candidates for the encapsulation of planar aromatic guest molecules. With a reduced but substantial fluorescence quantum yield of 21% (in $CHCl_3$) the free host **2PBI$_{(4\text{-}t\text{Bu})4}$** can be used as a dual fluorescence probe.

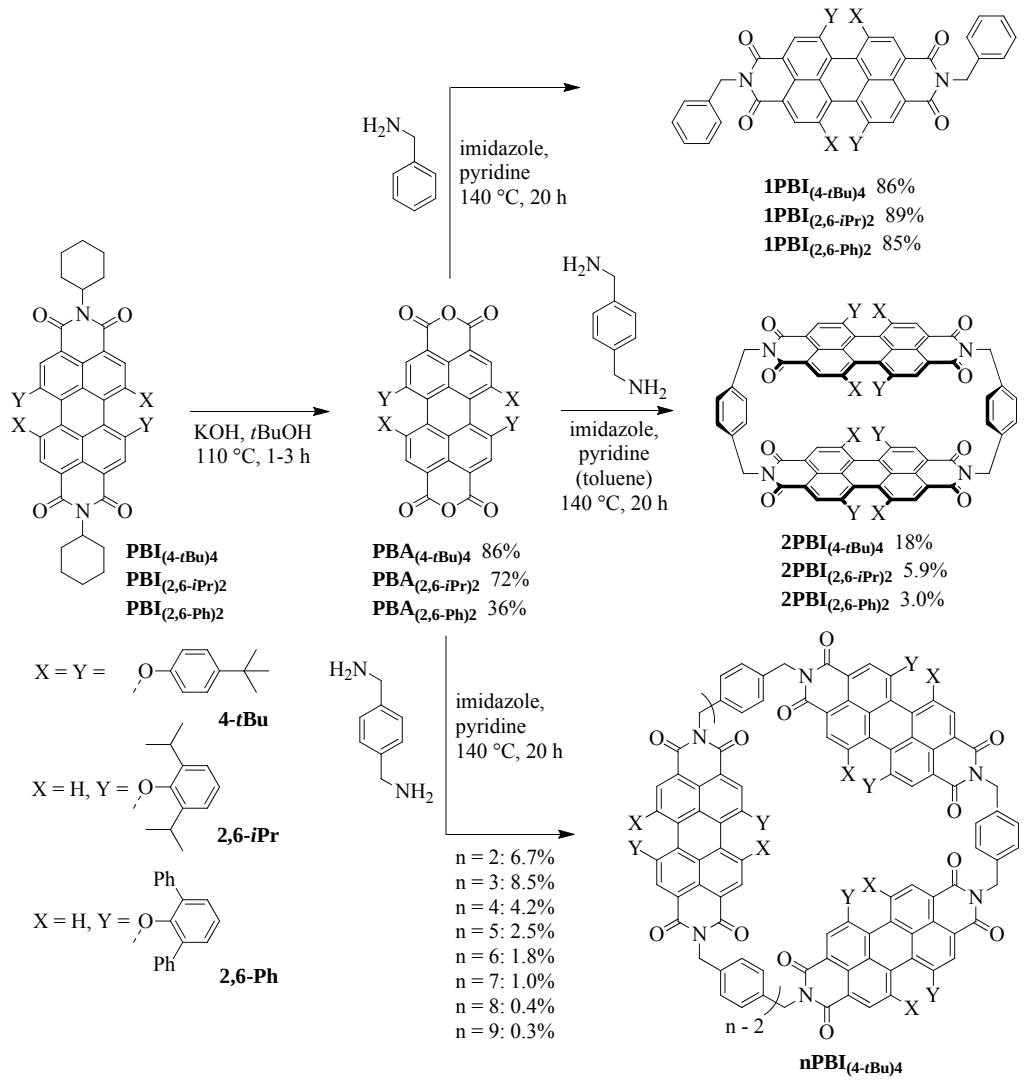

Figure 93. Synthesis of the discussed PBI macrocycles and cyclophanes **nPBI** with n = 2–9, as well as the monomeric reference compounds **1PBI**.

Upon encapsulation of rather electron-poor guests the fluorescence quenching interactions between the chromophores are prevented, leading to a significant fluorescence enhancement to > 90% ("turn-on"). On the other hand, the addition of electron-rich guest molecules induces an electron transfer from the guest to the electron-poor PBI chromophores and thus quenches the fluorescence entirely ("turn-off") (Figure 94).

The photophysical properties of the host-guest complexes were studied by transient absorption spectroscopy. These measurements revealed that the charge transfer between guest and **2PBI$_{(4\text{-}t\text{Bu})4}$** occurs in the "normal region" of the Marcus-parabola with the fastest charge separation rate for perylene. In contrast, the charge recombination back to the PBI ground state lies far in the "inverted region" of the Marcus-parabola.

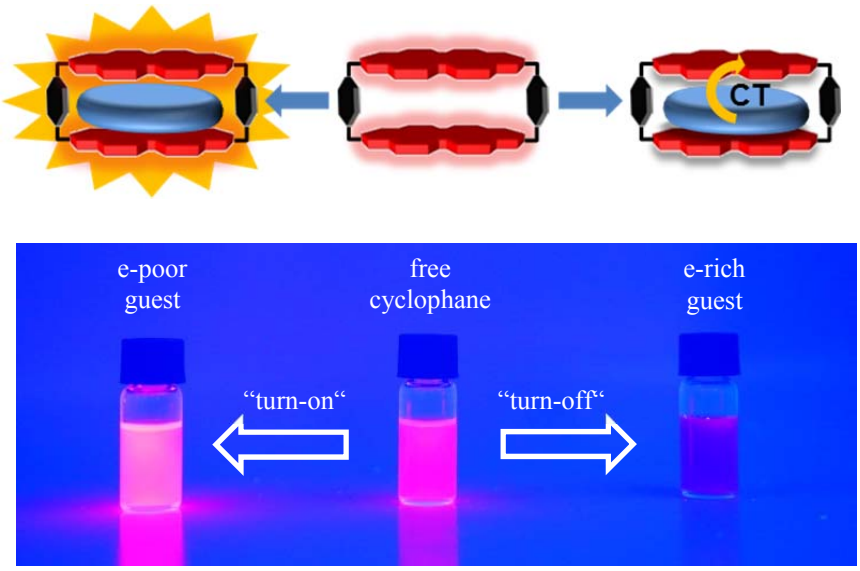

Figure 94. Schematic illustration (top) and representative photograph (bottom) for the "turn-on" (phenylnaphthalene@**2PBI**$_{(4\text{-}t\text{Bu})4}$) and "turn-off" (carbazole@**2PBI**$_{(4\text{-}t\text{Bu})4}$) fluorescence sensing of electron-poor and electron-rich aromatic hydrocarbons of the PBI cyclophane **2PBI**$_{(4\text{-}t\text{Bu})4}$.

Since the binding of the guests is caused by π-π interactions the binding strength increases with an increasing π-surface of the individual guest molecules. Furthermore, the tetrasubstituted PBIs exhibit a strong core twist that influences the binding strength. Thus, flexible hydrocarbons can better intercalate between the twisted PBIs, which increases the binding constant, while rigid molecules do not provide an optimal π-π contact, leading to lower binding strength within the cavity. With the encapsulation of chiral hydrocarbons a guest-promoted chirality transfer to the PBI core can be induced, forming diastereomers with homochiral chromphores in **2PBI**$_{(4\text{-}t\text{Bu})4}$.

By substitution of the PBIs in the 1,7-bay-position with two 2,6-di-*iso*-propylphenole and 2,6-diphenylphenole units cyclophanes with planar PBI skeletons were obtained in which a "self-encapsulation" of the *iso*-propyl and phenyl side arms was observed. This prevents an intramolecular chromophore contact and thus enhances the fluorescence quantum yield already in the free cyclophane close to 100%. Furthermore, these substituents facilitate with the planarization of the PBI units a stronger binding of aromatic guest molecules.

Beside complexation of planar aromatic hydrocarbons into the cavity of the cyclophanes an encapsulation of fullerene into the cyclic trimer **3PBI**$_{(4\text{-}t\text{Bu})4}$ was observed. **3PBI**$_{(4\text{-}t\text{Bu})4}$ provides a tube-like structure in which the PBI subunits represent the walls of those tubes. The cavity has the optimal size for hosting fullerenes, with C_{70} fitting better than C_{60} and a binding constant that is higher by a factor of 10. TA spectroscopy in toluene that was

performed on the C_{60}@**3PBI$_{(4\text{-}t\text{Bu})4}$** complex revealed two energy transfer processes. The first one comes from the excited PBI to the fullerene, which subsequently populates the triplet state. From the fullerene triplet state a second energy transfer occurs back to the PBI to generate the PBI triplet state.

In all cycles that were studied by TA spectroscopy, symmetry-breaking charge separation (SB-CS) was observed in dichloromethane (Figure 95). This process is fastest within the PBI cyclophane **2PBI$_{(4\text{-}t\text{Bu})4}$** and slows down for larger cycles, suggesting that the charge separation takes place through space and not through bonds. The charges then recombine to the PBI triplet state via a radical pair intersystem crossing (RP-ISC) mechanism, which could be used to generate singlet oxygen in yields of ~20%.

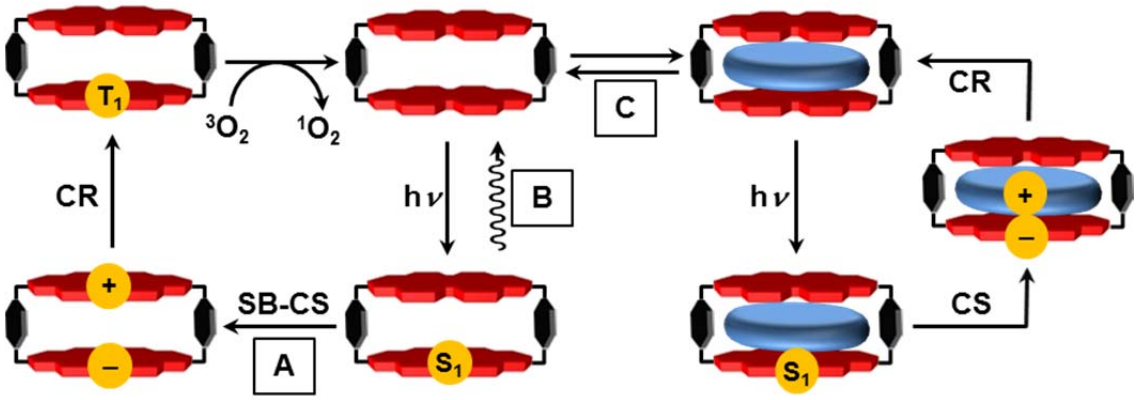

Figure 95. Schematic illustration of the different excited state photophysics upon excitation; A: symmetry-breaking charge separation and recombination to the PBI triplet within the PBI cyclophane **2PBI$_{(4\text{-}t\text{Bu})4}$** in dichloromethane that can be used for singlet oxygen generation; B: emission in toluene; C: encapsulation and oxidation of aromatic guests and recombination to the PBI ground state.

By changing the solvent to toluene an intramolecular folding of the even-numbered larger cycles was observed that quenches the fluorescence and increases the 0-1 transition band in the absorption spectra. Force field calculations of **4PBI$_{(4\text{-}t\text{Bu})4}$** suggested a folding into pairs of dimers, which explains the remarkable odd-even effect with respect to the number of connected PBI chromophores and the resulting alternation in the absorption and fluorescence properties (Figure 96). Thus, the even-numbered macrocycles can fold in a way that all chromophores are in a paired arrangement, while the odd-numbered cycles have open conformations (**3PBI$_{(4\text{-}t\text{Bu})4}$**, **5PBI$_{(4\text{-}t\text{Bu})4}$**, **7PBI$_{(4\text{-}t\text{Bu})4}$**) or at least additional unpaired PBI unit (**9PBI$_{(4\text{-}t\text{Bu})4}$**).

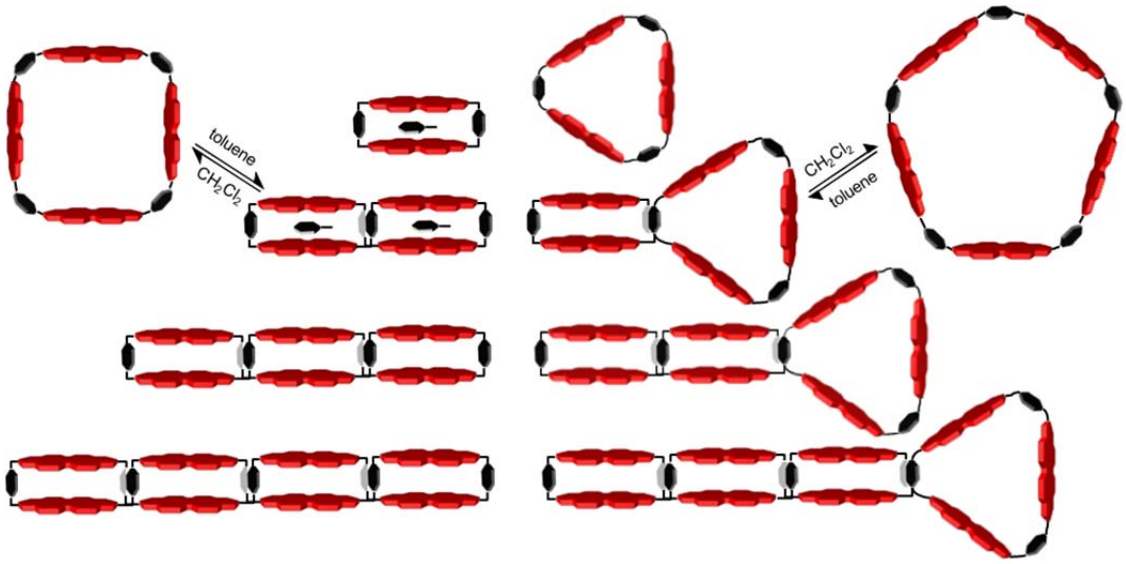

Figure 96. Schematic sketch of toluene-filled **2PBI$_{(4\text{-}t\text{Bu})4}$**, solvent-dependent conformational change of **4PBI$_{(4\text{-}t\text{Bu})4}$**, **6PBI$_{(4\text{-}t\text{Bu})4}$** and **8PBI$_{(4\text{-}t\text{Bu})4}$**, rather solvent-independent wide-stretched conformations of **3PBI$_{(4\text{-}t\text{Bu})4}$**, **5PBI$_{(4\text{-}t\text{Bu})4}$** and **7PBI$_{(4\text{-}t\text{Bu})4}$**, and the special partial folding transition of **9PBI$_{(4\text{-}t\text{Bu})4}$**.

With increasing ring size the amount of folded subunits is increased and thus the optical properties of the odd-numbered cycle **9PBI$_{(4\text{-}t\text{Bu})4}$** converges to the fully folded ones. In compliance to the observed folding in toluene no ordered structures of the macrocycles were found in AFM studies by spin-coating on HOPG out of toluene solutions. However, using dichloromethane lamellar or spherical structures were formed with monolayers of the open rings. For the tetrameric macrocycles a transition of lamellar to quadratic structures was observed that can be explained by perpendicularly arranged cycles with respect to the surface. These “standing” molecules have only weak contact to the surface and thus can be moved mechanically with the tip of the microscope by scanning the same area several times. Thus, a second transition of the structure can be induced under formation of molecular tubes (Figure 97).

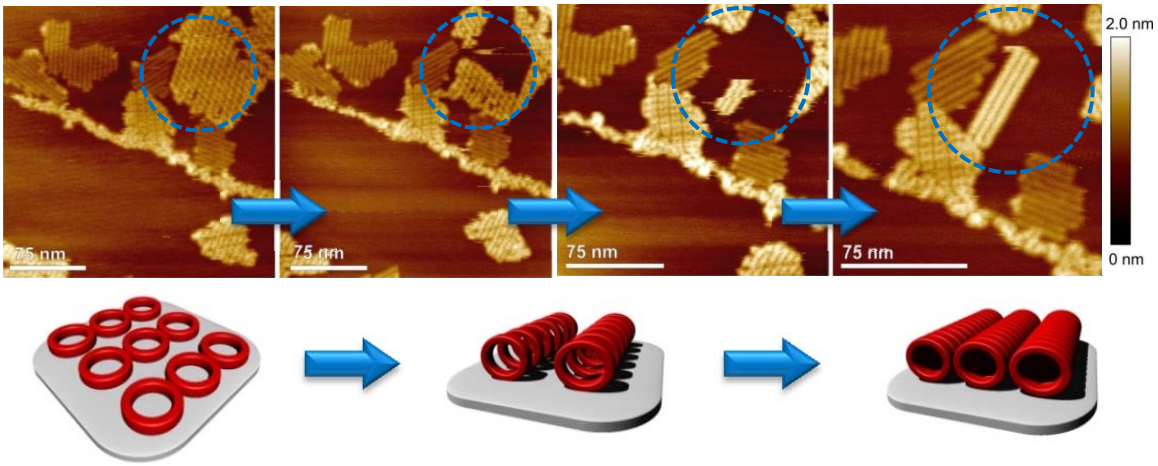

Figure 97. Tapping-mode AFM height images of **4PBI$_{(4\text{-}t\text{Bu})4}$** films spin coated onto HOPG; fist (left) to fourth (right) scan of the same area; 3000 rpm; DCM, c = 5 x 10^{-6} M; sketch at the bottom illustrates the transition between the individual 2D nanostructures.

With these experiments we could for the first time give insights in the interactions between cyclic PBI hosts and aromatic guest molecules. Associated with the encapsulation of guest molecules a variety of possible applications can be envisioned, like fluorescence sensing, chiral recognition and photodynamic therapy by singlet oxygen generation. Particularly, these macrocycles provide photophysical relaxation pathways of PBIs, like charge separation and recombination and triplet state formation that are hardly feasible in monomeric PBI dyes. Furthermore, diverse compound specific features were found, like the odd-even effect in the folding process or the transition of superficial nanostructures of the tetrameric cycle influenced by the AFM tip. The comprehensive properties of these macrocycles provide the basis for further oncoming studies and can serve as an inspiration for the synthesis of new macrocyclic compounds.

Chapter 5

–

Zusammenfassung

In dieser Arbeit wurde die Synthese *para*-Xylol-verbrückter Makrozyklen **nPBI** mit Ringgrößen von zwei bis neun PBI Einheiten beschrieben und deren photophysikalische Eigenschaften sowie Komplexierungsvermögen für polyzyklische aromatische Gastverbindungen analysiert.

Ausgehend von drei verschieden in Buchtpositionen substituierten **PBIs**, welche Cyclohexylgruppen in den Imidpositionen tragen, erfolgte zunächst eine basische Hydrolyse, um die entsprechenden Perylenbisanhydride **PBA** in Ausbeuten von 36–86% zu erhalten. Diese dienten dann als Vorstufen für die Synthese der Makrozyklen, Cyclophanen sowie monomeren Referenzverbindungen (Abbildung 1). Letztere wurden durch Imidisierung der jeweiligen **PBA**-Bausteine mit Benzylamin in Ausbeuten von 85–89% erhalten. Unter den gleichen Bedingungen konnten die Cyclophane in Ausbeuten von 3.0–6.7% und die größeren Makrozyklen in 8.7–0.3% synthetisiert werden. Dabei war es möglich im Falle von **2PBI$_{(4\text{-}t\mathrm{Bu})4}$** die Ausbeute durch Verdünnung der Reaktionsmischung mit Toluol auf 18% zu steigern. Die Verdünnung begünstigt hierbei den intramolekularen Ringschluss zu kleinen Ringsystemen. Außerdem weist Toluol einen zusätzlichen Templateffekt auf und bringt die PBI-Untereinheiten in eine kofaciale Anordnung zueinander. Auf Grund dieser parallelen Anordnung der PBI Einheiten mit einem interplanaren Abstand von ~7 Å erwiesen sich diese Cyclophane als ideale Verbindungen für die Aufnahme flacher aromatischer Gastmoleküle.

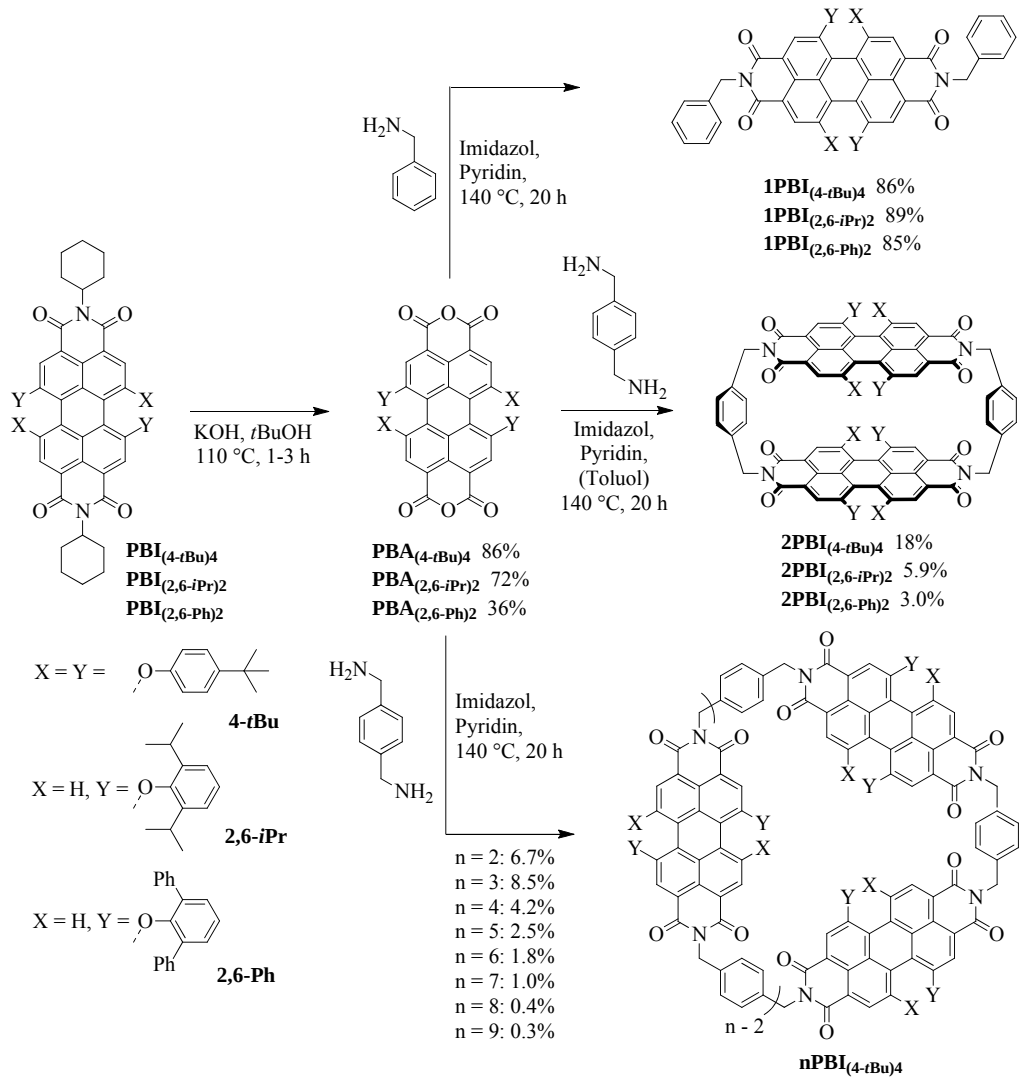

Abbildung 1. Synthese der in der vorliegenden Dissertation diskutierten PBI Makrozyklen und Cyclophane **nPBI** mit n = 2–9 und der monomeren Referenzverbindungen **1PBI**.

Mit einer reduzierten, aber noch substantiellen Fluoreszenzquantenausbeute von 21% in $CHCl_3$ eignet sich der freie Wirt **2PBI$_{(4\text{-}t\text{Bu})4}$** als dualer Fluoreszenzsensor. Durch die Aufnahme von elektronenarmen Gästen wird die zur Fluoreszenzlöschung führende Wechselwirkung zwischen den Chromophoren unterbunden, was sich in einer deutlichen Steigerung der Fluoreszenzquantenausbeute auf > 90% widerspiegelt („*turn-on*"). Andererseits führt die Zugabe elektronenreicher Gäste zu einem Elektronentransfer vom Gast auf die elektronenarmen PBI-Chromophore und quencht die Fluoreszenz damit nahezu vollständig („*turn-off*") (Abbildung 2).

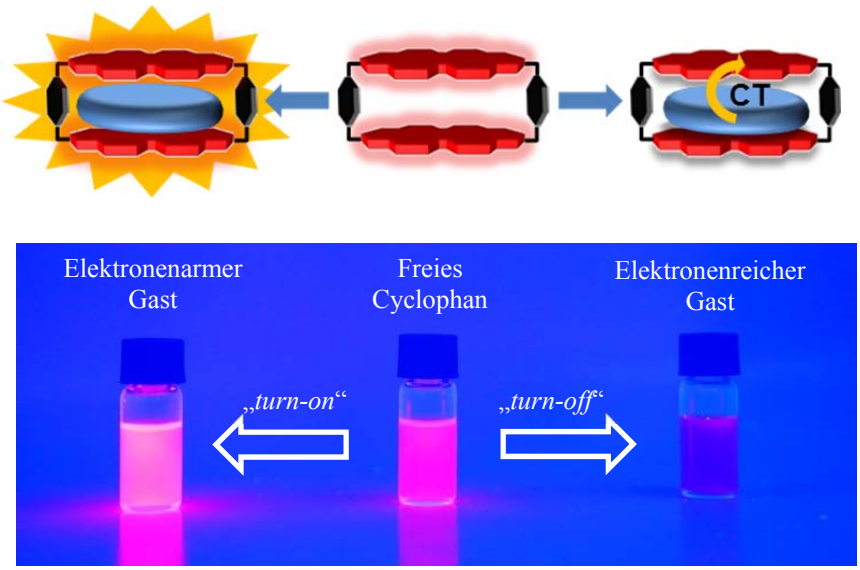

Abbildung 2. Schematische Darstellung (oben) und repräsentative Fotographie (unten) der „*turn-on*" (Phenylnaphthalin@**2PBI**$_{(4\text{-}t\text{Bu})4}$) und „*turn-off*" (Carbazol@**2PBI**$_{(4\text{-}t\text{Bu})4}$) Fluoreszenzerkennung von elektronenarmen und elektronenreichen aromatischen Kohlenwasserstoffen vom PBI-Cyclophan **2PBI**$_{(4\text{-}t\text{Bu})4}$.

Die photophysikalischen Eigenschaften der Wirt-Gast Komplexe wurden mittels transienter Absorptionsspektroskopie weitergehend untersucht. Diese Studien zeigten, dass die Ladungstrennung zwischen Gast und **2PBI**$_{(4\text{-}t\text{Bu})4}$ in der „normalen Region" der Marcus-Parabel stattfindet mit der schnellsten Ladungstrennungsrate für Perylen. Im Gegensatz dazu liegt die Ladungsrekombination zurück zum PBI Grundzustand weit in der „invertierten Region" der Marcus-Parabel.

Da die Bindung der Gäste über π-π-Wechselwirkungen erfolgt, erhöht sich die Bindungsstärke mit Vergrößerung der π-Oberfläche des jeweiligen Gastmoleküls. Zudem weisen die tetrasubstituierten PBIs eine starke Verdrehung des Kerns auf, was zusätzlichen Einfluss auf die Bindungsstärke nimmt. Daher können flexible Kohlenwasserstoffe besser zwischen die verdrehten PBIs interkalieren, was zu einer Erhöhung der Bindungskonstante führt. Rigide Moleküle hingegen weisen keinen optimalen π-π-Kontakt auf, was sich in einer verringerten Bindungsstärke in der Kavität widerspiegelt. Durch die Aufnahme chiraler Kohlenwasserstoffe konnte ein gastinduzierter Chiralitätstransfer zum PBI Kern beobachtet werden, wodurch ausschließlich Diastereomere mit homochiralen Chromophoren in **2PBI**$_{(4\text{-}t\text{Bu})4}$ gebildet werden.

Durch die Substitution der PBIs in den 1,7-Buchtpositionen mit zwei 2,6-di-*iso*-Propylphenol- und 2,6-di-Phenylphenoleinheiten resultierten Cyclophane mit planarem

PBI-Skelett, bei denen allerdings eine "Selbsteinkapselung" der *iso*-Propyl und Phenyl Seitenarme beobachtet wurde. Diese unterbindet einen intramolekularen Kontakt der PBI-Chromophore und steigert damit die Fluoreszenzquantenausbeute schon im freien Cyclophan auf beinahe 100%. Zudem ermöglichen diese Substituenten über die Planarisierung der PBI-Einheiten eine stärkere Bindung aromatischer Gastverbindungen.

Neben der Komplexierung flacher aromatischer Kohlenwasserstoffe in die Kavitäten der Cyclophane konnte auch die Aufnahme von Fullerenen in das zyklische Trimer **3PBI$_{(4\text{-}t\text{Bu})4}$** beobachtet werden. **3PBI$_{(4\text{-}t\text{Bu})4}$** weist eine röhrenartige Struktur auf, in der die PBI-Untereinheiten die Wände der Röhren darstellen. Damit hat die Kavität die optimale Größe für die Aufnahme von Fullerenen, wobei C_{70} besser hinein passt als C_{60} und damit eine um den Faktor 10 höhere Bindungskonstante besitzt. Transiente Absorptionsspektroskopie des C_{60}@**3PBI$_{(4\text{-}t\text{Bu})4}$** Komplexes zeigte in Toluol zwei Energietransferprozesse auf. Der erste erfolgt vom angeregten PBI zum Fulleren, welches daraufhin den Triplettzustand populiert. Vom Fulleren-Triplettzustand erfolgt ein zweiter Energietransfer zurück zum PBI, was schließlich im PBI-Triplett Zustand mündet.

Für alle mittels transienter Absorptionsspektroskopie untersuchten Zyklen konnte eine symmetriebrechende Ladungstrennung in Dichlormethan beobachtet werden (Abbildung 3). Dieser Prozess ist für das PBI-Cyclophan **2PBI$_{(4\text{-}t\text{Bu})4}$** am schnellsten und wird mit zunehmender Ringgröße langsamer. Demnach ist die Ladungstrennung abhängig von der räumlichen Nähe der PBI-Chromophore und nicht von deren Verbrückung.

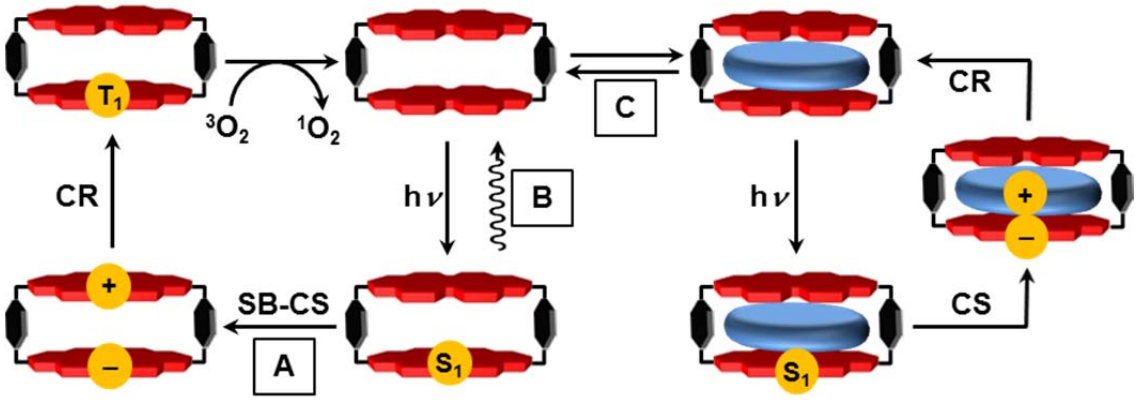

Abbildung 3. Schematische Darstellung der verschiedenen photophysikalischen Anregungszustände; A: symmetriebrechende Ladungstrennung und -rekombination zum PBI-Triplett des PBI-Cyclophans **2PBI$_{(4\text{-}t\text{Bu})4}$** in Dichlormethan, das zur Generierung von Singulettsauerstoff genutzt werden kann; B: Emission in Toluol; C: Aufnahme und Oxidation aromatischer Gäste und Rekombination zum PBI-Grundzustand.

Im Anschluss erfolgt eine Ladungsrekombination zum PBI-Triplettzustand über ein Radikalpaar (*radical pair intersystem crossing* RP-ISC-Mechanismus), was zur Gewinnung von Singulettsauerstoff in Ausbeuten von ~20% genutzt werden konnte.
Bei Verwendung von Toluol als Lösungsmittel wurde eine intramolekulare Faltung der geradzahligen größeren Zyklen beobachtet, wodurch die Fluoreszenz gequencht und die 0-1 Übergangsbande der Absorption verstärkt wird. Kraftfeldberechnungen für **4PBI$_{(4\text{-}t\text{Bu})4}$** legen eine Faltung zu Dimerpaaren nahe, welche den außergewöhnlichen gerade-ungerade Effekt bezogen auf die Anzahl der verknüpften PBI Chromophore und die daraus resultierende Alternanz in den Absorptions- und Fluoreszenzeigenschaften erklärt (Abbildung 4).

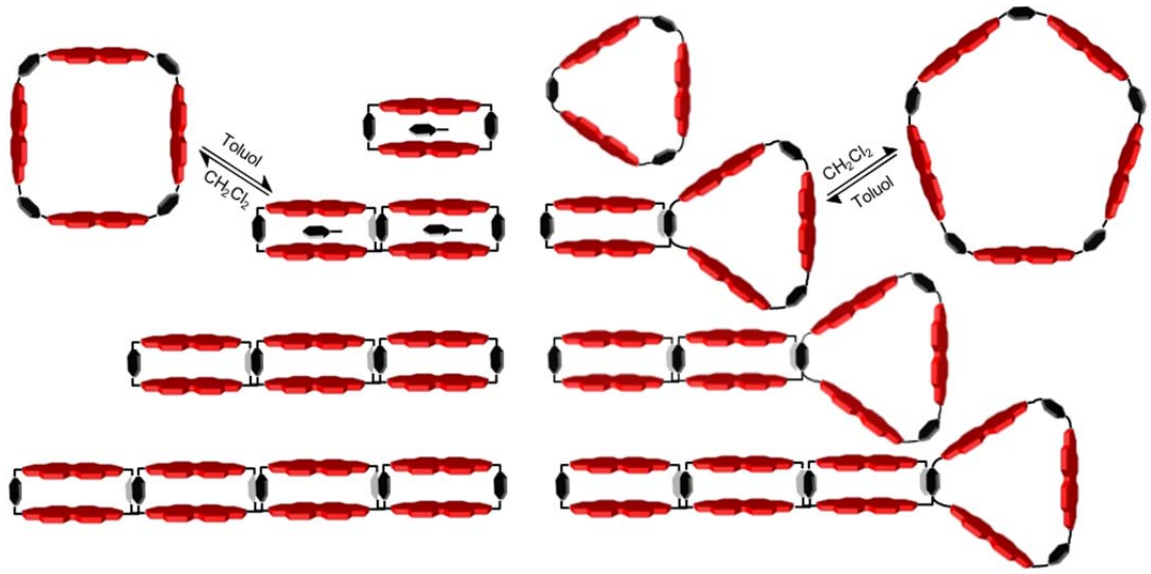

Abbildung 4. Schematische Darstellung des Toluol-gefüllten **2PBI$_{(4\text{-}t\text{Bu})4}$**, Lösungsmittelabhängige Konformationsänderung von **4PBI$_{(4\text{-}t\text{Bu})4}$**, **6PBI$_{(4\text{-}t\text{Bu})4}$** und **8PBI$_{(4\text{-}t\text{Bu})4}$**, eher Lösungmittel unabhängige ausgedehnte Konformationen von **3PBI$_{(4\text{-}t\text{Bu})4}$**, **5PBI$_{(4\text{-}t\text{Bu})4}$** and **7PBI$_{(4\text{-}t\text{Bu})4}$** und die spezielle teilweise gefaltete Konformation von **9PBI$_{(4\text{-}t\text{Bu})4}$**.

Dementsprechend können die geradzahligen Makrozyklen in der Art falten, dass alle Chromophore in einer gepaarten Anordnung vorliegen, während die ungeradzahligen Zyklen offene Konformationen (**3PBI$_{(4\text{-}t\text{Bu})4}$**, **5PBI$_{(4\text{-}t\text{Bu})4}$**, **7PBI$_{(4\text{-}t\text{Bu})4}$**) oder zumindest teilweise ungepaarte PBI-Einheiten (**9PBI$_{(4\text{-}t\text{Bu})4}$**) aufweisen. Mit zunehmender Ringgröße erhöht sich der Anteil an gefalteten Untereinheiten, was dazu führt, dass sich die optischen Eigenschaften des ungeradzahligen **9PBI$_{(4\text{-}t\text{Bu})4}$** Zyklus den vollständig gefalteten Systemen angleicht. In Einklang mit der beobachteten Faltung in Toluol konnten keine geordneten Strukturen durch Rotationsbeschichtung der Makrozyklen aus

Toluol-Lösungen auf HOPG Oberflächen mittels Rasterkraftmikroskopie gefunden werden. Im Gegensatz dazu konnten lamellare oder sphärische Monolagen der offenen Ringsysteme aus Dichlormethan beobachtet werden. Für den tetrameren Makrozyklus wurde eine Strukturänderung von lamellaren zu quadratischen Formen beobachtet, die durch aufrechtstehende Zyklen auf der Oberfläche erklärt werden kann. Diese „stehenden" Moleküle haben nur schwachen Kontakt zur Oberfläche und können deshalb mechanisch mit der Spitze des Mikroskops bewegt werden. Dazu wurde eine Stelle der Oberfläche mehrmals abgetastet, wodurch eine zweite Strukturänderung zu molekularen Röhren induziert werden konnte (Abbildung 5).

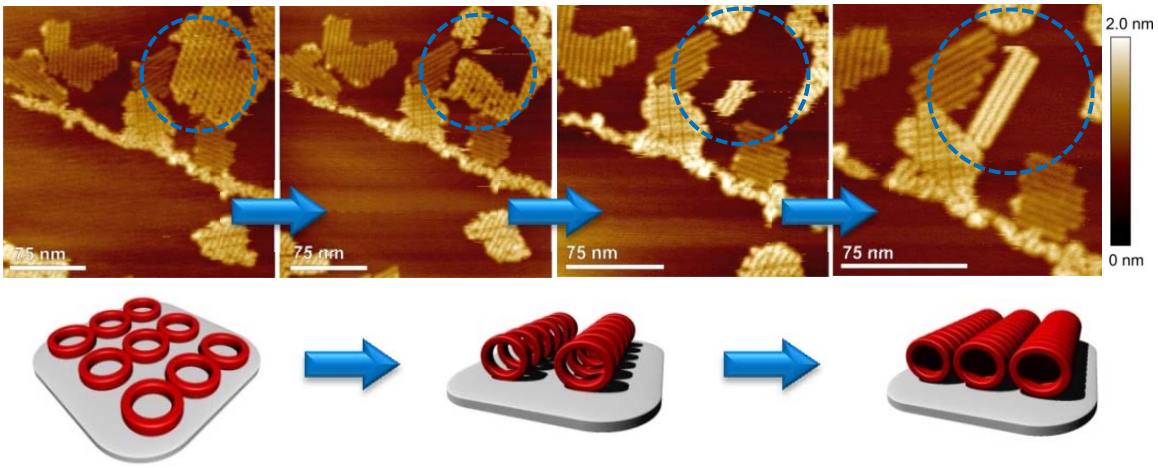

Abbildung 5. *Tapping-mode* AFM-Höhenbilder von **4PBI$_{(4\text{-}t\mathrm{Bu})4}$** Filmen, die durch Rotationsbeschichtung auf HOPG erhalten wurden; erste (links) bis vierte (rechts) Aufnahme desselben Bereichs; 3000 rpm; DCM, $c = 5 \times 10^{-6}$ M; die untere Abbildung stellt den Übergang zwischen den einzelnen 2D Nanostrukturen dar.

Mit diesen Experimenten konnten wir erstmals Enblicke in die Wechselwirkungen zwischen zyklischen PBI-Wirten und aromatischen Gastmolekülen geben. Verbunden mit der Aufnahme von Gastmolekülen ist eine Reihe möglicher Anwendungen wie Fluoreszenzsensorik, Chiralitätserkennung und photodynamische Therapie über die Generierung von Singulettsauerstoff denkbar. Insbesondere ermöglichen diese Makrozyklen photophysikalische Relaxationspfade von PBIs wie die Ladungstrennung und –rekombination und die Ausbildung von Triplettzuständen, welche in monomeren PBI-Frabstoffen nur schwer realisierbar sind. Weiterhin konnten einige verbindungs-spezifische Eigenschaften gefunden werden, wie den gerade-ungerade Effekt im Faltungsprozess oder die für den tetrameren Zyklus gefundene Umwandlung von Oberflächennanostrukturen unter dem Einfluß der AFM-Spitze. Die reichhaltigen Eigenschaften dieser Makrozyklen bilden damit die Basis für weitergehende

Untersuchungen und können als Inspiration für die Synthese neuer makrozyklischer Verbindungen dienen.

Chapter 6

—

Experimental Section

6.1 Materials and Methods

UV-vis Spectroscopy. UV-vis absorption spectra were recorded on a Perkin-Elmer Lambda 40 or Lambda 950 spectrometer. Solvents for spectroscopic studies were of spectroscopic grade and used without further purification.

Fluorescence Spectroscopy. Fluorescence quantum yields were determined by optical dilution method[223] ($OD_{max} < 0.05$) as the average value of at least four different excitation wavelengths using *N,N'*-(2,6-di-*iso*-propylphenyl)-1,6,7,12-tetraphenoxy-perylen-3,4:9,10-tetracarboxylic acid bisimide ($\Phi_{fl} = 0.96$ in chloroform) as reference. Singlet oxygen emission was recorded on a PTI spectrofluorimeter. The quantum yield of singlet oxygen was determined in an air-equilibrated solution in dichloromethane ($OD_{max} \sim 0.5$) as the average value of four different excitation wavelengths using methylene blue as reference ($\Phi_{\Delta} = 0.57$ in dichloromethane).[169]

UV-vis Absorption and Fluorescence Titration Experiments. A solution containing the individual PBI host ($c = 5 \times 10^{-5}$ M) and a large excess of the particular guest in chloroform or toluene was titrated to a solution of pure PBI host of the same concentration.

Data Analysis. The titration data obtained by fluorescence spectroscopy where fitted according to the following relationship:

$$I_{\mathrm{obs}} = I_{\mathrm{A}} + \frac{I_{\mathrm{AB}} - I_{\mathrm{A}}}{2c_{\mathrm{A}}^{0}}\left(c_{\mathrm{A}}^{0} + c_{\mathrm{B}}^{0} + \frac{1}{K_{\mathrm{a}}} \pm \sqrt{\left(c_{\mathrm{A}}^{0} + c_{\mathrm{B}}^{0} + \frac{1}{K_{\mathrm{a}}}\right)^{2} - 4c_{\mathrm{A}}^{0}c_{\mathrm{B}}^{0}}\right)$$

where I_A, I_{AB} and I_{obs} are the fluorescence intensities at a selected wavelength of the free host, the 1:1 complex and the measured intensity. ${c_A}^0$ and ${c_B}^0$ are the total concentrations of the host and the guest. K_a is the respective binding constant.

Transient Absorption Spectroscopy. Femtosecond and nanosecond transient absorption experiments were performed at the Northwestern University in Evanston using an instrument as previously described[224] with an approximately 120 fs output of a commercial Ti:sapphire oscillator/amplifier (Tsunami/Spitfire, Spectra-Physics) that was split to seed and pump a laboratory-constructed optical parametric amplifier used to generate the 569 nm excitation ("pump") beam and a femtosecond continuum probe, by using a 3 mm sapphire plate for the visible range or a proprietary crystal for the near-infrared (NIR) spectral region (Ultrafast Systems, LLC). Transient spectra were collected by using customized commercial detectors (Helios, Ultrafast Systems, LLC). Experiments were performed with a depolarized pump to eliminate contributions from orientational dynamics. The kinetic analysis is based on a global fit to selected single-wavelength kinetics. Several kinetic traces at different wavelengths were chosen and fitted globally to a kinetic model. The differential equations were solved and then convoluted with the instrument response function, before employing a least-square fitting to find the parameters, which result in matches to the same functions for all selected wavelengths (MATLAB). These parameters are then fed directly into the differential equations, which were solved for the populations of the states in model. Finally, the raw data matrix (with all the raw data) is deconvoluted with the populations as functions of time to produce the species-associated spectra.

Femtosecond Stimulated Raman Spectroscopy. To obtain FSRS data, a third pump pulse (Raman pump) is added to the unchopped actinic pump and continuum probe described previously for the TA spectroscopy. The Raman pump pulse is gained by optical parametric amplification of the transmitted portion of the beam split by BS3. The 800 nm fundamental is frequency doubled with a second harmonic bandwidth compressor (Light Conversion, SHBC) to result in a 400 nm pulse train, which feeds a second optical parametric amplifier (Light Conversion, TOPAS-400). A continuum seed from the SHBC enables a tunable Raman pump from 470 nm to 2600 nm. The Raman pump, the actinic

pump, and the probe pulse are focused on the sample in a 2 mm path length sample cell with a parabolic mirror and spatially overlapped with near-collinear alignment at the sample. To obtain the stimulated Raman spectrum, a mechanical 125 Hz chopper on only the Raman pump pulse facilitates pump-on/pump-off difference spectra to be obtained. The Raman gain signal is measured on the intense Raman probe through heterodyne detection. The FSRS spectra are obtained using 1 s exposure times, 15 scans, and 2 averages. On average, over 200 time points were obtained out to 7 ns, resulting in an average experiment length of 2 hours.

NMR Spectroscopy. NMR spectra were recorded on a Bruker Avance 400 or Bruker DMX 600 spectrometer. Chemical shifts (δ) are referenced internally to residual proton solvent resonances or to natural-abundance carbon resonances.

Mass Spectrometry. MALDI-TOF mass spectrometry was performed on an autoflex II mass spectrometer (Bruker Daltonik GmbH). High resolution ESI-TOF mass spectrometry was performed on a microTOF focus instrument (Bruker Daltronik GmbH).

Cyclic Voltammetry. Cyclic voltammetry was carried out with a standard commercial electrochemical analyzer (EC epsilon; BAS Instruments, UK) with a three electrode single-compartment cell. The supporting electrolyte tetrabutylammonium hexafluoro-phosphate (TBAHFP) was recrystallized from ethanol/water. The measurements were carried out using ferrocene/ferrocenium (Fc/Fc^+) as an internal standard for the calibration of the potential. Ag/AgCl reference electrode was used. A Pt disc and a Pt wire were used as working and auxiliary electrodes, respectively.

Circular Dichroism. CD spectra were measured with a JASCO J-810 spectrometer equipped with a CDF-42 peltier element.

Atomic Force Microscopy. AFM measurements were carried out under ambient conditions by using a Veeco MultiMode^{TM} Nanoscope IV system (Veeco Metrology Inc., USA) operating in tapping-mode in air. Silicon cantilevers (Olympus Corporation, Japan) with a resonance frequency of ~300 kHz were used. The 512 × 512 pixel images were collected at a rate of 2 scan lines per second. Solutions of **nPBI$_{(4\text{-}t\text{Bu})4}$** in dichloromethane ($c$ = 5 x 10^{-6} M) were spin-coated on a highly ordered pyrolytic graphite (HOPG, NanoTechnology Instruments - Europe, Netherlands) under 3000 rpm.

Recycling GPC. Gel permeation chromatography was performed on a Shimadzu Recycling GPC-System (LC-20AD Prominence Pump; SPDMA20A Prominence Diode Array Detector) with three preparative columns (Japan Analytical Industries Co., Ltd.; JAIGEL-1H, JAIGEL-2H and JAIGEL-2.5H) in chloroform (HPLC grade, stabilized with 0.1% EtOH); 3.5 mL/min.

Molecular Modelling. DFT calculations were performed by using the Gaussian 09 program package[225] with B3-LYP[226] as functional and 6-31+G* as basis set. The structures were geometry optimized, followed by frequency calculations on the optimized structures, which confirmed the existence of a minimum (one very small imaginary frequency of 4i cm^{-1} was obtained for cyclophane **2PBI$_{(4\text{-}t\text{Bu})4}$**. Small imaginary frequencies (< 100i cm^{-1}) are considered most likely to be an artefact of the calculation instead of an indication of a transition state[227]). Geometry optimized structures were obtained by force field optimization; Maestro 9.3, MacroModel 9.8, MM2*.

6.2 Synthesis

PBA$_{(4\text{-}t\text{Bu})4}$. The starting compound 1,6,7,12-tetrakis-4-*tert*-butylphenoxyperylene-3,4:9,10-tetracarboxylic acid bisanhydride (**PBA$_{(4\text{-}t\text{Bu})4}$**) was prepared according to literature.[228]

PBA$_{(2,6\text{-}i\text{Pr})2}$.[229] The literature known **PBI$_{(2,6\text{-}i\text{Pr})2}$** (880 mg, 971 μmol) was heated in 50 mL *tert*-butanol to 110 °C. After 30 min 1.13 g KOH were added in portions during one hour and the mixture was heated one additional hour. After cooling to room temperature, 50 mL 2 N hydrochloric acid were added, the formed precipitate was filtered off and washed with water and MeOH. The crude product was purified by column chromatography (silica gel, CH_2Cl_2) to obtain 521 mg pure **PBA$_{(2,6\text{-}i\text{Pr})2}$** (72% yield).

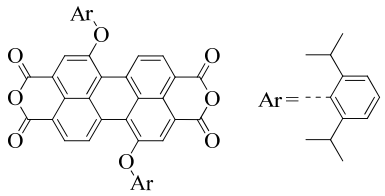

$C_{48}H_{40}O_8$ (744.83): Mp.: > 300 °C; ^{1}H-NMR (400 MHz, $CDCl_3$): δ = 9.94 (d, ^3J = 8.0 Hz, 2 H), 8.68 (d, ^3J = 8.0 Hz, 2 H), 8.07 (s, 2 H), 7.44 (m, 2 H), 7.39 (m, 4 H), 2.94 (m, 4 H), 1.25-1.13 (m, 24 H) ppm; ^{13}C-NMR (100 MHz, $CDCl_3$): δ = 159.7, 159.6, 157.3, 146.6,

141.0, 135.0, 131.8, 130.2, 129.4, 127.9, 126.6, 125.6, 121.7, 120.5, 120.0, 118.3, 27.6, 24.8, 22.7 ppm; HRMS (ESI, pos. mode, acetonitrile/chloroform 1:1): *m*/*z*: calculated for $C_{48}H_{40}KO_8$: 783.23548 $[M+K]^+$, found: 783.23411.

$PBA_{(2,6\text{-}Ph)2}$.[229] The literature known **$PBI_{(2,6\text{-}Ph)2}$** (222 mg, 213 μmol) was heated in 35 mL *tert*-butanol to 110 °C. After 30 min 16 g KOH were added in portions during 30 min and the mixture was further heated for 3 h. After cooling to room temperature 100 mL 2 N hydrochloric acid were added and the solution subsequently extracted with dichloromethane. The organic solvent was evaporated under reduced pressure and the crude product was purified by column chromatography (silica gel, CH_2Cl_2/hexane 9:1) to obtain 143 mg pure **$PBA_{(2,6\text{-}Ph)2}$** (76% yield).

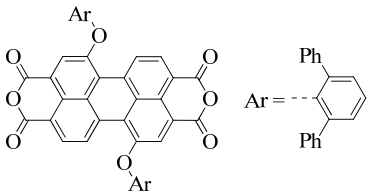

$C_{60}H_{32}O_8$ (880.89): Mp.: > 300 °C; ^{1}H-NMR (400 MHz, $CDCl_3$): δ = 9.18 (d, ^3J = 8.0 Hz, 2 H), 8.42 (d, ^3J = 8.0 Hz, 2 H), 7.94 (s, 2 H), 7.56 (s, 6 H), 7.36 (m, 8 H), 7.02 (m, 12 H) ppm; ^{13}C-NMR (100 MHz, $CDCl_3$): δ = 159.8, 159.7, 155.5, 147.1, 137.0, 136.1, 134.0, 131.4, 131.2, 129.1, 129.0, 128.8, 128.2, 127.7, 127.3, 125.9, 121.8, 121.4, 118.9, 117.7 ppm; HRMS (ESI, pos. mode, acetonitrile/chloroform 1:1): *m*/*z*: calculated for $C_{104}H_{33}O_8$: 881.21699 $[M+H]^+$, found: 881.21472.

$1PBI_{(4\text{-}t\text{Bu})4}$. 450 mg (459 μmol) of 1,6,7,12-tetrakis-4-*tert*-butylphenoxyperylene-3,4:9,10-tetracarboxylic acid bisanhydride (**$PBA_{(4\text{-}t\text{Bu})4}$**) and 1.5 mL (1.47 g, 13.8 mmol) benzylamine were suspended in 1.5 g imidazole and heated under nitrogen to 120 °C for 20 h. 100 mL 2 N hydrochloric acid were added to the reaction mixture at room temperature and the resulting precipitate was collected by filtration. The crude product was purified by column chromatography (silica gel, CH_2Cl_2) to obtain 459 mg pure **$1PBI_{(4\text{-}t\text{Bu})4}$** (86% yield) as a red solid.

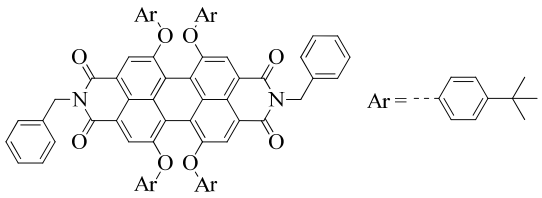

$C_{78}H_{70}N_2O_8$ (1163.40): Mp.: > 300 °C; ^{1}H-NMR (400 MHz, $CDCl_3$): δ = 8.23 (s, 4 H), 7.44 (m, 4 H), 7.26 (m, 14 H), 6.82 (d, ^3J(H,H) = 8.8 Hz, 8 H), 5.30 (s, 4 H), 1.29 (s, 36 H) ppm; ^{13}C-NMR (100 MHz, $CDCl_3$): δ = 163.5, 156.0, 152.8, 147.4, 137.1, 132.9, 128.7, 127.5, 126.7, 122.4, 120.6, 120.0, 119.5, 119.4, 43.8, 34.4, 31.5, 29.7 ppm; HRMS (ESI, pos. mode, acetonitrile/dichloromethane 1:1): *m*/*z*: calculated for $C_{78}H_{71}N_2O_8$: 1163.52104 $[M+H]^+$, found: 1163.52143; UV-vis ($CHCl_3$): λ_{max} (ε_{max}) = 589 nm (41000 M^{-1} cm^{-1}), 547 nm (25000 M^{-1} cm^{-1}); (tol): λ_{max} (ε_{max}) = 577 nm (43000 M^{-1} cm^{-1}), 535 nm (26000 M^{-1} cm^{-1}); Fluorescence ($CHCl_3$): λ_{max} = 620 nm (λ_{ex} = 530 nm), Φ_{fl} = 0.97; (tol): λ_{max} = 607 nm (λ_{ex} = 530 nm), Φ_{fl} = 0.86; CV (CH_2Cl_2, 0.1 M TBAHFP, vs. Fc/Fc^+): $E_{1/2}(PBI/PBI^+)$ = 0.85 V, $E_{1/2}(PBI/PBI^-)$ = –1.18 V, $E_{1/2}(PBI/PBI^{2-})$ = –1.30 V.

1PBI$_{(2,6\text{-}i\text{Pr})2}$. 90 mg (120 μmol) of the perylene bisanhydride **PBA$_{(2,6\text{-}i\text{Pr})2}$** and 0.5 mL (491 mg, 4.58 mmol) benzylamine were added to 1.0 g imidazole and heated under nitrogen to 120 °C overnight. After cooling to room temperature 100 mL 2 N hydrochloric acid were added and the solution subsequently extracted with dichloromethane. The organic solvent was evaporated under reduced pressure and the crude product was purified by column chromatography (silica gel, CH_2Cl_2) to obtain 99 mg pure **1PBI$_{(2,6\text{-}i\text{Pr})2}$** (89% yield).

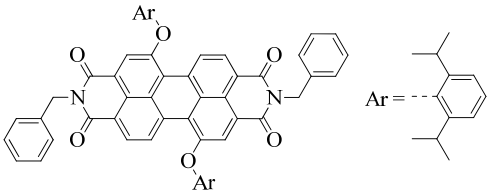

$C_{62}H_{54}N_2O_6$ (923.10): Mp.: > 300 °C; ^{1}H-NMR (400 MHz, $CDCl_3$): δ = 9.89 (d, ^3J = 8.5 Hz, 2 H), 8.67 (d, ^3J = 8.5 Hz, 2 H), 8.09 (s, 2 H), 7.52 (m, 4 H), 7.37 (m, 6 H), 7.27 (m, 6 H), 5.34 (s, 4 H), 2.97 (m, 4 H), 1.22 (d, ^3J = 6.8 Hz, 12 H), 1.11 (d, ^3J = 6.8 Hz, 12 H) ppm; ^{13}C-NMR (100 MHz, $CDCl_3$): δ = 163.6, 163.1, 156.9, 147.0, 141.3, 137.0, 134.2, 129.9, 129.8, 129.0, 128.8, 128.5, 127.6, 127.4, 125.4, 124.5, 123.6, 121.9, 120.9, 119.0, 43.8, 27.5, 24.9 ppm; HRMS (ESI, pos. mode, acetonitrile/chloroform 1:1): *m*/*z*: calculated for $C_{62}H_{55}N_2O_6$: 923.40546 $[M+H]^+$, found: 923.40514; UV-vis ($CHCl_3$): λ_{max} (ε_{max}) = 560 nm (74000 M^{-1} cm^{-1}), 519 nm (42000 M^{-1} cm^{-1}); Fluorescence ($CHCl_3$): λ_{max} = 576 nm (λ_{ex} = 530 nm), Φ_{fl} = 1.00.

1PBI$_{(2,6\text{-Ph})2}$. 100 mg (114 μmol) of the perylene bisanhydride **PBA$_{(2,6\text{-Ph})2}$** and 0.5 mL (491 mg, 4.58 mmol) benzylamine were added to 1.0 g imidazole and heated under nitrogen to 120 °C overnight. After cooling to room temperature 100 mL 2 N hydrochloric acid were added and the solution subsequently extracted with dichloromethane. The organic solvent was evaporated under reduced pressure and the crude product was purified by column chromatography (silica gel, CH_2Cl_2) to obtain 103 mg pure **1PBI$_{(2,6\text{-Ph})2}$** (85% yield).

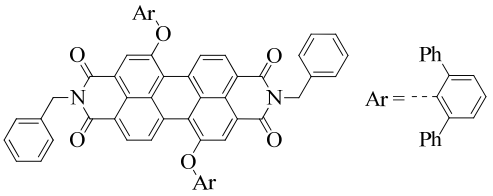

$C_{74}H_{46}N_2O_6$ (1059.17): Mp.: > 300 °C; ^{1}H-NMR (400 MHz, $CDCl_3$): δ = 9.14 (d, ^3J = 8.4 Hz, 2 H), 8.43 (d, ^3J = 8.4 Hz, 2 H), 7.97 (s, 2 H), 7.52 (m, 10 H), 7.35 (m, 14 H), 6.97 (m, 12 H), 5.32 (s, 4 H) ppm; ^{13}C-NMR (100 MHz, $CDCl_3$): δ = 163.6, 163.1, 155.2, 147.4, 137.3, 137.1, 136.2, 133.4, 131.2, 129.4, 129.0, 128.9, 128.7, 128.5, 128.4, 128.0, 127.6, 127.5 126.8, 123.8, 122.5, 121.3, 121.2, 199.9, 43.7 ppm; HRMS (ESI, pos. mode, acetonitrile/chloroform 1:1): *m*/*z*: calculated for $C_{74}H_{47}N_2O_6$: 1059.34286 $[M+H]^+$, found: 1059.34195; UV-vis ($CHCl_3$): λ_{max} (ε_{max}) = 564 nm (73000 M^{-1} cm^{-1}), 523 nm (41000 M^{-1} cm^{-1}); Fluorescence ($CHCl_3$): λ_{max} = 580 nm (λ_{ex} = 530 nm), Φ_{fl} = 1.00.

2PBI$_{(4\text{-}t\text{Bu})4}$. 100 mg (102 μmol, 1.0 eq.) of 1,6,7,12-tetrakis-4-*tert*-butylphenoxyperylene-3,4:9,10-tetracarboxylic acid bisanhydride (**PBA$_{(4\text{-}t\text{Bu})4}$**) and 14 mg (102 μmol, 1.0 eq.) *para*-xylylenediamine were added to a solution of 1.0 g imidazole and 10 mL pyridine in 200 mL toluene. The mixture was heated under nitrogen to 140 °C for 20 h. After cooling to room temperature the solution was extracted with hydrochloric acid (2 N, 250 mL). The aqueous solution was subsequently extracted with dichloromethane and the organic solvent was evaporated under reduced pressure. The crude product was purified by column chromatography (silica gel, CH_2Cl_2) to obtain 20 mg pure cyclophane **2PBI$_{(4\text{-}t\text{Bu})4}$** (18% yield) as a red solid.

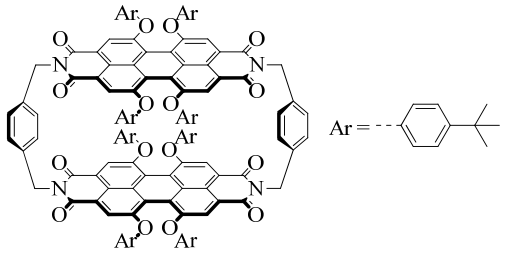

$C_{144}H_{128}N_4O_{16}$ (2169.57): Mp.: > 300 °C; ^{1}H-NMR (600 MHz, 360 K, $C_2D_2Cl_4$): δ = 8.07 (s, 8 H), 7.25 (s, 8 H), 7.23 (d, ^3J(H,H) = 8.8 Hz, 16 H), 6.78 (d, ^3J(H,H) = 8.8 Hz, 16 H), 5.20 (s, 8 H), 1.31 (s, 72 H) ppm; ^{13}C-NMR (150 MHz, 360 K, $C_2D_2Cl_4$): δ = 163.2, 156.0, 153.0, 147.8, 137.2, 132.6, 129.8, 126.8, 122.5, 120.7, 120.3, 119.6, 119.4, 42.9, 34.5, 31.7 ppm; HRMS (ESI, pos. mode, acetonitrile/chloroform 1:1): *m*/*z*: calculated for $C_{144}H_{129}N_4O_{16}$: 2169.93981 $[M+H]^+$, found: 2169.93890; UV-vis ($CHCl_3$): λ_{max} (ε_{max}) = 586 nm (60000 M^{-1} cm^{-1}), 547 nm (47000 M^{-1} cm^{-1}); (tol): λ_{max} (ε_{max}) = 575 nm (63000 M^{-1} cm^{-1}), 537 nm (50000 M^{-1} cm^{-1}); Fluorescence ($CHCl_3$): λ_{max} = 631 nm (λ_{ex} = 530 nm), Φ_{fl} = 0.21; (tol): λ_{max} = 612 nm (λ_{ex} = 530 nm), Φ_{fl} = 0.58; CV (CH_2Cl_2, 0.1 M TBAHFP, vs. Fc/Fc^+): $E_{1/2}(PBI/PBI^+)$ = 0.84 V, $E_{1/2}(PBI/PBI^-)$ = –1.15 V, $E_{1/2}(PBI/PBI^{2-})$ = –1.27 V.

***m*-2PBI$_{(4\text{-}t\text{Bu})4}$.** 100 mg (102 μmol, 1.0 eq.) of 1,6,7,12-tetrakis-4-*tert*-butylphenoxyperylene-3,4:9,10-tetracarboxylic acid bisanhydride (**PBA$_{(4\text{-}t\text{Bu})4}$**) and 14 mg (102 μmol, 1.0 eq.) of *meta*-xylylenediamine were added to 2.0 g imidazole and heated under nitrogen to 140 °C for 12 h. After cooling to room temperature 200 mL 2 N hydrochloric acid were added and the solution subsequently extracted with dichloromethane. The organic solvent was evaporated under reduced pressure and the crude product was purified by column chromatography (silica gel, CH_2Cl_2) to obtain 21 mg pure cyclophane ***m*-2PBI$_{(4\text{-}t\text{Bu})4}$** (19% yield) as a red solid.[4]

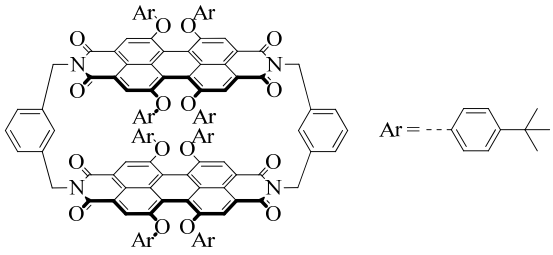

[4] Only minor traces of the cyclic trimer were obtained

$C_{144}H_{128}N_4O_{16}$ (2169.57): Mp.: > 300 °C; ^{1}H-NMR (400 MHz, $CDCl_3$): δ = 8.14 (s, 4 H), 7.99 (s, 4 H), 7.55 (m, 2 H), 7.47 (dd, ^4J(H,H) = 1.4 Hz, ^3J(H,H) = 7.7 Hz, 4 H), 7.33 (d, ^3J(H,H) = 8.6 Hz, 8 H), 7.20 (t, ^3J(H,H) = 7.7 Hz, 2 H), 7.10 (d, ^3J(H,H) = 8.6 Hz, 8 H), 7.01 (d, ^3J(H,H) = 8.6 Hz, 8 H), 6.35 (d, ^3J(H,H) = 8.6 Hz, 8 H), 5.61 (d, ^3J(H,H) = 13.5 Hz, 4 H), 4.81 (d, ^3J(H,H) = 13.5 Hz, 8 H), 1.38 (s, 36 H), 1.25 (s, 36 H) ppm; ^{13}C-NMR (100 MHz, $CDCl_3$): δ = 161.9, 155.4, 153.0, 152.7, 151.2, 146.3, 145.8, 136.2, 131.8, 130.2, 129.5, 126.6, 125.8, 125.6, 121.9, 121.3, 120.5, 120.3, 118.5, 118.4, 117.9, 117.1, 42.0, 33.4, 33.3, 30.5, 30.4, 28.7 ppm; HRMS (ESI, pos. mode, acetonitrile/chloroform 1:1): *m/z*: calculated for $C_{144}H_{129}N_4O_{16}$: 2169.93981 $[M+H]^+$, found: 2169.94021; UV-vis ($CHCl_3$): λ_{max} (ε_{max}) = 577 nm (66000 M^{-1} cm^{-1}), 541 nm (59000 M^{-1} cm^{-1}); Fluorescence ($CHCl_3$): λ_{max} = 627 nm (λ_{ex} = 530 nm), Φ_{fl} = 0.09.

2PBI$_{(2,6\text{-}i\text{Pr})2}$.[229] 50 mg (67 μmol, 1.0 eq.) of the perylene bisanhydride **PBA$_{(2,6\text{-}i\text{Pr})2}$** and 9.10 mg (67 μmol, 1.0 eq.) *para*-xylylenediamine were added to a solution of 1.0 g imidazole in 15 mL pyridine. The mixture was heated under nitrogen to 140 °C for 19 h. After cooling to room temperature 50 mL 2 N hydrochloric acid were added and the solution subsequently extracted with dichloromethane. The organic solvent was evaporated under reduced pressure and the crude product was purified by column chromatography (silica gel, CH_2Cl_2/MeOH 99:1) and recycling GPC ($CHCl_3$) to obtain 3.4 mg (5.9% yield) of an isomeric mixture (4:1, transoid:cisoid) of cyclophane **2PBI$_{(2,6\text{-}i\text{Pr})2}$** as a red solid.

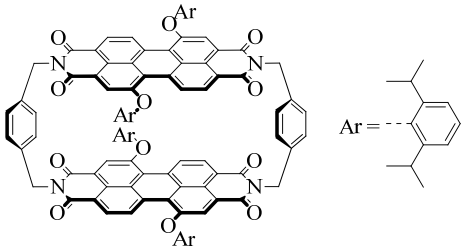

$C_{122}H_{96}N_4O_{12}$ (1690.72): Mp.: > 300 °C; ^{1}H-NMR (400 MHz, $CDCl_3$): **transoid**: δ = 9.58 (d, ^3J = 8.0 Hz, 4 H), 8.43 (d, ^3J = 8.0 Hz, 4 H), 7.91 (s, 4 H), 7.39 (m, 20 H), 5.27 (m, 8 H), 2.80 (m, 4 H), 2.72 (m, 4 H), 1.19 (d, ^3J = 8.0 Hz, 12 H), 1.10 (d, ^3J = 8.0 Hz, 12 H), 1.02 (d, ^3J = 8.0 Hz, 12 H), 0.93 (d, ^3J = 8.0 Hz, 12 H), ppm; **cisoid**: δ = 9.53 (d, ^3J = 8.0 Hz, 4 H), 8.42 (d, ^3J = 8.0 Hz, 4 H), 7.94 (s, 4 H), 7.29 (m, 20 H), 5.37 (d, ^3J = 12.0 Hz, 4 H), 5.14 (d, ^3J = 12.0 Hz, 4 H), 3.05 (m, 4 H), 2.72 (m, 4 H), 1.34 (m, 12 H), 1.28 (m, 12 H), 1.03 (m, 12 H), 0.85 (m, 12 H) ppm; ^{13}C-NMR (100 MHz, $CDCl_3$): **transoid**: δ =

162.6, 162.4, 156.9, 146.9, 141.2, 140.8, 137.0, 133.8, 130.4, 129.5, 129.2, 127.9, 127.5, 125.4, 125.3, 124.1, 123.5, 122.0, 120.4, 119.3, 42.5, 27.4, 27.2, 25.4, 24.3, 22.7, 22.5 ppm; **cisoid**: δ = 162.7, 162.5, 156.8, 147.1, 141.5, 140.7, 136.9, 133.4, 130.4, 129.8, 129.1, 127.8, 127.4, 125.4, 125.1, 124.1, 123.3, 121.8, 120.8, 119.3, 42.5, 27.5, 27.2, 25.2, 24.3, 22.6, 22.5 ppm; HRMS (ESI, pos. mode, acetonitrile/chloroform 1:1): *m*/*z*: calculated for $C_{112}H_{97}N_4O_{12}$: 1689.70975 $[M+H]^+$, found: 1689.70912; UV-vis ($CHCl_3$): λ_{max} (ε_{max}) = 557 nm (93000 M^{-1} cm^{-1}), 519 nm (77000 M^{-1} cm^{-1}); Fluorescence ($CHCl_3$): λ_{max} = 584 nm (λ_{ex} = 530 nm), Φ_{fl} = 0.97.

2PBI$_{(2,6\text{-Ph})2}$.[229] 100 mg (114 μmol, 1.0 eq.) of the perylene bisanhydride **PBA$_{(2,6\text{-Ph})2}$** and 15.5 mg (114 μmol, 1.0 eq.) *para*-xylylenediamine were added to a solution of 1.0 g imidazole in 10 mL pyridine. The mixture was heated under nitrogen to 140 °C for 20 h. After cooling to room temperature 100 mL 2 N hydrochloric acid were added and the solution subsequently extracted with dichloromethane. The organic solvent was evaporated under reduced pressure and the crude product was purified by column chromatography (silica gel, CH_2Cl_2/MeOH 97:3) and recycling GPC ($CHCl_3$) to obtain 3.3 mg (3.0% yield) of an isomeric mixture (12:1, transoid:cisoid) of cyclophane **2PBI$_{(2,6\text{-Ph})2}$** as a red solid.

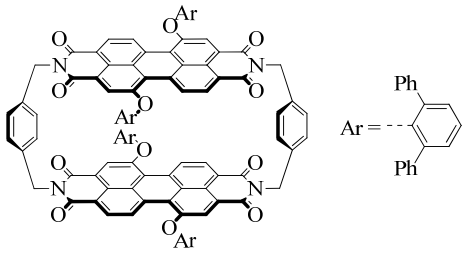

$C_{136}H_{80}N_4O_{12}$ (1962.15): Mp.: > 300 °C; ^{1}H-NMR (400 MHz, $CDCl_3$): **transoid**: δ = 8.81 (d, ^3J = 8.0 Hz, 4 H), 8.09 (d, ^3J = 8.0 Hz, 4 H), 7.73 (s, 4 H), 7.52 (m, 16 H), 7.43 (d, ^3J = 8.0 Hz, 4 H), 7.13 (d, ^3J = 8.0 Hz, 16 H), 6.75 (m, 12 H), 6.28 (t, ^3J = 8.0 Hz, 8 H), 5.98 (t, ^3J = 8.0 Hz, 4 H), 5.30 (m, 8 H) ppm; **cisoid**: δ = 8.79 (d, ^3J = 8.0 Hz, 4 H), 8.11 (d, ^3J = 8.0 Hz, 4 H), 7.75 (s, 4 H), 7.52 (m, 16 H), 7.43 (d, ^3J = 8.0 Hz, 4 H), 7.13 (d, ^3J = 8.0 Hz, 16 H), 6.75 (m, 12 H), 6.28 (t, ^3J = 8.0 Hz, 8 H), 5.98 (t, ^3J = 8.0 Hz, 4 H), 5.30 (m, 8 H) ppm; ^{13}C-NMR (100 MHz, $CDCl_3$): **transoid**: δ = 162.8, 162.6, 154.7, 147.8, 137.5, 137.2, 136.0, 135.4, 132.7, 131.3, 131.1, 130.4, 128.9, 128.8, 128.6, 127.9, 127.7, 127.6, 127.5, 127.1, 126.5, 123.4, 122.2, 121.2, 121.1, 120.9, 42.3 ppm; **cisoid**: δ = 162.8, 162.6, 154.7, 147.8, 137.5, 137.2, 136.0, 135.4, 132.7, 131.3, 131.1, 130.4, 128.9,

128.8, 128.6, 127.9, 127.7, 127.6, 127.5, 127.1, 126.5, 123.4, 122.2, 121.2, 121.1, 120.9, 42.3 ppm; HRMS (ESI, pos. mode, acetonitrile/chloroform 1:1): *m*/*z*: calculated for $C_{136}H_{81}N_4O_{12}$: 1961.58455 $[M+H]^+$, found: 1961.58423; UV-vis ($CHCl_3$): λ_{max} (ε_{max}) = 563 nm (95000 M^{-1} cm^{-1}), 525 nm (78000 M^{-1} cm^{-1}); Fluorescence ($CHCl_3$): λ_{max} = 594 nm (λ_{ex} = 530 nm), Φ_{fl} = 0.99.

nPBI$_{(4\text{-}t\text{Bu})4}$. 300 mg (305 μmol, 1.0 eq.) 1,6,7,12-tetrakis-4-*tert*-butylphenoxy-perylene-3,4:9,10-tetracarboxylic acid bisanhydride (**PBA$_{(4\text{-}t\text{Bu})4}$**) and 42 mg (305 μmol, 1.0 eq.) *para*-xylylenediamine were added to a solution of 1.0 g imidazole and 10 mL pyridine. The mixture was heated under nitrogen to 140 °C for 20 h. After cooling to room temperature 100 mL CH_2Cl_2 were added and the solution was extracted with hydrochloric acid (2 N, 100 mL). The aqueous solution was subsequently extracted with dichloromethane and the organic solvent was filtered to remove insoluble oligomers and polymers and evaporated under reduced pressure. The crude product was purified by column chromatography (silica gel, CH_2Cl_2) to obtain 21 mg pure dimer **2PBI$_{(4\text{-}t\text{Bu})4}$** (6.7% yield) as a red solid and a mixture of larger cycles **3PBI$_{(4\text{-}t\text{Bu})4}$**–**9PBI$_{(4\text{-}t\text{Bu})4}$**. These were then isolated by recycling GPC ($CHCl_3$) in their pure form in yields of 8.5% to 0.3%.

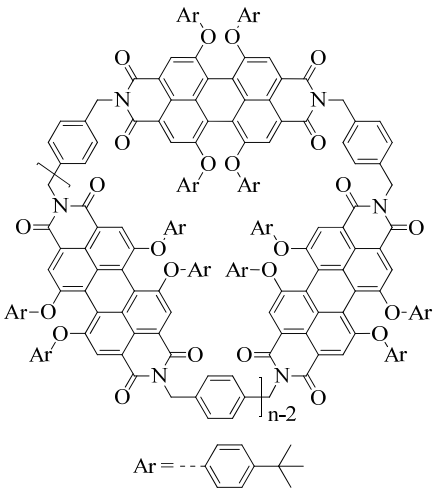

2PBI$_{(4\text{-}t\text{Bu})4}$: $C_{144}H_{128}N_4O_{16}$ (2169.57); 21 mg (10.0 μmol, 6.7%); ^{1}H-NMR (600 MHz, 360 K, $C_2D_2Cl_4$): δ = 8.07 (s, 8 H), 7.25 (s, 8 H), 7.23 (d, ^3J(H,H) = 8.8 Hz, 16 H), 6.78 (d, ^3J(H,H) = 8.8 Hz, 16 H), 5.20 (s, 8 H), 1.31 (s, 72 H) ppm; ^{13}C-NMR (150 MHz, 360 K, $C_2D_2Cl_4$): δ = 163.2, 156.0, 153.0, 147.8, 137.2, 132.6, 129.8, 126.8, 122.5, 120.7, 120.3, 119.6, 119.4, 42.9, 34.5, 31.7 ppm; HRMS (ESI, pos. mode,

acetonitrile/chloroform 1:1): *m*/*z*: calculated for $C_{144}H_{129}N_4O_{16}$: 2169.93981 $[M+H]^+$, found: 2169.93890; UV-vis (CH_2Cl_2): λ_{max} (ε_{max}) = 581 nm (57000 M^{-1} cm^{-1}), 543 nm (46000 M^{-1} cm^{-1}); (tol): 575 nm (63000 M^{-1} cm^{-1}), 537 nm (50000 M^{-1} cm^{-1}); Fluorescence (CH_2Cl_2): λ_{max} = 622 nm (λ_{ex} = 530 nm), Φ_{fl} = 0.07; (tol): λ_{max} = 612 nm (λ_{ex} = 530 nm), Φ_{fl} = 0.58.

3PBI$_{(4\text{-}t\text{Bu})4}$: $C_{216}H_{192}N_6O_{24}$ (3255.86); 28 mg (8.60 μmol, 8.5%); ^{1}H-NMR (400 MHz, $CDCl_3$): δ = 8.13 (s, 12 H), 7.41 (s, 12 H), 7.16 (d, ^3J(H,H) = 8.6 Hz, 24 H), 6.73 (d, ^3J(H,H) = 8.6 Hz, 24 H), 5.22 (s, 12 H), 1.26 (s, 108 H) ppm; ^{13}C-NMR (100 MHz, $CDCl_3$): δ = 163.4, 156.0, 152.9, 147.3, 136.5, 132.9, 129.5, 126.7, 122.4, 120.6, 120.1, 119.5, 119.4, 43.6, 34.5, 31.6 ppm; HRMS (ESI, pos. mode, acetonitrile/chloroform 1:1): *m*/*z*: calculated for $C_{216}H_{193}N_6O_{24}$: 3256.41334 $[M+H]^+$, found: 3256.40855; UV-vis (CH_2Cl_2): λ_{max} (ε_{max}) = 579 nm (114000 M^{-1} cm^{-1}), 541 nm (80000 M^{-1} cm^{-1}); (tol): 573 nm (109000 M^{-1} cm^{-1}), 535 nm (76000 M^{-1} cm^{-1}); Fluorescence (CH_2Cl_2): λ_{max} = 619 nm (λ_{ex} = 530 nm), Φ_{fl} = 0.64; (tol): λ_{max} = 611 nm (λ_{ex} = 530 nm), Φ_{fl} = 0.79.

4PBI$_{(4\text{-}t\text{Bu})4}$: $C_{288}H_{256}N_8O_{32}$ (4341.15); 14 mg (3.23 μmol, 4.2%); ^{1}H-NMR (400 MHz, $CDCl_3$): δ = 8.16 (s, 16 H), 7.35 (s, 16 H), 7.16 (d, ^3J(H,H) = 8.8 Hz, 32 H), 6.75 (d, ^3J(H,H) = 8.8 Hz, 32 H), 5.22 (s, 16 H), 1.24 (s, 144 H) ppm; ^{13}C-NMR (100 MHz, $CDCl_3$): δ = 163.5, 156.1, 152.9, 147.4, 136.6, 133.0, 129.1, 126.8, 122.4, 120.6, 120.1, 119.5, 43.6, 34.5, 31.6 ppm; MS (MALDI-TOF, pos. mode, DCTB in chloroform 1:1): *m*/*z*: calculated for $C_{288}H_{256}N_8O_{32}$: 4340.875 $[M]^+$, found: 4340.374; UV-vis (CH_2Cl_2): λ_{max} (ε_{max}) = 581 nm (160000 M^{-1} cm^{-1}), 542 nm (105000 M^{-1} cm^{-1}); (tol): 585 nm (147000 M^{-1} cm^{-1}), 544 nm (113000 M^{-1} cm^{-1}); Fluorescence (CH_2Cl_2): λ_{max} = 618 nm (λ_{ex} = 530 nm), Φ_{fl} = 0.53; (tol): λ_{max} = 617 nm (λ_{ex} = 530 nm), Φ_{fl} = 0.16.

5PBI$_{(4\text{-}t\text{Bu})4}$: $C_{360}H_{320}N_{10}O_{40}$ (5426.44); 8.2 mg (1.51 μmol, 2.5%); ^{1}H-NMR (400 MHz, $CDCl_3$): δ = 8.16 (s, 20 H), 7.35 (s, 20 H), 7.17 (d, ^3J(H,H) = 8.8 Hz, 40 H), 6.76 (d, ^3J(H,H) = 8.8 Hz, 40 H), 5.22 (s, 20 H), 1.25 (s, 180 H). ^{13}C-NMR (100 MHz, $CDCl_3$): δ = 163.5, 156.1, 152.9, 147.4, 136.5, 133.0, 129.1, 126.8, 122.4, 120.7, 120.1, 119.5, 43.6, 34.5, 31.6 ppm; MS (MALDI-TOF, pos. mode, DCTB in chloroform 1:1): *m*/*z*: calculated for $C_{360}H_{320}N_{10}O_{40}$: 5425.341 $[M]^+$, found: 5425.227; UV-vis (CH_2Cl_2): λ_{max} (ε_{max}) = 582 nm (194000 M^{-1} cm^{-1}), 543 nm (123000 M^{-1} cm^{-1}); (tol): 576 nm (185000

M^{-1} cm^{-1}), 536 nm (120000 M^{-1} cm^{-1}); Fluorescence (CH_2Cl_2): λ_{max} = 620 nm (λ_{ex} = 530 nm), Φ_{fl} = 0.59; (tol): λ_{max} = 611 nm (λ_{ex} = 530 nm), Φ_{fl} = 0.78.

6PBI$_{(4\text{-}t\text{Bu})4}$: $C_{432}H_{384}N_{12}O_{48}$ (6511.72); 6.0 mg (0.92 μmol, 1.8%); ^{1}H-NMR (400 MHz, $CDCl_3$): δ = 8.16 (s, 24 H), 7.35 (s, 24 H), 7.17 (d, ^3J(H,H) = 8.8 Hz, 48 H), 6.76 (d, ^3J(H,H) = 8.8 Hz, 48 H), 5.22 (s, 24 H), 1.25 (s, 216 H) ppm; ^{13}C-NMR (100 MHz, $CDCl_3$): δ = 163.5, 156.1, 152.9, 147.4, 136.5, 133.0, 129.1, 126.8, 122.4, 120.7, 120.1, 119.5, 43.6, 34.5, 31.6 ppm; MS (MALDI-TOF, pos. mode, DCTB in chloroform 1:1): *m*/*z*: calculated for $C_{432}H_{384}N_{12}O_{48}$: 6510.81 $[M]^+$, found: 6510.72; UV-vis (CH_2Cl_2): λ_{max} (ε_{max}) = 583 nm (239000 M^{-1} cm^{-1}), 543 nm (152000 M^{-1} cm^{-1}); (tol): 584 nm (210000 M^{-1} cm^{-1}), 543 nm (163000 M^{-1} cm^{-1}); Fluorescence (CH_2Cl_2): λ_{max} = 620 nm (λ_{ex} = 530 nm), Φ_{fl} = 0.56; (tol): λ_{max} = 620 nm (λ_{ex} = 530 nm), Φ_{fl} = 0.15.

7PBI$_{(4\text{-}t\text{Bu})4}$: $C_{504}H_{448}N_{14}O_{56}$ (7597.01); 3.3 mg (0.34 μmol, 1.0%); ^{1}H-NMR (400 MHz, $CDCl_3$): δ = 8.16 (s, 28 H), 7.35 (s, 28 H), 7.17 (d, ^3J(H,H) = 8.8 Hz, 56 H), 6.76 (d, ^3J(H,H) = 8.8 Hz, 56 H), 5.21 (s, 28 H), 1.25 (s, 252 H) ppm; ^{13}C-NMR (100 MHz, $CDCl_3$): δ = 163.5, 156.1, 152.9, 147.4, 136.5, 133.0, 129.1, 126.8, 122.4, 120.7, 120.1, 119.5, 43.6, 34.5, 31.6 ppm; MS (MALDI-TOF, pos. mode, DCTB in chloroform 1:1): *m*/*z*: calculated for $C_{504}H_{449}N_{14}O_{56}$: 7598.02 $[M+H]^+$, found: 7598.27; UV-vis (CH_2Cl_2): λ_{max} (ε_{max}) = 583 nm (255000 M^{-1} cm^{-1}), 543 nm (160000 M^{-1} cm^{-1}); (tol): 578 nm (229000 M^{-1} cm^{-1}), 539 nm (158000 M^{-1} cm^{-1}); Fluorescence (CH_2Cl_2): λ_{max} = 620 nm (λ_{ex} = 530 nm), Φ_{fl} = 0.52; (tol): λ_{max} = 617 nm (λ_{ex} = 530 nm), Φ_{fl} = 0.53.

8PBI$_{(4\text{-}t\text{Bu})4}$: $C_{576}H_{512}N_{16}O_{64}$ (8682.30); 1.4 mg (0.16 μmol, 0.4%); ^{1}H-NMR (400 MHz, $CDCl_3$): δ = 8.17 (s, 32 H), 7.35 (s, 32 H), 7.17 (d, ^3J(H,H) = 8.8 Hz, 64 H), 6.76 (d, ^3J(H,H) = 8.8 Hz, 64 H), 5.22 (s, 32 H), 1.25 (s, 288 H) ppm; ^{13}C-NMR (100 MHz, $CDCl_3$): δ = 163.5, 156.1, 152.9, 147.4, 136.5, 133.0, 129.1, 126.8, 122.4, 120.7, 120.1, 119.5, 43.6, 34.5, 31.6 ppm MS (MALDI-TOF, pos. mode, DCTB in chloroform 1:1): *m*/*z*: calculated for $C_{576}H_{513}N_{16}O_{64}$: 8683.31 $[M+H]^+$, found: 8683.87; UV-vis (CH_2Cl_2): λ_{max} (ε_{max}) = 583 nm (276000 M^{-1} cm^{-1}), 543 nm (173000 M^{-1} cm^{-1}); (tol): 582 nm (226000 M^{-1} cm^{-1}), 542 nm (171000 M^{-1} cm^{-1}); Fluorescence (CH_2Cl_2): λ_{max} = 618 nm (λ_{ex} = 530 nm), Φ_{fl} = 0.56; (tol): λ_{max} = 620 nm (λ_{ex} = 530 nm), Φ_{fl} = 0.14.

9PBI$_{(4\text{-}t\text{Bu})4}$: $C_{648}H_{576}N_{18}O_{72}$ (9767.58); 1.1 mg (0.11 μmol, 0.3%); ^{1}H-NMR (400 MHz, $CDCl_3$): δ = 8.17 (s, 36 H), 7.35 (s, 36 H), 7.17 (d, ^{3}J(H,H) = 8.8 Hz, 72 H), 6.76 (d, ^{3}J(H,H) = 8.8 Hz, 72 H), 5.21 (s, 36 H), 1.25 (s, 324 H) ppm; ^{13}C-NMR (100 MHz, $CDCl_3$): δ = 163.5, 156.1, 152.9, 147.4, 136.5, 133.0, 129.1, 126.8, 122.4, 120.7, 120.1, 119.5, 43.6, 34.5, 31.6 ppm MS (MALDI-TOF, pos. mode, DCTB in chloroform 1:1): *m*/*z*: calculated for $C_{648}H_{576}N_{18}O_{72}$: 9767.58 $[M]^+$, found: 9767.32; UV-vis (CH_2Cl_2): λ_{max} (ε_{max}) = 584 nm (295000 M^{-1} cm^{-1}), 543 nm (185000 M^{-1} cm^{-1}); (tol): 580 nm (239000 M^{-1} cm^{-1}), 540 nm (200000 M^{-1} cm^{-1}); Fluorescence (CH_2Cl_2): λ_{max} = 618 nm (λ_{ex} = 530 nm), Φ_{fl} = 0.54; (tol): λ_{max} = 621 nm (λ_{ex} = 530 nm), Φ_{fl} = 0.13.

Appendix

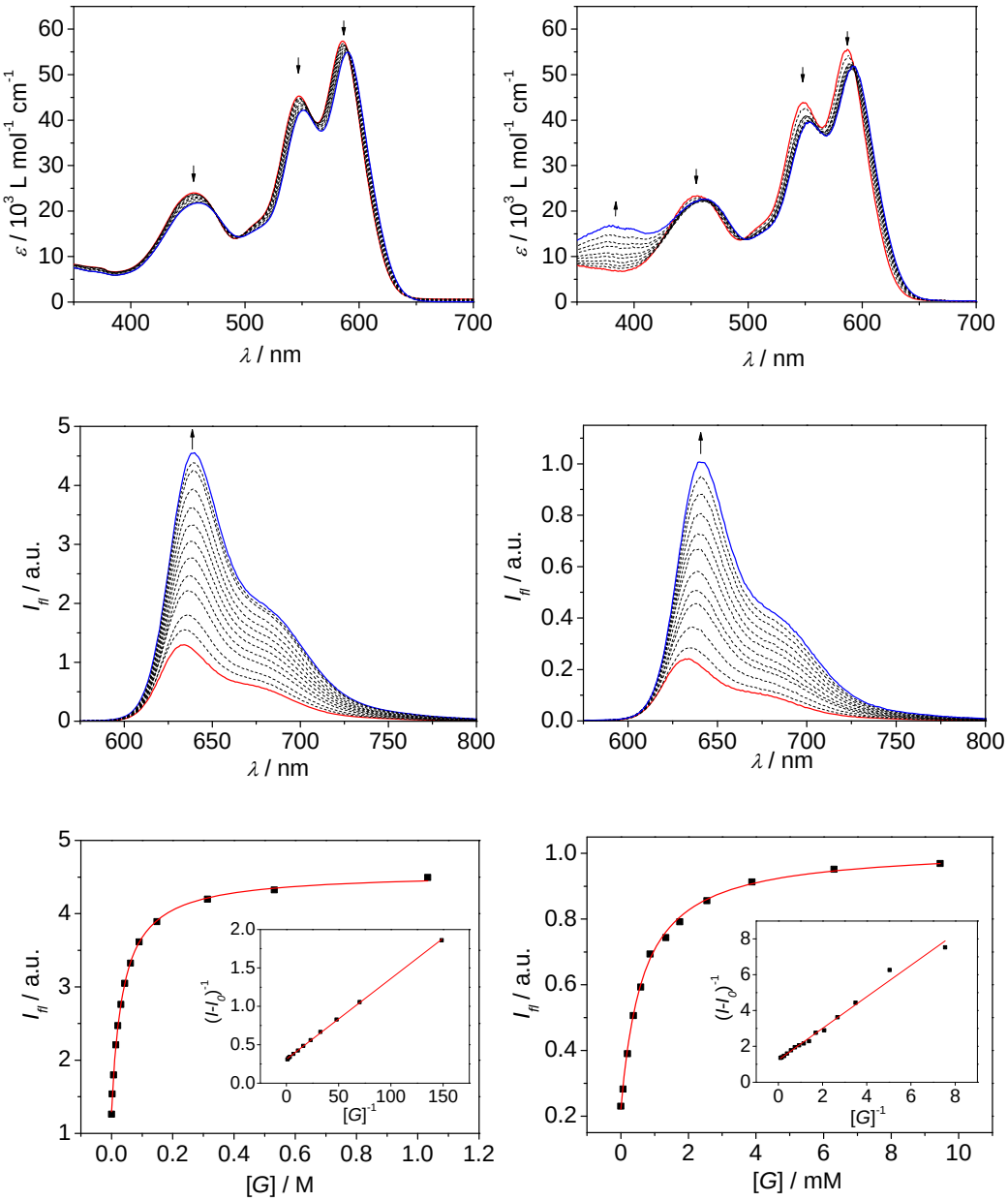

Figure 98. Changes in the UV-vis absorption (top) and emission spectra (middle) of PBI cyclophane **2PBI$_{(4\text{-}t\text{Bu})4}$** upon titration with naphthalene (a) and 9-fluorenone (b); c(**2PBI$_{(4\text{-}t\text{Bu})4}$**) = 5.8 x 10^{-5} M in $CHCl_3$; red line: spectra before titration; blue line: spectra after the individual guest is completely added; arrows indicate spectral changes; bottom: non-linear least square fitting curves of the fluorescence intensities vs. the guest concentration (inset: Benesi-Hildebrand plot confirming the 1:1 stoichiometry).

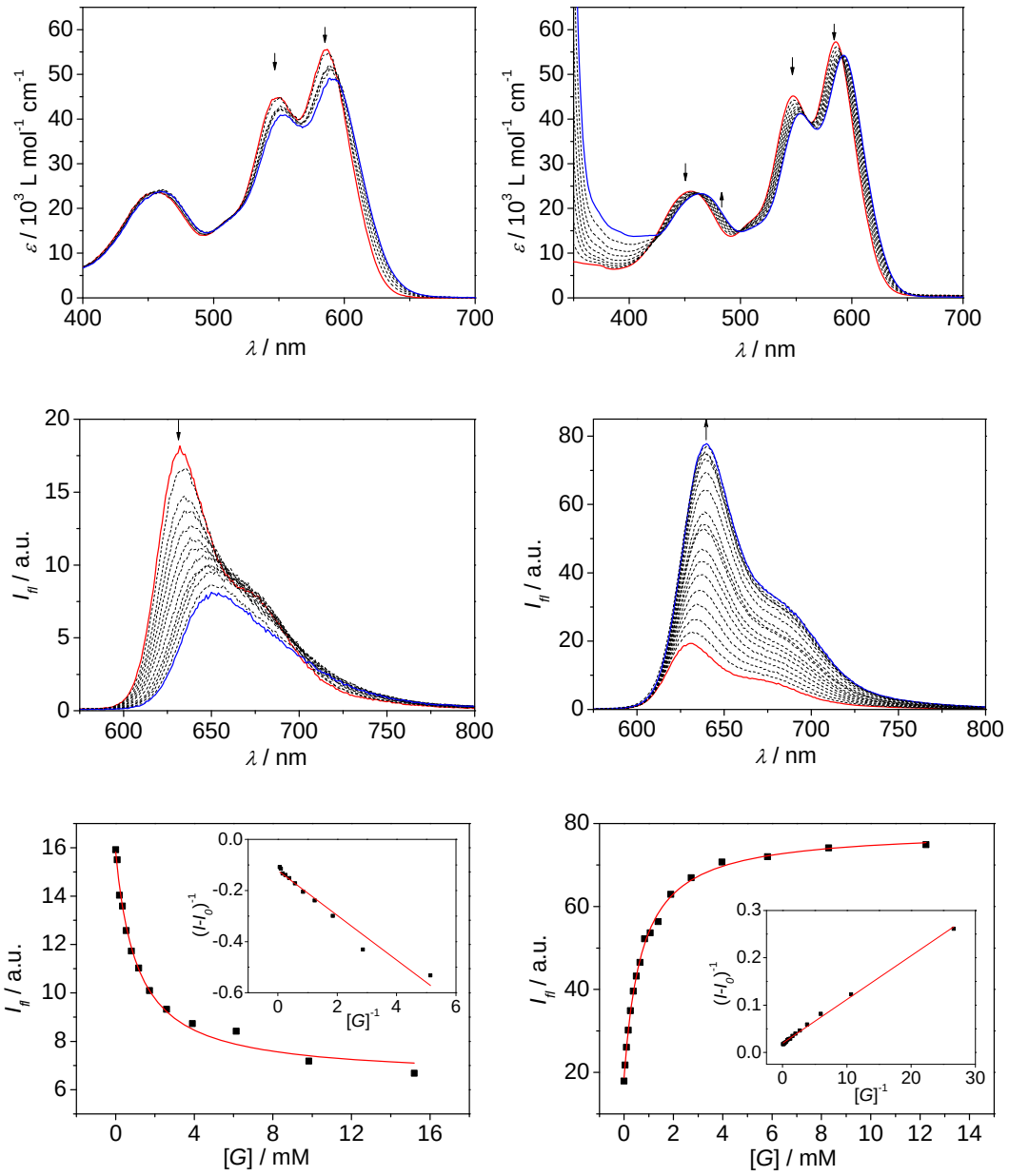

Figure 99. Changes in the UV-vis absorption (top) and emission spectra (middle) of PBI cyclophane **2PBI$_{(4\text{-}t\text{Bu})4}$** upon titration with carbazole (a) and anthraquinone (b); c(**2PBI$_{(4\text{-}t\text{Bu})4}$**) = 5.8 x 10^{-5} M in $CHCl_3$; red line: spectra before titration; blue line: spectra after the individual guest is completely added; arrows indicate spectral changes; bottom: non-linear least square fitting curves of the fluorescence intensities vs. the guest concentration (inset: Benesi-Hildebrand plot confirming the 1:1 stoichiometry).

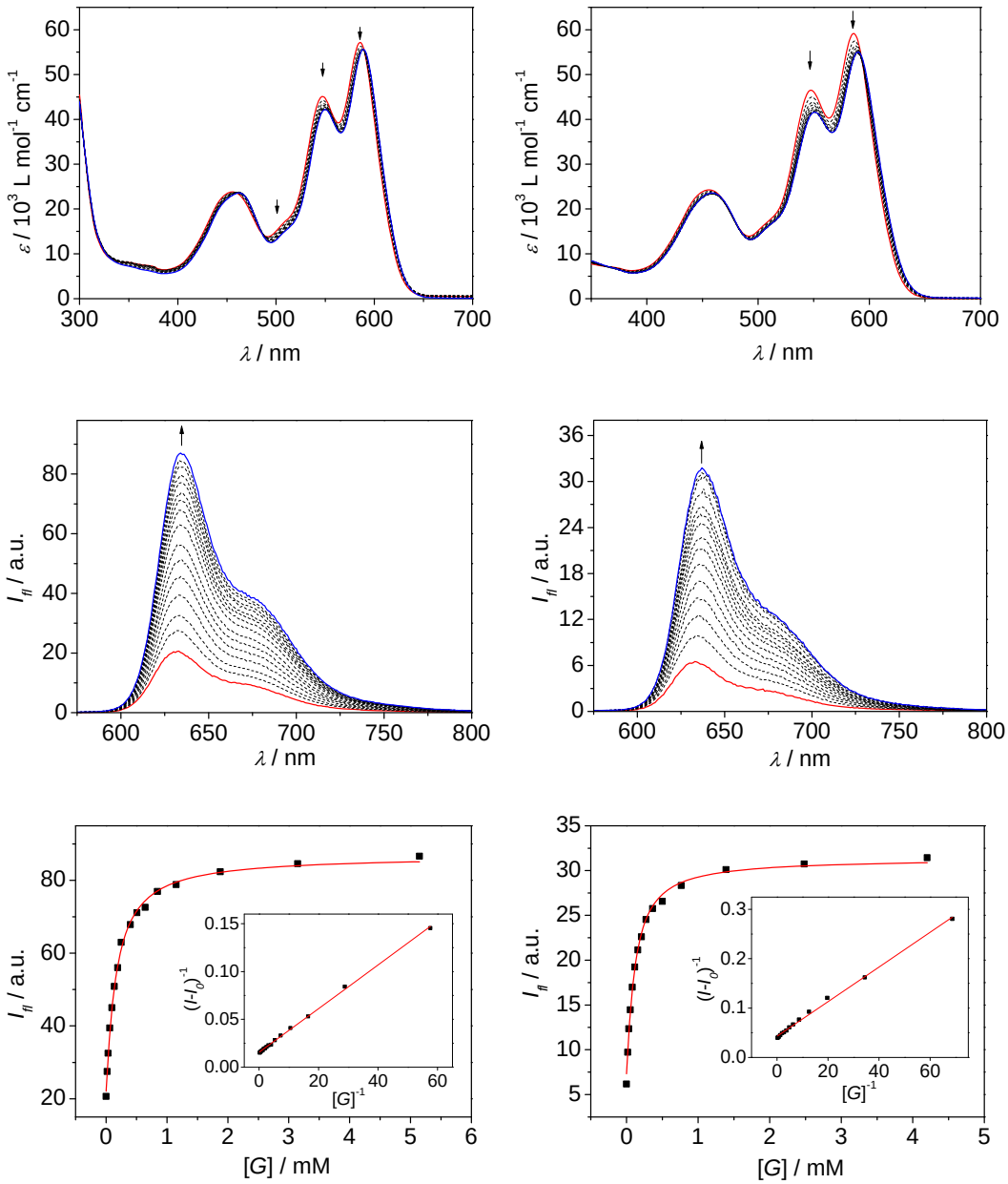

Figure 100. Changes in the UV-vis absorption (top) and emission spectra (middle) of PBI cyclophane **2PBI$_{(4\text{-}t\text{Bu})4}$** upon titration with biphenyl (a) and phenylnaphthalene (b); c(**2PBI$_{(4\text{-}t\text{Bu})4}$**) = 5.8 x 10^{-5} M in $CHCl_3$; red line: spectra before titration; blue line: spectra after the individual guest is completely added; arrows indicate spectral changes; bottom: non-linear least square fitting curves of the fluorescence intensities vs. the guest concentration (inset: Benesi-Hildebrand plot confirming the 1:1 stoichiometry).

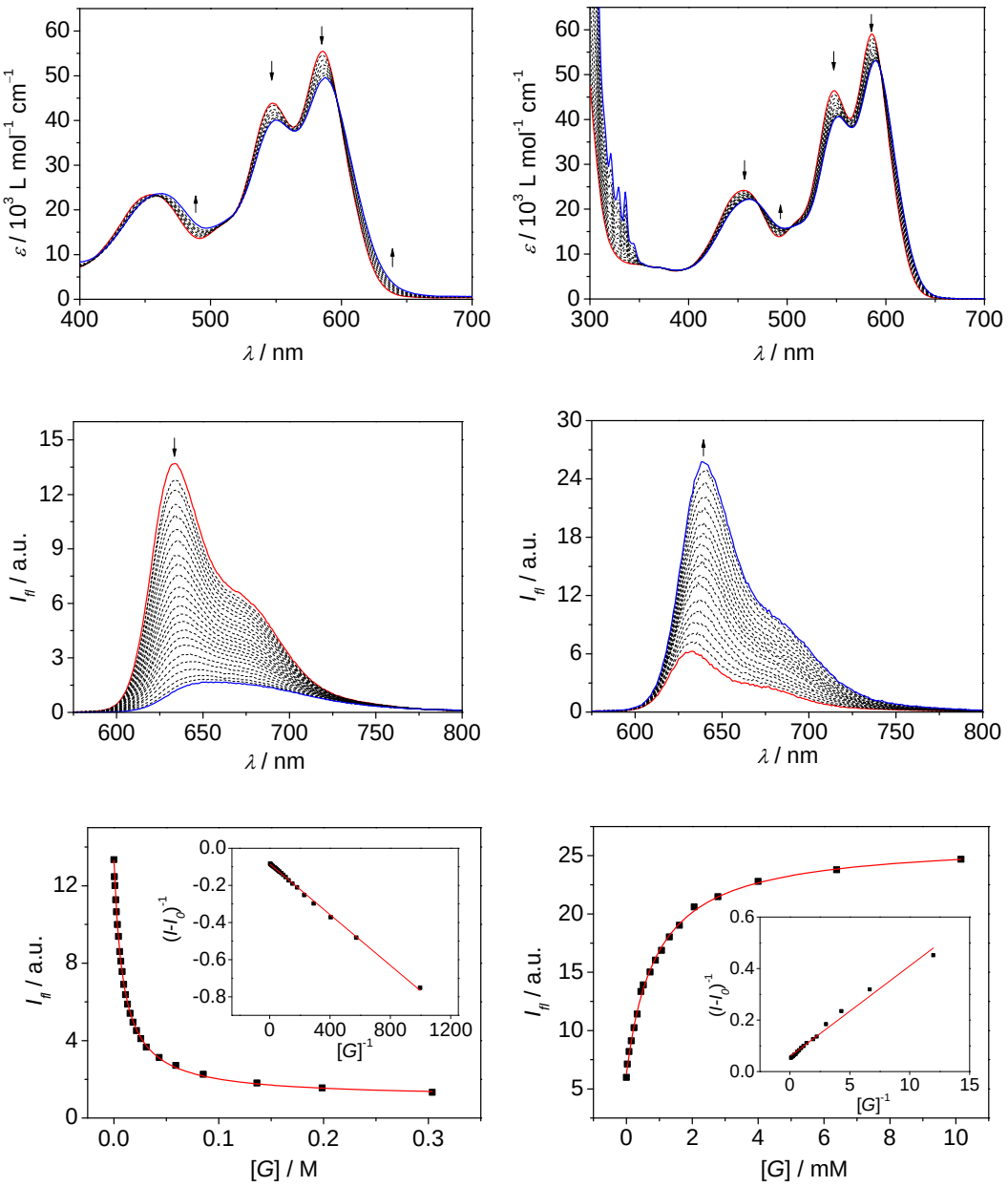

Figure 101. Changes in the UV-vis absorption (top) and emission spectra (middle) of PBI cyclophane **2PBI$_{(4\text{-}t\text{Bu})4}$** upon titration with pyrene (a) and triphenylene (b); c(**2PBI$_{(4\text{-}t\text{Bu})4}$**) = 5.8 x 10^{-5} M in $CHCl_3$; red line: spectra before titration; blue line: spectra after the individual guest is completely added; arrows indicate spectral changes; bottom: non-linear least square fitting curves of the fluorescence intensities vs. the guest concentration (inset: Benesi-Hildebrand plot confirming the 1:1 stoichiometry).

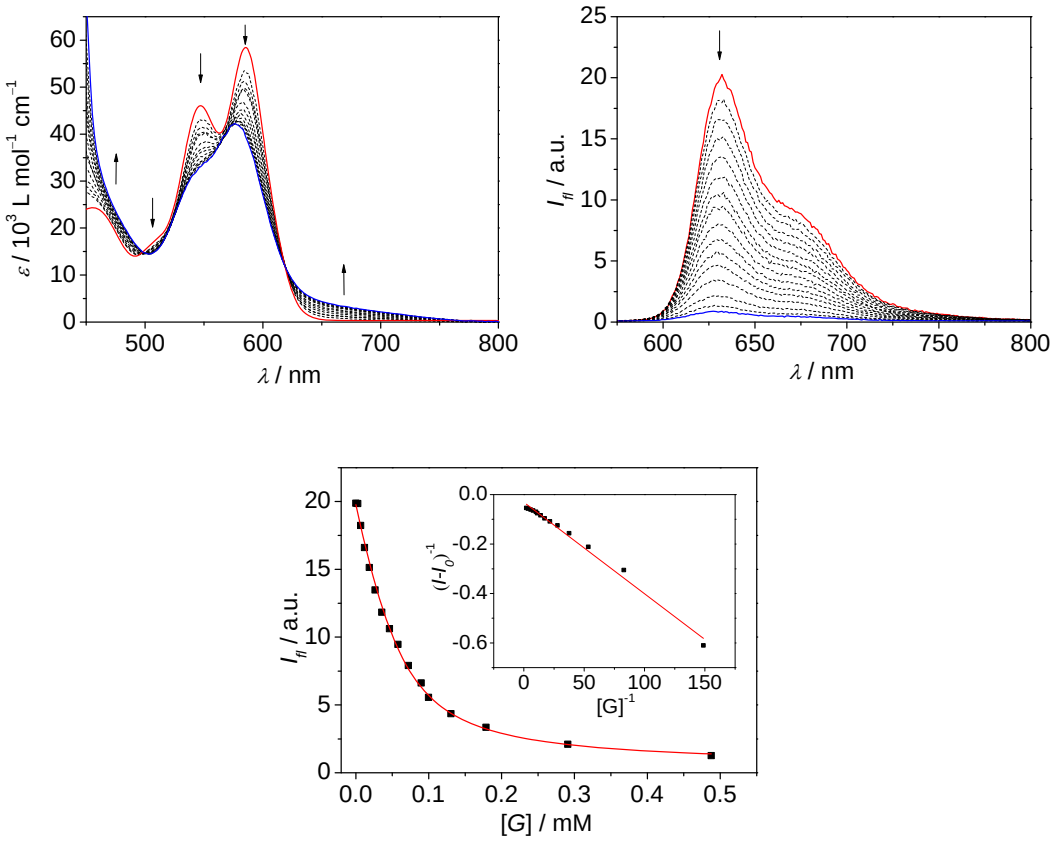

Figure 102. Changes in the UV-vis absorption (a) and emission spectra (b) of PBI cyclophane **2PBI**$_{(4\text{-}t\text{Bu})4}$ upon titration with perylene; c(**2PBI**$_{(4\text{-}t\text{Bu})4}$) = 5.8 x 10^{-5} M in $CHCl_3$; red line: spectra before titration; blue line: spectra after the individual guest is completely added; arrows indicate spectral changes; c) non-linear least square fitting curves of the fluorescence intensities vs. the guest concentration (inset: Benesi-Hildebrand plot confirming the 1:1 stoichiometry).

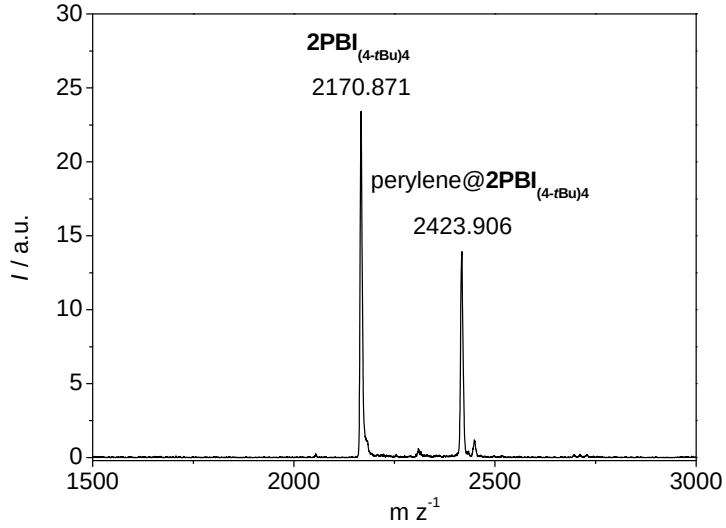

Figure 103. Mass spectrum of the free cyclophane **2PBI**$_{(4\text{-}t\text{Bu})4}$ and the 1:1 complex perylene@**2PBI**$_{(4\text{-}t\text{Bu})4}$; MALDI, linear positive mode, DCTB in $CHCl_3$.

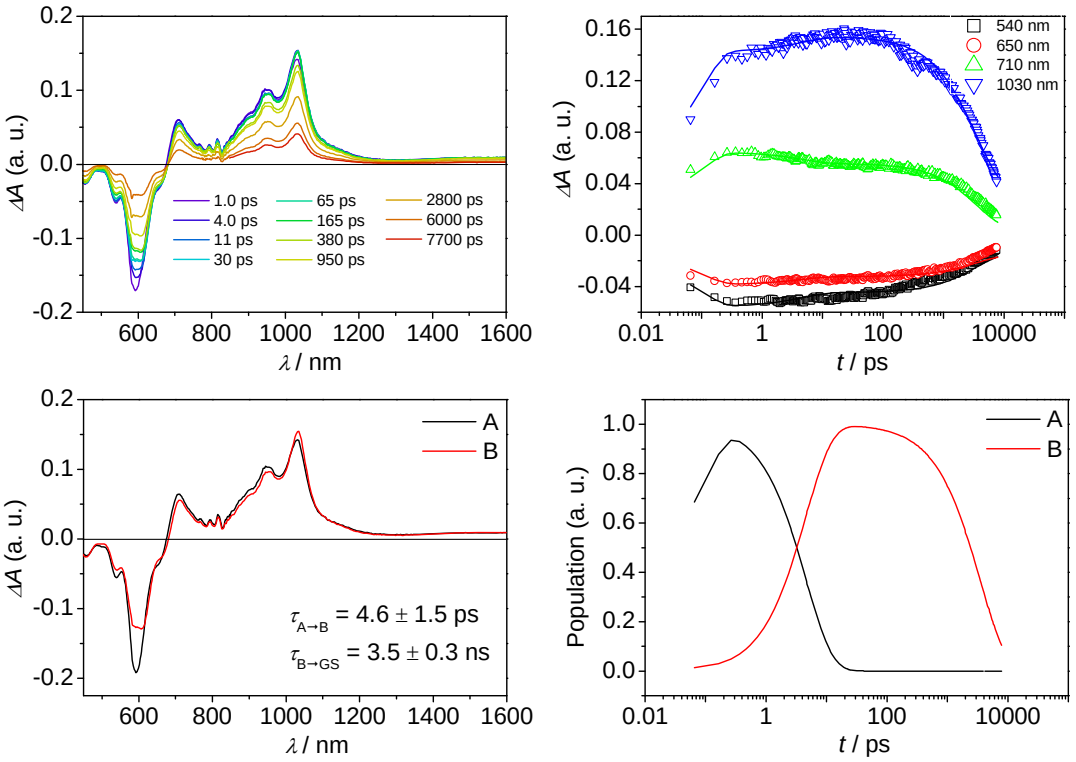

Figure 104. a) Femtosecond transient absorption of **1PBI$_{(4\text{-}t\text{Bu})4}$** in dichloromethane showing excited state dynamics after photoexcitation; b) plots of selected kinetic traces superimposed with matching curves at different wavelengths; c) species-associated spectra plots; d) kinetic model plots (λ_{ex} = 580 nm, 1.0 μJ/pulse, 298 K). A and B: singlet excited state S_1 (A → B likely presents relaxation on the singlet state based on the timescale and the similarity of the spectra).

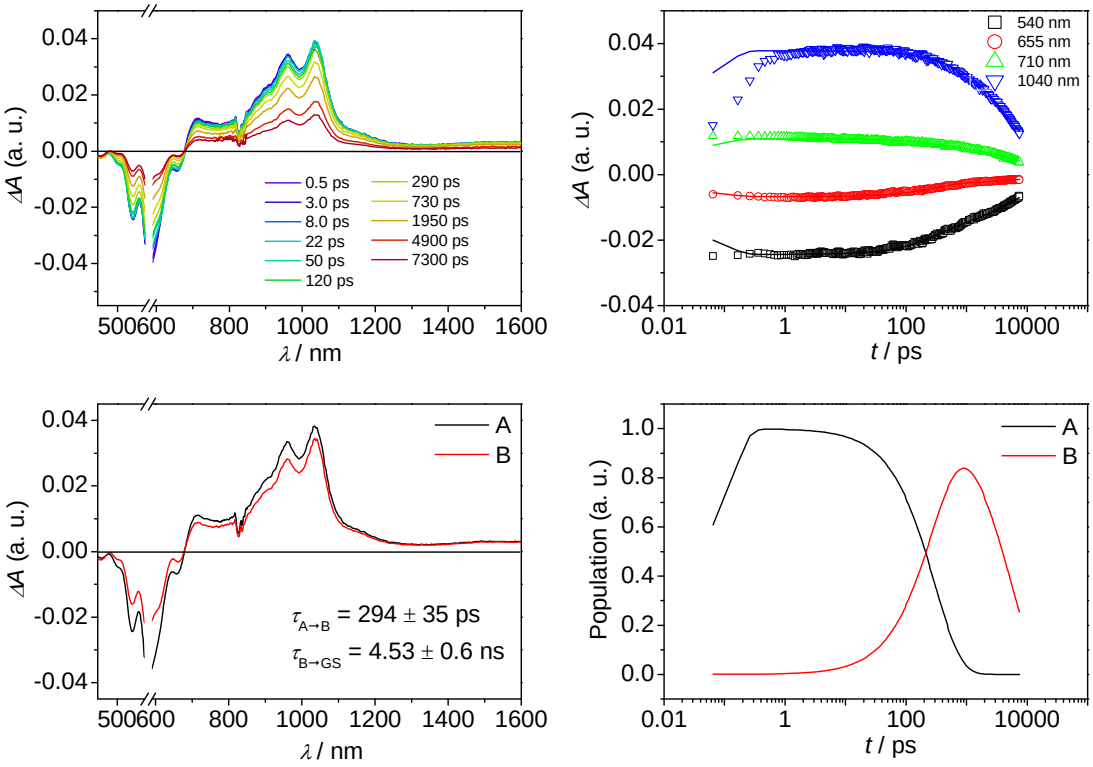

Figure 105. a) Femtosecond transient absorption of **2PBI$_{(4\text{-}t\text{Bu})4}$** in toluene showing excited state dynamics after photoexcitation; b) plots of selected kinetic traces superimposed with matching curves at different wavelengths; c) species-associated spectra plots; d) kinetic model plots (λ_{ex} = 580 nm, 1.0 μJ/pulse, 298 K). A and B: singlet excited state S_1 (A → B likely presents relaxation on the singlet state based on the timescale and the similarity of the spectra).

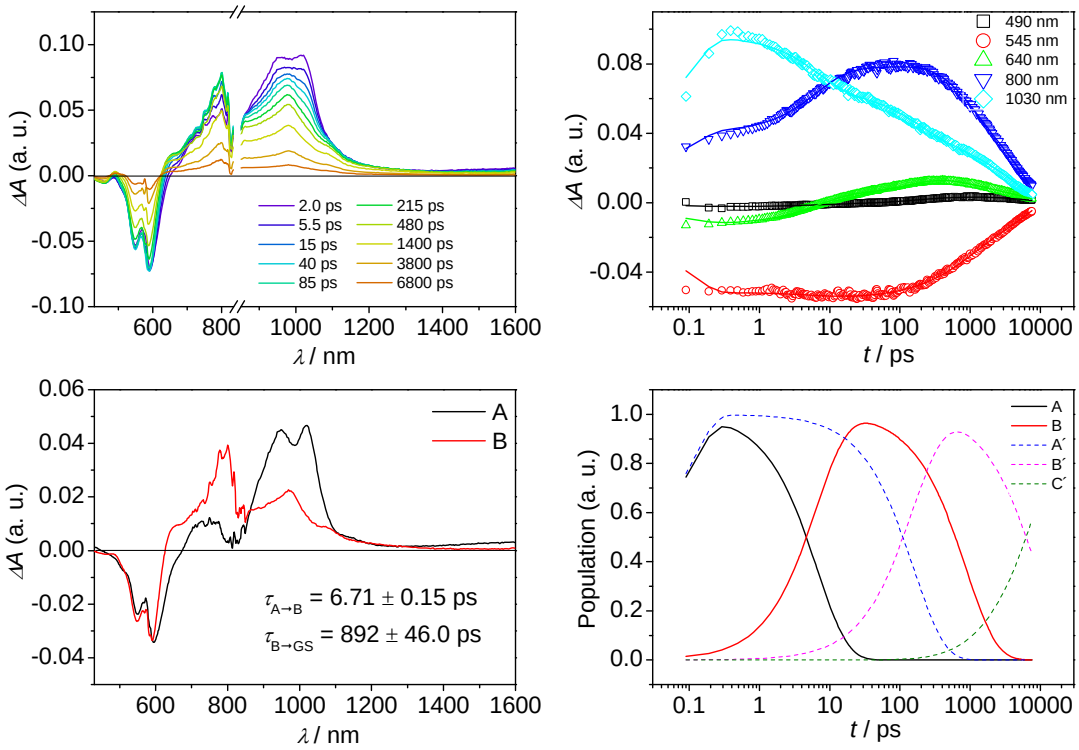

Figure 106. a) Femtosecond transient absorption of the carbazole@**2PBI**$_{(4\text{-}t\text{Bu})4}$ complex in dichloromethane showing excited state dynamics after photoexcitation; b) plots of selected kinetic traces superimposed with matching curves at different wavelength; c) species-associated spectra plots; d) kinetic model plots (λ_{ex} = 580 nm, 1.0 μJ/pulse, 298 K). A: singlet excited state S_1; B: charge transfer state CT; A´, B´ and C´ correspond to the free **2PBI**$_{(4\text{-}t\text{Bu})4}$ and are not shown in c) for clarity reasons.

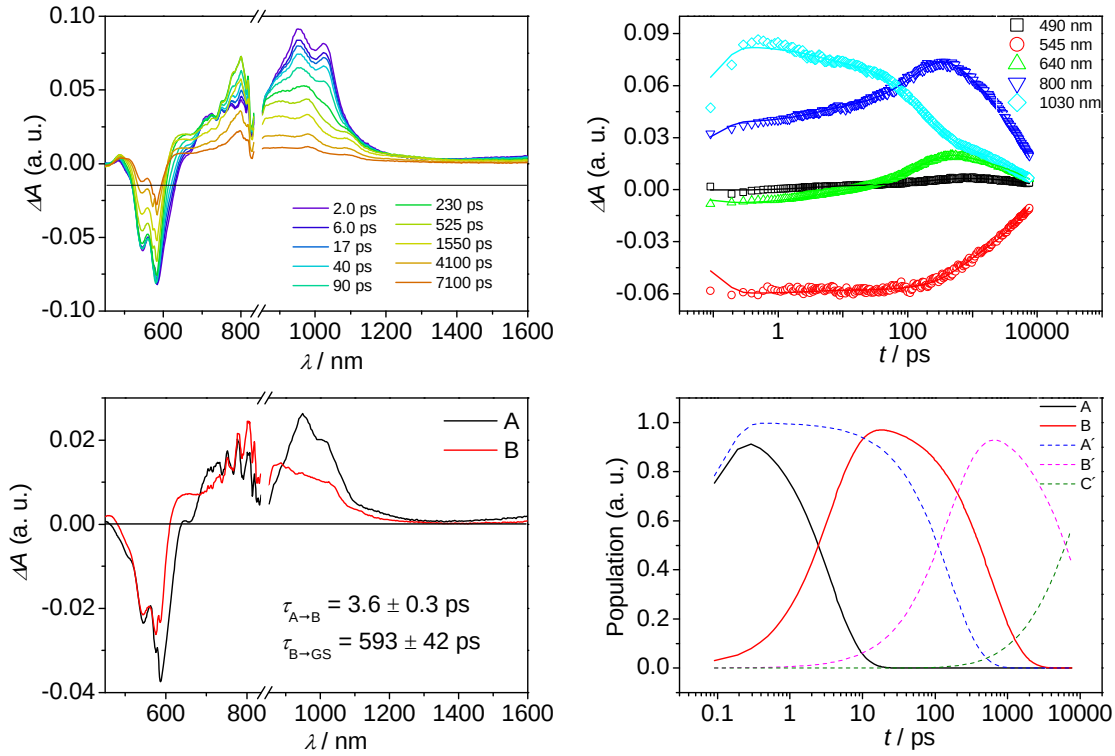

Figure 107. a) Femtosecond transient absorption of the pyrene@**2PBI$_{(4\text{-}t\text{Bu})4}$** complex in dichloromethane showing excited state dynamics after photoexcitation; b) plots of selected kinetic traces superimposed with matching curves at different wavelength; c) species-associated spectra plots; d) kinetic model plots (λ_{ex} = 580 nm, 1.0 μJ/pulse, 298 K). A: singlet excited state S_1; B: charge transfer state CT; A´, B´ and C´ correspond to the free **2PBI$_{(4\text{-}t\text{Bu})4}$** and are not shown in c) for clarity reasons.

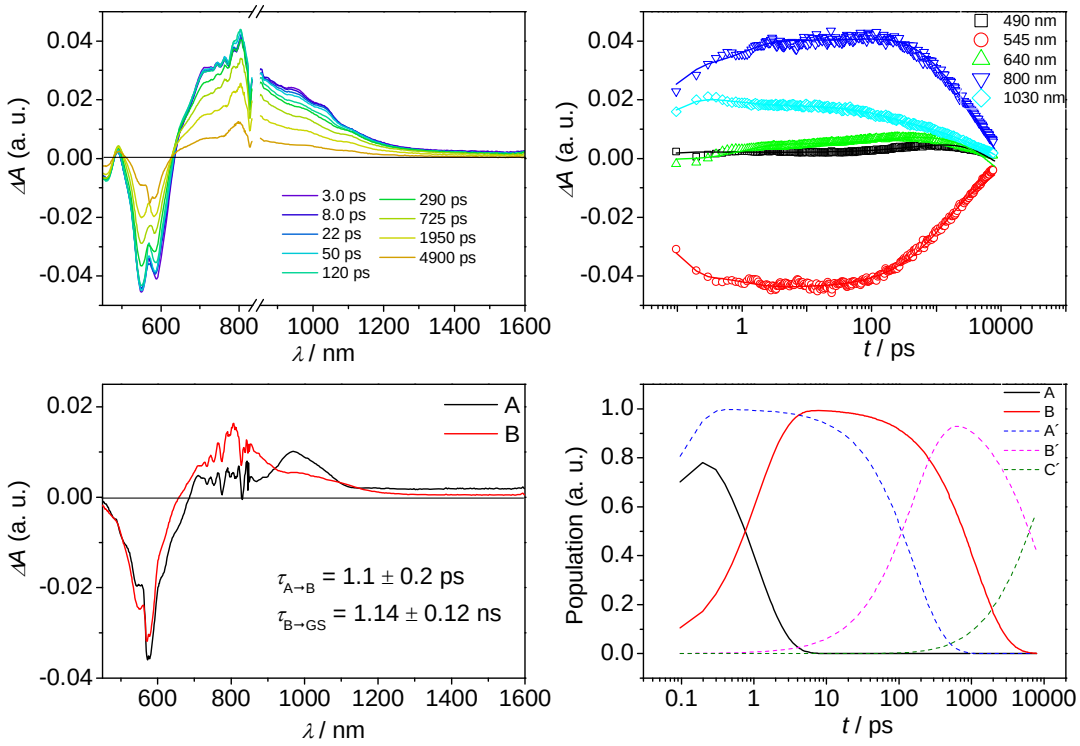

Figure 108. a) Femtosecond transient absorption of the anthracene@**2PBI$_{(4\text{-}t\text{Bu})4}$** complex in dichloromethane showing excited state dynamics after photoexcitation; b) plots of selected kinetic traces superimposed with matching curves at different wavelength; c) species-associated spectra plots; d) kinetic model plots (λ_{ex} = 580 nm, 1.0 μJ/pulse, 298 K). A: singlet excited state S_1; B: charge transfer state CT; A´, B´ and C´ correspond to the free **2PBI$_{(4\text{-}t\text{Bu})4}$** and are not shown in c) for clarity reasons.

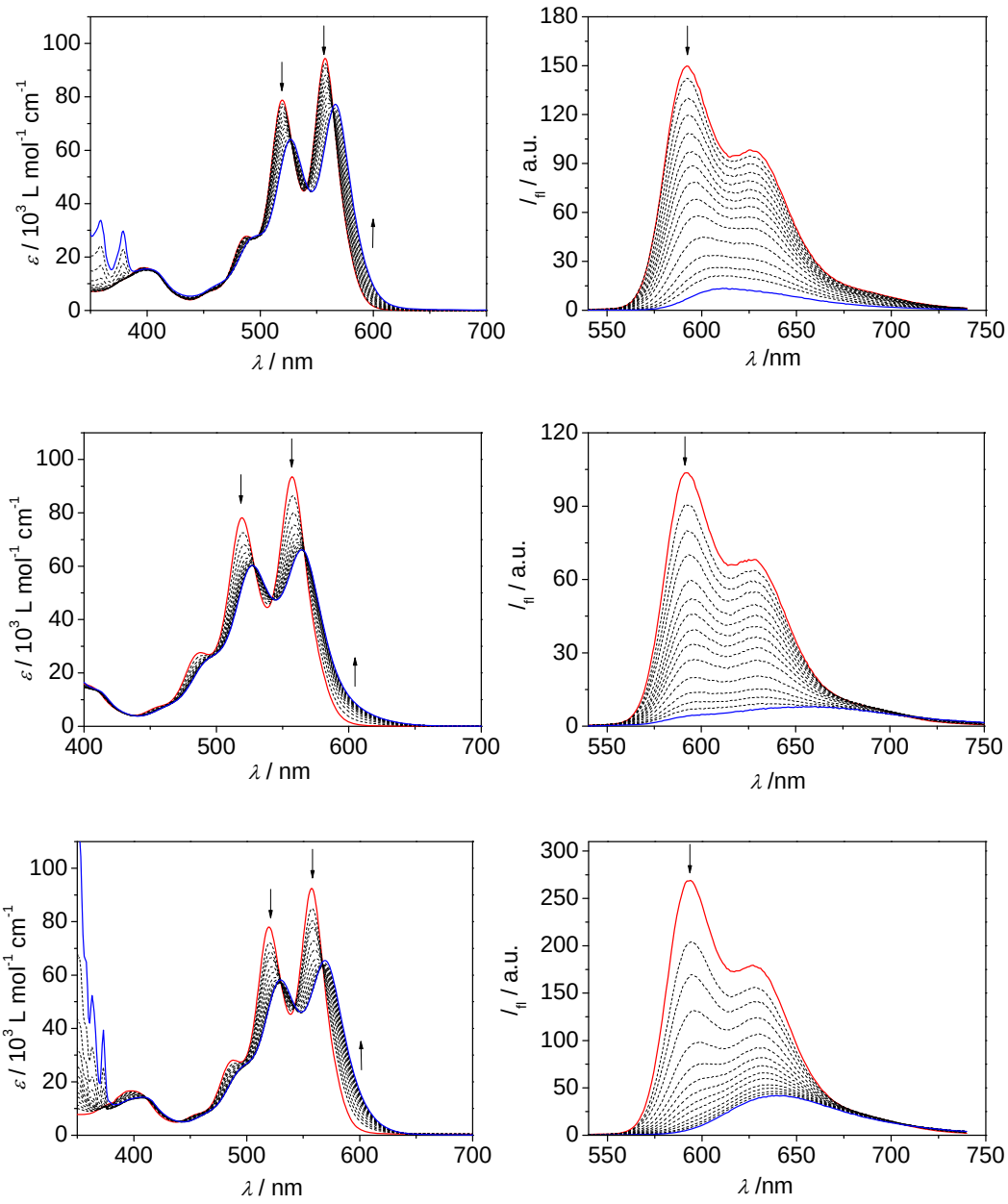

Figure 109. Changes in the UV-vis absorption (left) and emission spectra (right) of PBI cyclophane **2PBI$_{(2,6\text{-}i\text{Pr})2}$** upon titration with the individual guest molecules; a) carbazole, b) anthracene, c) pyrene; c(**2PBI$_{(2,6\text{-}i\text{Pr})2}$**) = 5.0 x 10^{-5} M in $CHCl_3$; red line: spectra before titration; blue line: spectra after the individual guest is completely added; arrows indicate spectral changes.

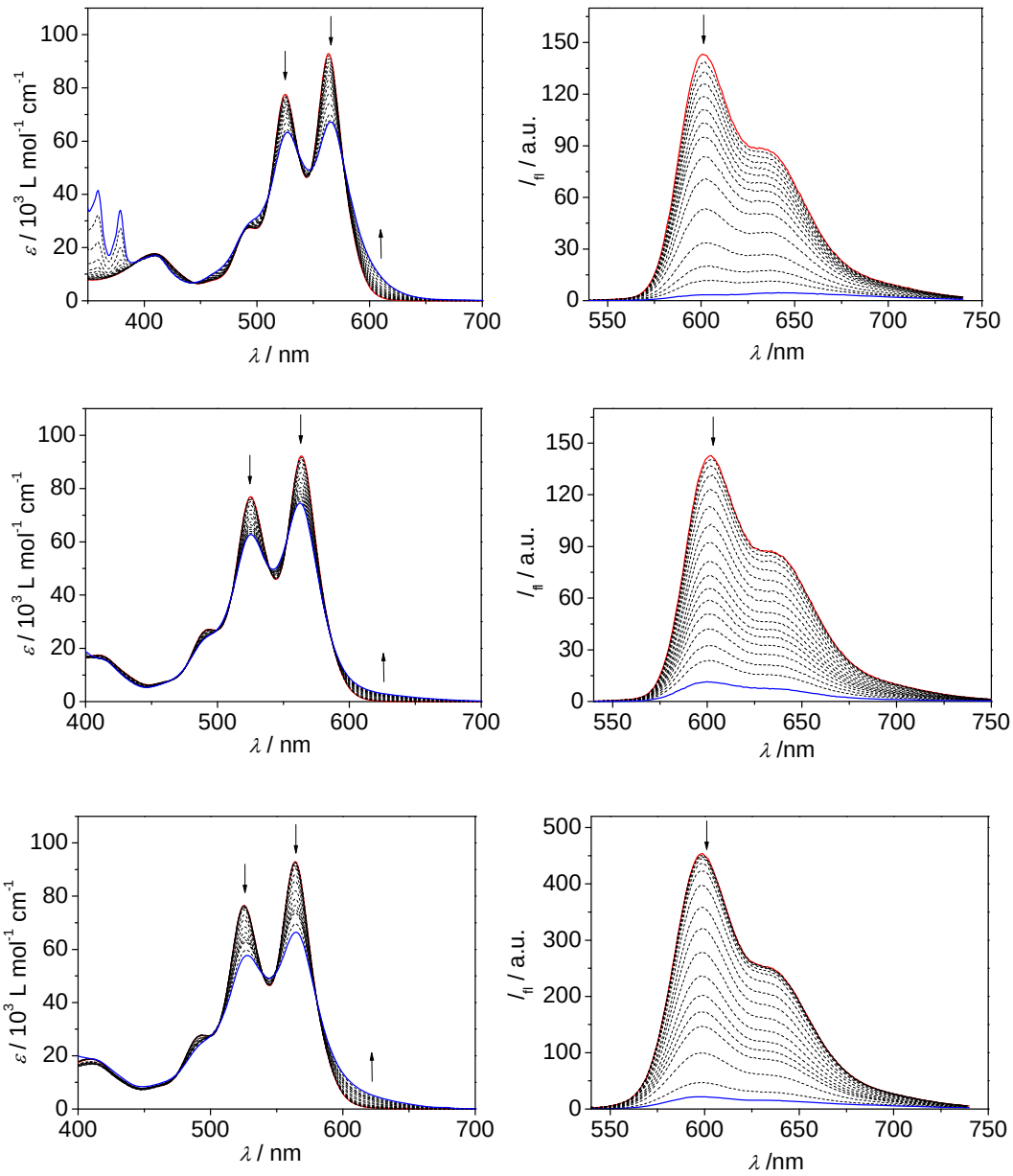

Figure 110. Changes in the UV-vis absorption (left) and emission spectra (right) of PBI cyclophane **2PBI$_{(2,6\text{-Ph})2}$** upon titration with the individual guest molecules; a) carbazole, b) anthracene, c) pyrene; c(**2PBI$_{(2,6\text{-Ph})2}$**) = 5.0 x 10^{-5} M in $CHCl_3$; red line: spectra before titration; blue line: spectra after the individual guest is completely added; arrows indicate spectral changes.

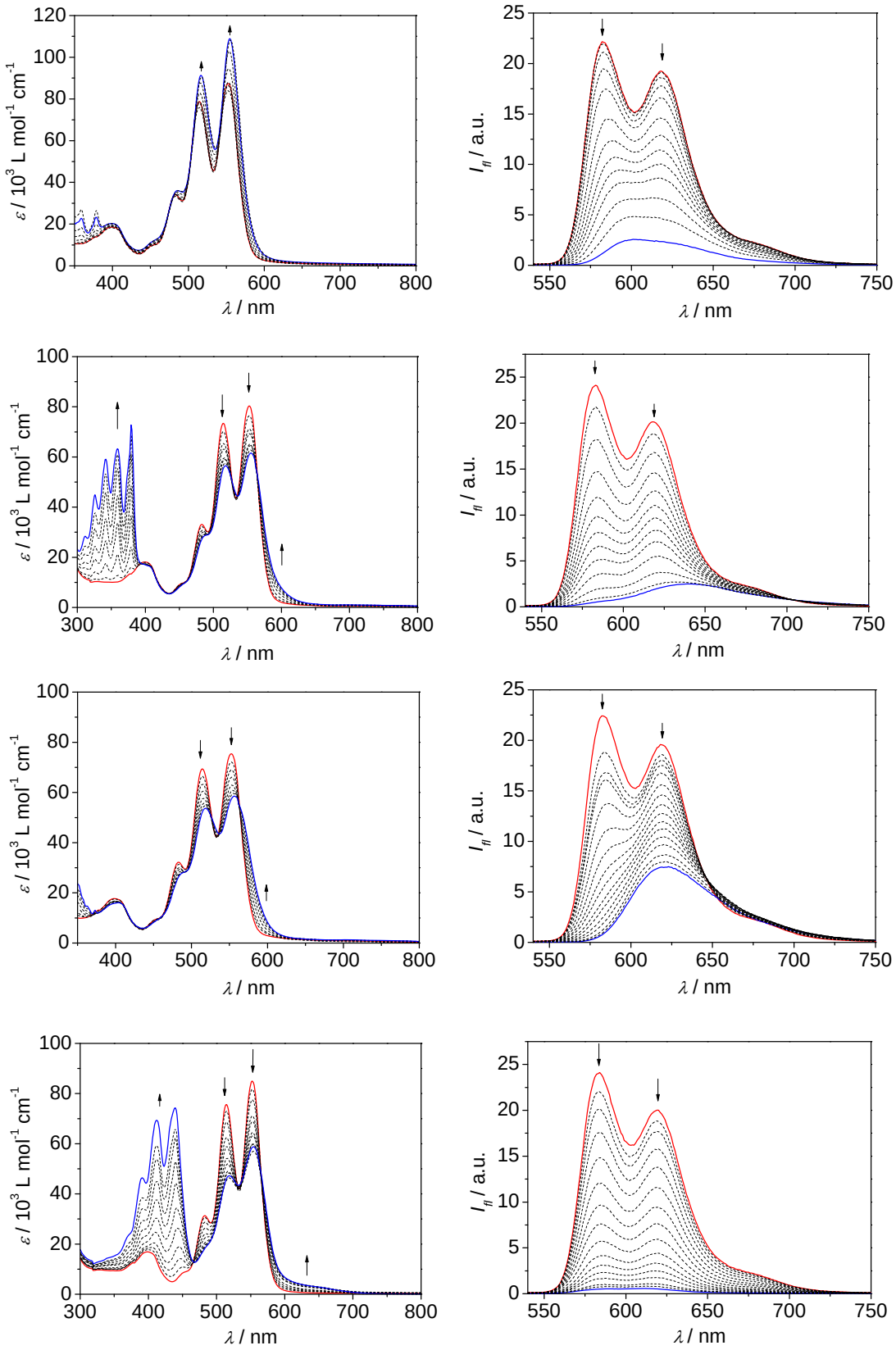

Figure 111. Changes in the UV-vis absorption (left) and emission spectra (right) of PBI cyclophane **2PBI$_{(2,6\text{-}iPr)2}$** upon titration with the individual guest molecules; a) carbazole, b) anthracene, c) pyrene, d) perylene; c(**2PBI$_{(2,6\text{-}iPr)2}$**) = 5.0 x 10^{-5} M in toluene; red line: spectra before titration; blue line: spectra after the individual guest is completely added; arrows indicate spectral changes.

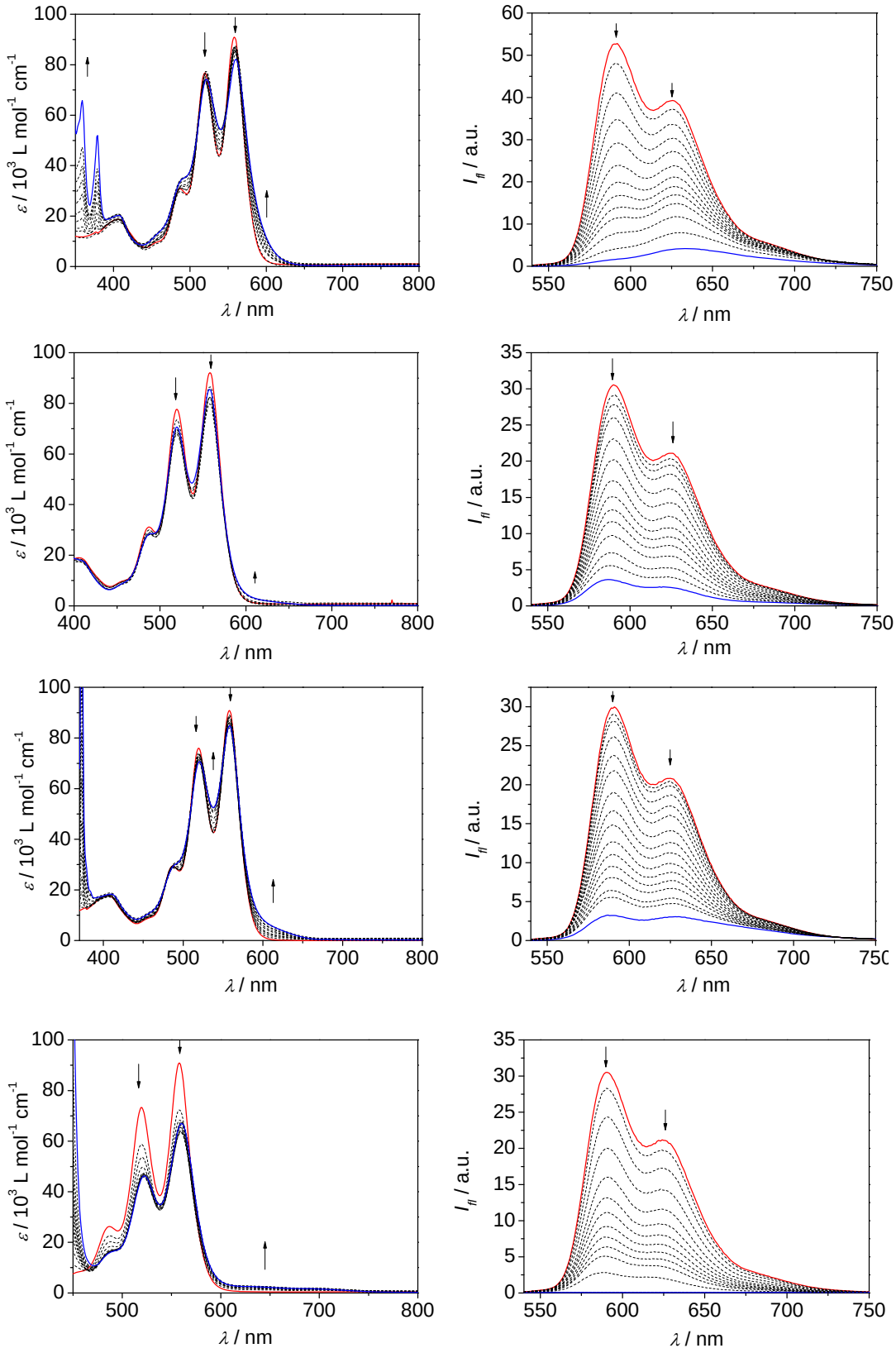

Figure 112. Changes in the UV-vis absorption (left) and emission spectra (right) of PBI cyclophane **2PBI$_{(2,6\text{-Ph})2}$** upon titration with the individual guest molecules; a) carbazole, b) anthracene, c) pyrene, d) perylene; c(**2PBI$_{(2,6\text{-Ph})2}$**) = 5.0 x 10^{-5} M in toluene; red line: spectra before titration; blue line: spectra after the individual guest is completely added; arrows indicate spectral changes.

Table 7. Binding constants K_a [M^{-1}] and Gibbs free energies ΔG^0_{298} [kJ mol^{-1}] calculated from fluorescence data for the 1:1 complexes of aromatic hydrocarbons by PBI cyclophanes **2PBI$_{(2,6\text{-}iPr)2}$** and **2PBI$_{(2,6\text{-}Ph)2}$** in toluene; c(**2PBI**) = 5 x 10^{-5} M.

guest	host	K_a (toluene)	R^2	$-\Delta G^0_{298}$
carbazole	**2PBI$_{(2,6\text{-}iPr)2}$**	357 ± 8.5	0.999	14.6
	2PBI$_{(2,6\text{-}Ph)2}$	662 ± 16	0.999	16.1
anthracene	**2PBI$_{(2,6\text{-}iPr)2}$**	(1.4 ± 0.06) x 10^4	0.998	23.7
	2PBI$_{(2,6\text{-}Ph)2}$	(1.4 ± 0.06) x 10^3	0.999	17.9
pyrene	**2PBI$_{(2,6\text{-}iPr)2}$**	(3.0 ± 0.2) x 10^4	0.996	25.5
	2PBI$_{(2,6\text{-}Ph)2}$	354 ± 12	0.999	14.5
perylene	**2PBI$_{(2,6\text{-}iPr)2}$**	(2.6 ± 0.03) x 10^5	0.993	30.9
	2PBI$_{(2,6\text{-}Ph)2}$	(7.5 ± 0.7) x 10^4	0.996	27.8

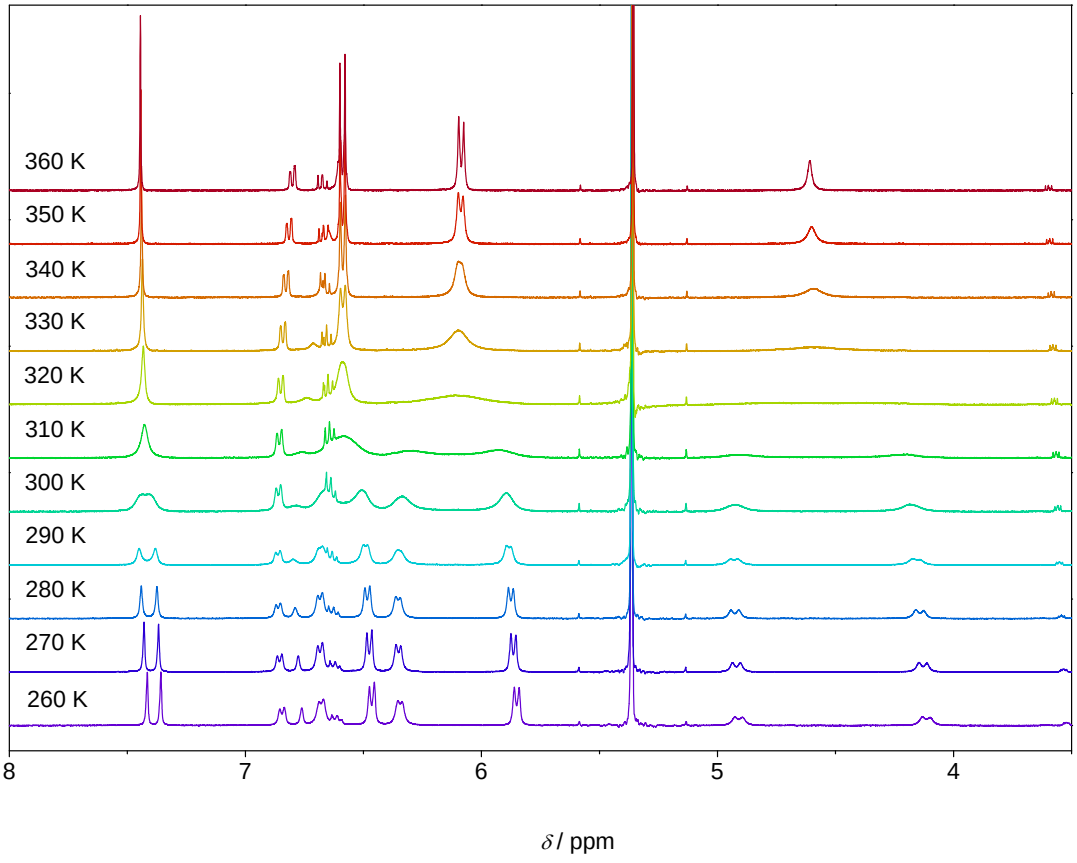

Figure 113. Temperature-dependent ^{1}H-NMR spectra of ***m*-2PBI$_{(4\text{-}tBu)4}$** from 360 K to 260 K in steps of 10 K; tetrachloroethane-d2; 400 MHz; c(***m*-2PBI$_{(4\text{-}tBu)4}$**) = 1 x 10^{-4} M.

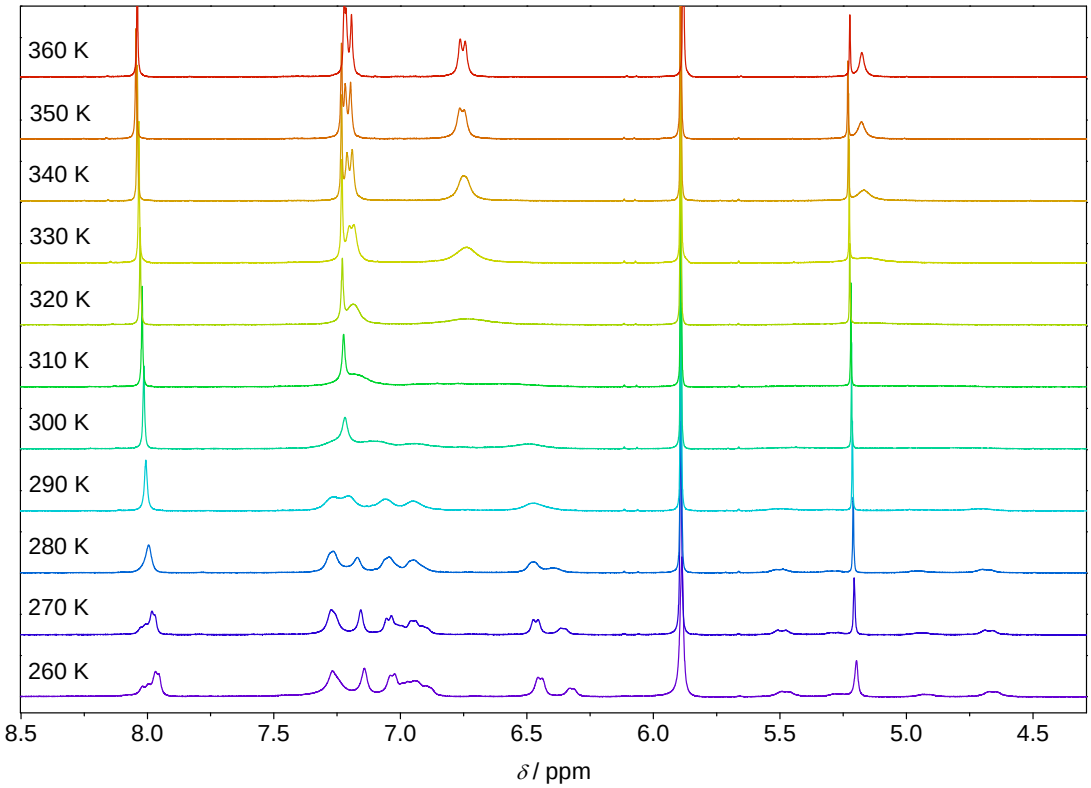

Figure 114. Temperature-dependent ^{1}H-NMR spectra of **2PBI$_{(4\text{-}t\text{Bu})4}$** from 360 K to 260 K in steps of 10 K; tetrachloroethane-d2; 400 MHz; c(**2PBI$_{(4\text{-}t\text{Bu})4}$**) = 1 x 10^{-4} M.

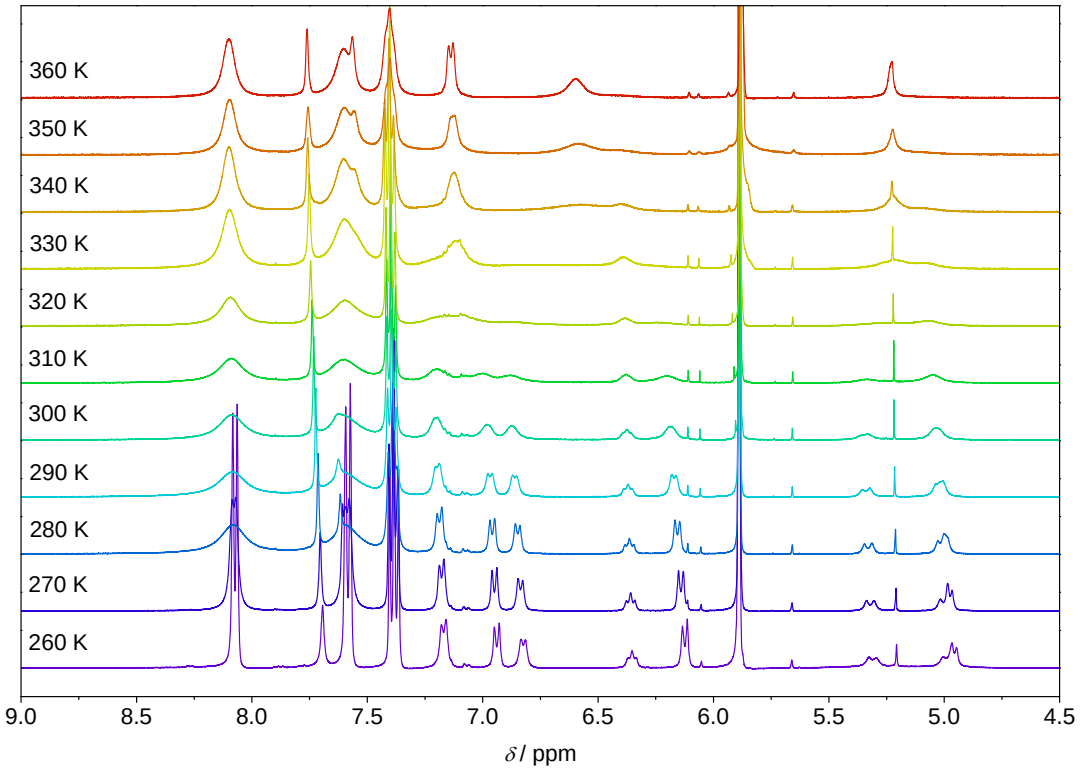

Figure 115. Temperature-dependent ^{1}H-NMR spectra of the perylene@**2PBI$_{(4\text{-}t\text{Bu})4}$** complex from 360 K to 260 K in steps of 10 K; tetrachloroethane-d2; 400 MHz; c(**2PBI$_{(4\text{-}t\text{Bu})4}$**) = 1 x 10^{-4} M; 8 eq. of perylene.

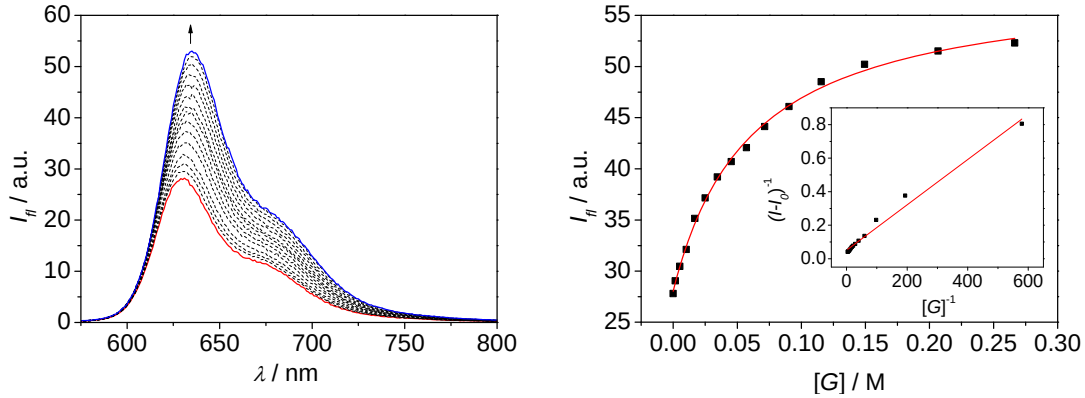

Figure 116. Changes in the emission spectra (left) of PBI cyclophane **2PBI$_{(4\text{-}t\text{Bu})4}$** upon titration with (*R*)-naphthylethylamine; *c*(**2PBI$_{(4\text{-}t\text{Bu})4}$**) = 6.0 x 10^{-5} M in $CHCl_3$; red line: spectrum before titration; blue line: spectrum after the guest is completely added; arrow indicates the spectral changes upon addition of guest molecules; right: non-linear least square fitting curve of the fluorescence intensities vs. the guest concentration (inset: Benesi-Hildebrand plot confirming the 1:1 stoichiometry).

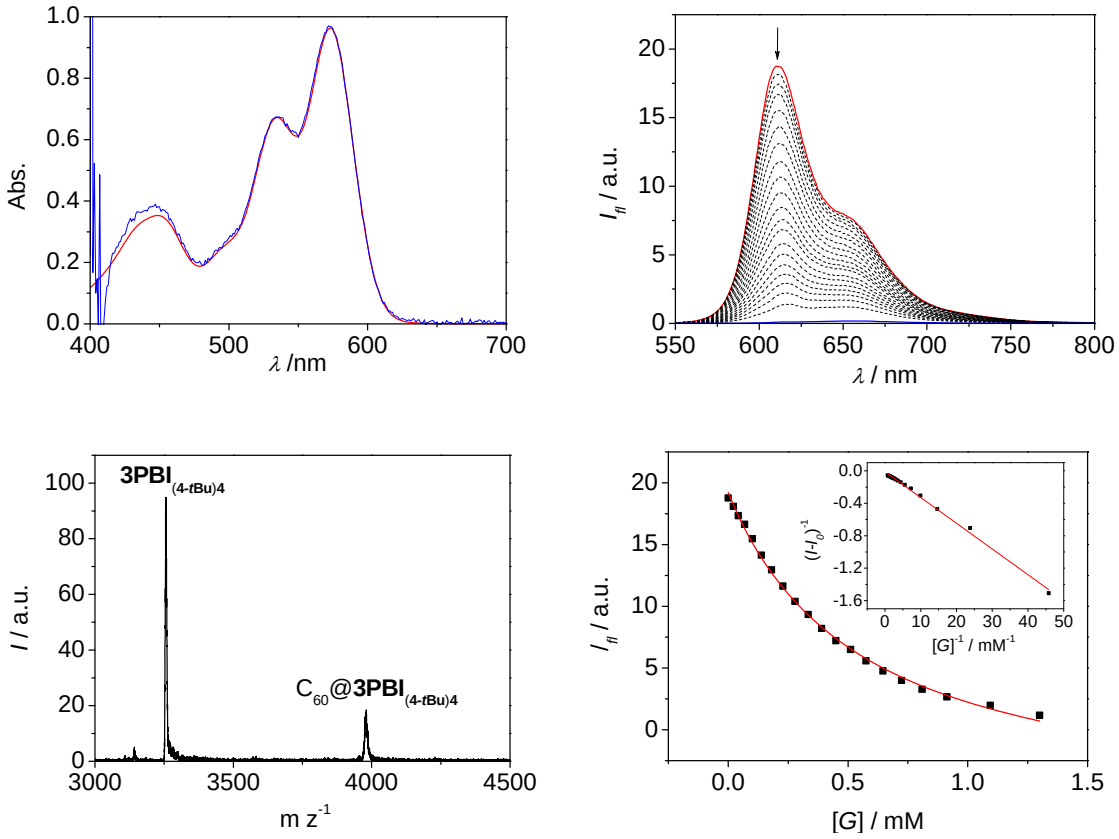

Figure 117. UV-vis absorption (a) and fluorescence (b) spectra of **3PBI$_{(4\text{-}t\text{Bu})4}$** upon addition of fullerene C_{60} in toluene (c = 5 x 10^{-5} M, RT); red line: spectra before titration; blue line: spectra after the guest is completely added (fullerene absorption is substracted from the measured spectrum); arrow indicates spectral changes; c) MALDI-TOF mass spectrum of the C_{60}@**3PBI$_{(4\text{-}t\text{Bu})4}$** complex; d) least square fitting of the fluorescence data (inset: Benesi-Hildebrand plot confirming the 1:1 stoichiometry).

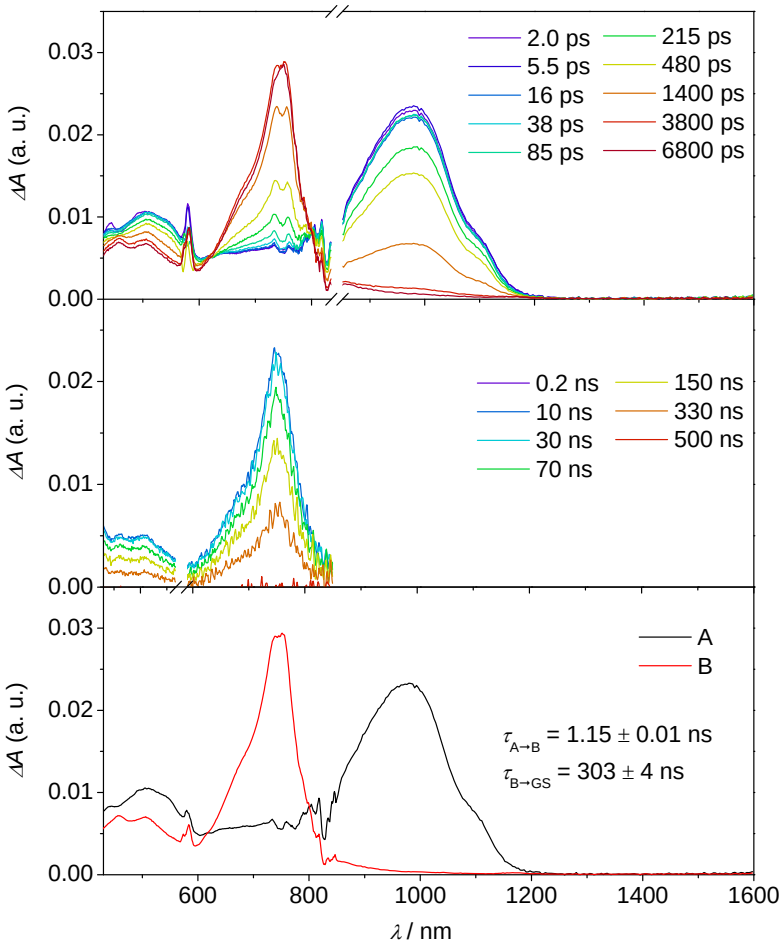

Figure 118. Femtosecond (a) and nanosecond (b) transient absorption spectra of fullerene C_{60} in toluene showing the excited state dynamics after photoexcitation. Species-associated spectra (c) reconstructed from global fits to the sequential A → B → ground state model, where A is ^{1}*C_{60} and B is ^{3}*C_{60}; λ_{ex} = 580 nm, 1.0 μJ/pulse, 298 K.

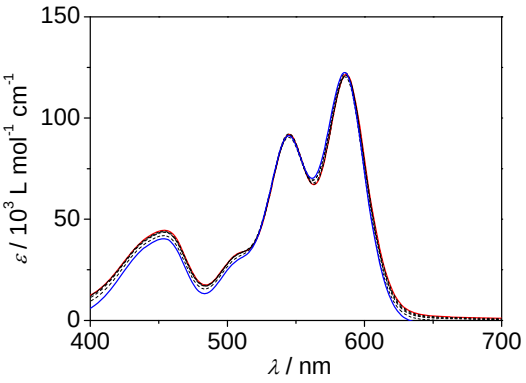

Figure 119. Concentration-dependent UV-vis spectra of **4PBI$_{(4\text{-}t\text{Bu})4}$** in toluene (2.5 x 10^{-5} M (red line) – 3.5 x 10^{-7} M (blue line)). The spectra are nearly superimposed revealing that there is no concentration effect on absorption properties of this macrocycle.

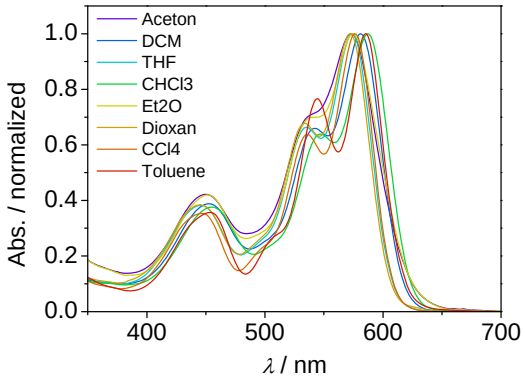

Figure 120. UV-vis spectra of **4PBI$_{(4\text{-}t\text{Bu})4}$** in various solvents; c = 5 x 10^{-6} M; RT.

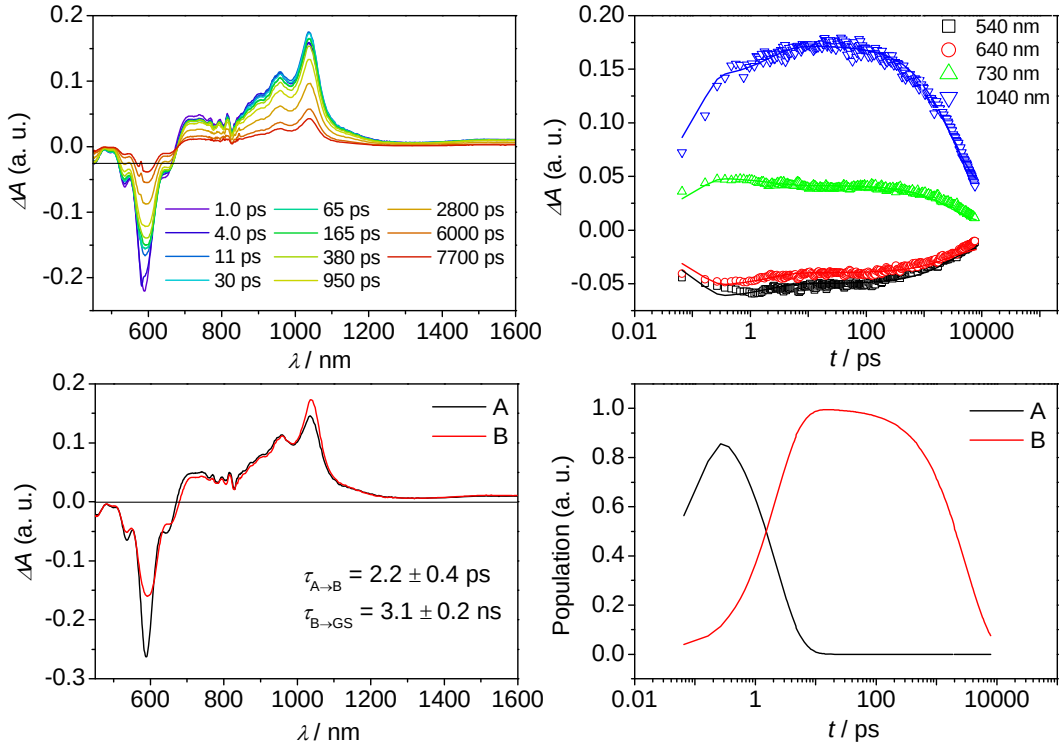

Figure 121. a) Femtosecond transient absorption spectra of reference **1PBI$_{(4\text{-}t\text{Bu})4}$** in toluene showing excited state dynamics after photoexcitation; b) plots of selected kinetic traces superimposed with matching curves at different wavelengths; c) species-associated spectra plots; d) kinetic model plots (λ_{ex} = 580 nm, 1.0 μJ/pulse, 298 K). A and B: singlet excited state S_1 (A → B likely presents relaxation on the singlet state based on the timescale and the similarity of the spectra).

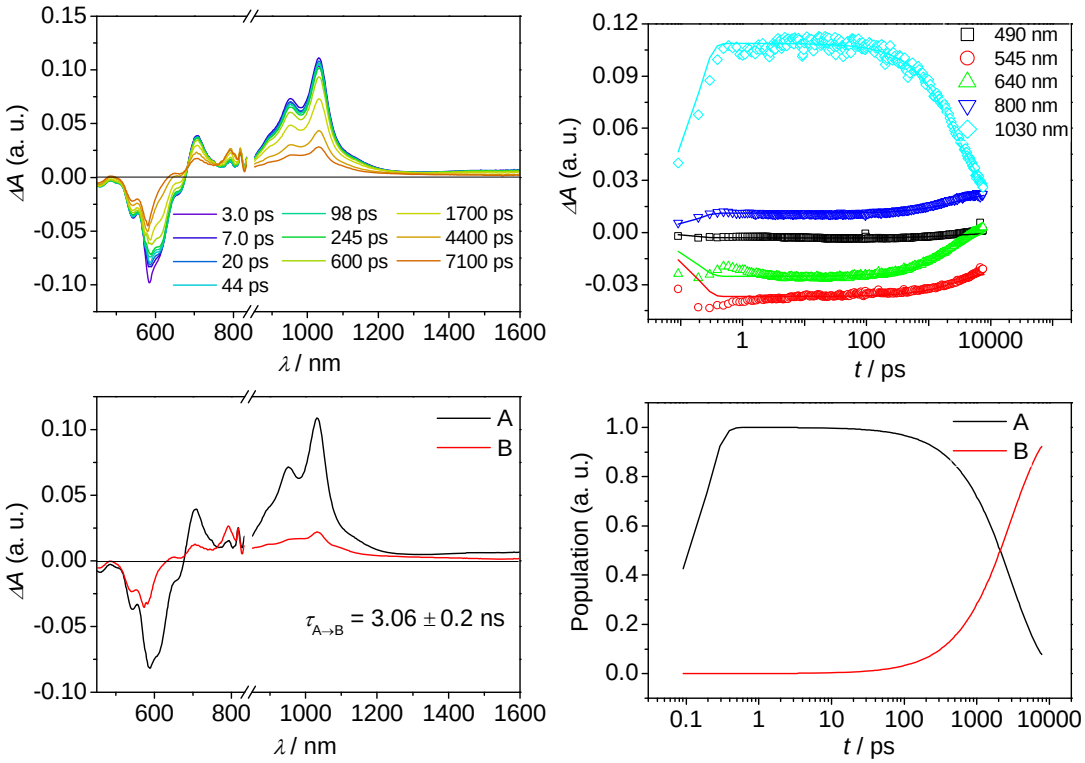

Figure 122. a) Femtosecond transient absorption spectra of **3PBI$_{(4\text{-}t\text{Bu})4}$** in dichloromethane showing excited state dynamics after photoexcitation; b) plots of selected kinetic traces superimposed with matching curves at different wavelengths; c) species-associated spectra plots; d) kinetic model plots (λ_{ex} = 580 nm, 1.0 μJ/pulse, 298 K). A: singlet excited state S_1; B: charge separated state SB-CS.

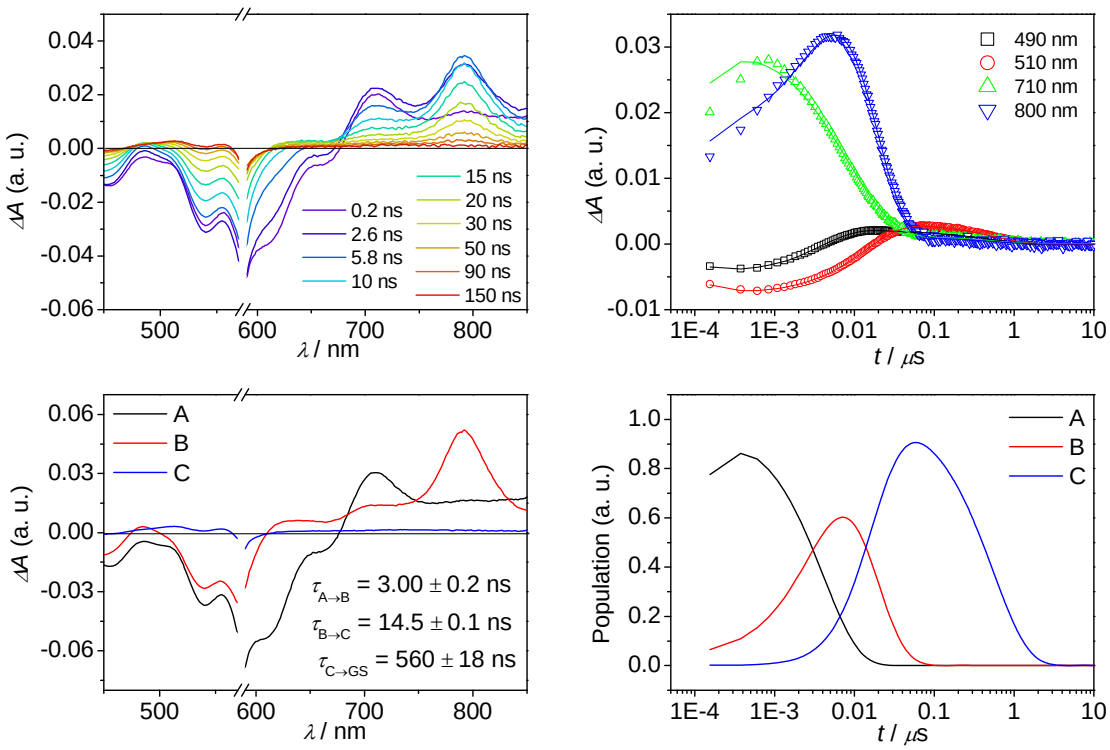

Figure 123. a) Nanosecond transient absorption spectra of **3PBI$_{(4\text{-}t\text{Bu})4}$** in dichloromethane showing excited state dynamics after photoexcitation; b) plots of selected kinetic traces superimposed with matching curves at different wavelengths; c) species-associated spectra plots; d) kinetic model plots (λ_{ex} = 580 nm, 1.0 μJ/pulse, 298 K). A: singlet excited state S_1; B: charge separated state SB-CS; C: PBI triplet T_1.

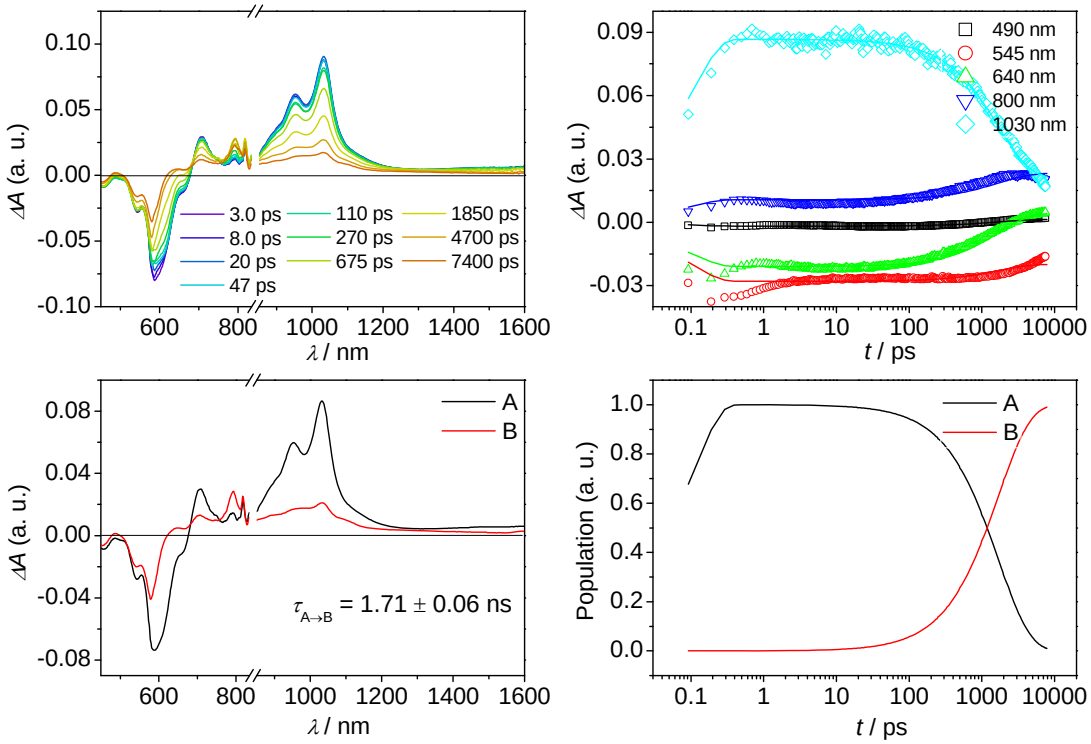

Figure 124. a) Femtosecond transient absorption spectra of **4PBI$_{(4\text{-}t\text{Bu})4}$** in dichloromethane showing excited state dynamics after photoexcitation; b) plots of selected kinetic traces superimposed with matching curves at different wavelengths; c) species-associated spectra plots; d) kinetic model plots (λ_{ex} = 580 nm, 1.0 μJ/pulse, 298 K). A: singlet excited state S_1; B: charge separated state SB-CS.

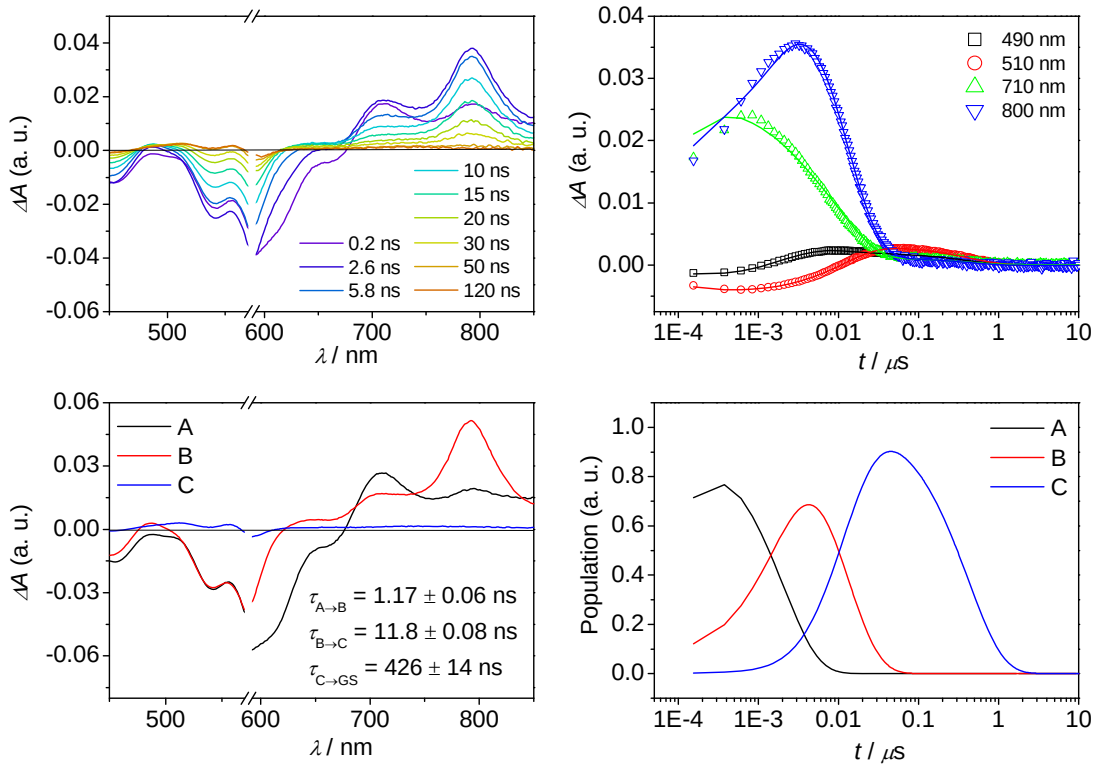

Figure 125. a) Nanosecond transient absorption spectra of **4PBI$_{(4\text{-}t\text{Bu})4}$** in dichloromethane showing excited state dynamics after photoexcitation; b) plots of selected kinetic traces superimposed with matching curves at different wavelengths; c) species-associated spectra plots; d) kinetic model plots (λ_{ex} = 580 nm, 1.0 μJ/pulse, 298 K). A: singlet excited state S_1; B: charge separated state SB-CS; C: PBI triplet T_1.

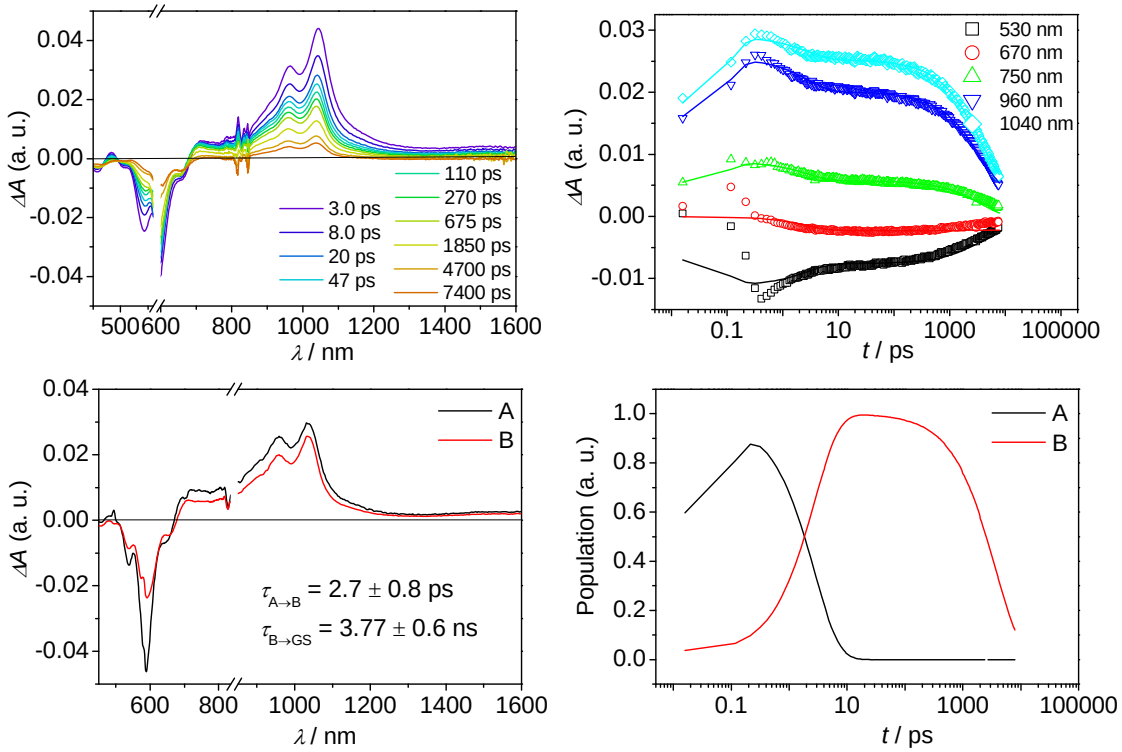

Figure 126. a) Femtosecond transient absorption spectra of **4PBI$_{(4\text{-}t\text{Bu})4}$** in toluene showing excited state dynamics after photoexcitation; b) plots of selected kinetic traces superimposed with matching curves at different wavelengths; c) species-associated spectra plots; d) kinetic model plots (λ_{ex} = 580 nm, 1.0 μJ/pulse, 298 K). A and B: singlet excited state S_1 (A → B likely presents relaxation on the singlet state based on the timescale and the similarity of the spectra).

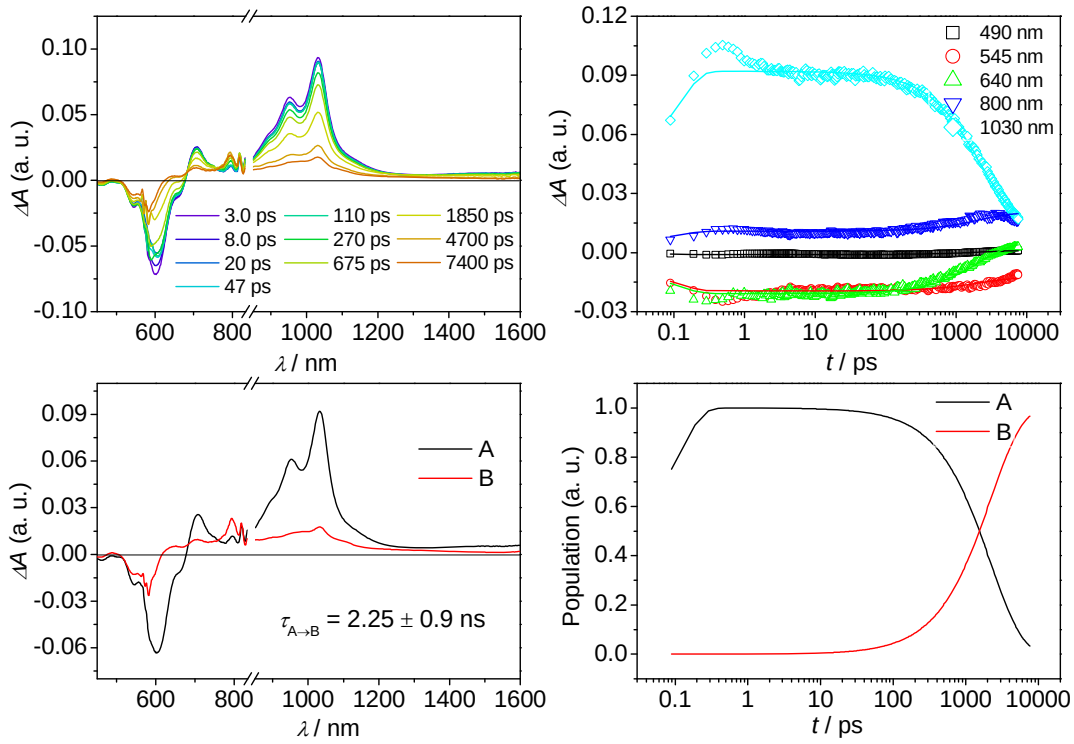

Figure 127. a) Femtosecond transient absorption spectra of **5PBI$_{(4\text{-}tBu)4}$** in dichloromethane showing excited state dynamics after photoexcitation; b) plots of selected kinetic traces superimposed with matching curves at different wavelengths; c) species-associated spectra plots; d) kinetic model plots (λ_{ex} = 580 nm, 1.0 μJ/pulse, 298 K). A: singlet excited state S_1; B: charge separated state SB-CS.

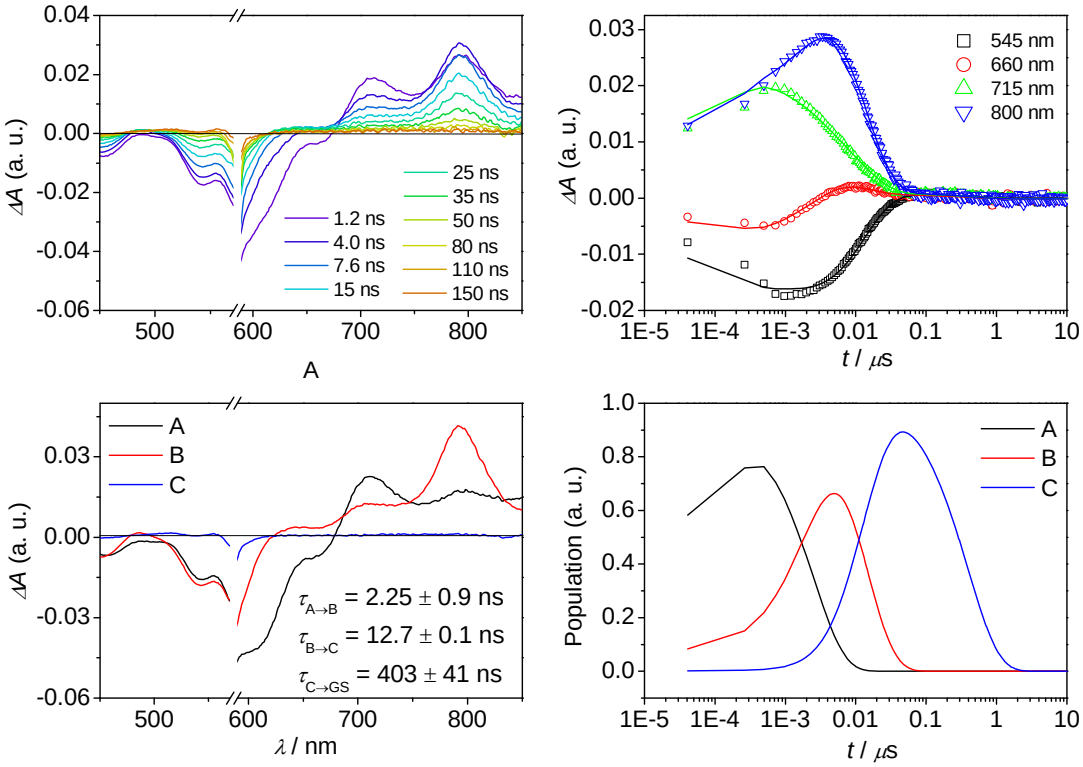

Figure 128. a) Nanosecond transient absorption spectra of **5PBI$_{(4\text{-}t\text{Bu})4}$** in dichloromethane showing excited state dynamics after photoexcitation; b) plots of selected kinetic traces superimposed with matching curves at different wavelengths; c) species-associated spectra plots; d) kinetic model plots (λ_{ex} = 580 nm, 1.0 μJ/pulse, 298 K). A: singlet excited state S_1; B: charge separated state SB-CS; C: PBI triplet T_1.

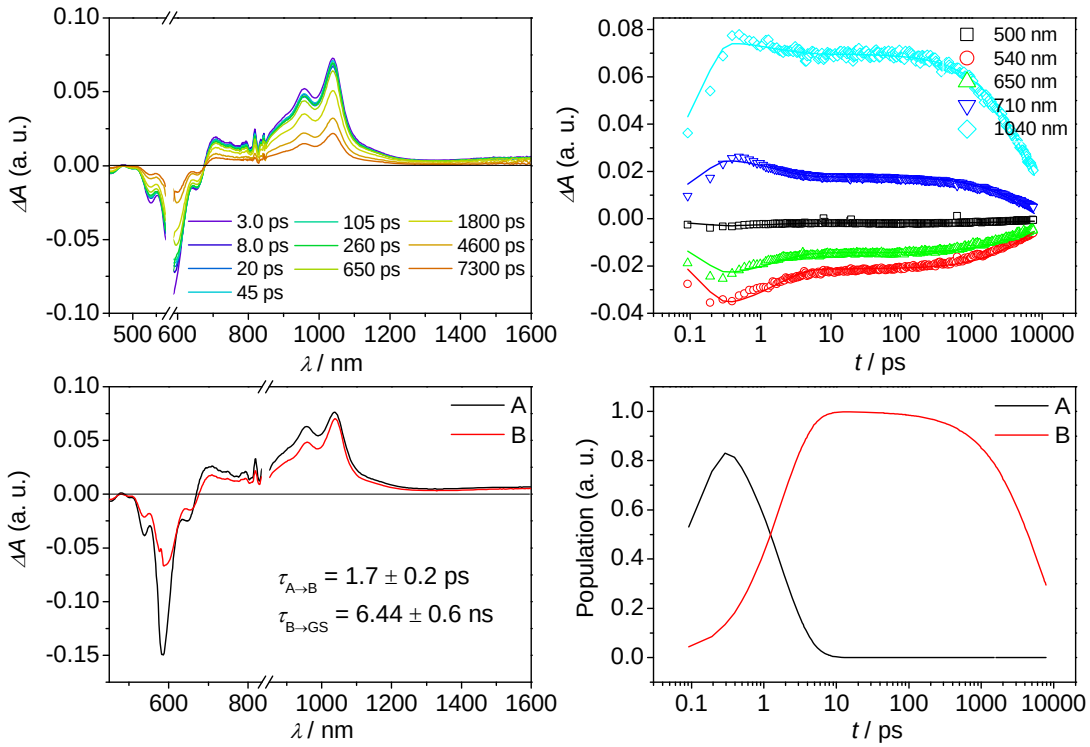

Figure 129. a) Femtosecond transient absorption spectra of **5PBI$_{(4\text{-}t\text{Bu})4}$** in toluene showing excited state dynamics after photoexcitation; b) plots of selected kinetic traces superimposed with matching curves at different wavelengths; c) species-associated spectra plots; d) kinetic model plots (λ_{ex} = 580 nm, 1.0 μJ/pulse, 298 K). A and B: singlet excited state S_1 (A → B likely presents relaxation on the singlet state based on the timescale and the similarity of the spectra).

List of Publications

Nondestructive Photoluminescence Read-Out by Intramolecular Electron Transfer in a Perylene Bisimide-Diarylethene Dyad, M. Berberich, M. Natali, P. Spenst, C. Chiorboli, F. Scandola, F. Würthner, *Chem. Eur. J.* **2012**, *18*, 13651-13664.

Supramolecular Adducts of Squaraine and Protein for Noninvasive Tumor Imaging and Photothermal Therapy in vivo, F.-P. Gao, Y.-X. Lin, L.-L. Li, Y. Liu, U. Mayerhöffer, P. Spenst, J.-G. Su, J.-Y. Li, F. Würthner, H. Wang, *Biomat.* **2014**, *35*, 1004-1014.

Nano-Confined Squaraine Dye Assemblies: New Photoacoustic and Near-Infrared Fluorescence Dual-Modular Imaging Probes in Vivo, D. Zhang, Y.-X. Zhao, Z.-Y. Qiao, U. Mayerhöffer, P. Spenst, X.-J. Li, F. Würthner, H. Wang, *Biocon. Chem.* **2014**, *25*, 2021-2029.

A Perylene Bisimide Cyclophane as a "Turn-On" and "Turn-Off" Fluorescence Probe, P. Spenst, F. Würthner, *Angew. Chem. Int. Ed*. **2015**, *54*, 10165-10168; *Angew. Chem*. **2015**, *127*, 10303-10306.

Ultrafast Photoinduced Symmetry-Breaking Charge Separation and Electron Sharing in Perylenediimide Molecular Triangles, Y. Wu, R. M. Young, M. Frasconi, S. T. Schneebeli, P. Spenst, D. M. Gardner, K. E. Brown, F. Würthner, J. F. Stoddart, M. R. Wasielewski, *J. Am. Chem. Soc.* **2015**, *137*, 13236-13239.

Guest and Solvent Modulated Photo-driven Charge Separation and Triplet Generation in a Perylene Bisimide Cyclophane, P. Spenst, R. M. Young, M. R. Wasielewski, F. Würthner, *Chem. Sci.* **2016**, *7*, 5428-5434.

References

[1] a) J.-M. Lehn, *Science* **1985**, *227*, 849-856; b) M. Yoshizawa, J. K. Klosterman, M. Fujita, *Angew. Chem. Int. Ed.* **2009**, *48*, 3418-3438; c) J. Rebek, *Acc. Chem. Res.* **2009**, *42*, 1660-1668.

[2] a) X. Ma, Y. Zhao, *Chem. Rev.* **2015**, *115*, 7794-7839; b) E. J. Lee, N. K. Lee, I.-S. Kim, *Adv. Drug Deliver. Rev.* **2016**; c) G. Yu, K. Jie, F. Huang, *Chem. Rev.* **2015**, *115*, 7240-7303.

[3] a) J. S. Kim, D. T. Quang, *Chem. Rev.* **2007**, *107*, 3780-3799; b) J. Hu, S. Liu, *Acc. Chem. Res.* **2014**, *47*, 2084-2095.

[4] a) W. R. Browne, B. L. Feringa, *Nat. Nano* **2006**, *1*, 25-35; b) W. Gao, J. Wang, *ACS Nano* **2014**, *8*, 3170-3180.

[5] a) D. Ranganathan, *Acc. Chem. Res.* **2001**, *34*, 919-930; b) V. Blažek Bregović, N. Basarić, K. Mlinarić-Majerski, *Coord. Chem. Rev.* **2015**, *295*, 80-124.

[6] a) H. Bakirci, A. L. Koner, M. H. Dickman, U. Kortz, W. M. Nau, *Angew. Chem. Int. Ed.* **2006**, *45*, 7400-7404; b) J.-N. Rebilly, B. Colasson, O. Bistri, D. Over, O. Reinaud, *Chem. Soc. Rev.* **2015**, *44*, 467-489.

[7] G. Zhang, M. Mastalerz, *Chem. Soc. Rev.* **2014**, *43*, 1934-1947.

[8] a) D.-H. Qu, Q.-C. Wang, Q.-W. Zhang, X. Ma, H. Tian, *Chem. Rev.* **2015**, *115*, 7543-7588; b) V. Blanco, D. A. Leigh, V. Marcos, *Chem. Soc. Rev.* **2015**, *44*, 5341-5370.

[9] H. H. Dam, D. N. Reinhoudt, W. Verboom, *Chem. Soc. Rev.* **2007**, *36*, 367-377.

[10] H. L. Hoffman, G. R. Breeden, R. W. Liggett, *J. Org. Chem.* **1964**, *29*, 3440-3441.

[11] C. J. Pedersen, *J. Am. Chem. Soc.* **1967**, *89*, 7017-7036.

[12] a) H. E. Simmons, C. H. Park, *J. Am. Chem. Soc.* **1968**, *90*, 2428-2429; b) B. Dietrich, J. M. Lehn, J. P. Sauvage, *Tetrahedron Lett.* **1969**, *10*, 2885-2888.

[13] J. Jazwinski, J.-M. Lehn, D. Lilienbaum, R. Ziessel, J. Guilhem, C. Pascard, *J. Chem. Soc.* **1987**, 1691-1694.

[14] D. J. Cram, T. Kaneda, R. C. Helgeson, S. B. Brown, C. B. Knobler, E. Maverick, K. N. Trueblood, *J. Am. Chem. Soc.* **1985**, *107*, 3645-3657.

[15] a) D. J. Cram, S. Karbach, Y. H. Kim, L. Baczynskyj, G. W. Kallemeyn, *J. Am. Chem. Soc.* **1985**, *107*, 2575-2576; b) R. Warmuth, in *Supramolecular Chemistry*, John Wiley & Sons, Ltd, **2012**.

[16] a) K. Nakamura, K. N. Houk, *J. Am. Chem. Soc.* **1995**, *117*, 1853-1854; b) F. Liu, R. C. Helgeson, K. N. Houk, *Acc. Chem. Res.* **2014**, *47*, 2168-2176.

[17] a) Y. Yamashoji, M. Tanaka, T. Shono, *Chem. Lett.* **1990**, *19*, 945-948; b) B. V. K. J. Schmidt, M. Hetzer, H. Ritter, C. Barner-Kowollik, *Prog. Polym. Sci.* **2014**, *39*, 235-249.

[18] V. Böhmer, *Angew. Chem. Int. Ed.* **1995**, *34*, 713-745.

[19] H. Zhang, Y. Zhao, *Chem. Eur. J.* **2013**, *19*, 16862-16879.

[20] K. I. Assaf, W. M. Nau, *Chem. Soc. Rev.* **2015**, *44*, 394-418.

[21] a) T. Kawase, N. Fujiwara, M. Tsutumi, M. Oda, Y. Maeda, T. Wakahara, T. Akasaka, *Angew. Chem. Int. Ed.* **2004**, *43*, 5060-5062; b) D. Canevet, M. Gallego, H. Isla, A. de Juan, E. M. Pérez, N. Martín, *J. Am. Chem. Soc.* **2011**, *133*, 3184-3190; c) T. Iwamoto, Y. Watanabe, T. Sadahiro, T. Haino, S. Yamago, *Angew. Chem. Int. Ed.* **2011**, *50*, 8342-8344.

[22] a) H.-Y. Gong, B. M. Rambo, E. Karnas, V. M. Lynch, J. L. Sessler, *Nat. Chem.* **2010**, *2*, 406-409; b) S. T. J. Ryan, J. Del Barrio, I. Ghosh, F. Biedermann, A. I. Lazar, Y. Lan, R. J. Coulston, W. M. Nau, O. A. Scherman, *J. Am. Chem. Soc.* **2014**, *136*, 9053-9060.

[23] D. J. Cram, H. Steinberg, *J. Am. Chem. Soc.* **1951**, *73*, 5691-5704.

[24] a) G. Chen, J. T. Lean, M. Alcalá, T. E. Mallouk, *J. Org. Chem.* **2001**, *66*, 3027-3034; b) S.-i. Kato, T. Nakagaki, T. Shimasaki, T. Shinmyozu, *CrystEngComm* **2008**, *10*, 483-486; c) H. M. Colquhoun, Z. Zhu, D. J. Williams, M. G. B. Drew, C. J. Cardin, Y. Gan, A. G. Crawford, T. B. Marder, *Chem. Eur. J.* **2010**, *16*, 907-918.

[25] a) B. Odell, M. V. Reddington, A. M. Z. Slawin, N. Spencer, J. F. Stoddart, D. J. Williams, *Angew. Chem. Int. Ed.* **1988**, *27*, 1547-1550; b) E. J. Dale, N. A. Vermeulen, A. A. Thomas, J. C. Barnes, M. Juríček, A. K. Blackburn, N. L. Strutt, A. A. Sarjeant, C. L. Stern, S. E. Denmark, J. F. Stoddart, *J. Am. Chem. Soc.* **2014**, *136*, 10669-10682.

[26] a) M. S. Khoshbin, M. V. Ovchinnikov, K. S. Salaita, C. A. Mirkin, C. L. Stern, L. N. Zakharov, A. L. Rheingold, *Chem. Asian J.* **2006**, *1*, 686-692; b) Y.-R. Zheng, Z. Zhao, M. Wang, K. Ghosh, J. B. Pollock, T. R. Cook, P. J. Stang, *J.*

Am. Chem. Soc. **2010**, *132*, 16873-16882; c) T. Nakamura, H. Ube, M. Shionoya, *Angew. Chem. Int. Ed.* **2013**, *52*, 12096-12100.

[27] a) F. Diederich, H. D. Lutter, *J. Am. Chem. Soc.* **1989**, *111*, 8438-8446; b) D. H. Camacho, E. V. Salo, J. W. Ziller, Z. Guan, *Angew. Chem. Int. Ed.* **2004**, *43*, 1821-1825.

[28] a) B. Das, S. Abe, *J. Phys. Chem. B* **2006**, *110*, 23806-23811; b) B. Shirinfar, N. Ahmed, Y. S. Park, G.-S. Cho, I. S. Youn, J.-K. Han, H. G. Nam, K. S. Kim, *J. Am. Chem. Soc.* **2013**, *135*, 90-93; c) N. Ahmed, B. Shirinfar, I. S. Youn, M. Yousuf, K. S. Kim, *Org. Biomol. Chem.* **2013**, *11*, 6407-6413.

[29] a) F. Diederich, K. Dick, *J. Am. Chem. Soc.* **1984**, *106*, 8024-8036; b) P. Rajakumar, A. M. A. Rasheed, *Tetrahedron* **2005**, *61*, 5351-5362.

[30] a) H. Langhals, R. Ismael, *Eur. J. Org. Chem.* **1998**, *1998*, 1915-1917; b) W. Wang, A. D. Shaller, A. D. Q. Li, *J. Am. Chem. Soc.* **2008**, *130*, 8271-8279; c) J. Feng, Y. Zhang, C. Zhao, R. Li, W. Xu, X. Li, J. Jiang, *Chem. Eur. J.* **2008**, *14*, 7000-7010; d) F. Schlosser, M. Moos, C. Lambert, F. Würthner, *Adv. Mater.* **2013**, *25*, 410-414; e) K. E. Brown, W. A. Salamant, L. E. Shoer, R. M. Young, M. R. Wasielewski, *J. Phys. Chem. Lett.* **2014**, *5*, 2588-2593.

[31] A. W. Roszak, T. D. Howard, J. Southall, A. T. Gardiner, C. J. Law, N. W. Isaacs, R. J. Cogdell, *Science* **2003**, *302*, 1969-1972.

[32] R. Croce, H. van Amerongen, *J. Photoch. Photobio. B* **2011**, *104*, 142-153.

[33] a) M. Stomp, J. Huisman, L. J. Stal, H. C. P. Matthijs, *ISME J.* **2007**, *1*, 271-282; b) M. Chen, M. Schliep, R. D. Willows, Z.-L. Cai, B. A. Neilan, H. Scheer, *Science* **2010**, *329*, 1318-1319; c) M. F. Hohmann-Marriott, R. E. Blankenship, *Annu. Rev. Plant Biol.* **2011**, *62*, 515-548.

[34] D. Noy, C. C. Moser, P. L. Dutton, *BBA-Bioenergetics* **2006**, *1757*, 90-105.

[35] a) M. Schliep, G. Cavigliasso, R. G. Quinnell, R. Stranger, A. W. D. Larkum, *Plant Cell Environ.* **2013**, *36*, 521-527; b) K. Aravindu, O. Mass, P. Vairaprakash, J. W. Springer, E. Yang, D. M. Niedzwiedzki, C. Kirmaier, D. F. Bocian, D. Holten, J. S. Lindsey, *Chem. Sci.* **2013**, *4*, 3459-3477; c) K. R. Reddy, J. Jiang, M. Krayer, M. A. Harris, J. W. Springer, E. Yang, J. Jiao, D. M. Niedzwiedzki, D. Pandithavidana, P. S. Parkes-Loach, C. Kirmaier, P. A. Loach, D. F. Bocian, D. Holten, J. S. Lindsey, *Chem. Sci.* **2013**, *4*, 2036-2053.

[36] E. Songaila, R. Augulis, A. Gelzinis, V. Butkus, A. Gall, C. Büchel, B. Robert, D. Zigmantas, D. Abramavicius, L. Valkunas, *J. Phys. Chem. Lett.* **2013**, *4*, 3590-3595.

[37] a) M. Kuhl, M. Chen, P. J. Ralph, U. Schreiber, A. W. D. Larkum, *Nature* **2005**, *433*, 820-820; b) M. Chen, R. E. Blankenship, *Trends Plant Sci.* **2011**, *16*, 427-431.

[38] B. Lepetit, R. Goss, T. Jakob, C. Wilhelm, *Photosynth. Res.* **2011**, *111*, 245-257.

[39] R. Croce, H. van Amerongen, *Nat. Chem. Biol.* **2014**, *10*, 492-501.

[40] T. Polívka, H. A. Frank, *Acc. Chem. Res.* **2010**, *43*, 1125-1134.

[41] A. Krieger-Liszkay, C. Fufezan, A. Trebst, *Photosynth. Res.* **2008**, *98*, 551-564.

[42] P. D. Frischmann, K. Mahata, F. Würthner, *Chem. Soc. Rev.* **2013**, *42*, 1847-1870.

[43] a) R. J. Cogdell, A. Gall, J. Köhler, *Q. Rev. Biophys.* **2006**, *39*, 227-324; b) S. Niwa, L.-J. Yu, K. Takeda, Y. Hirano, T. Kawakami, Z.-Y. Wang-Otomo, K. Miki, *Nature* **2014**, *508*, 228-232.

[44] T. Schulte, D. M. Niedzwiedzki, R. R. Birge, R. G. Hiller, T. Polívka, E. Hofmann, H. A. Frank, *P. Natl. Acad. Sci.* **2009**, *106*, 20764-20769.

[45] a) G. J. S. Fowler, R. W. Visschers, G. G. Grief, R. van Grondelle, C. N. Hunter, *Nature* **1992**, *355*, 848-850; b) E. Wientjes, G. Roest, R. Croce, *BBA-Bioenergetics* **2012**, *1817*, 711-717.

[46] a) R. van Grondelle, *BBA-Rev. Bioenergetics* **1985**, *811*, 147-195; b) R. van Grondelle, J. P. Dekker, T. Gillbro, V. Sundstrom, *BBA-Bioenergetics* **1994**, *1187*, 1-65.

[47] G. S. Beddard, *Philos. Trans. R. Soc. London, Ser. A* **1998**, *356*, 421-448.

[48] T. Förster, *Ann. Phys.* **1948**, *437*, 55-75.

[49] a) A. G. Redfield, in *Advances in Magnetic and Optical Resonance, Vol. 1* (Ed.: S. W. John), Academic Press, **1965**, pp. 1-32; b) A. M. Walsh, R. D. Coalson, *Chem. Phys. Lett.* **1992**, *198*, 293-299.

[50] a) G. S. Engel, T. R. Calhoun, E. L. Read, T.-K. Ahn, T. Mancal, Y.-C. Cheng, R. E. Blankenship, G. R. Fleming, *Nature* **2007**, *446*, 782-786; b) E. Collini, C. Y. Wong, K. E. Wilk, P. M. G. Curmi, P. Brumer, G. D. Scholes, *Nature* **2010**, *463*, 644-647; c) R. Hildner, D. Brinks, J. B. Nieder, R. J. Cogdell, N. F. van Hulst, *Science* **2013**, *340*, 1448-1451.

[51] J. Dostál, T. Mančal, R. Augulis, F. Vácha, J. Pšenčík, D. Zigmantas, *J. Am. Chem. Soc.* **2012**, *134*, 11611-11617.

[52] G. T. Oostergetel, H. Amerongen, E. J. Boekema, *Photosynth. Res.* **2010**, *104*, 245-255.

[53] T. Pullerits, V. Sundström, *Acc. Chem. Res.* **1996**, *29*, 381-389.

[54] J. Deisenhofer, O. Epp, K. Miki, R. Huber, H. Michel, *Nature* **1985**, *318*, 618-624.

[55] a) J. P. Allen, G. Feher, T. O. Yeates, D. C. Rees, J. Deisenhofer, H. Michel, R. Huber, *P. Natl. Acad. Sci.* **1986**, *83*, 8589-8593; b) J. Deisenhofer, H. Michel, *Science* **1989**, *245*, 1463-1473; c) J. Deisenhofer, O. Epp, I. Sinning, H. Michel, *J. Mol. Biol.* **1995**, *246*, 429-457; d) P. Jordan, P. Fromme, H. T. Witt, O. Klukas, W. Saenger, N. Krausz, *Nature* **2001**, *411*, 909-917.

[56] N. Nelson, C. F. Yocum, *Annu. Rev. Plant Biol.* **2006**, *57*, 521-565.

[57] a) W. Zhang, J. S. Moore, *Angew. Chem. Int. Ed.* **2006**, *45*, 4416-4439; b) Y. Nakamura, N. Aratani, A. Osuka, *Chem. Soc. Rev.* **2007**, *36*, 831-845; c) M. Iyoda, J. Yamakawa, M. J. Rahman, *Angew. Chem. Int. Ed.* **2011**, *50*, 10522-10553; d) J. Yang, M.-C. Yoon, H. Yoo, P. Kim, D. Kim, *Chem. Soc. Rev.* **2012**, *41*, 4808-4826; e) S.-L. Huang, G.-X. Jin, H.-K. Luo, T. S. A. Hor, *Chem. Asian J.* **2015**, *10*, 24-42.

[58] M. Kasha, *Discussions of the Faraday Society* **1950**, *9*, 14-19.

[59] Y. Wu, Y. Zhen, Y. Ma, R. Zheng, Z. Wang, H. Fu, *J. Phys. Chem. Lett.* **2010**, *1*, 2499-2502.

[60] a) H. Yoo, J. Yang, A. Yousef, M. R. Wasielewski, D. Kim, *J. Am. Chem. Soc.* **2010**, *132*, 3939-3944; b) A. Nowak-Krol, B. Fimmel, M. Son, D. Kim, F. Würthner, *Faraday Discussions* **2015**, *185*, 507-527.

[61] a) S. W. Eaton, L. E. Shoer, S. D. Karlen, S. M. Dyar, E. A. Margulies, B. S. Veldkamp, C. Ramanan, D. A. Hartzler, S. Savikhin, T. J. Marks, M. R. Wasielewski, *J. Am. Chem. Soc.* **2013**, *135*, 14701-14712; b) R. J. Lindquist, K. M. Lefler, K. E. Brown, S. M. Dyar, E. A. Margulies, R. M. Young, M. R. Wasielewski, *J. Am. Chem. Soc.* **2014**, *136*, 14912-14923; c) C. M. Mauck, K. E. Brown, N. E. Horwitz, M. R. Wasielewski, *J. Phys. Chem. A* **2015**, *119*, 5587-5596.

[62] N. Renaud, P. A. Sherratt, M. A. Ratner, *J. Phys. Chem. Lett.* **2013**, *4*, 1065-1069.

[63] a) N. Banerji, G. Duvanel, A. Perez-Velasco, S. Maity, N. Sakai, S. Matile, E. Vauthey, *J. Phys. Chem. A* **2009**, *113*, 8202-8212; b) E. Vauthey, *ChemPhysChem* **2012**, *13*, 2001-2011.

[64] M. T. Colvin, E. M. Giacobbe, B. Cohen, T. Miura, A. M. Scott, M. R. Wasielewski, *J. Phys. Chem. A* **2010**, *114*, 1741-1748.

[65] R. Aroca, T. Del Caño, J. A. de Saja, *Chem. Mat.* **2003**, *15*, 38-45.

[66] a) R. M. Williams, N. Vân Anh, I. H. M. van Stokkum, *J. Phys. Chem. B* **2013**, *117*, 11239-11248; b) P. E. Hartnett, S. M. Dyar, E. A. Margulies, L. E. Shoer, A. W. Cook, S. W. Eaton, T. J. Marks, M. R. Wasielewski, *Chem. Sci.* **2015**, *6*, 402-411.

[67] a) T. Miura, R. Carmieli, M. R. Wasielewski, *J. Phys. Chem. A* **2010**, *114*, 5769-5778; b) M. T. Colvin, A. B. Ricks, A. M. Scott, D. T. Co, M. R. Wasielewski, *J. Phys. Chem. A* **2012**, *116*, 1923-1930; c) K. M. Lefler, K. E. Brown, W. A. Salamant, S. M. Dyar, K. E. Knowles, M. R. Wasielewski, *J. Phys. Chem. A* **2013**, *117*, 10333-10345.

[68] a) R. T. Cheriya, K. Nagarajan, M. Hariharan, *J. Phys. Chem. C* **2013**, *117*, 3240-3248; b) C. Ramanan, C. H. Kim, T. J. Marks, M. R. Wasielewski, *J. Phys. Chem. C* **2014**, *118*, 16941-16950.

[69] S. T. J. Ryan, R. M. Young, J. J. Henkelis, N. Hafezi, N. A. Vermeulen, A. Hennig, E. J. Dale, Y. Wu, M. D. Krzyaniak, A. Fox, W. M. Nau, M. R. Wasielewski, J. F. Stoddart, O. A. Scherman, *J. Am. Chem. Soc.* **2015**, *137*, 15299-15307.

[70] a) T. E. Kaiser, I. G. Scheblykin, D. Thomsson, F. Würthner, *J. Phys. Chem. B* **2009**, *113*, 15836-15842; b) H. Marciniak, X.-Q. Li, F. Würthner, S. Lochbrunner, *J. Phys. Chem. A* **2011**, *115*, 648-654; c) W. Steffen, A. Janis, F. Franziska, S. Marcus, W. Frank, K. Oliver, L. Stefan, *New J. Phys.* **2012**, *14*, 105027; d) Y. Tian, V. Stepanenko, T. E. Kaiser, F. Würthner, I. G. Scheblykin, *Nanoscale* **2012**, *4*, 218-223; e) S. Long, Y. Wang, S. Vdovic, M. Zhou, L. Yan, Y. Niu, Q. Guo, A. Xia, *Phys. Chem. Chem. Phys.* **2015**, *17*, 18567-18576; f) J. Sung, P. Kim, B. Fimmel, F. Würthner, D. Kim, *Nat. Commun.* **2015**, *6*.

[71] a) S.-i. Kato, T. Matsumoto, K. Ideta, T. Shimasaki, K. Goto, T. Shinmyozu, *J. Org. Chem.* **2006**, *71*, 4723-4733; b) T. Iwanaga, R. Nakamoto, M. Yasutake, H. Takemura, K. Sako, T. Shinmyozu, *Angew. Chem. Int. Ed.* **2006**, *45*, 3643-3647; c) S.-i. Kato, Y. Nonaka, T. Shimasaki, K. Goto, T. Shinmyozu, *J. Org. Chem.* **2008**, *73*, 4063-4075; d) T. Nakagaki, A. Harano, Y. Fuchigami, E. Tanaka, S. Kidoaki, T. Okuda, T. Iwanaga, K. Goto, T. Shinmyozu, *Angew. Chem. Int. Ed.* **2010**, *49*, 9676-9679; e) T. Nakagaki, K. Shin-ichiro, A. Harano, T. Shinmyozu,

Tetrahedron **2010**, *66*, 976-985; f) M. Ershad Halim, A. Bandyopadhyay, L. Sun, K. Tao, Y. S. Sangvikar, T. Miyazaki, M. Watanabe, K. Ideta, T. Matsumoto, K. Goto, T. Shinmyozu, *Tetrahedron Lett.* **2015**, *56*, 6970-6974.

[72] J. Gawroński, M. Brzostowska, K. Gawrońska, J. Koput, U. Rychlewska, P. Skowronek, B. Nordén, *Chem. Eur. J.* **2002**, *8*, 2484-2494.

[73] P. Ponce, L. Fomina, P. García, S. Fomine, *Polym. Int.* **2003**, *52*, 1454-1461.

[74] C. Marchetti, A. Minarini, V. Tumiatti, F. Moraca, L. Parrotta, S. Alcaro, R. Rigo, C. Sissi, M. Gunaratnam, S. A. Ohnmacht, S. Neidle, A. Milelli, *Bioorgan. Med. Chem.* **2015**, *23*, 3819-3830.

[75] a) H. M. Colquhoun, D. J. Williams, Z. Zhu, *J. Am. Chem. Soc.* **2002**, *124*, 13346-13347; b) Z. Zhu, C. J. Cardin, Y. Gan, H. M. Colquhoun, *Nat. Chem.* **2010**, *2*, 653-660.

[76] Y. Li, Y. Zhao, R. Jiang, H. Liu, Y. Li, *Inorg. Chem. Front.* **2014**, *1*, 661-667.

[77] Y. Yu, Y. Li, S. Chen, T. Liu, Z. Qin, H. Liu, Y. Li, *Eur. J. Org. Chem.* **2012**, *2012*, 4287-4292.

[78] J. Jazwinski, A. J. Blacker, J.-M. Lehn, M. Cesario, J. Guilhem, C. Pascard, *Tetrahedron Lett.* **1987**, *28*, 6060.

[79] M. E. Ozser, D. Uzun, I. Elci, H. Icil, M. Demuth, *Photochem. Photobio. Sci.* **2003**, *2*, 218-223.

[80] a) S. Gabutti, M. Knutzen, M. Neuburger, G. Schull, R. Berndt, M. Mayor, *Chem. Commun.* **2008**, 2370-2372; b) F. Matino, G. Schull, F. Köhler, S. Gabutti, M. Mayor, R. Berndt, *P. Natl. Acad. Sci.* **2011**, *108*, 961-964.

[81] S. Gabutti, S. Schaffner, M. Neuburger, M. Fischer, G. Schäfer, M. Mayor, *Org. Biomol. Chem.* **2009**, *7*, 3222-3229.

[82] R. E. Dawson, A. Hennig, D. P. Weimann, D. Emery, V. Ravikumar, J. Montenegro, T. Takeuchi, S. Gabutti, M. Mayor, J. Mareda, C. A. Schalley, S. Matile, *Nat. Chem.* **2010**, *2*, 533-538.

[83] S. T. Schneebeli, M. Frasconi, Z. Liu, Y. Wu, D. M. Gardner, N. L. Strutt, C. Cheng, R. Carmieli, M. R. Wasielewski, J. F. Stoddart, *Angew. Chem. Int. Ed.* **2013**, *52*, 13100-13104.

[84] D. Chen, A.-J. Avestro, Z. Chen, J. Sun, S. Wang, M. Xiao, Z. Erno, M. M. Algaradah, M. S. Nassar, K. Amine, Y. Meng, J. F. Stoddart, *Adv. Mater.* **2015**, *27*, 2907-2912.

[85] S. K. M. Nalluri, Z. Liu, Y. Wu, K. R. Hermann, A. Samanta, D. J. Kim, M. D. Krzyaniak, M. R. Wasielewski, J. F. Stoddart, *J. Am. Chem. Soc.* **2016**, *138*, 5968-5977.

[86] Z. Liu, G. Liu, Y. Wu, D. Cao, J. Sun, S. T. Schneebeli, M. S. Nassar, C. A. Mirkin, J. F. Stoddart, *J. Am. Chem. Soc.* **2014**, *136*, 16651-16660.

[87] Z. Liu, J. Sun, Y. Zhou, Y. Zhang, Y. Wu, S. K. M. Nalluri, Y. Wang, A. Samanta, C. A. Mirkin, G. C. Schatz, J. F. Stoddart, *J. Org. Chem.* **2016**, *81*, 2581-2588.

[88] Y. Wu, M. Frasconi, D. M. Gardner, P. R. McGonigal, S. T. Schneebeli, M. R. Wasielewski, J. F. Stoddart, *Angew. Chem. Int. Ed.* **2014**, *53*, 9476-9481.

[89] Y. Wu, S. K. M. Nalluri, R. M. Young, M. D. Krzyaniak, E. A. Margulies, J. F. Stoddart, M. R. Wasielewski, *Angew. Chem. Int. Ed.* **2015**, *54*, 11971-11977.

[90] M. Kaik, J. Gawroński, *Org. Lett.* **2006**, *8*, 2921-2924.

[91] H. Y. Au-Yeung, P. Pengo, G. D. Pantos, S. Otto, J. K. M. Sanders, *Chem. Commun.* **2009**, 419-421.

[92] N. Ponnuswamy, F. B. L. Cougnon, J. M. Clough, G. D. Pantoş, J. K. M. Sanders, *Science* **2012**, *338*, 783-785.

[93] W. Drożdż, M. Kołodziejski, G. Markiewicz, A. Jenczak, A. Stefankiewicz, *Int. J. Mol. Sci.* **2015**, *16*, 16300-16312.

[94] a) J. M. Lim, P. Kim, M.-C. Yoon, J. Sung, V. Dehm, Z. Chen, F. Würthner, D. Kim, *Chem. Sci.* **2013**, *4*, 388-397; b) M. Son, K. H. Park, C. Shao, F. Würthner, D. Kim, *J. Phys. Chem. Lett.* **2014**, *5*, 3601-3607.

[95] J. M. Giaimo, A. V. Gusev, M. R. Wasielewski, *J. Am. Chem. Soc.* **2002**, *124*, 8530-8531.

[96] a) F. C. Spano, *Acc. Chem. Res.* **2010**, *43*, 429-439; b) F. Gao, Y. Zhao, W. Liang, *J. Phys. Chem. B* **2011**, *115*, 2699-2708.

[97] L. Feng, Z. Chen, *Sensor. Actuat. B-Chem.* **2007**, *122*, 600-604.

[98] J. Sung, A. Nowak-Król, F. Schlosser, B. Fimmel, W. Kim, D. Kim, F. Würthner, *J. Am. Chem. Soc.* **2016**, DOI: 10.1021/jacs.1026b04591.

[99] W. Wang, L. Wang, B. J. Palmer, G. J. Exarhos, A. D. Q. Li, *J. Am. Chem. Soc.* **2006**, *128*, 11150-11159.

[100] A. E. Clark, C. Qin, A. D. Q. Li, *J. Am. Chem. Soc.* **2007**, *129*, 7586-7595.

[101] a) Z. Chen, U. Baumeister, C. Tschierske, F. Würthner, *Chem. Eur. J.* **2007**, *13*, 450-465; b) P. Osswald, M. Reichert, G. Bringmann, F. Würthner, *J. Org. Chem.* **2007**, *72*, 3403-3411.

[102] M. M. Safont-Sempere, P. Osswald, M. Stolte, M. Grüne, M. Renz, M. Kaupp, K. Radacki, H. Braunschweig, F. Würthner, *J. Am. Chem. Soc.* **2011**, *133*, 9580-9591.

[103] W. Wang, A. D. Bain, L.-Q. Wang, G. J. Exarhos, A. D. Q. Li, *J. Phys. Chem. A* **2008**, *112*, 3094-3103.

[104] A. D. Shaller, W. Wang, H. Gan, A. D. Q. Li, *Angew. Chem. Int. Ed.* **2008**, *47*, 7705-7709.

[105] M. Ball, B. Fowler, P. Li, L. A. Joyce, F. Li, T. Liu, D. Paley, Y. Zhong, H. Li, S. Xiao, F. Ng, M. L. Steigerwald, C. Nuckolls, *J. Am. Chem. Soc.* **2015**, *137*, 9982-9987.

[106] a) F. Zhang, G. Götz, H. D. F. Winkler, C. A. Schalley, P. Bäuerle, *Angew. Chem. Int. Ed.* **2009**, *48*, 6632-6635; b) T. Iwamoto, Y. Watanabe, Y. Sakamoto, T. Suzuki, S. Yamago, *J. Am. Chem. Soc.* **2011**, *133*, 8354-8361; c) E. Kayahara, Y. Sakamoto, T. Suzuki, S. Yamago, *Org. Lett.* **2012**, *14*, 3284-3287.

[107] F. Schlosser, V. Stepanenko, F. Würthner, *Chem. Commun.* **2010**, *46*, 8350-8352.

[108] F. Schlosser, J. Sung, P. Kim, D. Kim, F. Würthner, *Chem. Sci.* **2012**, *3*, 2778-2785.

[109] a) S. E. Bradforth, R. Jimenez, F. van Mourik, R. van Grondelle, G. R. Fleming, *J. Phys. Chem.* **1995**, *99*, 16179-16191; b) R. Jimenez, S. N. Dikshit, S. E. Bradforth, G. R. Fleming, *J. Phys. Chem.* **1996**, *100*, 6825-6834; c) G. Trinkunas, J. L. Herek, T. Polívka, V. Sundström, T. Pullerits, *Phys. Rev. Lett.* **2001**, *86*, 4167-4170; d) G. Trinkunas, *J. Lumin.* **2003**, *102–103*, 532-535.

[110] J.-E. Lee, V. Stepanenko, J. Yang, H. Yoo, F. Schlosser, D. Bellinger, B. Engels, I. G. Scheblykin, F. Würthner, D. Kim, *ACS Nano* **2013**, *7*, 5064-5076.

[111] S. Ham, J. Yang, F. Schlosser, F. Würthner, D. Kim, *J. Phys. Chem. Lett.* **2014**, *5*, 2830-2835.

[112] Y. Wu, R. M. Young, M. Frasconi, S. T. Schneebeli, P. Spenst, D. M. Gardner, K. E. Brown, F. Würthner, J. F. Stoddart, M. R. Wasielewski, *J. Am. Chem. Soc.* **2015**, *137*, 13236-13239.

[113] a) J. Wang, *Nanomachines: Fundamentals and Applications*, WILEY-VCH Verlag, Weinheim, **2013**; b) C. J. Bruns, J. F. Stoddart, *Acc. Chem. Res.* **2014**, *47*, 2186-2199.

[114] L. Raehm, D. G. Hamilton, J. K. M. Sanders, *Synlett* **2002**, *2002*, 1743-1761.

[115] D. G. Hamilton, D. E. Lynch, K. A. Byriel, C. H. L. Kennard, *Aust. J. Chem.* **1997**, *50*, 439 439-446.

[116] a) D. G. Hamilton, J. K. M. Sanders, J. E. Davies, W. Clegg, S. J. Teat, *Chem. Commun.* **1997**, 897-898; b) D. G. Hamilton, J. E. Davies, L. Prodi, J. K. M. Sanders, *Chem. Eur. J.* **1998**, *4*, 608-620; c) Q. Zhang, D. G. Hamilton, N. Feeder, S. J. Teat, J. M. Goodman, J. K. M. Sanders, *New J. Chem.* **1999**, *23*, 897-903; d) D. G. Hamilton, M. Montalti, L. Prodi, M. Fontani, P. Zanello, J. K. M. Sanders, *Chem. Eur. J.* **2000**, *6*, 608-617; e) J. G. Hansen, N. Feeder, D. G. Hamilton, M. J. Gunter, J. Becher, J. K. M. Sanders, *Org. Lett.* **2000**, *2*, 449-452.

[117] G. D. Fallon, M. A. P. Lee, S. J. Langford, P. J. Nichols, *Org. Lett.* **2004**, *6*, 655-658.

[118] D. G. Hamilton, J. K. M. Sanders, *Chem. Commun.* **1998**, 1749-1749.

[119] D. Cao, M. Amelia, L. M. Klivansky, G. Koshkakaryan, S. I. Khan, M. Semeraro, S. Silvi, M. Venturi, A. Credi, Y. Liu, *J. Am. Chem. Soc.* **2010**, *132*, 1110-1122.

[120] M. J. Gunter, S. M. Farquhar, *Org. Biomol. Chem.* **2003**, *1*, 3450-3457.

[121] a) Y. Nakamura, S. Minami, K. Iizuka, J. Nishimura, *Angew. Chem. Int. Ed.* **2003**, *42*, 3158-3162; b) Y. Kasai, C. Sakamoto, N. Muroya, S.-i. Kato, Y. Nakamura, *Tetrahedron Lett.* **2011**, *52*, 623-625.

[122] a) L. J. McCormick, D. R. Turner, *CrystEngComm* **2013**, *15*, 8234-8236; b) S. A. Boer, C. S. Hawes, D. R. Turner, *Chem. Commun.* **2014**, *50*, 1125-1127.

[123] H. M. Colquhoun, R. A. Fairman, P. Tootell, D. J. Williams, *J. Chem. Soc. Dalton* **1999**, 2651-2652.

[124] A. Bilyk, M. M. Harding, *J. Chem. Soc.* **1995**, 1697-1698.

[125] M. A. Houghton, A. Bilyk, M. M. Harding, P. Turner, T. W. Hambley, *J. Chem. Soc. Dalton* **1997**, 2725-2734.

[126] M. Licchelli, L. Linati, A. Orbelli Biroli, E. Perani, A. Poggi, D. Sacchi, *Chem. Eur. J.* **2002**, *8*, 5161-5169.

[127] H. N. Lee, Z. Xu, S. K. Kim, K. M. K. Swamy, Y. Kim, S.-J. Kim, J. Yoon, *J. Am. Chem. Soc.* **2007**, *129*, 3828-3829.

[128] a) P. H. Dinolfo, M. E. Williams, C. L. Stern, J. T. Hupp, *J. Am. Chem. Soc.* **2004**, *126*, 12989-13001; b) W.-Y. Zhang, Y.-F. Han, L.-H. Weng, G.-X. Jin, *Organometallics* **2014**, *33*, 3091-3095.

[129] C. Addicott, I. Oesterling, T. Yamamoto, K. Müllen, P. J. Stang, *J. Org. Chem.* **2005**, *70*, 797-801.

[130] a) F. Würthner, A. Sautter, *Chem. Commun.* **2000**, 445-446; b) F. Würthner, A. Sautter, D. Schmid, P. J. A. Weber, *Chem. Eur. J.* **2001**, *7*, 894-902.

[131] F. Würthner, A. Sautter, *Org. Biomol. Chem.* **2003**, *1*, 240-243.

[132] A. Sautter, B. K. Kaletaş, D. G. Schmid, R. Dobrawa, M. Zimine, G. Jung, I. H. M. van Stokkum, L. De Cola, R. M. Williams, F. Würthner, *J. Am. Chem. Soc.* **2005**, *127*, 6719-6729.

[133] C.-C. You, C. Hippius, M. Grüne, F. Würthner, *Chem. Eur. J.* **2006**, *12*, 7510-7519.

[134] C.-C. You, F. Würthner, *J. Am. Chem. Soc.* **2003**, *125*, 9716-9725.

[135] V. Stepanenko, F. Würthner, *Small* **2008**, *4*, 2158-2161.

[136] V. L. Gunderson, A. L. Smeigh, C. H. Kim, D. T. Co, M. R. Wasielewski, *J. Am. Chem. Soc.* **2012**, *134*, 4363-4372.

[137] L. Flamigni, M. R. Johnston, *New J. Chem.* **2001**, *25*, 1368-1370.

[138] M. T. Indelli, C. Chiorboli, F. Scandola, E. Iengo, P. Osswald, F. Würthner, *J. Phys. Chem. B* **2010**, *114*, 14495-14504.

[139] A. I. Oliva, B. Ventura, F. Würthner, A. Camara-Campos, C. A. Hunter, P. Ballester, L. Flamigni, *Dalton Transactions* **2009**, 4023-4037.

[140] S. P. Black, D. M. Wood, F. B. Schwarz, T. K. Ronson, J. J. Holstein, A. R. Stefankiewicz, C. A. Schalley, J. K. M. Sanders, J. R. Nitschke, *Chem. Sci.* **2016**, *7*, 2614-2620.

[141] K. Mahata, P. D. Frischmann, F. Würthner, *J. Am. Chem. Soc.* **2013**, *135*, 15656-15661.

[142] P. D. Frischmann, V. Kunz, V. Stepanenko, F. Würthner, *Chem. Eur. J.* **2015**, *21*, 2766-2769.

[143] P. D. Frischmann, V. Kunz, F. Würthner, *Angew. Chem. Int. Ed.* **2015**, *54*, 7285-7289.

[144] D. Dotcheva, M. Klapper, K. Müllen, *Macromol. Chem. Phys.* **1994**, *195*, 1905-1911.

[145] A. J. Jimenez, M.-J. Lin, C. Burschka, J. Becker, V. Settels, B. Engels, F. Würthner, *Chem. Sci.* **2014**, *5*, 608-619.

[146] M.-J. Lin, A. J. Jimenez, C. Burschka, F. Würthner, *Chem. Commun.* **2012**, *48*, 12050-12052.

[147] V. Stepanenko, M. Stocker, P. Müller, M. Büchner, F. Würthner, *J. Mat. Chem.* **2009**, *19*, 6816-6826.

[148] a) J. Seibt, P. Marquetand, V. Engel, Z. Chen, V. Dehm, F. Würthner, *Chem. Phys.* **2006**, *328*, 354-362; b) J. Seibt, T. Winkler, K. Renziehausen, V. Dehm, F. Würthner, H. D. Meyer, V. Engel, *J. Phys. Chem. A* **2009**, *113*, 13475-13482; c) K. A. Kistler, C. M. Pochas, H. Yamagata, S. Matsika, F. C. Spano, *J. Phys. Chem. B* **2012**, *116*, 77-86; d) C. M. Pochas, K. A. Kistler, H. Yamagata, S. Matsika, F. C. Spano, *J. Am. Chem. Soc.* **2013**, *135*, 3056-3066; e) N. J. Hestand, F. C. Spano, *J. Chem. Phys.* **2015**, *143*, 244707.

[149] I. Seguy, P. Jolinat, P. Destruel, R. Mamy, H. Allouchi, C. Courseille, M. Cotrait, H. Bock, *ChemPhysChem* **2001**, *2*, 448-452.

[150] H. A. Benesi, J. H. Hildebrand, *J. Am. Chem. Soc.* **1949**, *71*, 2703-2707.

[151] P. Thordarson, *Chem. Soc. Rev.* **2011**, *40*, 1305-1323.

[152] C. A. Hunter, *Chem. Soc. Rev.* **1994**, *23*, 101-109.

[153] Y. Tanaka, K. M.-C. Wong, V. W.-W. Yam, *Chem. Eur. J.* **2013**, *19*, 390-399.

[154] F. Würthner, *Pure Appl. Chem.* **2006**, *78*, 2341-2349.

[155] Z. Chen, B. Fimmel, F. Würthner, *Org. Biomol. Chem.* **2012**, *10*, 5845-5855.

[156] a) K. N. Ferreira, T. M. Iverson, K. Maghlaoui, J. Barber, S. Iwata, *Science* **2004**, *303*, 1831-1838; b) T. Weil, T. Vosch, J. Hofkens, K. Peneva, K. Müllen, *Angew. Chem. Int. Ed.* **2010**, *49*, 2-28; c) R. Bhosale, J. Misek, N. Sakai, S. Matile, *Chem. Soc. Rev.* **2010**, *39*, 138-149.

[157] D. Noy, C. C. Moser, P. L. Dutton, *Biochim. Biophys. Acta, Bioenerg.* **2006**, *1757*, 90-105.

[158] a) M. R. Wasielewski, M. P. Niemczyk, W. A. Svec, E. B. Pewitt, *J. Am. Chem. Soc.* **1985**, *107*, 1080-1082; b) M. H. Schwartz, *J. Inclusion Phenom. Mol.* **1990**, *9*, 1-35; c) T. Kircher, H. G. Löhmannsröben, *Phys. Chem. Chem. Phys.* **1999**, *1*, 3987-3992; d) A. M. Brouwer, S. M. Fazio, C. Frochot, F. G. Gatti, D. A. Leigh, J. K. Y. Wong, G. W. H. Wurpel, *Pure Appl. Chem.* **2003**, *75*, 1055-1060; e) D. I. Schuster, P. Cheng, P. D. Jarowski, D. M. Guldi, C. Luo, L. Echegoyen, S. Pyo, A. R. Holzwarth, S. E. Braslavsky, R. M. Williams, G. Klihm, *J. Am. Chem. Soc.*

2004, *126*, 7257-7270; f) J. M. Baumes, J. J. Gassensmith, J. Giblin, J.-J. Lee, A. G. White, W. J. Culligan, W. M. Leevy, M. Kuno, B. D. Smith, *Nat. Chem.* **2010**, *2*, 1025-1030; g) C. C. Hofmann, S. M. Lindner, M. Ruppert, A. Hirsch, S. A. Haque, M. Thelakkat, J. Koehler, *J. Phys. Chem. B* **2010**, *114*, 9148-9156; h) D. M. Bassani, L. Jonusauskaite, A. Lavie-Cambot, N. D. McClenaghan, J.-L. Pozzo, D. Ray, G. Vives, *Coord. Chem. Rev.* **2010**, *254*, 2429-2445; i) M. T. Whited, N. M. Patel, S. T. Roberts, K. Allen, P. I. Djurovich, S. E. Bradforth, M. E. Thompson, *Chem. Commun.* **2012**, *48*, 284-286; j) M. Kumar, K. Venkata Rao, S. J. George, *Phys. Chem. Chem. Phys.* **2014**, *16*, 1300-1313.

[159] a) R. A. Marcus, *J. Chem. Phys.* **1956**, *24*, 966-978; b) R. A. Marcus, *J. Chem. Phys.* **1965**, *43*, 679-701; c) R. A. Marcus, N. Sutin, *Biochim. Biophys. Acta* **1985**, *811*, 265-322.

[160] a) J. R. Miller, L. T. Calcaterra, G. L. Closs, *J. Am. Chem. Soc.* **1984**, *106*, 3047-3049; b) E. H. A. Beckers, S. C. J. Meskers, A. P. H. J. Schenning, Z. Chen, F. Würthner, R. A. J. Janssen, *J. Phys. Chem. A* **2004**, *108*, 6933-6937.

[161] a) T. Häberle, J. Hirsch, F. Pöllinger, H. Heitele, M. E. Michel-Beyerle, C. Anders, A. Döhling, C. Krieger, A. Rückermann, H. A. Staab, *J. Phys. Chem.* **1996**, *100*, 18269-18274; b) A. Osuka, G. Noya, S. Taniguchi, T. Okada, Y. Nishimura, I. Yamazaki, N. Mataga, *Chem. - Eur. J.* **2000**, *6*, 33-46.

[162] A. Weller, *Z. Phys. Chem.* **1982**, *133*, 93-98.

[163] D. Veldman, S. M. A. Chopin, S. C. J. Meskers, M. M. Groeneveld, R. M. Williams, R. A. J. Janssen, *J. Phys. Chem. A* **2008**, *112*, 5846-5857.

[164] a) W. E. Ford, P. V. Kamat, *J. Phys. Chem.* **1987**, *91*, 6373-6380; b) A. A. Rachford, S. Goeb, F. N. Castellano, *J. Am. Chem. Soc.* **2008**, *130*, 2766-2767; c) Y. Wu, Y. Zhen, Y. Ma, R. Zheng, Z. Wang, H. Fu, *J. Phys. Chem. Lett.* **2010**, *1*, 2499-2502.

[165] a) M. A. El-Sayed, *J. Chem. Phys.* **1974**, *60*, 4502-4507; b) T. Okada, I. Karaki, E. Matsuzawa, N. Mataga, Y. Sakata, S. Misumi, *J. Phys. Chem.* **1981**, *85*, 3957-3960; c) K. M. Lefler, K. E. Brown, W. A. Salamant, S. M. Dyar, K. E. Knowles, M. R. Wasielewski, *J. Phys. Chem. A* **2013**, *117*, 10333-10345.

[166] a) C. D. Buckley, D. A. Hunter, P. J. Hore, K. A. McLauchlan, *Chem. Phys. Lett.* **1987**, *135*, 307-312; b) M. T. Colvin, A. B. Ricks, A. M. Scott, A. L. Smeigh, R. Carmieli, T. Miura, M. R. Wasielewski, *J. Am. Chem. Soc.* **2011**, *133*, 1240-1243.

[167] E. A. Weiss, M. J. Ahrens, L. E. Sinks, A. V. Gusev, M. A. Ratner, M. R. Wasielewski, *J. Am. Chem. Soc.* **2004**, *126*, 5577-5584.

[168] E. A. Weiss, M. A. Ratner, M. R. Wasielewski, *J. Phys. Chem. A* **2003**, *107*, 3639-3647.

[169] Y. Usui, *Chem. Lett.* **1973**, *2*, 743-744.

[170] N. Banerji, G. Angulo, I. Barabanov, E. Vauthey, *J. Phys. Chem. A* **2008**, *112*, 9665-9674.

[171] K. Karon, M. Lapkowski, *J. Solid State Electrochem.* **2015**, *19*, 2601-2610.

[172] J. Daub, R. Engl, J. Kurzawa, S. E. Miller, S. Schneider, A. Stockmann, M. R. Wasielewski, *J. Phys. Chem. A* **2001**, *105*, 5655-5665.

[173] V. D. Parker, O. Hammerich, *Acta Chem. Scand., Ser. B* **1977**, *B31*, 883-889.

[174] B. S. Veldkamp, W.-S. Han, S. M. Dyar, S. W. Eaton, M. A. Ratner, M. R. Wasielewski, *Energy Envir. Sci.* **2013**, *6*, 1917-1928.

[175] V. V. Danilov, A. S. Panfutova, A. I. Khrebtov, S. Ambrosini, D. A. Videnichev, *Opt. Lett.* **2012**, *37*, 3948-3950.

[176] F. N. Castellano, *Dalton Transactions* **2012**, *41*, 8493-8501.

[177] a) T. W. Bell, N. M. Hext, *Chem. Soc. Rev.* **2004**, *33*, 589-598; b) L. Pu, *Chem. Rev.* **2004**, *104*, 1687-1716.

[178] a) J. Ding, D. W. Armstrong, *Chirality* **2005**, *17*, 281-292; b) K. Muñiz, *Chem. unserer Zeit* **2006**, *40*, 112-124.

[179] P. Fischer, F. Hache, *Chirality* **2005**, *17*, 421-437.

[180] B. L. Feringa, R. A. van Delden, N. Koumura, E. M. Geertsema, *Chem. Rev.* **2000**, *100*, 1789-1816.

[181] a) J. P. Riehl, F. S. Richardson, *Chem. Rev.* **1986**, *86*, 1-16; b) R. P. Lemieux, *Acc. Chem. Res.* **2001**, *34*, 845-853.

[182] G. Bringmann, A. J. Price Mortimer, P. A. Keller, M. J. Gresser, J. Garner, M. Breuning, *Angew. Chem. Int. Ed.* **2005**, *44*, 5384-5427.

[183] L. Pu, *Chem. Rev.* **1998**, *98*, 2405-2494.

[184] a) C. Schmuck, *Angew. Chem. Int. Ed.* **2003**, *42*, 2448-2452; b) R. Fasel, M. Parschau, K.-H. Ernst, *Nature* **2006**, *439*, 449-452.

[185] C. Wolf, W. A. König, C. Roussel, *Liebigs Annalen* **1995**, *1995*, 781-786.

[186] a) F. Würthner, Z. Chen, F. J. M. Hoeben, P. Osswald, C.-C. You, P. Jonkheijm, J. v. Herrikhuyzen, A. P. H. J. Schenning, P. P. A. M. van der Schoot, E. W. Meijer, E. H. A. Beckers, S. C. J. Meskers, R. A. J. Janssen, *J. Am. Chem. Soc.* **2004**, *126*,

10611-10618; b) E. H. A. Beckers, Z. Chen, S. C. J. Meskers, P. Jonkheijm, A. P. H. J. Schenning, X.-Q. Li, P. Osswald, F. Würthner, R. A. J. Janssen, *J. Phys. Chem. B* **2006**, *110*, 16967-16978.

[187] a) D. Franke, M. Vos, M. Antonietti, N. A. J. M. Sommerdijk, C. F. J. Faul, *Chem. Mat.* **2006**, *18*, 1839-1847; b) Y. Huang, Y. Yan, B. M. Smarsly, Z. Wei, C. F. J. Faul, *J. Mat. Chem.* **2009**, *19*, 2356-2362.

[188] a) P. Osswald, D. Leusser, D. Stalke, F. Würthner, *Angew. Chem. Int. Ed.* **2005**, *44*, 250-253; b) P. Osswald, F. Würthner, *Chem. Eur. J.* **2007**, *13*, 7395-7409.

[189] P. Osswald, F. Würthner, *J. Am. Chem. Soc.* **2007**, *129*, 14319-14326.

[190] Z. Xie, V. Stepanenko, K. Radacki, F. Würthner, *Chem. Eur. J.* **2012**, *18*, 7060-7070.

[191] N. Berova, L. D. Bari, G. Pescitelli, *Chem. Soc. Rev.* **2007**, *36*, 914-931.

[192] a) P. Csermely, R. Palotai, R. Nussinov, *Trends Biochem. Sci.* **2010**, *35*, 539-546; b) S. Gianni, J. Dogan, P. Jemth, *Biophys. Chem.* **2014**, *189*, 33-39.

[193] D. E. Koshland, *J. Cell. Comp. Physiol.* **1959**, *54*, 245-258.

[194] J. Monod, J. Wyman, J.-P. Changeux, *J. Mol. Biol.* **1965**, *12*, 88-118.

[195] H. W. Kroto, J. R. Heath, S. C. O'Brien, R. F. Curl, R. E. Smalley, *Nature* **1985**, *318*, 162-163.

[196] T. Kawase, H. Kurata, *Chem. Rev.* **2006**, *106*, 5250-5273.

[197] a) E. Huerta, G. A. Metselaar, A. Fragoso, E. Santos, C. Bo, J. de Mendoza, *Angew. Chem. Int. Ed.* **2007**, *46*, 202-205; b) E. Huerta, E. Cequier, J. d. Mendoza, *Chem. Commun.* **2007**, 5016-5018; c) Y. Shoji, K. Tashiro, T. Aida, *J. Am. Chem. Soc.* **2010**, *132*, 5928-5929.

[198] T. Nakanishi, *Chem. Commun.* **2010**, *46*, 3425-3436.

[199] a) T. Kawase, K. Tanaka, N. Fujiwara, H. R. Darabi, M. Oda, *Angew. Chem. Int. Ed.* **2003**, *42*, 1624-1628; b) T. Kawase, K. Tanaka, Y. Seirai, N. Shiono, M. Oda, *Angew. Chem. Int. Ed.* **2003**, *42*, 5597-5600; c) T. Kawase, K. Tanaka, N. Shiono, Y. Seirai, M. Oda, *Angew. Chem. Int. Ed.* **2004**, *43*, 1722-1724.

[200] a) T. Haino, Y. Matsumoto, Y. Fukazawa, *J. Am. Chem. Soc.* **2005**, *127*, 8936-8937; b) E. M. Perez, N. Martin, *Chem. Soc. Rev.* **2008**, *37*, 1512-1519; c) K. A. Nielsen, G. H. Sarova, L. Martín-Gomis, P. C. Stein, L. Sanguinet, E. Levillain, J. L. Sessler, D. M. Guldi, Á. Sastre-Santos, J. O. Jeppesen, *J. Am. Chem. Soc.* **2008**, *130*, 460-462.

[201] a) S. Mizyed, P. E. Georghiou, M. Bancu, B. Cuadra, A. K. Rai, P. Cheng, L. T. Scott, *J. Am. Chem. Soc.* **2001**, *123*, 12770-12774; b) A. Sygula, F. R. Fronczek, R. Sygula, P. W. Rabideau, M. M. Olmstead, *J. Am. Chem. Soc.* **2007**, *129*, 3842-3843; c) C. Muck-Lichtenfeld, S. Grimme, L. Kobryn, A. Sygula, *Phys. Chem. Chem. Phys.* **2010**, *12*, 7091-7097.

[202] a) E. M. Pérez, L. Sánchez, G. Fernández, N. Martín, *J. Am. Chem. Soc.* **2006**, *128*, 7172-7173; b) E. M. Pérez, M. Sierra, L. Sánchez, M. R. Torres, R. Viruela, P. M. Viruela, E. Ortí, N. Martín, *Angew. Chem. Int. Ed.* **2007**, *46*, 1847-1851; c) E. M. Perez, A. L. Capodilupo, G. Fernandez, L. Sanchez, P. M. Viruela, R. Viruela, E. Orti, M. Bietti, N. Martin, *Chem. Commun.* **2008**, 4567-4569; d) E. Huerta, H. Isla, E. M. Pérez, C. Bo, N. Martín, J. d. Mendoza, *J. Am. Chem. Soc.* **2010**, *132*, 5351-5353.

[203] M. Yanagisawa, K. Tashiro, M. Yamasaki, T. Aida, *J. Am. Chem. Soc.* **2007**, *129*, 11912-11913.

[204] a) J.-Y. Zheng, K. Tashiro, Y. Hirabayashi, K. Kinbara, K. Saigo, T. Aida, S. Sakamoto, K. Yamaguchi, *Angew. Chem. Int. Ed.* **2001**, *40*, 1857-1861; b) K. Tashiro, Y. Hirabayashi, T. Aida, K. Saigo, K. Fujiwara, K. Komatsu, S. Sakamoto, K. Yamaguchi, *J. Am. Chem. Soc.* **2002**, *124*, 12086-12087; c) H. Sato, K. Tashiro, H. Shinmori, A. Osuka, Y. Murata, K. Komatsu, T. Aida, *J. Am. Chem. Soc.* **2005**, *127*, 13086-13087; d) K. Tashiro, T. Aida, *Chem. Soc. Rev.* **2007**, *36*, 189-197; e) J. Song, N. Aratani, H. Shinokubo, A. Osuka, *J. Am. Chem. Soc.* **2010**, *132*, 16356-16357; f) K.-i. Sakaguchi, T. Kamimura, H. Uno, S. Mori, S. Ozako, H. Nobukuni, M. Ishida, F. Tani, *J. Org. Chem.* **2014**, *79*, 2980-2992.

[205] H. Yao, H. Zhang, M. Han, Z. Ding, Z. Zhang, Y. Liu, *Sci. China Chem.* **2010**, *53*, 1982-1986.

[206] a) J. Baffreau, S. Leroy-Lhez, N. Vân Anh, R. M. Williams, P. Hudhomme, *Chem. Eur. J.* **2008**, *14*, 4974-4992; b) L. Feng, M. Rudolf, S. Wolfrum, A. Troeger, Z. Slanina, T. Akasaka, S. Nagase, N. Martín, T. Ameri, C. J. Brabec, D. M. Guldi, *J. Am. Chem. Soc.* **2012**, *134*, 12190-12197; c) Y. Liu, J. Zhao, *Chem. Commun.* **2012**, *48*, 3751-3753; d) S. Pla, L. Martín-Gomis, K. Ohkubo, S. Fukuzumi, F. Fernández-Lázaro, Á. Sastre-Santos, *Asian J. Org. Chem.* **2014**, *3*, 185-197.

[207] C. C. Hofmann, S. M. Lindner, M. Ruppert, A. Hirsch, S. A. Haque, M. Thelakkat, J. Köhler, *J. Phys. Chem. B* **2010**, *114*, 9148-9156.

[208] a) E. Fron, R. Pilot, G. Schweitzer, J. Qu, A. Herrmann, K. Müllen, J. Hofkens, M. Van der Auweraer, F. C. De Schryver, *Photochem. Photobio. Sci.* **2008**, *7*, 597-604; b) E. Fron, G. Schweitzer, P. Osswald, F. Würthner, P. Marsal, D. Beljonne, K. Müllen, F. C. De Schryver, M. Van der Auweraer, *Photochem. Photobio. Sci.* **2008**, *7*, 1509-1521.

[209] O. Ito, *Res. Chem. Intermed.* **1997**, *23*, 389-402.

[210] J. D. Watson, F. H. C. Crick, *Nature* **1953**, *171*, 737-738.

[211] a) G. McDermott, S. M. Prince, A. A. Freer, A. M. Hawthornthwaite-Lawless, M. Z. Papiz, R. J. Cogdell, N. W. Isaacs, *Nature* **1995**, *374*, 517-521; b) J. Koepke, X. Hu, C. Muenke, K. Schulten, H. Michel, *Structure* **1996**, *4*, 581-597.

[212] a) U. Michelsen, C. A. Hunter, *Angew. Chem. Int. Ed.* **2000**, *39*, 764-767; b) C. Ikeda, A. Satake, Y. Kobuke, *Org. Lett.* **2003**, *5*, 4935-4938; c) D. Kim, A. Osuka, *Acc. Chem. Res.* **2004**, *37*, 735-745; d) J. K. Sprafke, B. Odell, T. D. W. Claridge, H. L. Anderson, *Angew. Chem. Int. Ed.* **2011**, *50*, 5572-5575; e) S. A. L. Rousseaux, J. Q. Gong, R. Haver, B. Odell, T. D. W. Claridge, L. M. Herz, H. L. Anderson, *J. Am. Chem. Soc.* **2015**, *137*, 12713-12718; f) H.-W. Jiang, T. Tanaka, T. Kim, Y. M. Sung, H. Mori, D. Kim, A. Osuka, *Angew. Chem. Int. Ed.* **2015**, *54*, 15197-15201; g) Y. M. Sung, M.-C. Yoon, J. M. Lim, H. Rath, K. Naoda, A. Osuka, D. Kim, *Nat. Chem.* **2015**, *7*, 418-422.

[213] F. Würthner, C. R. Saha-Möller, B. Fimmel, S. Ogi, P. Leowanawat, D. Schmidt, *Chem. Rev.* **2015**, *116*, 962-1052.

[214] a) F. C. De Schryver, T. Vosch, M. Cotlet, M. Van der Auweraer, K. Müllen, J. Hofkens, *Acc. Chem. Res.* **2005**, *38*, 514-522; b) T. Weil, T. Vosch, J. Hofkens, K. Peneva, K. Müllen, *Angew. Chem. Int. Ed.* **2010**, *49*, 9068-9093.

[215] a) B. Rybtchinski, L. E. Sinks, M. R. Wasielewski, *J. Phys. Chem. A* **2004**, *108*, 7497-7505; b) C. Hippius, F. Schlosser, M. O. Vysotsky, V. Böhmer, F. Würthner, *J. Am. Chem. Soc.* **2006**, *128*, 3870-3871.

[216] a) V. Dehm, M. Büchner, J. Seibt, V. Engel, F. Würthner, *Chem. Sci.* **2011**, *2*, 2094-2100; b) M. Son, B. Fimmel, V. Dehm, F. Würthner, D. Kim, *ChemPhysChem* **2015**, *16*, 1757-1767; c) B. Fimmel, M. Son, Y. M. Sung, M. Grüne, B. Engels, D. Kim, F. Würthner, *Chem. Eur. J.* **2015**, *21*, 615-630.

[217] a) S. Hecht, I. Huc, *Foldamers: Structure, Properties and Applications*, Wiley-VCH, Weinheim, **2007**; b) W. S. Horne, S. H. Gellman, *Acc. Chem. Res.* **2008**, *41*, 1399-1408; c) I. Saraogi, A. D. Hamilton, *Chem. Soc. Rev.* **2009**, *38*, 1726-

1743; d) G. Guichard, I. Huc, *Chem. Commun.* **2011**, *47*, 5933-5941; e) T. A. Martinek, F. Fülöp, *Chem. Soc. Rev.* **2012**, *41*, 687-702.

[218] a) K. Tahara, Y. Tobe, *Chem. Rev.* **2006**, *106*, 5274-5290; b) E. L. Spitler, C. A. Johnson, M. M. Haley, *Chem. Rev.* **2006**, *106*, 5344-5386.

[219] J. S. Moore, C. R. Ray, *Poly(arylene ethynylene)s: From Synthesis to Application*, Springer Berlin Heidelberg, Berlin, Heidelberg, **2005**.

[220] C. N. Pace, B. A. Shirley, J. A. Thompson, *Protein Structure: A Practical Approach*, IRL Press, New York, **1989**.

[221] K. E. Brown, B. S. Veldkamp, D. T. Co, M. R. Wasielewski, *J. Phys. Chem. Lett.* **2012**, *3*, 2362-2366.

[222] Z. Xiang, D. Cao, L. Dai, *Polym. Chem.* **2015**, *6*, 1896-1911.

[223] J. R. Lakowicz, *Principles of Fluorescence Spectroscopy*, 2 ed., New York, **1999**.

[224] R. M. Young, S. M. Dyar, J. C. Barnes, M. Juríček, J. F. Stoddart, D. T. Co, M. R. Wasielewski, *J. Phys. Chem. A* **2013**, *117*, 12438-12448.

[225] M. J. Frisch, G. W. Trucks, H. B. Schlegel, G. E. Scuseria, M. A. Robb, J. R. Cheeseman, G. Scalmani, V. Barone, B. Mennucci, G. A. Petersson, H. Nakatsuji, M. Caricato, X. Li, H. P. Hratchian, A. F. Izmaylov, J. Bloino, G. Zheng, J. L. Sonnenberg, M. Hada, M. Ehara, K. Toyota, R. Fukuda, J. Hasegawa, M. Ishida, T. Nakajima, Y. Honda, O. Kitao, H. Nakai, T. Vreven, J. A. Montgomery, Jr. J. E. Peralta, F. Ogliaro, M. Bearpark, J. J. Heyd, E. Brothers, K. N. Kudin, V. N. Staroverov, R. Kobayashi, J. Normand, K. Raghavachari, A. Rendell, J. C. Burant, S. S. Iyengar, J. Tomasi, M. Cossi, N. Rega, J. M. Millam, M. Klene, J. E. Knox, J. B. Cross, V. Bakken, C. Adamo, J. Jaramillo, R. Gomperts, R. E. Stratmann, O. Yazyev, A. J. Austin, R. Cammi, C. Pomelli, J. W. Ochterski, R. L. Martin, K. Morokuma, V. G. Zakrzewski, G. A. Voth, P. Salvador, J. J. Dannenberg, S. Dapprich, A. D. Daniels, Ö. Farkas, J. B. Foresman, J. V. Ortiz, J. Cioslowski, D. J. Fox, *Gaussian 09, Revision A.02, Gaussian, Inc.*, Wallingford CT, **2009**.

[226] a) A. D. Becke, *Phys. Rev. A* **1988**, *38*, 3098-3100; b) C. Lee, W. Yang, R. G. Parr, *Phys. Rev. B* **1988**, *37*, 785-789; c) A. D. Becke, *J. Chem. Phys.* **1993**, *98*, 5648-5652.

[227] E. A. Cobar, R. Z. Khaliullin, R. G. Bergman, M. Head-Gordon, *P. Natl. Acad. Sci.* **2007**, *104*, 6963-6968.

[228] F. Würthner, C. Thalacker, A. Sautter, W. Schärtl, W. Ibach, O. Hollricher, *Chem. Eur. J.* **2000**, *6*, 3871-3886.

[229] A. Sieblist, Bachelor Thesis, Universität Würzburg **2014**.